UNIVERSITAT ROVIRA I VIRGILI

UNCOVERING THE MECHANISTIC SCENARIOS OF NUCLEOPHILIC COUPLINGS IN CP*CO SYSTEMS

Sara López Resano

ADVERTIMENT. L'accés als continguts d'aquesta tesi doctoral i la seva utilització ha de respectar els drets de la persona autora. Pot ser utilitzada per a consulta o estudi personal, així com en activitats o materials d'investigació i docència en els termes establerts a l'art. 32 del Text Refós de la Llei de Propietat Intel·lectual (RDL 1/1996). Per altres utilitzacions es requereix l'autorització prèvia i expressa de la persona autora. En qualsevol cas, en la utilització dels seus continguts caldrà indicar de forma clara el nom i cognoms de la persona autora i el títol de la tesi doctoral. No s'autoritza la seva reproducció o altres formes d'explotació efectuades amb finalitats de lucre ni la seva comunicació pública des d'un lloc aliè al servei TDX. Tampoc s'autoritza la presentació del seu contingut en una finestra o marc aliè a TDX (framing). Aquesta reserva de drets afecta tant als continguts de la tesi com als seus resums i índexs.

ADVERTENCIA. El acceso a los contenidos de esta tesis doctoral y su utilización debe respetar los derechos de la persona autora. Puede ser utilizada para consulta o estudio personal, así como en actividades o materiales de investigación y docencia en los términos establecidos en el art. 32 del Texto Refundido de la Ley de Propiedad Intelectual (RDL 1/1996). Para otros usos se requiere la autorización previa y expresa de la persona autora. En cualquier caso, en la utilización de sus contenidos se deberá indicar de forma clara el nombre y apellidos de la persona autora y el título de la tesis doctoral. No se autoriza su reproducción u otras formas de explotación efectuadas con fines lucrativos ni su comunicación pública desde un sitio ajeno al servicio TDR. Tampoco se autoriza la presentación de su contenido en una ventana o marco ajeno a TDR (framing). Esta reserva de derechos afecta tanto al contenido de la tesis como a sus resúmenes e índices.

WARNING. Access to the contents of this doctoral thesis and its use must respect the rights of the author. It can be used for reference or private study, as well as research and learning activities or materials in the terms established by the 32nd article of the Spanish Consolidated Copyright Act (RDL 1/1996). Express and previous authorization of the author is required for any other uses. In any case, when using its content, full name of the author and title of the thesis must be clearly indicated. Reproduction or other forms of for profit use or public communication from outside TDX service is not allowed. Presentation of its content in a window or frame external to TDX (framing) is not authorized either. These rights affect both the content of the thesis and its abstracts and indexes.

UNIVERSITAT ROVIRA I VIRGILI
UNCOVERING THE MECHANISTIC SCENARIOS OF NUCLEOPHILIC COUPLINGS IN CP*CO SYSTEMS
Sara López Resano

UNIVERSITAT
ROVIRA i VIRGILI

Uncovering the Mechanistic Scenarios of Nucleophilic Couplings in Cp*Co Systems

---

SARA LÓPEZ RESANO

DOCTORAL THESIS

2023

Sara Lopez Resano

Uncovering the Mechanistic Scenarios of Nucleophilic Couplings in Cp*Co Systems

DOCTORAL THESIS
Supervised by
Prof. Feliu Maseras Cuní and Prof. Mónica Helvia Pérez Temprano
Institute of Chemical Research of Catalonia (ICIQ)

Tarragona, 2023

ICIQ
Institut
Català
d'Investigació
Química

UNIVERSITAT ROVIRA i VIRGILI

ICIQ
Institut
Català
d'Investigació
Química

UNIVERSITAT ROVIRA i VIRGILI

ICIQ - Institut Català d'Investigació Química
Avgda, Països Catalans 16,
43007 Tarragona (Spain)

Prof. Feliu Maseras Cuní and Prof. Mónica Helvia Pérez Temprano, group leaders at the Institute of Chemical Research of Catalonia,

We STATE that the present study, entitled " Uncovering the Mechanistic Scenarios of Nucleophilic Couplings in Cp*Co Systems " presented by Sara López Resano for the award of the degree of Doctor, has been carried out under our supervision in our groups at the Institute of Chemical Research of Catalonia and that it fulfills all the requirements to be eligible for the International Doctor Distinction.

Tarragona, June 5th, 2023

Doctoral Thesis Supervisors

Prof. Feliu Maseras Cuní

Prof. Mónica Helvia Pérez Temprano

List of publications

The following publications are based on the work described below in this Doctoral Thesis:

*"Redefining the Mechanistic Scenario of Carbon−Sulfur Nucleophilic Coupling via High-Valent Cp*Co(III) Species"*
S. López-Resano, S. Martínez de Salinas, F. A. Garcés-Pineda, A. Moneo-Corcuera, J. R. Galán-Mascarós, F. Maseras, M. H. Pérez-Temprano, *Angew. Chemie. Int. Ed.* **2021**, *60*, 11217–11221.

"Transition metal-catalysed directed C–H functionalization with nucleophiles"
S. Barranco, J. Zhang, S. López-Resano, A. Casnati, M. H. Pérez-Temprano, *Nat. Synth.* **2022**, *1*, 841–853.

The following publication has been also developed during this Thesis, but it will not be disclosed here.

"Non-innocent Role of the Halide Ligand in the Copper-Catalyzed Olefin Aziridination Reaction "
M. R. Rodríguez, A. M Rodríguez, S. López-Resano, M. A. Pericàs, M. M. Díaz-Requejo, F. Maseras, P. J. Pérez, *ACS Catal.* **2023**, *13*, 706–713.

Table of Contents

Chapter 1. General Introduction

Chapter 2. Redefining the Mechanistic Scenario of Carbon–Sulfur Nucleophilic Coupling via High-Valent Cp*Co(IV) Species

Chapter 3. Study on the Mechanism of the Oxidatively Induced C–I Reductive Elimination from high-valent Cp*Co species with F^+ oxidants

Chapter 4. Reactivity Studies on C–X and C–C bond forming reactions from cyclometalated Cp*Co complexes

Abbreviations and Acronyms

The abbreviations and acronyms used in the following manuscript are those standardized by the “Guideline of Authors” of the ACS. For ease of reading, the meaning of each abbreviation and acronym has been specified the first time that appears. Additional abbreviations and acronyms used in this manuscript are listed below:

Å	angstrom(s)
acm	acetamide
AcOH	acetic acid
ald	aldehyde
Alk	alkyl
amd	amide
Ar	argon, aryl
BHT	butylated hydroxytoluene
bpy	bipiridine
Bu	Butyl
Bu	Butyl
CA	Chtonoamperometry
cat.	catalitic
COSY	homonuclear correlation spectroscopy
Cp	cyclopentadientyl
Cp*	pentamethylcyclopentadienyl
CV	Cyclic Voltammetry
d	doublet
DCE	1,2-Dichloroethane
DCM	dichloromethane
DFT	density functional theory
DG	directing group
DMSO	dimethyl sulfoxide
E	electrophile
e-	electron
EPR	electron paramagnetic resonance
equiv.	equivalent
ESI	electrospray ionization
Et	ethyl
Et2O	diethyl ether
Fc	Ferrocene
FG	functional group
g	gram(s); prefix to NMR abbreviation denoting gradient-selected
GGA	generalized gradient approximation
h	hour(s)
HF	Hartree-Fock
HMBC	heteronuclear multiple bond correlation
HR	high resolution
HRMS	high-resolution mass spectrometry

HSQC	heteronuclear single quantum correlation
Hz	hertz
imi	imine
IR	infrared
IRC	intrinsic reaction coordinate
J	coupling constant (in NMR spectrometry)
K	kelvin(s) (absolute temperature)
KBB	Knowledge building blocks
L	liter(s)
LED	Light Emitting Diode
LSF	Late-stage functionalization
LUMO	Lowest Occupied Molecular Orbital
M	Metal; molar (moles per liter)
m	multiplet (spectral); meter(s); milli
m/z	mass-to-charge ratio
Me	methyl
MeCN	acetonitrile
MECP	Minimum-energy crossing point
MHz	Megahertz
min	minute(s)
MO	Molecular Orbital
mol	mole(s)
MS	mass spectrometry; molecular sieves
MW	molecular weight
NBO	Natural Bond Orbitals
NFSI	N-Fluorobenzenesulfonimide
NFTPB	1-Fluoro-2,4,6-trimethylpyridinium tetrafluoroborate
NFTPT	1-Fluoro-2,4,6-trimethylpyridinium triflate
nHex	hexane
NMR	nuclear magnetic resonance
NOESY	Nuclear Overhauser effect spectroscopy
Nuc	Nucleophile
OAc	acetate
ºC	degrees Celsius
on	Over night
ORE	Oxidatively induced reductive elimination
ORTEP	Oak Ridge Thermal Ellipsoid Plot
OTf	trifluoromethanesulfonate
OTFA	trifluoro acetate
ox	Oxidant
p	para
PCM	Polarizable Continuum Model
Ph	Phenyl
PIDA	(Diacetoxyiodo)benzene
PIFA	(Bis(trifluoroacetoxy)iodo)benzene
PivOH	pivalic acid
ppm	part(s) per million
ppy	phenylpyridine
py	pyridine

q	Quartet (state); quartet (spectral)
R	Carbon based organic substituent, alkyl or aryl
RE	Reductive elimination
ref.	reference
RI-NMR	rapid-injection NMR spectroscopy
rt	room temperature
s	singlet (spectral, state); second(s)
SCF	self-consistent field
SET	single electron transfer
SHE	standard hydrogen electrode
S_N2	bimolecular nucleophilic substitution
SQUID	superconducting quantum interference device
SRP	standard reduction potential
t	triplet (spectral;state); time
tBu-amd	tButyl amide
TDTT	S-(trifluoromethyl)-dibenzothiophenium triflate
TEMPO	2,2,6,6,tetramethylpiperidin-1-oxyl
Tf	trifluoromethanesulfonyl (triflyl)
THF	tetrahydrofuran
TM	transition metal
TMS	trimethylsilyl; tetramethylsilane
TOF	time-of-flight; turnover frequency
TON	turnover number
Tp	trispyrazolylborate
Ts	para-toluenesulfonyl (tosyl)
TS	transition state
UV	ultraviolet
Vis	visible
vol	volume
VTMS	Vinyltrimethylsilane
X	Heteroatom
XRD	x-ray diffraction
δ	chemical shift (in part per million) downfield from tetramethylsilane
µ	micro

UNIVERSITAT ROVIRA I VIRGILI
UNCOVERING THE MECHANISTIC SCENARIOS OF NUCLEOPHILIC COUPLINGS IN CP*CO SYSTEMS
Sara López Resano

Abstract

The ability to create complex molecules is a fundamental aspect of chemistry, with wide-ranging applications in fields such as pharmaceuticals or materials science. In recent decades, there has been a notable focus on developing efficient synthetic methodologies for constructing complex molecules. Transition metal-catalyzed C–H functionalization and cross coupling reactions, initially relying on noble transition metals like palladium (Pd), rhodium (Rh), or ruthenium (Ru), have revolutionized synthetic chemistry by enabling the direct formation of carbon-carbon and carbon-heteroatom bonds in a predictable and regioselective manner. These advances have reshaped the way chemists approach synthesis and have opened up new avenues for forging chemical bonds by utilizing the direct interaction of the transition metal center with organic fragments.

The progress made with noble transition metals has been largely driven by a deep understanding of reaction mechanisms, reactive intermediates, and the factors governing their catalytic activity. As a result, these metals have reached a level of maturity in their applications. However, there has been a growing emphasis on enhancing the sustainability of chemical processes on a global scale. This renewed focus has sparked interest in exploring the potential of first-row transition metals, such as cobalt (Co), in catalysis. First-row metals like cobalt offer distinct advantages due to their intrinsic properties, including the access to high-valent cobalt intermediates that can trigger unprecedented transformations that cannot procced at lower oxidation states. These properties enable the discovery of new reaction modes and catalytic cycles, potentially opening doors to novel reactivities. However, these same properties have also limited their widespread use, as they are often perceived as unpredictable and difficult to control. To overcome these challenges, a fundamental understanding of these systems is essential.

In this thesis, the research aims to investigate nucleophilic couplings with Cp*Co-base systems. This type of catalysts have shown remarkable potential in C-H functionalization reactions particularly involving electrophiles as coupling partners. However, methodologies involving nucleophiles in conjunction with Cp*Co^{III} complexes remain limited. Through systematic studies and characterization of reactive

intermediates, this work intends to shed light on the factors influencing the nucleophilic couplings from Cp*Co complexes with the goal of gaining a deeper understanding of these systems and exploring the intermediary of high-valent species. We envision that our results can contribute to expand the reactivity patterns of these first-row metal systems and their use in synthetic chemistry.

In the course of this thesis, the reader will be driven through first a general introduction, which will give an overview of the reported examples of first-row high-valent organometallic complexes and their reactivity. Next, three main research chapters containing the main results of the thesis, finishing with a general conclusion.

Chapter 2, entitled '*Redefining the Mechanistic Scenario of Carbon–Sulfur Nucleophilic Coupling via High-Valent Cp*Co^{IV} Species'* provides the first experimental and computational evidences of the intermediacy of high-valent cobalt systems in Cp*Co-catalyzed C–H functionalizations. Our work oxidatively induced reductive elimination (ORE) events, via high-valent Cp*Co^{IV} species, that can be triggered under chemical and electrochemical oxidative conditions. This work has been published in *Angew. Chem. Int. Ed.* **2021**, *60*, 11217–11221.

Chapter 3, entitled '*Study on the Mechanism of the Oxidatively Induced C–I Reductive Elimination from high-valent Cp*Co species with F^{+} oxidants'* uncovers the capability of F^{+} oxidants, widely used in high-valent transition metal catalysis, to trigger C–I bond-forming reactions. By combining experimental and computational approaches, we have discovered the participation of slightly different reaction pathways depending on the nature of the employed oxidant, along with the involvement of Co^{V} species.

Chapter 4, entitled *'Reactivity Studies on C–X and C–C bond forming reactions from cyclometalated Cp*Co complexes'* investigate the reactivity towards reductive elimination events of a family of metalacyclic Cp*Co^{III} complexes that contain different heteroatom- and carbon-based nucleophilic moieties. We reveal that the nature of nucleophile and/or directing group plays a major role in the reductive elimination step. Furthermore, we demonstrate that cobalt(III) complexes can directly participate in C–C reductive eliminations. An account about the nucleophilic coupling with transition metals, including Co in directed C–H activation was published in *Nat. Synth.* **2022**, *1*, 841–853.

UNIVERSITAT ROVIRA I VIRGILI
UNCOVERING THE MECHANISTIC SCENARIOS OF NUCLEOPHILIC COUPLINGS IN CP*CO SYSTEMS
Sara López Resano

Chapter 1. General Introduction

1.1. High-Valent Organometallic species

Molecules are the building blocks of everything around us, from the air we breathe to the clothes we wear. The ability to create complex molecules is a fundamental aspect of chemistry, with applications ranging from drug development to materials science. The development of new synthetic methodologies that allow for the efficient construction of complex molecules has been a major focus of research over the past few decades. The effort was highlighted in 2010 by the Nobel Prize in Chemistry, awarded to Heck, Negishi, and Suzuki for their ground-breaking contributions to the development of palladium-catalyzed cross-coupling reactions. This breakthrough has enabled the construction of new C–C bonds for synthesizing carbon-based molecules that resemble those found in nature and has become an essential tool in the field of synthetic chemistry.[1] The reaction proceeds with an organic electrophile and an organometallic nucleophile, usually catalyzed by palladium, see Scheme 1.1.

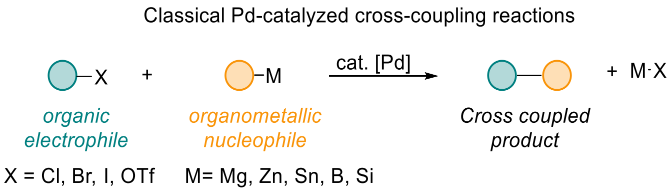

Scheme 1.1 Classical Pd-catalyzed cross-coupling reactions.

The development of new chemical transformations has traditionally relied on trial-and-error experiments and serendipitous discoveries, with little emphasis on rational design based on knowledge-driven approaches. However, a shift towards a more sustainable approach has highlighted the importance of utilizing rational design in chemical synthesis, in order to save time and resources. In this context, understanding the mechanisms of chemical reactions is essential. Both experimental and computational methods have been crucial for developing and improving sustainable transition metal-catalyzed transformations, by using key reaction intermediates. These intermediates can be used as knowledge building blocks (KBBs), which depend on the concept that *'the success or failure of a whole chemical process relies on the performance of the reaction intermediates involved in each elementary step that constitutes the catalytic*

---

[1] The Nobel Prize in Chemistry 2010. Press Release. 6 October 2010. https://www.nobelprize.org/prizes/chemistry/2010/press-release/

cycle'.[2] The study of the reactivity of these intermediates could lead to overcoming limitations and developing efficient and novel transformations.

In this regard, we focus our attention on one of the key differences in organometallic chemistry, the use of high-valent and low-valent systems, which refers to the oxidation state of the metal center. The formal oxidation state of a central atom in a transition metal complex is typically determined by the charge left after the ligands have been removed in their most stable form. In this definition, the bonding electron pairs between the metal center and the ligands are assigned solely to the most electronegative bonding partners, typically the ligands.[3] When the bonding between metal and ligands is mostly ionic, assigning a formal oxidation state is straightforward. However, when there is significant covalent bonding or the presence of redox-active ligands, it can be more complex and the assigned formal oxidation state may not reflect the true electronic charge distribution. High-valent refers to the metal being in an oxidation state greater than its typical oxidation state, which can vary for each metal, for example, high-valent compounds of palladium are Pd(III) and Pd(IV).[4] For a long time, it has been suggested that high-valent organometallic intermediates are involved in cross-coupling and C–H bond functionalization reactions, especially involving C–C and C–heteroatom bond forming reactions. However, despite the proposal of these intermediates, their detection has been elusive for many years, leading to significant controversy over the mechanistic details of these reactions.

An illustrative example of the significance of high-valent organometallic catalysis is the field of Pd chemistry (Scheme 1.2). For several decades now, the use of palladium catalysts in transition metal-catalyzed reactions has been a highly effective and dependable approach for creating new chemical bonds.[5] Most of these cross-coupling reactions involve $Pd^{0/II}$ catalytic cycles, also known as low-valent Pd catalysis. Although these systems are widely used and hold significant synthetic value, certain

---

[2] J. Sanjosé-Orduna, Á. L. Mudarra, S. Martínez de Salinas, M. H. Pérez-Temprano, *ChemSusChem* **2019**, *12*, 2882–2897.

[3] S. Riedel, M. Kaupp, *Coord. Chem. Rev.* **2009**, *253*, 606–624.

[4] A. J. Hickman, M. S. Sanford, *Nature* **2012**, *484*, 177–185.

[5] a) J. K. Stille, *Angew. Chemie Int. Ed. English* **1986**, *25*, 508–524. b) A. F. Littke, G. C. Fu, *Angew. Chemie - Int. Ed.* **2002**, *41*, 4176–4211. c) C. C. C. Johansson Seechurn, M. O. Kitching, T. J. Colacot, V. Snieckus, *Angew. Chemie - Int. Ed.* **2012**, *51*, 5062–5085. d) D. Roy, Y. Uozumi, *Adv. Synth. Catal.* **2018**, *360*, 602–625.

types of transformations still cannot be achieved through the low-valent pathway. Examples include the formation of C(sp^3)–halogen and C–CF$_3$ bonds, which remain difficult to achieve through low-valent Pd mechanisms.[6] The efficiency of these reactions may be hindered by high kinetic barriers to reductive elimination. However, high-valent Pd complexes generally exhibit low activation barriers and high thermodynamic driving forces during reductive elimination.[7] This unique feature has expanded the range of feasible coupling reactions, offering distinct mechanisms and selectivities.[8] High-valent Pd catalysis complements low-valent Pd catalysis in terms of both substrate scope and the types of bonds that can be formed.

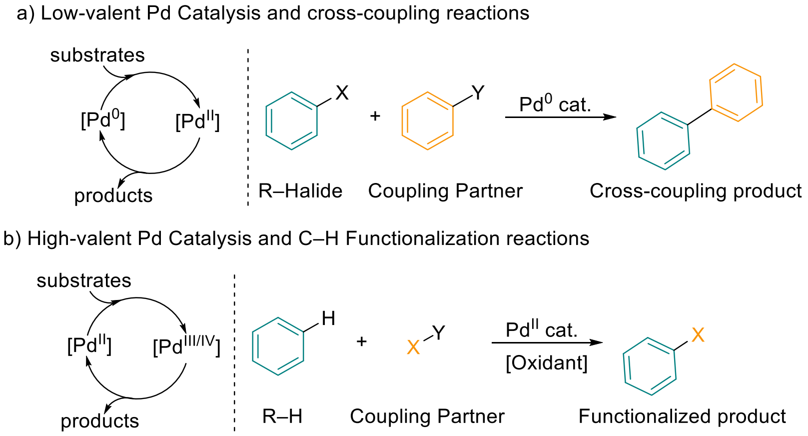

Scheme 1.2 Comparison between Pd catalysis at low-valent and high-valent systems.[9]

---

[6] a) D. A. Watson, M. Su, G. Teverovskiy, Y. Zhang, J. Garcia-Fortanet, T. Kinzel, S. L. Buchwaldf, *Science* **2009**, *325*, 1661–1664. b) X. Chen, K. M. Engle, D. H. Wang, Y. Jin-Quan, *Angew. Chemie - Int. Ed.* **2009**, *48*, 5094–5115. c) E. J. Cho, T. D. Senecal, T. Kinzel, Y. Zhang, D. A. Watson, S. L. Buchwald, *Science* **2010**, *328*, 1679–1681. d) V. V. Grushin, *Acc. Chem. Res.* **2010**, *43*, 160–171. e) O. A. Tomashenko, V. V. Grushin, *Chem. Rev.* **2011**, *111*, 4475–4521. f) S. L. Marquard, J. F. Hartwig, *Angew. Chemie - Int. Ed.* **2011**, *50*, 7119–7123.

[7] J. F. Hartwig, *Nature* **2008**, *455*, 314–322.

[8] For selective reviews on Pd(IV) as catalyst: a) K. Muñiz, *Angew. Chemie - Int. Ed.* **2009**, *48*, 9412–9423. b) T. W. Lyons, M. S. Sanford, *Chem. Rev.* **2010**, *110*, 1147–1169. c) A. J. Hickman, M. S. Sanford, *Nature* **2012**, *484*, 177–185. d) K. M. Engle, T. S. Mei, M. Wasa, J. Q. Yu, *Acc. Chem. Res.* **2012**, *45*, 788–802. e) J. J. Topczewski, M. S. Sanford, *Chem. Sci.* **2015**, *6*, 70–76.

[9] In some cases, the oxidant can be the coupling partner

UNIVERSITAT ROVIRA I VIRGILI
UNCOVERING THE MECHANISTIC SCENARIOS OF NUCLEOPHILIC COUPLINGS IN CP*CO SYSTEMS
Sara López Resano

While Pd is well-known for its proficiency in cross-coupling and C–H activation reactions, the other precious metals like Pt,[10] Ir,[11,12] and Rh,[12,13] have also demonstrated their effectiveness in these types of reactions throughout history. However, the desire to develop more sustainable and cost-effective methods has led to focus on first-row transition metals that are more abundant and less toxic.[14] Besides, as they can undergo one electron processes, they can offer new and complementary reactivities. While there are already several reported methods using first-row transition metals, understanding the underlying mechanisms of these reactions is limited due to the instability of intermediates and their ability to undergo both one- and two-electron processes. Over the last few decades, significant advances have been made in these systems, resulting in a substantial increase in the knowledge acquired.[15] In the context of high-valent systems, while Cu and Ni systems have been extensively studied, other systems such as Fe, Mn, and Co are still in their infancy. In what follows, we will provide an overview of the reported examples of first-row high-valent organometallic complexes and their reactivity.

---

[10] a) J. A. Labinger, *Chem. Rev.* **2017**, *117*, 8483–8496. b) M. Albrecht, G. Van Koten, *Angew. Chemie - Int. Ed.* **2001**, *40*, 3750–3781.

[11] X. Li, W. Ouyang, J. Nie, S. Ji, Q. Chen, Y. Huo, *ChemCatChem* **2020**, *12*, 2358–2384.

[12] a) J. Wencel-Delord, F. W. Patureau, F. Glorius, *Top. Organomet. Chem.* **2016**, *55*, 1–28. b) J. G. Kim, K. Shin, S. Chang, *Top. Organomet. Chem.* **2016**, *55*, 29–52.

[13] a) G. Song, F. Wang, X. Li, *Chem. Soc. Rev.* **2012**, *41*, 3651–3678. b) S. S. Li, L. Qin, L. Dong, *Org. Biomol. Chem.* **2016**, *14*, 4554–4570. c) R. Wang, X. Xie, H. Liu, Y. Zhou, *Catalysts* **2019**, *9*, DOI 10.3390/catal9100823.

[14] a) T. Dalton, T. Faber, F. Glorius, *ACS Cent. Sci.* **2021**, *7*, 245–261. b) N. Kaplaneris, L. Ackermann, *Beilstein J. Org. Chem.* **2022**, *18*, 86–88.

[15] P. Gandeepan, T. Müller, D. Zell, G. Cera, S. Warratz, L. Ackermann, *Chem. Rev.* **2019**, *119*, 2192–2452.

1.2. Copper

For a long time, researchers have suggested that high-valent copper intermediates, specifically organometallic Cu(III) species, play a crucial role in both copper-catalyzed cross-coupling and organocuprate reactions. The product-releasing step of many of these transformations is thought to involve the formation of a carbon–carbon and/or carbon–heteroatom bond from an organo–Cu(III) species. However, despite their proposed importance, these high-valent copper intermediates have remained undetected for many years, leading to considerable debate over the precise mechanisms behind the abovementioned transformations. In fact, until recently, these two methods were among the least understood synthetic techniques in the field of organometallic chemistry. As a result, the controversy and open questions regarding their mechanisms have provided significant motivation for investigating the accessibility and reactivity of organo–Cu(III) species.

Only a few examples of high-valent organometallic copper complexes were reported in the literature before the year 2000. These compounds were stabilized by rigid, chelating, and/or perfluorinated ligands (Scheme 1.3).[16] There has been significant debate surrounding the oxidation state of copper in the complex synthesized by Naumann. A theoretical study conducted by Snyder suggested that the CF_3 ligands can create an inverted ligand field. This means that the empty orbital in the complex had primarily ligand-based character, with little contribution from metal d_{x2-y2}, thus better described as a Cu(I) complex.[17a] Although Snyder's work faced criticism and conflicting reports, recent studies have supported Snyder's proposal.[17] Spectroscopic evidence has confirmed near-complete occupation of the 3d orbitals of Cu in the

---

[16] a) M. A. Willert-Porada, D. J. Burton, N. C. Baenziger, *J. Chem. Soc. Chem. Commun.* **1989**, 1633–1634. b) D. Naumann, T. Roy, K. -F Tebbe, W. Crump, *Angew. Chemie Int. Ed. English* **1993**, *32*, 1482–1483. c) R. Eujen, B. Hoge, D. J. Brauer, *J. Organomet. Chem.* **1996**, *519*, 7–20. d) H. Furuta, H. Maeda, A. Osuka, *J. Am. Chem. Soc.* **2000**, *122*, 803–807. e) R. Santo, R. Miyamoto, R. Tanaka, T. Nishioka, K. Sato, K. Toyota, M. Obata, S. Yano, I. Kinoshita, A. Ichimura, T. Takui, *Angew. Chemie - Int. Ed.* **2006**, *45*, 7611–7614.

[17] a) J. P. Snyder, *Angew. Chemie Int. Ed. English* **1995**, *34*, 80–81. b) R. Hoffmann, S. Alvarez, C. Mealli, A. Falceto, T. J. Cahill, T. Zeng, G. Manca, *Chem. Rev.* **2016**, *116*, 8173–8192. c) J. S. Steen, G. Knizia, J. E. M. N. Klein, *Angew. Chemie - Int. Ed.* **2019**, *58*, 13133–13139. d) I. M. Dimucci, J. T. Lukens, S. Chatterjee, K. M. Carsch, C. J. Titus, S. J. Lee, D. Nordlund, T. A. Betley, S. N. MacMillan, K. M. Lancaster, *J. Am. Chem. Soc.* **2019**, *141*, 18508–18520.

complex.[18] These complexes are structurally interesting but not reactive towards carbon-carbon and carbon-heteroatom bond-forming reactions, making their relevance to copper catalysis uncertain.

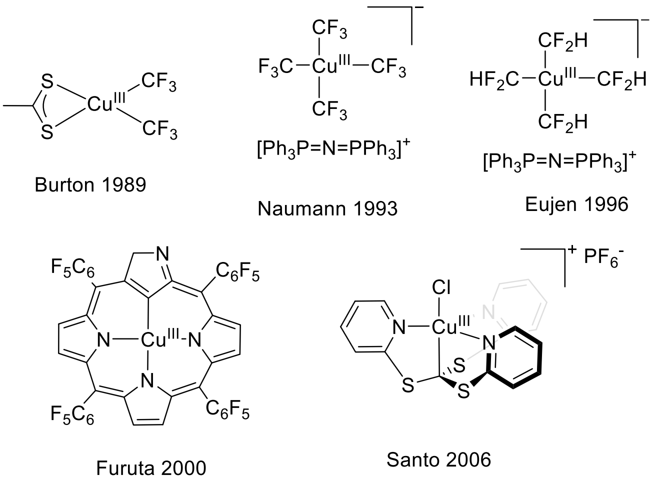

Scheme 1.3 First stable and isolatable high-valent Cu(III) organometallic complexes.

Next, we will discuss the two representative areas involving high-valent Cu(III) organometallic complexes are C–heteroatom and C–C couplings.

1.2.1. C–heteroatom bond formation

The ability of copper catalysts to promote the amination of aryl boronic acids,[19] aryl halides,[20] and carbon-hydrogen bonds[21] is widely known. Pyrazole, pyridone, and phthalimide are among the nitrogen heterocycles that are the most effective coupling partners, and the reactions typically occur under mild conditions. While some researchers proposed the involvement of Cu(III) as intermediates in these transformations, there was significant debate surrounding this hypothesis, with others suggesting that single-electron transfer, halide atom transfer, or σ-bond metathesis at

---

[18] R. C. Walroth, J. T. Lukens, S. N. MacMillan, K. D. Finkelstein, K. M. Lancaster, *J. Am. Chem. Soc.* **2016**, *138*, 1922–1931.

[19] J. X. Qiao, P. Y. S. Lam, *Synthesis (Stuttg).* **2011**, 829–856.

[20] K. Kunz, U. Scholz, D. Ganzer, *Synlett* **2003**, 2428–2439.

[21] a) G. Brasche, S. L. Buchwald, *Angew. Chemie - Int. Ed.* **2008**, *47*, 1932–1934. b) R. T. Gephart, T. H. Warren, *Organometallics* **2012**, *31*, 7728–7752.

low-valent Cu(I) or Cu(II) are more probable mechanisms.[22] A turning point for this field was done in 2002. Ribas reported the synthesis of the first Cu(III)–monoaryl species (Scheme 1.4) obtained through C–H bond activation of a Cu(II) species, which disproportionated into a Cu(I) and a Cu(III) species.[23] Similar to other early examples, the Cu(III) metal center is stabilized by an electron-donating macrocyclic ligand. Further study by Stahl *et al.* showed their reactivity with amines (pyridine, oxazolidinone, or acetanilide) to form C–N bonds. This report represents a significant advancement in the understanding of these reactions, as no direct observation of C–N bond formation from a Cu(III) complex had been previously reported.[24]

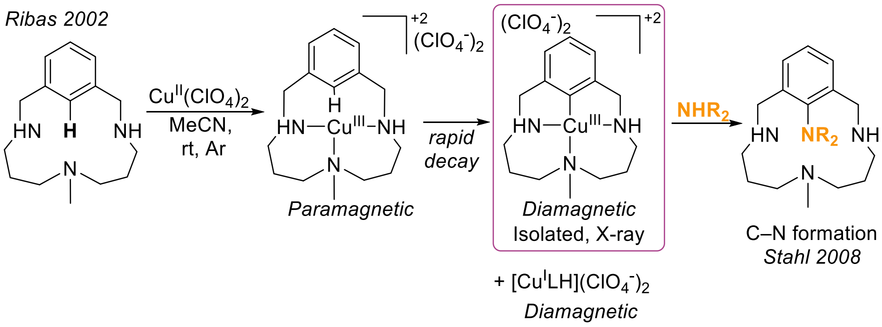

Scheme 1.4 First Cu(III)-monoaryl species and its reactivity with amines.

The Ullman condensation reaction is a reliable and efficient method for building C–heteroatom (O, S, N) bonds from aryl halides. However, despite numerous proposed mechanistic pathways, it was not until 2010 that a mechanistic study was conducted on a well-defined aryl–Cu(III) complex, and evidence of a Cu(III) species in catalysis had been observed.[25] Typically, the activation of the aryl halide is the rate-limiting step, and the intermediates that follow are short-lived, making it challenging to capture a putative Cu(III) intermediate.[26] Ribas and Stahl's groups observed for the first time the fundamental oxidative addition and reductive elimination steps at a copper(I) complex

---

[22] a) T. Cohen, J. Wood, A. G. Dietz, *Tetrahedron Lett.* **1974**, *15*, 3555–3558. b) G. O. Jones, P. Liu, K. N. Houk, S. L. Buchwald, *J. Am. Chem. Soc.* **2010**, *132*, 6205–6213. c) H. Z. Yu, Y. Y. Jiang, Y. Fu, L. Liu, *J. Am. Chem. Soc.* **2010**, *132*, 18078–18091.

[23] X. Ribas, D. A. Jackson, B. Donnadieu, J. Mahía, T. Parella, R. Xifra, B. Hedman, K. O. Hodgson, A. Llobet, T. D. P. Stack, *Angew. Chemie - Int. Ed.* **2002**, *41*, 2991–2994.

[24] L. M. Huffman, S. S. Stahl, *J. Am. Chem. Soc.* **2008**, *130*, 9196–9197.

[25] A. Casitas, A. E. King, T. Parella, M. Costas, S. S. Stahl, X. Ribas, *Chem. Sci.* **2010**, *1*, 326–330.

[26] A. Casitas, X. Ribas, *Chem. Sci.* **2013**, *4*, 2301–2318.

using pentacoordinated aryl–Cu(III)-halide complexes stabilized by triazamacrocyclic ligands (Scheme 1.5).[25] They were able to directly observe aryl halide reductive elimination triggered by the addition of Brønsted acids, and the reversal step, aryl halide oxidative addition at copper(I) to form the corresponding copper(III) species, was found to be favorable and fast. The two redox states were demonstrated to be in reversible interconversion via the sequential addition of triflic acid and Protonsponge® to an acetonitrile solution of aryl–Cu(III)–bromide complex.

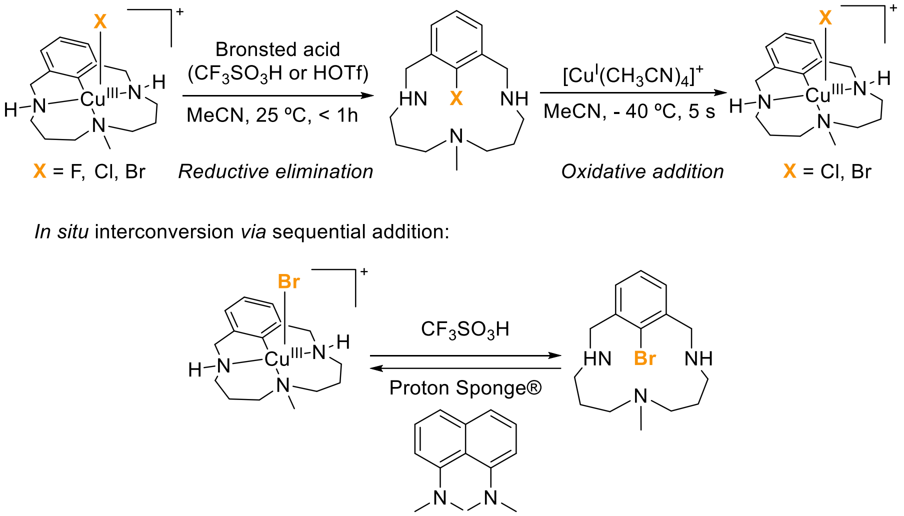

Scheme 1.5 Top: Reductive elimination to form a C–heteroatom bond from a well stablished Cu(III) species and oxidative addition. Bottom: *In situ* conversion between the two redox states.

Besides, they provided the first experimental evidence of the participation of aryl–Cu(III) in a catalytic C–N bond formation species, since a constant concentration of Cu(III) intermediate was observed by UV-vis and NMR spectroscopy. Subsequent studies by the same group showed the role of Cu(III) species in various C–H bond functionalization reactions. For example, in 2011 they demonstrated the feasibility of halide-exchange reactions using a $Cu^{I/III}$ redox catalytic cycle.[27]

Stahl and Ribas demonstrated that aryl–Cu(III)-halide complexes can be intermediates in not only copper-catalyzed C–N bond-formation, but also in C–O, C–S, C–Se and C–

---

[27] A. Casitas, M. Canta, M. Solà, M. Costas, X. Ribas, *J. Am. Chem. Soc.* **2011**, *133*, 19386–19392.

P bond-forming reactions (Scheme 1.6).[28] They were able to couple a wide variety of nucleophiles, such as amides, phenols, alcohols, carboxylic acids, thiols, bezeneselenol, and H-phosphonate diesters.

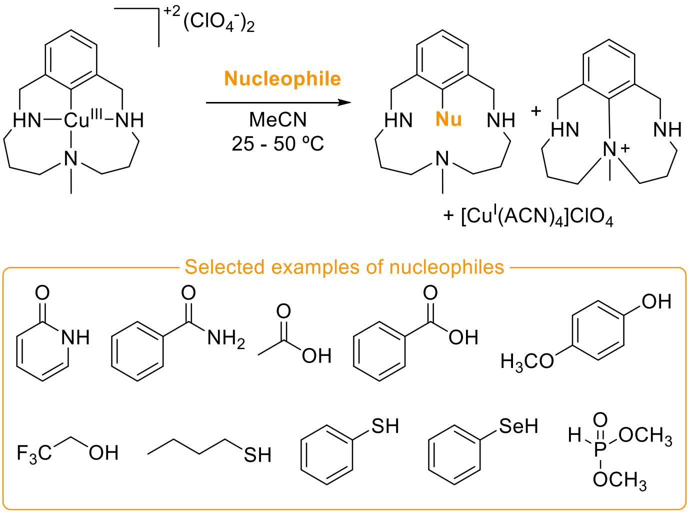

Scheme 1.6 C–heteroatom (N, O, S, Se and P) bond formation from well stablished macrocyclic triaza-ligated aryl–Cu(III) complex reported by Sthal and Ribas.

Similarly, Wang and co-workers reported the synthesis of a Cu(III) complex stabilized by a azacalix[1]arene[3]pyridine macrocylic ligand (Scheme 1.7).[29] This compound showed reactivity towards nucleophiles to form C–heteroatom bonds (carboxylates, halide salts, cyanides, aliphatic alcohols and phenols);[30] and C–C bonds (phenulacetydes and alkyllithium reagents).[31] These reactivity patterns support the feasibility of aryl–Cu(III) intermediates in Ullmann condensation reactions and suggest the implication of these intermediates in other copper-catalyzed reactions.

---

[28] C–N formation: L. M. Huffman, S. S. Stahl, *J. Am. Chem. Soc.* **2008**, *130*, 9196–9197. C–O formation: L. M. Huffman, A. Casitas, M. Font, M. Canta, M. Costas, X. Ribas, S. S. Stahl, *Chem. - A Eur. J.* **2011**, *17*, 10643–10650. C–S,Se,P formation: M. Font, T. Parella, M. Costas, X. Ribas, *Organometallics* **2012**, *31*, 7976–7982.

[29] a) B. Yao, D. X. Wang, Z. T. Huang, M. X. Wang, *Chem. Commun.* **2009**, 2899–2901. b) B. Yao, Z. L. Wang, H. Zhang, D. X. Wang, L. Zhao, M. X. Wang, *J. Org. Chem.* **2012**, *77*, 3336–3340.

[30] Z. L. Wang, L. Zhao, M. X. Wang, *Org. Lett.* **2011**, *13*, 6560–6563.

[31] a) Z. L. Wang, L. Zhao, M. X. Wang, *Org. Lett.* **2012**, *14*, 1472–1475. b) Z. L. Wang, L. Zhao, M. X. Wang, *Chem. Commun.* **2012**, *48*, 9418–9420.

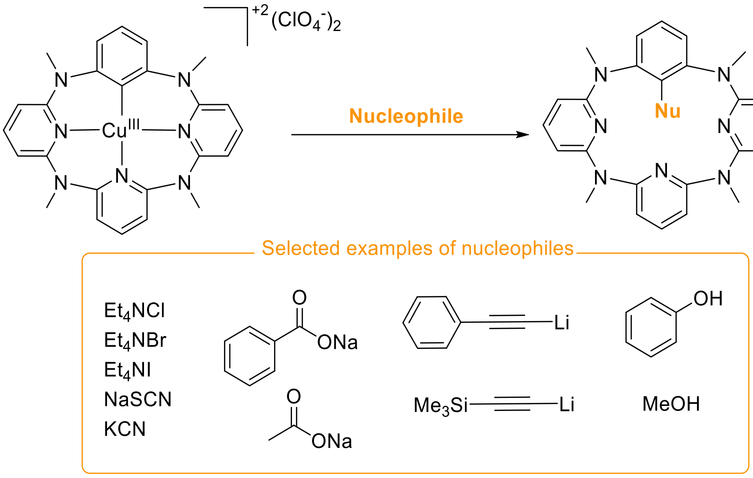

Scheme 1.7 Wang's study on azacalix[1]arene[3]pyridine Cu(III) complex platform, coupling several nucleophiles, to form either C–O and C–C bonds.

1.2.2. C–C bond formation

The formation of C–C bonds from high-valent Cu(III) species remains a relatively unexplored area, with only a handful of examples reported to date. The relevancy of Cu(III) intermediates for the C–C bond forming step on reactions of organocuprates with enones, allyl and alkyl halides was uncover by computational studies.[32] However, until 2007 when rapid-injection NMR spectroscopy (RI-NMR) was developed, there was no experimental observation of these species. RI-NMR at low temperature (-100 ºC) enabled the characterization of unstable intermediates (Scheme 1.8).[33] Additionally, when heated, these distinct organo–Cu(III) intermediates suffer a reductive elimination process that resulted in forming carbon-carbon bonds.

---

[32] a) N. Yoshikai, E. Nakamura, *Chem. Rev.* **2012**, *112*, 2339–2372. b) T. Cohen, J. Wood, A. G. Dietz, *Tetrahedron Lett.* **1974**, *15*, 3555–3558 c) A. E. Dorigo, J. Wanner, P. von Ragué Schleyer, *Angew. Chemie Int. Ed.* **1995**, *34*, 476–478. d) J. P. Snyder, *J. Am. Chem. Soc.* **1995**, *117*, 11025–11026.

[33] S. H. Bertz, S. Cope, M. Murphy, C. A. Ogle, B. J. Taylor, *J. Am. Chem. Soc.* **2007**, *129*, 7208–7209.

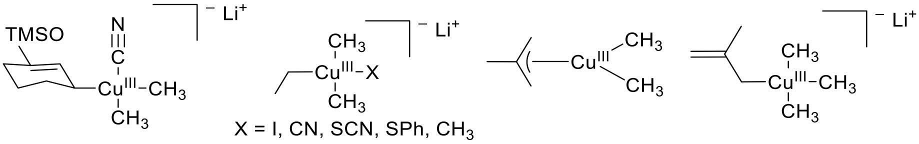

Scheme 1.8 Cu(III) intermediates of organocuprate reactions detected at -100 ºC using rapid-injection NMR spectroscopy.

In 2015, Grushin developed a more robust synthesis of a neutral Cu(III) complex by reacting bipyridine and the homoleptic $[Bu_4N][Cu(CF_3)_4]$ salt, as shown in Scheme 1.9.[34] The resulting Cu(III) complex can act as a precursor to various other Cu(III) species that are capable of forming C–C bonds, as we will discuss further later on.

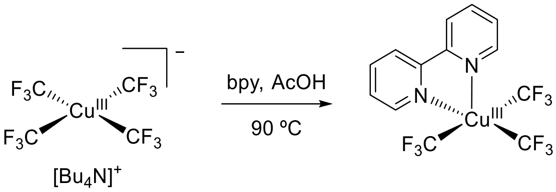

Scheme 1.9 Grushin's neutral Cu(III) complex.

Shortly after, Xi used spiro-structure ligands to stabilize organocopper(III) species, Scheme 1.10.[35] This complex is stable when being heated to reflux in THF, however, it reacts with HCl, I_2, or MeI to form aryl–aryl bonds at room temperature. The C(sp^2)–C(sp^2) bond-forming process might proceed via an electrophilic attack from methylation reagent and then further reductive elimination reaction of Cu(III) intermediate. The detection of an arylcopper(I) complex, although without the possibility of isolation or characterization, provides supporting evidence for a reductive elimination of Cu(III).

---

[34] A. M. Romine, N. Nebra, A. I. Konovalov, E. Martin, J. Benet-Buchholz, V. V. Grushin, *Angew. Chemie - Int. Ed.* **2015**, *54*, 2745–2749.

[35] L. Liu, M. Zhu, H. T. Yu, W. X. Zhang, Z. Xi, *J. Am. Chem. Soc.* **2017**, *139*, 13688–13691.

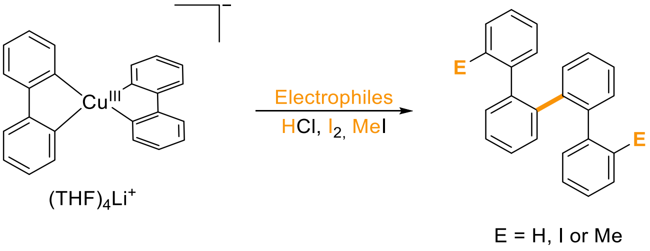

Scheme 1.10 Spiro-aryl–Cu(III) and C–C reductive elimination in the presence of electrophiles.

Despite the two reported examples by Xi and Wang demonstrating the formation of C–C bonds from a well-established Cu(III) species, the requirement of a special ligand or specific structures limits their applicability. Consequently, controversy still exists regarding the mechanism of Cu-catalyzed C–C bond formation. Liu utilized the stabilizing properties of the CF_3 group in Cu(III) complexes to report the first example of reductive elimination resulting in the formation of a C(sp^3)–CF_3 bond from a well-defined transition metal complex, shown in Scheme 1.11.[36] They reported the synthesis,[37] and reductive elimination activity of a novel class of organometallic copper(III) complexes, [alkylCu^{III}(CF_3)$_3$]$^-$ with diverse functional groups.

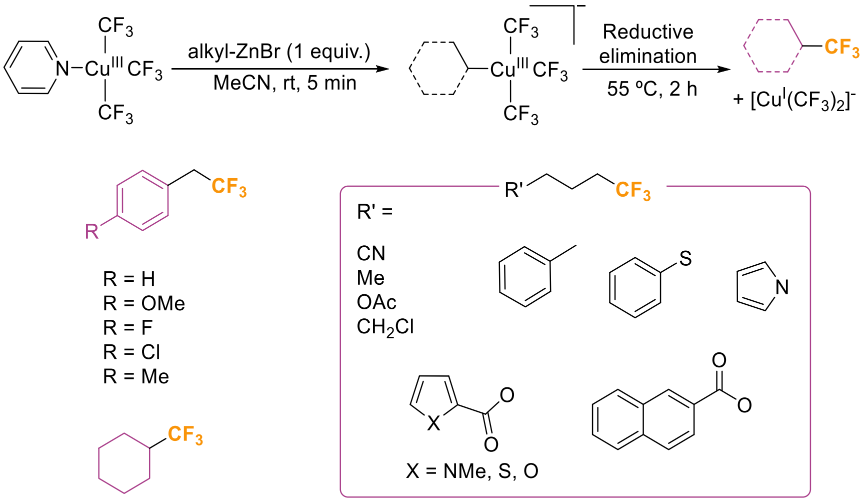

Scheme 1.11 C(sp^3)–CF_3 reductive elimination from a stable ionic Cu(III) species.

---

[36] M. Paeth, S. B. Tyndall, L. Y. Chen, J. C. Hong, W. P. Carson, X. Liu, X. Sun, J. Liu, K. Yang, E. M. Hale, D. L. Tierney, B. Liu, Z. Cao, M. J. Cheng, W. A. Goddard, W. Liu, *J. Am. Chem. Soc.* **2019**, *141*, 3153–3159.

[37] Using Grushin's Cu(III) as the precursor

The Cu(III) compounds containing diverse functional groups, such as alkenyl, nitrile, acetal, thiol ether, and heterocyclic were synthesized via transmetalation with alkyl zinc reagents. The stability of these compounds was observed for hours at room temperature and weeks at -20 ºC. Primary and secondary alkyl–Cu species were detected by HR ESI-MS, while tertiary species were not observed. In addition, late-stage functionalization was performed on estrone, gemfibrozil, Vitamin E, indomethacin, and thalidomide. The formation of a C(sp^3)–CF_3 bond through reductive elimination was facilitated by heating the high-valent complexes. Mechanistic studies, including DFT, NBO analysis, Hammet plot, Eyring plot analysis, Cu(I) detection support the reductive elimination path.

Shortly after, Shen demonstrated the formation of aryl–CF_3 bonds from a well-defined Cu(III) complex[37] (Scheme 1.12) via a three-membered ring transition state in a concerted bond-forming process, which was supported by various methods, including radical inhibitors, EPR experiments, measuring rate constants, Eyring analysis, and DFT.[38] It should be noted that all of Liu's examples involve highly fluorinated substituted aryls with only a functional group in the para position to the CF_3.

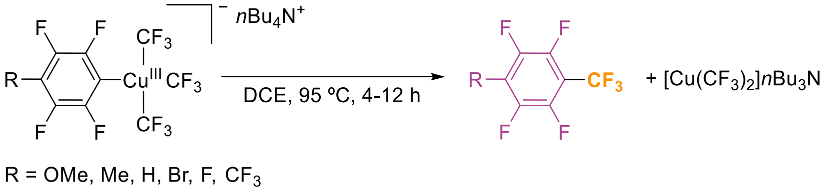

Scheme 1.12 C(sp2)–CF_3 reductive elimination from a stable ionic Cu(III) species.

The same authors observed the formation of Me–CF_3 from a neutral five-coordinated organocopper(III) complex[37] (Scheme 1.13) through a synchronous bond-breaking/bond-forming process via a similar three-membered ring transition state, with THF as the only effective solvent.[39] This concerted reductive elimination pathway was confirmed by radical inhibitors, kinetics and rate constants, Eyring analysis, and DFT calculations.

---

[38] Z. Lu, H. Liu, S. Liu, X. Leng, Y. Lan, Q. Shen, *Angew. Chemie - Int. Ed.* **2019**, *58*, 8510–8514.

[39] S. Liu, S. Liu, H. Liu, S. Liu, Z. Lu, C. Lu, X. Leng, Y. Lan, Q. Shen, *J. Am. Chem. Soc.* **2020**, *142*, 9785–9791.

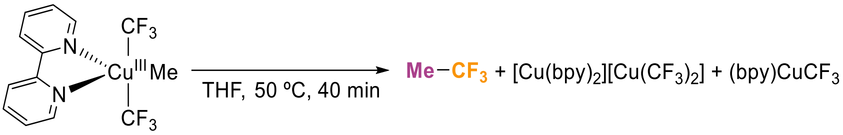

Scheme 1.13 CH_3–CF_3 reductive elimination from a neutral Cu(III) complex.

In general, significant progress has been made understanding of high-valent copper complexes in the study of carbon-carbon and carbon-heteroatom bond formation using organo-Cu(III) species in stoichiometric and catalytic transformations. As fundamental studies of organo-Cu(III) continue, a better understanding of mechanisms involved is anticipated, leading to the development of new synthetic methods.

1.3. *Nickel*

Despite nickel was considered the spirited horse among TMs, over the past decades this metal has emerged as a privilege catalyst for cross-couplings and C-H activation reaction. In part, this has been possible to its wide range of oxidation state, including III and IV that it has been shown can play a crucial role in C–C and C–heteroatom bond formation reactions.[40] The first Ni(III) and Ni(IV) organometallic complexes were reported more than 40 years ago by Kochi in 1978 and Smart in 1982 (Scheme 1.14).[41] However, in the past decades, significant advances were made in the synthesis of high-valent organometallic Ni complexes and their reactivity in various organic transformations.

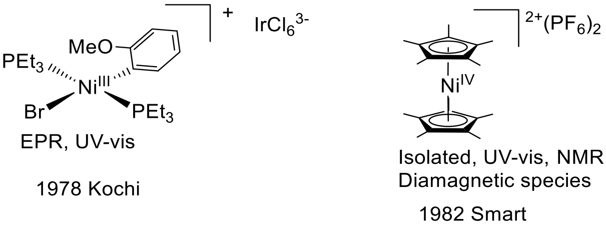

Scheme 1.14 First observed organometallic Ni(III) and Ni(IV) species.

---

[40] a) V. B. Phapale, D. J. Cárdenas, *Chem. Soc. Rev.* **2009**, *38*, 1598–1607. b) J. B. Diccianni, T. Diao, *Trends Chem.* **2019**, *1*, 830–844.

[41] a) T. T. Tsou, J. K. Kochi, *J. Am. Chem. Soc.* **1978**, *100*, 1634–1635. b) J. L. Robbins, N. Edelstein, B. Spencer, J. C. Smart, *J. Am. Chem. Soc.* **1982**, *104*, 1882–1893.

Ni(III) and Ni(IV) species, which were previously challenging to access, are now enabling a diverse range of organic transformations in a complementary fashion to reactions involving Ni(0) and Ni(II) intermediates.

1.3.1. Organometallic Ni(III) complexes

The first reported Ni(III) complex by Kochi (Scheme 1.14) underwent reductive elimination while warming up the solution as evidenced by EPR experiments.[41b] In 1983, van Koten and colleagues used a pincer ligand to stabilize the Ni(III) center. They managed to synthesize a family of Ni[$C_6H_3(CH_2NMe_2)_2$-2,6]X_2, (X = Cl, Br, I) by the chemical or electrochemical oxidation of the corresponding Ni(II) pincer complex with electrophiles (Scheme 1.15).[42] Later in 1995, they introduced a chiral pincer ligand containing amino acid-derived moieties.[43] In more recent studies, Sanford demonstrated that a Ni(III) pincer complex is capable of facilitating C–Br reductive elimination,[44] while Zargarian's studies explored its effectiveness forming the C–Cl, O, N bonds.[45] Zargarian's group managed to isolate several Ni(III) complexes with different pincer ligands (PCP, PCN). [46]

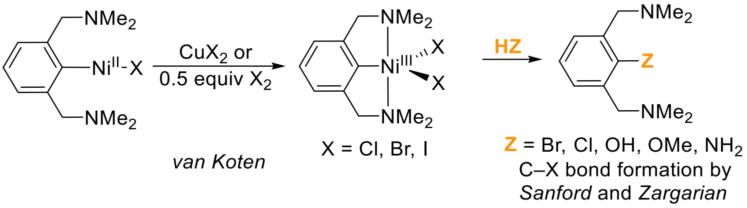

Scheme 1.15 The first isolated organometallic Ni(III) complex, with a NCN pincer ligand and subsequent reactivity to form C–heteroatom bonds.

In 2014, Mirica and coworkers synthesized a range of Ni(III) (aryl)halide complexes that were stable at low temperatures. They can undergo transmetalation with Grignard

---

[42] D. M. Grove, G. van Koten, R. Zoet, N. W. Murrall, A. J. Welch, *J. Am. Chem. Soc.* **1983**, *105*, 1379–1380.

[43] L. A. van de Kuil, Y. S. J. Veldhuizen, D. M. Grove, J. W. Zwikker, L. W. Jenneskens, W. Drenth, W. J. J. Smeets, A. L. Spek, G. van Koten, *J. Organomet. Chem.* **1995**, *488*, 191–197.

[44] A. T. Higgs, P. J. Zinn, S. J. Simmons, M. S. Sanford, *Organometallics* **2009**, *28*, 6142–6144.

[45] J. P. Cloutier, D. Zargarian, *Organometallics* **2018**, *37*, 1446–1455.

[46] a) A. Castonguay, A. L. Beauchamp, D. Zargarian, *Organometallics* **2008**, *27*, 5723–5732. b) V. Pandarus, D. Zargarian, *Organometallics* **2007**, *26*, 4321–4334.

reagents, substituting the Br/Cl for a Me group, Scheme 1.16.[47] These complexes exhibited rapid formation of C–Br, and C–C bonds at room temperature. Besides, they are also competent catalysts for Negishi and Kumada couplings. Overall, these results are strong evidence of the involvement of Ni(III) species in cross-coupling events.

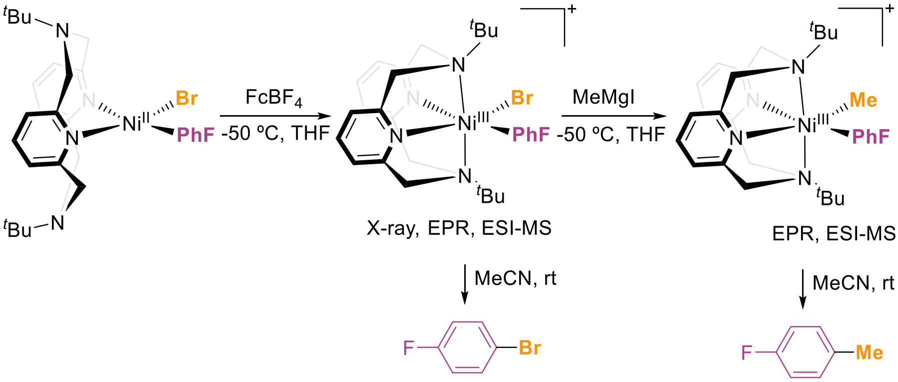

Scheme 1.16 Mirica's Ni(III) complexes and their reductive elimination, forming C–Br and C–C bonds.

One year later, the same research group reported a Ni(III) complex containing two CF_3 moieties, which remained stable at room temperature under N_2 atmosphere (Scheme 1.17).[48] No C–C reductive elimination is obtained upon heating or under photolysis conditions and only trace amounts of CF_3H and C_2F_6 were observed. The lack of reactivity of the complex is in agreement with the stabilization properties of both the tetradentate N-donor ligand, *N,N'*-dialkyl-2,11-diaza[3.3](2,6)pyridinophane (also used to stabilize Pd(III) complexes) and the CF_3 moieties.

---

[47] B. Zheng, F. Tang, J. Luo, J. W. Schultz, N. P. Rath, L. M. Mirica, *J. Am. Chem. Soc.* **2014**, *136*, 6499–6504.

[48] F. Tang, N. P. Rath, L. M. Mirica, *Chem. Commun.* **2015**, *51*, 3113–3116.

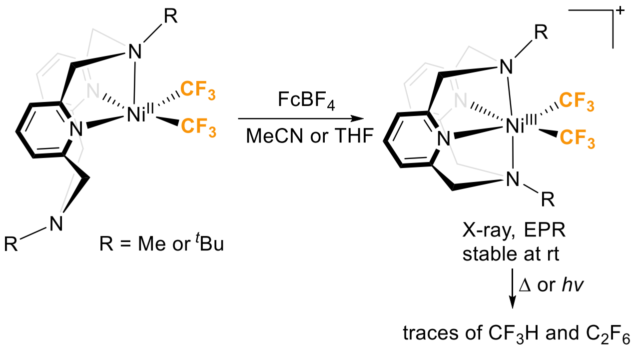

Scheme 1.17 Mirica's Ni(III)CF$_3$ complex.

In 2015, Mirica's group modified the tetradentate pyridinophane ligand, by adding one phenyl group (Scheme 1.18).[49] To obtain the Ni(III) species the authors oxidize the Ni(II) precursor with ferrocenium, followed by halide abstraction with AgSbF$_6$. The formation of C–O bond was obtained either by NaOMe addition to the disolvento complex or by addition of an oxidant to the dimethoxide Ni(III). Because of the effectiveness of the oxidation, they proposed that the reaction occurs through a Ni(IV) complex.[50]

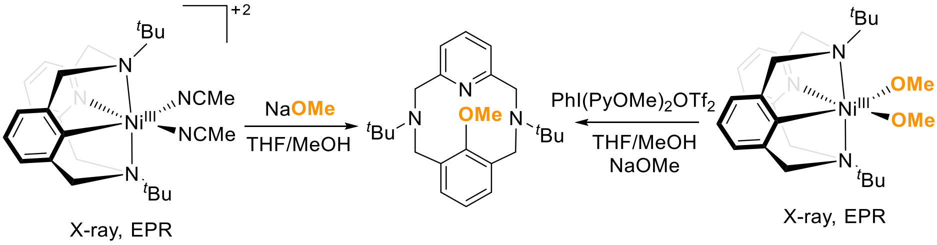

Scheme 1.18 C–O bond formation from well-established Ni(III) complexes.

In 2016, Sanford conducted a study on the C–C bond formation from a family of Ni(III) complexes stabilized by anionic trispyrazolylborate (Tp) ligand.[51] The Ni(II) precursors were isolated to examine their electrochemical properties. They observed two different behaviors (Scheme 1.19). On one hand, the Ni(II) complexes that have a reversible Ni$^{II/III}$ redox peak, they could isolate the corresponding Ni(III) complexes:

---

[49] W. Zhou, J. W. Schultz, N. P. Rath, L. M. Mirica, *J. Am. Chem. Soc.* **2015**, *137*, 7604–7607.

[50] By this time the report by Sanford[57] on Ni(IV) species was already published

[51] J. R. Bour, N. M. Camasso, E. A. Meucci, J. W. Kampf, A. J. Canty, M. S. Sanford, *J. Am. Chem. Soc.* **2016**, *138*, 16105–16111.

$TpNi^{III}(CF_3)_2$, $TpNi^{III}CF_3Ph$ and [$TpNi^{III}$(cyclo-neophenyl)]. On the other hand, [$TpNi^{II}CF_3CH_3$] and $TpNi^{II}(C_6F_5)_2$ exhibited irreversible redox peaks and their corresponding Ni(III) complexes were not able to be isolated. However, their reactivity with a one electron oxidant, $FcBF_4$, led to the formation of reductive elimination products. The Ni(III) intermediate was not detected by EPR. In the case of the isolated Ni(III) complexes, upon mild heating, two of these complexes underwent reductive elimination to form a C–C bond, resulting in the formation of (trifluoromethyl)benzene and benzocyclobutane, but no CF_3–CF_3 coupling was observed. Mechanistic investigations indicated that the direct reductive elimination from Ni(III) was the most probable mechanism.

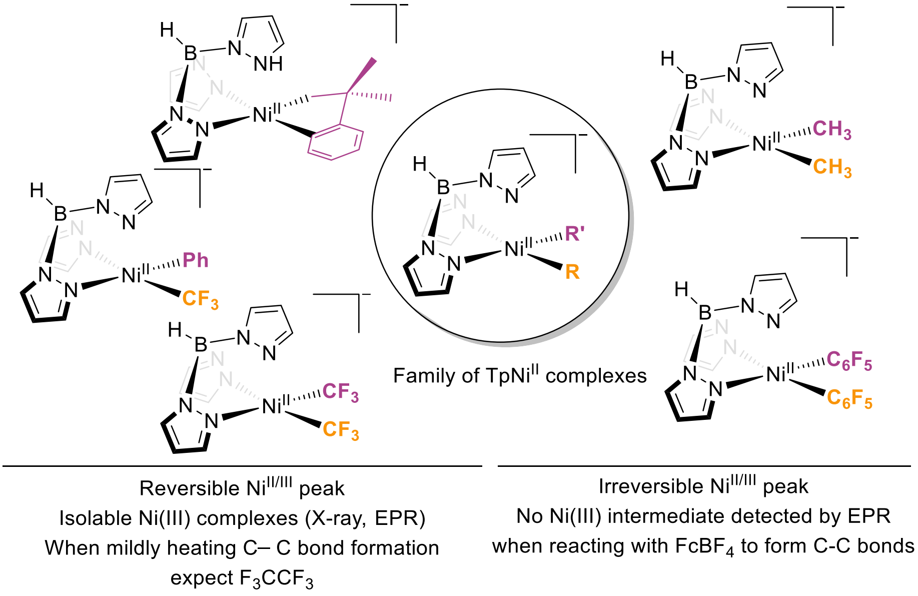

Scheme 1.19 Study on C-C bond formation from a family of [$TpNi^{II}RR'$]$^-$ complexes.

The process of creating carbon-heteroatom bonds through reductive elimination becomes increasingly challenging with the rise of heteroatom electronegativity, reduction in polarizability, and enhancement of the metal-ligand bond strength. For example, the formation of C–F bonds is particularly rare when compared to C–C, C–N, and C–O bonds. Therefore, the exploitation of high-valent TM complexes, including first-row metals, has been explored in order to unlock this challenging but interesting transformation..[52] In 2017 Ritter reported the formation of an C(sp^2)–F from well-defined Ni(III) complex (Scheme 1.20).[53] They used a bidentate ligand, 2-(2-pyridinyl)phenyl-2-nitrovenzenesulfonamide, and a F$^+$ oxidant, selectfluor, to oxidize the Ni(II) complex. By doing EPR studies of different Ni systems, they could characterize two intermediate Ni(III) species, which were in equilibrium even at low temperature, subsequent heating of the mixture afforded the fluorinated product.

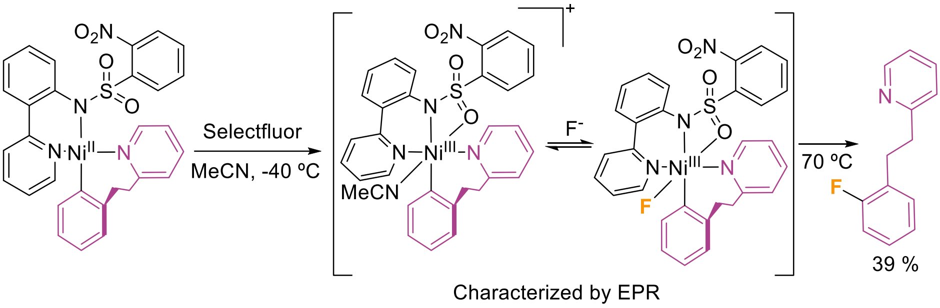

Scheme 1.20 C–F bond formation from a Ni(III) intermediate.

1.3.2. Organometallic Ni(IV) complexes

In 1994, Klein reported the first example of structurally characterized Ni(IV) species, which was accessed by the two electron oxidation of a Ni(II) precursor with methyl iodine.[54] Dimitrov and Linden synthesized a quasi-tetrahedral Ni(IV) complex in 2003, with more exotic carbon-donor ligand, which consisted of three 1-norboryl ligands and a halide ion. Their attempt to isolate a homoleptic Ni(IV) complex by adding 1-norbornyl lithium to remove the halide ligand was unsuccessful. Instead, they observed the formation of di-norbornene, a product resulting from C–C bond formation.[55]

In 2009, Nuckolls and colleagues reported a stable tetraalkyl Ni(IV) complex, which was also supported by carbon donor ligands, two (5*Z*,11*E*)-dibenzo[a,e]cyclooctatetraene. Notably, this Ni(IV) complex is air-stable and can

---

[52] a) T. Furuya, C. A. Kuttruff, T. Ritter, **2008**, *11*, 803–819. b) T. Furuya, A. S. Kamlet, T. Ritter, *Nature* **2011**, *473*, 470–477. c) A. N. Ragan, Y. Kraemer, W. Y. Kong, S. Prasad, D. J. Tantillo, C. R. Pitts, *Angew. Chemie - Int. Ed.* **2022**, *61*, 1–6.

[53] H. Lee, J. Börgel, T. Ritter, *Angew. Chemie - Int. Ed.* **2017**, *56*, 6966–6969.

[54] H. F. Klein, A. Bickelhaupt, T. Jung, G. Cordier, *Organometallics* **1994**, *13*, 2557–2559.

[55] V. Dimitrov, A. Linden, *Angew. Chemie - Int. Ed.* **2003**, *42*, 2631–2633.

withstand temperatures above 290 °C without any decomposition, probably because of metal shielding by the bulky ligands.[56]

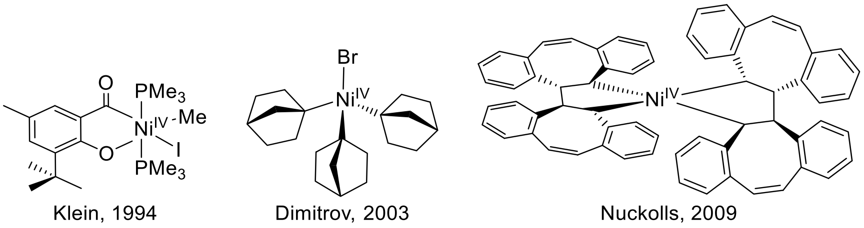

Scheme 1.21 First examples of high-valen Ni(IV) organometallic complexes.

Despite the existence of stable Ni(IV) complexes for approximately 40 years, Camasso and Sanford disclosed the first Ni(IV) compounds capable of promoting cross-coupling events, which clarified uncertainties about the role of Ni(IV) species in these reactions.[57] By drawing upon their knowledge of related Pd(IV)-chemistry, a stable Ni(IV) platform was designed. First, they used a Ni(cyclo-neophenyl) core, recognized to increase stability vs H_β-elimination and reductive elimination, however, when oxidizing, $[(bpy)Ni^{II}(CH_2CMe_2\text{-}o\text{-}C_6H_4)]$ complex with three different oxidants (NFTPT, PIDA or $PhICl_2$),[58] the formation of benzocyclobutane was observed in a few minutes at rt, without being able to detect Ni(IV) (Scheme 1.22, top). They could stabilize the Ni(IV) complex by replacing one of the X-type ligand for σ-donating CF_3 ligand, using S-(trifluoromethyl)-dibenzothiophenium triflate (TDTT) as an oxidant, which transfers a CF_3^+ moiety. In this case, the Ni(IV) compound, that undergoes reductive elimination at rt after 15 h, was characterized *in situ* by ^{19}F and ^{1}H NMR.

---

[56] M. Carnes, D. Buccella, J. Y. C. Chen, A. P. Ramirez, N. J. Turro, C. Nuckolls, M. Steigerwald, *Angew. Chemie - Int. Ed.* **2009**, *48*, 290–294.

[57] N. M. Camasso, M. S. Sanford, *Science* **2015**, *347*, 1218–1220.

[58] PIDA stands for (Diacetoxyiodo)benzene and NFTPT is 1-Fluoro-2,4,6-trimethylpyridinium triflate.

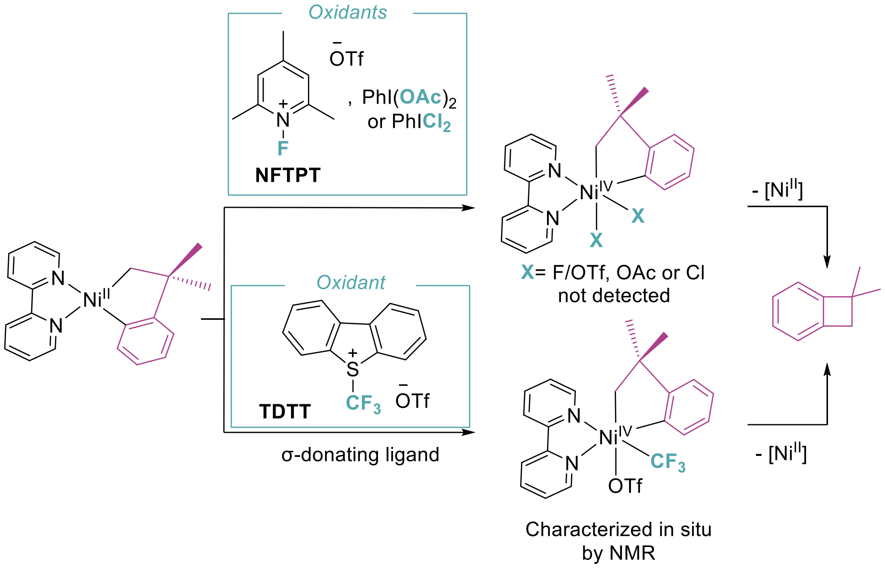

Scheme 1.22 Reaction of [(bpy)Ni^{II}(cyclo-neophenyl)] with different oxidants.

To increase the stability of the suggested Ni(IV) intermediate, a facial tridentate ligand, tris(2-pyridyl)methane (Py_3CH) was used to replace the bidentate ligand (Scheme 1.23). In this case, the reaction between [Py_3CH)Ni^{II}(cyclo-neophenyl)] and TDTT afforded a Ni(IV) complex that could be isolated and unambiguously characterized by X-ray spectroscopy. By heating the Ni(IV) complex at 95 ºC, the authors observed the quantitative formation of benzocyclobutane, while C–O bond formation was observed at room temperature in the presence of NMe_4OAc. In sharp contrast, additional exogenous nucleophiles, such as NMe_4OPh or NMe_4SPh, led to difficult mixtures of products due to the high electrophilicity of the Ni(IV) complex, which was attributed to its overall +1 charge.

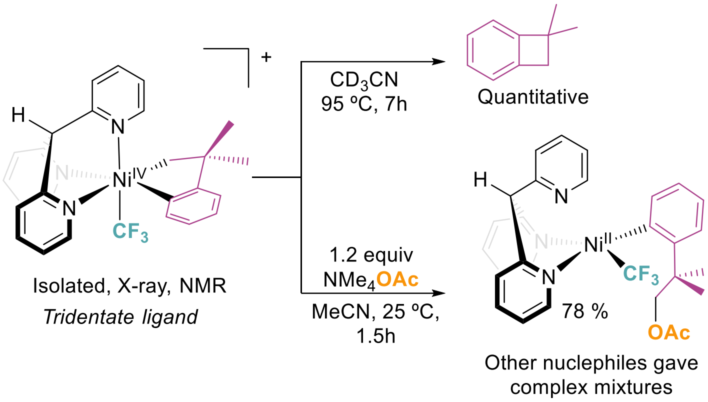

Scheme 1.23 Reactivity of [Py$_3$CHNi^{IV}(cyclo-neophenyl)][OTf] complex.

By replacing the Py$_3$CH ligand with trispyrazolylborate (Tp), the Sanford group obtained a stable Ni(IV) complex that demonstrated high selectivity and participated in the formation of C–O, C–S, and C–N bonds with various nucleophiles (Scheme 1.24). The mechanistic studies showed first-order kinetics in [Ni] and [NMe$_4$OAc], and linear correlation with Swain-Scott nucleophilicity parameters, pointed towards a S$_N$2-type attack on the metal–C bond by the nucleophile. Two years later, the same group studied the mechanism in more detail including DFT studies with (TpNi^{IV}CF$_3$) complex and compared it with the system of Pd(IV).[59] The results suggest that while the chemistry of Ni(IV) and Pd(IV) complexes shares many similarities, Ni(III) plays a crucial role in enabling distinct reactivity, such as C(sp^2)-N insertion, not observed with Pd. The study also shows that both, Ni(IV) and Pd(IV) species, can be accessed under comparable conditions, and that they undergo C(sp^3)−heteroatom bond-forming reactions, with the Ni system requiring milder conditions.

---

[59] N. M. Camasso, A. J. Canty, A. Ariafard, M. S. Sanford, *Organometallics* **2017**, *36*, 4382–4393.

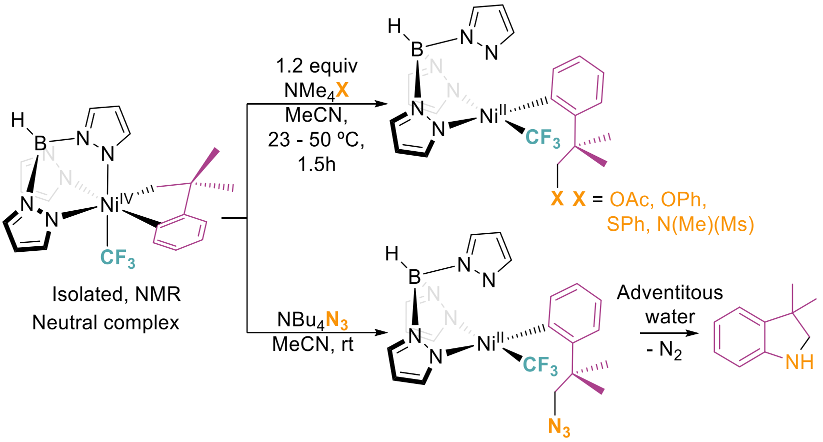

Scheme 1.24 Reactivity of [TpNi^{IV}(cyclo-neophenyl)] complex, forming several C–X bonds.

The first example of a C–CF_3 bond formation from a discrete high-valent Ni(IV) complex was unveiled by Sanford and coworkers. They published a study of the synthesis of various Ni^{IV}(aryl)$(CF_3)_2$ complexes, using either a trifluoromethylating agent or aryl electrophiles (Scheme 1.25).[60] Upon heating, these complexes undergo selective and efficient trifluoromethylation of the Ni-aryl group, with the electron-donating aryl group undergo faster reductive elimination. A computational study was conducted by Klein to determine the oxidation state of Ni,[61] similarly to the controversy surrounding the oxidation state of $CuCF_3$ species.[17,18] The study revealed that the complexes are best described as Ni(II) due to the σ-noninnocence of the CF_3 group. Additionally, the study revealed that C–C bond formation, is not reductive but essentially redox neutral.

---

[60] J. R. Bour, N. M. Camasso, M. S. Sanford, *J. Am. Chem. Soc.* **2015**, *137*, 8034–8037.

[61] J. S. Steen, G. Knizia, J. E. M. N. Klein, *Angew. Chemie - Int. Ed.* **2019**, *58*, 13133–13139.

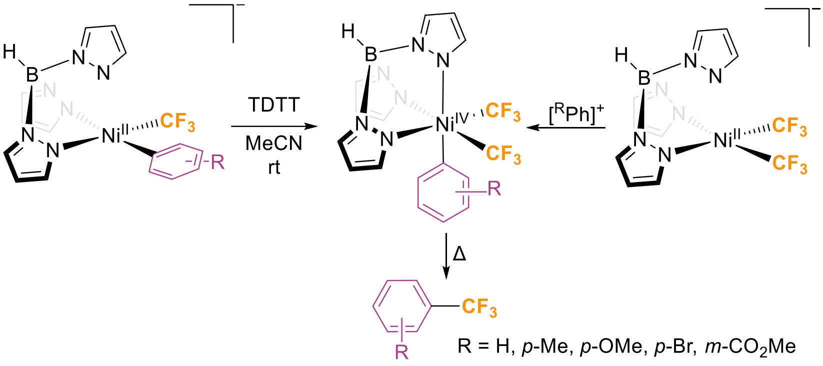

Scheme 1.25 First C–CF3 bond formation from a isolated Ni(IV) complex.

Despite the vast majority of reported examples on TM-mediated C−H metalation involve low-valent species, growing evidence suggests that higher oxidation state group 10 metal centers can also be engaged in C−H bond-cleavages. In 2017, the Sanford group disclosed the intramolecular C–H activation by Ni(IV) by using NFTPT as an oxidizing agent (Scheme 1.26).[62] They reported a series of oxidatively induced intermolecular arene C−H activation of the C_{ipso}-H bond of the aryl ring in the ligand, under one of the mildest conditions for C–H bond cleavage at a Ni center, 10 min at room temperature. The reaction mechanism was studied through DFT and experimental mechanistic studies. The findings demonstrate that the reaction initially involves a 2 e$^-$ oxidation of Ni(II) by the F$^+$ oxidant, which in turn transfers the F$^+$. Subsequently, triflate assists in the C−H activation at Ni(IV) to yield the desired product.

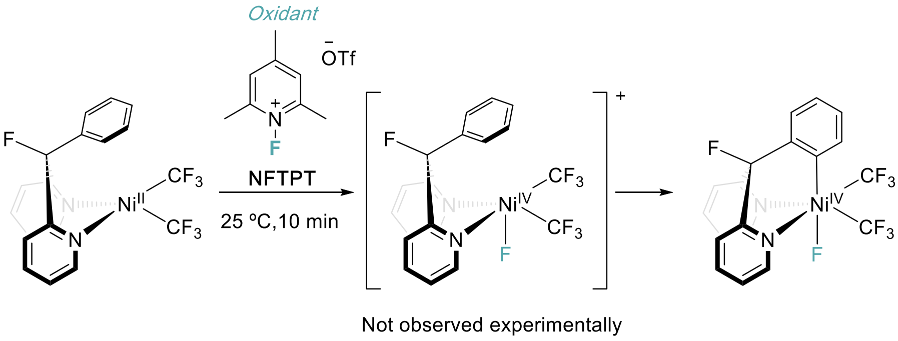

Scheme 1.26 Intramolecular oxidatively induced C–H activation.

---

[62] E. Chong, J. W. Kampf, A. Ariafard, A. J. Canty, M. S. Sanford, *J. Am. Chem. Soc.* **2017**, *139*, 6058–6061.

Nevertheless, they could not discard the possibility of two consecutive 1 e$^-$ oxidations because previously Mirica had suggested a possibility of C–H activation on a Ni(III) center,[63] and NFTPT has been also proposed as one electron oxidant.[64]

In another work, Mirica *et al.* studied the reactivity of Ni(III) and Ni(IV) compounds under photochemical conditions. They reported the complete synthesis and characterization of Ni(III) and Ni(IV) compounds utilizing a tridentate ligand, 1,4,7-trimethyl-1,4,7-triazacyclononane (Me$_3$tacn), and a cyclo-neophyl ligand (Scheme 1.27).[65] The complexes were obtained in high yield from the Ni(II)-precursor by two successive 1 e$^-$ oxidation steps and were thoroughly characterized by X-ray spectroscopy along with either EPR or NMR techniques.

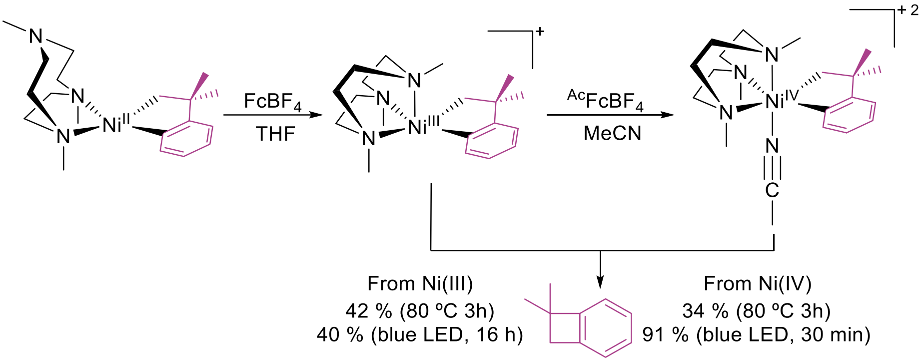

Scheme 1.27 Reductive elimination from high-valent Me$_3$tacn-Ni(III) and -Ni(IV) species under thermal or photochemical conditions.

Reductive elimination from the Ni(III) complex, either by heating or using blue LED irradiation, resulted in only a moderate yield of the desired product. Additionally, when the Ni(IV) species was heated, a comparable yield was obtained. However, in this case, the use of light significantly improved the yield to 91%. These results suggest that the Ni(IV) species is the key intermediate in Ni/photocatalysis, rather than the generally presumed Ni(III) species.

---

[63] W. Zhou, S. Zheng, J. W. Schultz, N. P. Rath, L. M. Mirica, *J. Am. Chem. Soc.* **2016**, *138*, 5777–5780.

[64] a) L. Strekowski, A. S. Kiselyov, in *Adv. Heterocycl. Chem.*, **1995**, pp. 1–17. b) J. R. Barrio, M. Namavari, M. E. Phelps, N. Satyamurthy, *J. Am. Chem. Soc.* **1996**, *118*, 10408–10411.

[65] M. B. Watson, N. P. Rath, L. M. Mirica, *J. Am. Chem. Soc.* **2017**, *139*, 35–38.

Finally, the catalytic activity of TpNi^{IV}(CF$_3$)$_3$, a high-valent Ni(IV) complex, was successfully demonstrated in the C–H trifluoromethylation of (hetero)arenes (Scheme 1.28).[66] Initially, a stoichiometric reaction was developed, which was subsequently translated into a catalytic version using electron-rich arenes and heteroarenes. Experimental and computational studies revealed a radical chain pathway in which the Ni(IV) complex played a role in both the initiation and propagation phases. Importantly, this marks the first time that spectroscopic evidence has been presented for the involvement of a Ni(IV) complex in a catalytic reaction.

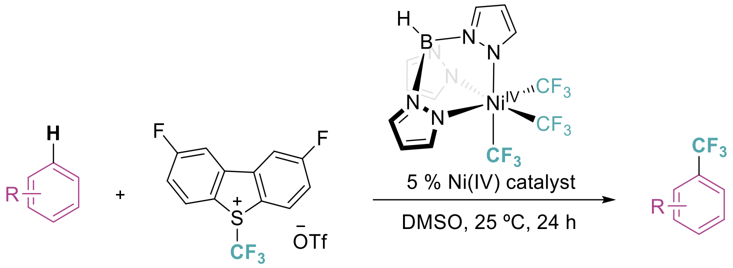

Scheme 1.28 Catalytic activity of a Ni(IV) complex for C–H trifluoromethylation of (hetero)arenes.

Over the past decade, significant strides have been made in advancing our knowledge of C–heteroatom and C–C bond-forming reactions that involve high-valent nickel species. This has been an area of intensive research, and we have examined some noteworthy examples of high-valent Ni organometallic complexes. Some common features observed across these examples include the use of chelating, N-containing, stabilizing ligands (such as pincer and Tp ligands) and the presence of CF$_3$ groups.

---

[66] E. A. Meucci, S. N. Nguyen, N. M. Camasso, E. Chong, A. Ariafard, A. J. Canty, M. S. Sanford, *J. Am. Chem. Soc.* **2019**, *141*, 12872–12879.

1.4. Iron

High-valent iron complexes play a crucial role in biological catalytic cycles and organic transformations, inspiring the development of synthetic Fe(IV) chemistry.[67] Most of these complexes can be stabilized by Π-donating auxiliary ligands (PDALs) such as oxide, nitride and imide with varying degrees of stability.[68] N-heterocyclic carbene ligands have also been used to stabilize Fe(IV) species.[69] Besides, the electron-donating effect of carbanions can be utilized to stabilize the higher oxidation states in organometallic iron complexes. Bower's pioneering work on a homoleptic Fe species with four 1-norbornyl ligands was the first demonstration of this approach.[70] In more recent reports, other carbanions have been used to obtain Fe(IV) species, as shown in Scheme 1.29.[71]

---

[67] a) J. T. Groves, *J. Inorg. Biochem.* **2006**, *100*, 434–447. b) L. Que, W. B. Tolman, *Nature* **2008**, *455*, 333–340. c) J. Hohenberger, K. Ray, K. Meyer, *Nat. Commun.* **2012**, *3*, 720.

[68] a) J. U. Rohde, J. H. In, M. H. Lim, W. W. Brennessel, M. R. Bukowski, A. Stubna, E. Münck, W. Nam, L. Que, *Science* **2003**, *299*, 1037–1039. b) C. Vogel, F. W. Heinemann, J. Sutter, C. Anthon, K. Meyer, *Angew. Chemie - Int. Ed.* **2008**, *47*, 2681–2684. c) B. Mondal, L. Roy, F. Neese, S. Ye, *Isr. J. Chem.* **2016**, *56*, 763–772. d) C. Kupper, B. Mondal, J. Serrano-Plana, I. Klawitter, F. Neese, M. Costas, S. Ye, F. Meyer, *J. Am. Chem. Soc.* **2017**, *139*, 8939–8949. e) S. Hong, K. D. Sutherlin, A. K. Vardhaman, J. J. Yan, S. Park, Y. M. Lee, S. Jang, X. Lu, T. Ohta, T. Ogura, E. I. Solomon, W. Nam, *J. Am. Chem. Soc.* **2017**, *139*, 8800–8803.

[69] a) C. Vogel, F. W. Heinemann, J. Sutter, C. Anthon, K. Meyer, *Angew. Chemie - Int. Ed.* **2008**, *47*, 2681–2684. b) I. Nieto, F. Ding, R. P. Bontchev, H. Wang, J. M. Smith, *J. Am. Chem. Soc.* **2008**, *130*, 2716–2717. c) S. Meyer, I. Klawitter, S. Demeshko, E. Bill, F. Meyer, *Angew. Chemie - Int. Ed.* **2013**, *52*, 901–905. d) M. R. Anneser, G. R. Elpitiya, J. Townsend, E. J. Johnson, X. B. Powers, J. F. DeJesus, K. D. Vogiatzis, D. M. Jenkins, *Angew. Chemie - Int. Ed.* **2019**, *58*, 8115–8118. e) O. Prakash, P. Chábera, N. W. Rosemann, P. Huang, L. Häggström, T. Ericsson, D. Strand, P. Persson, J. Bendix, R. Lomoth, K. Wärnmark, *Chem. - A Eur. J.* **2020**, *26*, 12728–12732. f) K. P. Carter, K. M. Shield, K. F. Smith, Z. R. Jones, J. N. Wacker, L. Arnedo-Sanchez, T. M. Mattox, L. M. Moreau, K. E. Knope, S. A. Kozimor, C. H. Booth, R. J. Abergel, *Nature* **2021**, *590*, 85–88.

[70] B. K. Bower, H. G. Tennent, *J. Am. Chem. Soc.* **1972**, *94*, 2512–2514.

[71] a) M. Malischewski, M. Adelhardt, J. Sutter, K. Meyer, K. Seppelt, *Science* **2016**, *353*, 678–682. b) A. Casitas, J. A. Rees, R. Goddard, E. Bill, S. DeBeer, A. Fürstner, *Angew. Chemie - Int. Ed.* **2017**, *56*, 10108–10113. c) M. Malischewski, K. Seppelt, J. Sutter, D. Munz, K. Meyer, *Angew. Chemie - Int. Ed.* **2018**, *57*, 14597–14601.

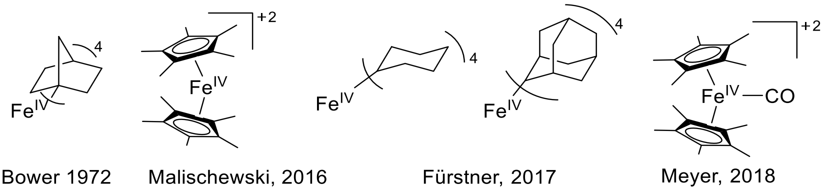

Scheme 1.29 Fe(IV) organometallic complexes stabilized by carbanions.

Additionally, macrocycles with strong donating properties, such as porphyrin, tetraamide, triamidoamine or tris(phosphino)silyl ligands have also been successful in stabilizing high-valent iron complexes.[72]

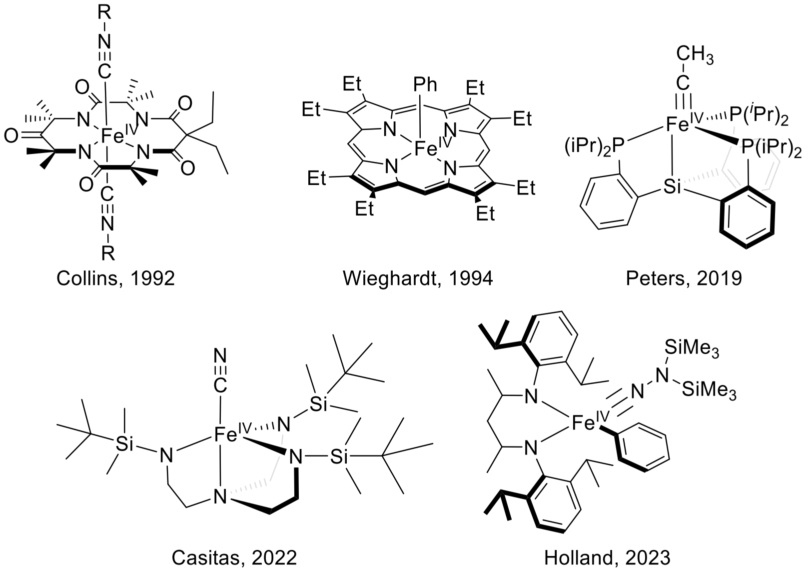

Scheme 1.30 Fe(IV) organometallic complexes stabilized by N-donating or P-donating ligands.

In the report by Peters they discussed the activation of acetylene gas by Fe. Not only they obtained stable Fe(IV) alkylcarbene complex, but also Fe(V).

---

[72] T. J. Collins, B. G. Fox, Z. G. Hu, K. L. Kostka, C. E. F. Rickard, L. J. Wright, *J. Am. Chem. Soc.* **1992**, *114*, 8724–8725.

1.5. Manganese

Understanding the mechanism behind Mn-catalyzed C−C and C–X bond formation reactions is complex due to the paramagnetism of the majority of Mn intermediates involved in stoichiometric and catalytic reactions. This is caused by the wide range of available oxidation states for this metal and the frequent instability of organomanganese compounds, resulting in numerous paramagnetic decomposition products.[73] Although most Mn-catalyzed C–H functionalization reactions are proposed to occur via closed-shell Mn(I) species, without a change in the formal oxidation state during the reactions, different groups have suggested the intermediacy of high-valent, Mn(III) or Mn(IV). So far, there is a significant scarcity of experimental data confirming the presence of these highly oxidized compounds in catalysis.[74] In fact, to date, the sole indication of a high-valent Mn complex's intermediacy in catalysis comes from Taillefer's observation of a Mn(IV) diaryl complex involved in C–C coupling,[75] which was identified via ESI-MS spectrometry.

From a stoichiometric perspective, the Khusnutdinova's group managed to isolate stable cyclometalated high-valent aryl–Mn(III)-X_2 (X = Br, I, BF_4)[76] complexes with tetradentate pyridinophane ligands, which are similar to the Ni(III) complexes reported by Mirica in 2015.[77] Upon heating Mn(III)–Br_2 in toluene at 150 ºC, no reductive elimination product was observed (Scheme 1.32). Cyclovoltammetry analysis indicated the relatively low potential for the first oxidation, implying the possibility for accessing aryl–Mn(IV) species using conventional 1e$^-$ oxidants.

---

[73] D. A. Valyaev, G. Lavigne, N. Lugan, *Coord. Chem. Rev.* **2016**, *308*, 191–235.

[74] a) R. Dakarapu, J. R. Falck, *J. Org. Chem.* **2018**, *83*, 1241–1251. b) G. Cahiez, D. Bernard, J. F. Normant, *J. Organomet. Chem.* **1976**, *113*, 99–106. c) T. Sato, T. Yoshida, H. H. Al Mamari, L. Ilies, E. Nakamura, *Org. Lett.* **2017**, *19*, 5458–5461. d) C. Zhu, J. C. A. Oliveira, Z. Shen, H. Huang, L. Ackermann, *ACS Catal.* **2018**, *8*, 4402–4407.

[75] Y. Liu, J. Bergès, Y. Zaid, F. O. Chahdi, A. Van Der Lee, D. Harakat, E. Clot, F. Jaroschik, M. Taillefer, *J. Org. Chem.* **2019**, *84*, 4413–4420.

[76] The Cl-containing Mn(III)-aryl complex was successfully isolated in their next paper[78]

[77] A. Sarbajna, Y. T. He, M. H. Dinh, O. Gladkovskaya, S. M. W. Rahaman, A. Karimata, E. Khaskin, S. Lapointe, R. R. Fayzullin, J. R. Khusnutdinova, *Organometallics* **2019**, *38*, 4409–4419.

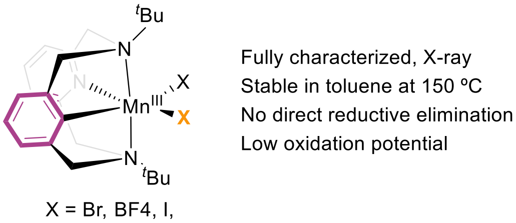

Scheme 1.31 Stable aryl-Mn(III)-halide complexes.

These complexes react with various 1e$^-$ oxidants, such as $NOBF_4$, arylaminium radical “magic Blue” or even H_2O_2, resulting in facile oxidatively induced reductive elimination at room temperature to form C–X bonds (X = Br, I, or CN), and the concomitant formation of a Mn(II) product. Mechanistic investigations using the aryl–Mn(III)–Br_2 as a model system suggested that C–Br bond formation arises via a non-radical mechanism, possibly through an Ar–Mn(IV) intermediate. However, this intermediate has not been detected via variable temperature UV-vis analysis.

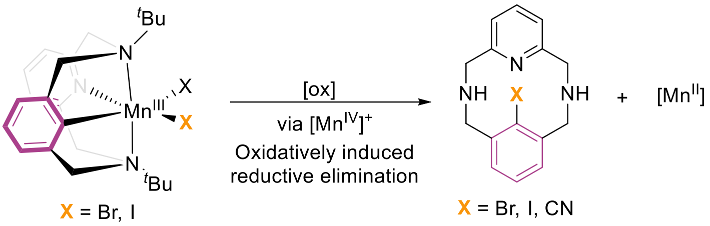

Scheme 1.32 Reductive elimination accessed by oxidation of isolated aryl-Mn^{III} complexes.

In a following investigation conducted in 2021, the same group explored the feasibility of C–C bond-forming reactions from stable and well-defined Mn(III) aryl complexes (Scheme 1.33).[78] Several alkylating agents, including organomagnesium, zinc, and lithium reagents, were employed in an attempt to form the bis(aryl)Mn(III) intermediate via transmetalation. However, the exclusive formation of the C–C reductive elimination product was observed in all cases, and no transmetalation intermediates were detected, even at low temperatures, in contrast to what observed in the previous study, where the Ar–halide elimination reaction did not occur directly from Mn(III) aryl complexes.

---

[78] Y. T. He, A. Karimata, O. Gladkovskaya, E. Khaskin, R. R. Fayzullin, A. Sarbajna, J. R. Khusnutdinova, *Organometallics* **2021**, *40*, 2320–2331.

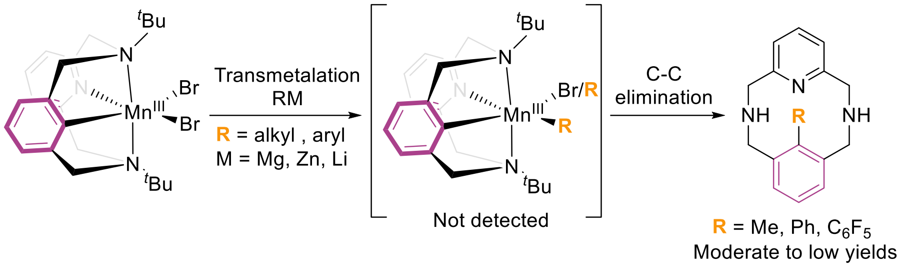

Scheme 1.33 C–C bond formation via Mn(III).

The efficiency of the aforementioned process was moderate to low, and it was constrained by the alkylating reagent scope. However, a notable finding was the enhanced selectivity and efficiency of the aryl–C bond elimination reaction when TEMPO or other one-electron oxidants were added to the aryl Mn(III) complex in the presence of alkylating agents. This effect is believed to be mediated through an alternative pathway that involves high-valent Mn(IV) intermediates.

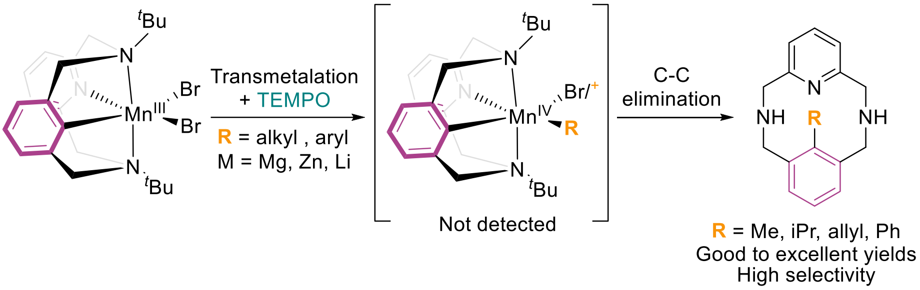

Scheme 1.34 C–C bond formation via Mn(IV).

In this case, the authors suggested two possible pathways for C–C coupling involving Mn(III) or Mn(IV) centers, respectively. While a catalytic protocol was developed through the Mn(III) pathway, the Mn(IV) pathway showed better yield and selectivity with the need of a sacrificial oxidant.

Although research on high-valent manganese systems is still in its early stages, these studies have shown promising evidence that these species may play a crucial role in facilitating C–heteroatom and C–C bond forming reactions.

1.6. Cobalt

There are only a few examples of organometallic Co(IV) and Co(V) complexes in the literature, which have not catalytical relevance (Scheme 1.35). The first one by Bower in 1972, a homoleptic Co(IV) complex with 4 1-norbornyl ligands.[70] In 2000, Brookhart reported the discovery of a Co(V) species whose structure was confirmed by both DFT calculations and X-ray spectroscopy.[79] Remarkably, this complex exhibits a high degree of stability towards reductive elimination, likely due to the stabilizing properties of its hydrido ligands, which help to stabilize the metal in its high oxidation state. More recently, in 2016 Groysman revealed the synthesis of a formally Co(IV)–carbene, which structure has been studied by X-ray and EPR spectroscopy along by DFT calculations.[80]

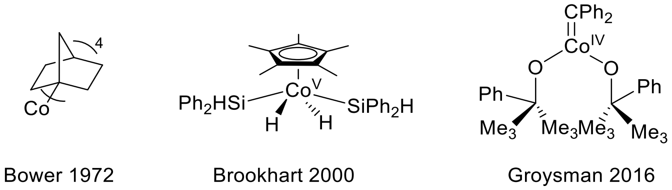

Scheme 1.35 Isolated high-valent cobalt organometallic complexes.

---

[79] M. Brookhart, B. E. Grant, C. P. Lenges, M. H. Prosenc, P. S. White, *Angew. Chem., Int. Ed.* **2000**, *39*, 1676–1679.

[80] J. A. Bellow, S. A. Stoian, J. Van Tol, A. Ozarowski, R. L. Lord, S. Groysman, *J. Am. Chem. Soc.* **2016**, *138*, 5531–5534.

1.7. *DFT studies*

Density functional theory (DFT) studies have become an indispensable tool for understanding high-valent organometallic chemistry. Theoretical methods such as DFT allow for the calculation of electronic and geometric properties of metal complexes with accuracy and efficiency, providing insights into the reaction mechanisms and reactivity of these complexes. High-valent organometallic species have unique electronic structures and reactivity that are difficult to study experimentally due to their short lifetimes and sensitivity to air and moisture. DFT studies can help to elucidate the electronic structures of high-valent organometallic species, predict their reactivity, and guide the design of new catalysts with improved performance. In this context, DFT studies play a crucial role in advancing our understanding of high-valent organometallic chemistry and the development of new chemical processes.

UNIVERSITAT ROVIRA I VIRGILI
UNCOVERING THE MECHANISTIC SCENARIOS OF NUCLEOPHILIC COUPLINGS IN CP*CO SYSTEMS
Sara López Resano

1.8. General objectives

In this introduction, we have shown a brief overview of the current state-of-the-art of organometallic high-valent first-row TMs relevant for C–C and C–bond-forming reactions. This type of species have been commonly invoked as reactive intermediates specially in copper- and nickel-catalyzed transformations. On the contrary, the intermediacy of high-valent organometallic species based on other first-row TM, such as cobalt, remains underexplored. Hence, the primary scientific objective of this Thesis is to uncover the participation of high-valent Cp*Co species in C–H functionalization and provide a better fundamental understanding of the underlying mechanisms, by combining experimental and computational approaches. Specifically, our aims are:

- Elucidate the mechanistic picture of nucleophilic C–SCF_3 bond formation in Cp*Co-catalyzed C–H functionalization reactions.
- Establish whether widely used F^+ oxidants can trigger oxidative induced reductive elimination events from high-valent Cp*Co^{IV} or Cp*Co^{V}.
- Investigate the effects of directing groups and nucleophiles in carbon-heteroatom and carbon-carbon bond-forming reactions from Cp*Co systems.

Each chapter of this manuscript provides a detailed description of the specific objectives.

*Chapter 2. Redefining the Mechanistic Scenario of Carbon–Sulfur Nucleophilic Coupling via High-Valent Cp*Co(IV) Species*

2.1. Introduction

Undoubtedly, organometallic chemistry holds a prominent position in organic synthesis.[1] Since the second half of the 20th century, homogeneous transition metal (TM) catalysis has unlocked innovative pathways for forging new bonds, making it an indispensable tool for building molecular complexity.[2] A clear illustration of the profound utility and impact of these processes can be seen in palladium-catalyzed cross-couplings (Scheme 2.1a).[3] These transformative reactions have revolutionized the synthetic landscape, reshaping the way chemists construct C–C bonds in a predictable and regioselective manner. Indeed, the groundbreaking contributions of Suzuki, Negishi, and Heck in enhancing the efficiency of organic synthesis were recognized with the Nobel Prize in Chemistry in 2010.[4] However, despite their remarkable achievements, these methodologies are not without limitations. Challenges include the generation of waste due to the stoichiometric use of organometallic nucleophiles or the requirement for pre-functionalized starting materials. To overcome these hurdles, the synthetic community has explored alternative strategies for synthesizing C–C and C–X bonds, including the implementation of ligand-directed TM-catalyzed C–H functionalization reactions (Scheme 2.1b).[5]

---

[1] *Organotransition Metal Chemistry: From Bonding to Catalysis*, 1st ed.; Hartwig, J. F. (Ed.); Palgrave Macmillan, **2009**. (b) *Organometallics in Synthesis, Third Manual*; Schlosser, M. (Ed.); Wiley, **2013**. (c) *The Organometallic Chemistry of the Transition Metals*, 7th ed.; Crabtree, R. H. (Ed.); Wiley, **2019**.

[2] (a) *Organometallics as Catalysts in the Fine Chemical Industry*; Beller, M., Blaser, H.-U. (Eds.); Springer-Verlag Berlin Heidelberg, **2012**. (b) *Applied Cross-Coupling Reactions*; Nishihara, Y. (Ed.); Springer-Verlag Berlin Heidelberg, **2013**.

[3] (a) *Cross-Coupling Reactions: A Practical Guide*; Miyaura, N., (Ed.) in *Topics in Current Chemistry Series 2019*; Springer-Verlag Berlin Heidelberg, **2002**. (b) *Metal-Catalyzed Cross-Coupling Reactions and More*, 1st ed.; de Meijere, A., Bräse, S., Oestreich, M. (Eds.); Wiley-VCH, **2014**.

[4] Johansson Seechurn, C. C. C.; Kitching, M. O.; Colacot, T. J.; Snleckus, V. *Angew. Chem. Int. Ed.* **2012**, *51*, 5062.

[5] (a) Lyons, T. W.; Sanford, M. S. *Chem. Rev.* **2010**, *110*, 1147. (b) Engle, K. M.; Mei, T.-S.; Wasa, M.; Yu, J.-Q. *Acc. Chem. Rev*. **2012**, *45*, 788. (c) Rouquet, G.; Chatani, N. *Angew. Chem. Int. Ed*. **2013**, *52*, 11726. (d) Wencel-Delord, J.; Glorius, F. *Nat. Chem.* **2013,** *5*, 369. (e) Daugulis, O.; Roane, J.; Tran, L. D. *Acc. Chem. Res.* **2015**, *48*, 1053. (f) He, J.; Wasa, M.; Chan, K. S. L.; Shao, Q.; Yu, J.-Q. *Chem. Rev.* **2017**, *117*, 8754. (g) Sambiagio, C.; Schönbauer, D.; Blieck, R.; Dao-Huy, T.; Pototschnig, G; Schaaf, P.; Wiesinger, T.; Zia, M. F.; Wencel-Delord, J.; Besset, T.; Maes, B. U. W.; Schnürch, M. *Chem. Soc. Rev.* **2018**, *47*, 6603. (h) Gandeepan, P.; Ackermann, L. *Chem* **2018**, *4*, 199. (i) Gandeepan, G.; Müller, T.; Zell, D.; Cera, G.; Warratz, S.; Ackermann, L. *Chem. Rev.* **2019**, *4*, 2192.

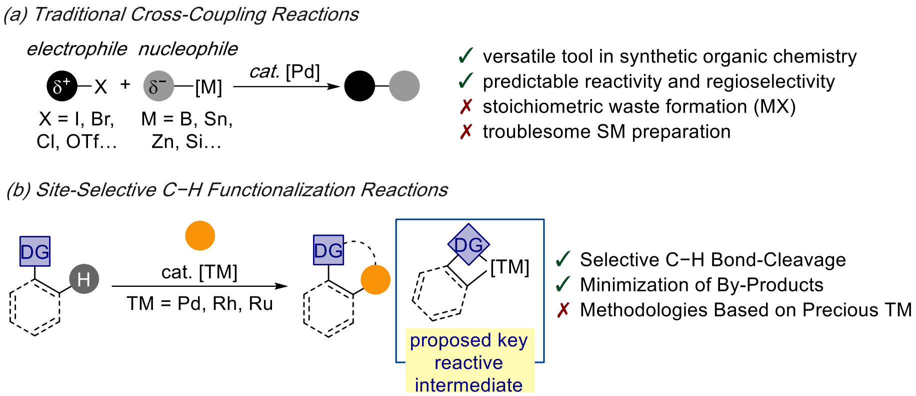

Scheme 2.1 Traditional cross-coupling *vs* Directed C–H functionalization

Directed C–H functionalizations hold immense potential in various aspects. Firstly, they enable the coupling with a diverse range of coupling partners, ranging from organometallic nucleophiles to electrophiles such as aryl halides or unsaturated molecules (alkynes, alkenes). Secondly, they minimize the formation of unwanted by-products, leading to higher atom economy. And least but not less, the use of substrates that contain Lewis basic functional groups, commonly referred to as directing groups (DGs), allows to control the site-selectivity of the process. These DGs, such as pyridine, pyrimidine, and imine (considered strong DGs), or ketone, aldehyde, ester, and amide (considered weak DGs), bind to the metal center, enhancing reactivity at specific proximal sites in molecules that possess multiple C–H bonds. Traditionally, these catalytic systems have heavily relied on noble TMs such as Pd, Rh or Ru, given their exceptional reactivity and efficiency.[5a-i] However, in recent years, catalysts based on more cost-effective first-row metals,[5j] such cobalt,[6] have emerged as highly attractive alternatives to precious metals. Besides being abundant and inexpensive (cobalt costs around $0.03 per gram compared to $222 per gram for rhodium),[7] cobalt catalysts offer a diverse range of reactivity patterns. They not only mimic the behavior of precious

---

[6] a) M. Moselage, J. Li, L. Ackermann, *ACS Catal.* **2016**, *6*, 498. b) D. Wei, X. Zhu, J.-L. Niu, M.-P. Song, *ChemCatChem* **2016**, *8*, 1242. c) P. G. Chirila, C. J. Whiteoak, *Dalton Trans.* **2017**, *46*, 9721. d) S. Wang, S. Y. Chen, X. Q. Yu, *Chem. Commun.* **2017**, *53*, 3165. e) T. Yoshino, S. Matsunaga, *Adv. Synth. Catal.* **2017**, *359*, 1245. f) T. Yoshino, S. Matsunaga, *Adv. Organomet. Chem.* **2017**, *68*, 197. g) S. Prakash, R. Kuppusamy, C.-H. Cheng, *ChemCatChem* **2018**, *10*, 683. h) D. A. Loginov, L. S. Shul'pina, D. V. Muratov, G. B. Shu'pin, *Coord. Chem. Rev.* **2019**, *387*, 1. i) Ghorai, J.; Anbarasan, P. *Asian J. Org. Chem.* **2019**, *8*, 430. j) Mei, R.; Dhawa, U.; Samanta, R. C.; Ma, W.; Wencel-Delord, J.; Ackermann, L. *ChemSusChem* **2020**, *13*, 3306.

[7] https://www.dailymetalprice.com/ accessed on 31/05/2023

metals but also exhibit unique and versatile reactivity due to its low electronegativity, hard nature and the ability to access multiple oxidation states through 1- or 2-electron processes. The first example of chelation-assisted transition-metal catalyzed C–H functionalization utilizing a cobalt catalyst was reported by Murahashi in the 1950s.[8] However, despite this early discovery, the tremendous potential of cobalt in facilitating directed C–H functionalization reactions remained largely unexplored for over 50 years. It is only in recent times that cobalt has experienced a renaissance as a promising tool in organic synthesis.[6a] Specifically, the utilization of Cp*Co^{III} complexes,[6] analogous to the active Rh^{III} catalysts for C–H activation[9] and known since the mid-70s,[10] has represented a significant advancement in cobalt catalysis, propelling the field forward and opening up new opportunities in organic synthesis.

Since the seminal work by Kanai and Matsunaga in 2013,[11] numerous research groups have showcased the potential of Cp*Co^{III} complexes in driving C–C and C–heteroatom bond-forming reactions, particularly when employing electrophilic coupling partners.[6] This distinct behavior can be attributed to the unique nature of the Cp*Co^{III}–C bond in the putative cobaltacycle formed after the C–H activation step (Scheme 2.2, left).[12] In comparison to rhodium, cobalt exhibits lower electronegativity, resulting in a more polarized Co–C bond than the one present analogous metalacyclic Cp*Rh^{III} intermediates. Consequently, the increased nucleophilicity of the A-type intermediates in Scheme 2.2 enables the reaction with less electrophilic moieties. Despite considerable progress, these Cp*Co^{III}-based systems are still in their early stages compared to well-established Rh- and Pd-based catalysts, primarily due to limited fundamental organometallic understanding at the molecular level. Until 2017, experimental investigations into the underlying reaction mechanisms were hindered by the proposed reversibility of the C–H metalation step and/or the instability of the transient cobalt intermediates made them difficult to be captured or even identify. Consequently, available experimental information was primarily derived from

---

[8] Murahashi, S. *J. Am. Chem. Soc.* **1955**, *77*, 6403.

[9] a) Colby, D. A.; Tsai, A. S.; Bergman, R. G.; Ellman, J. A. *Acc. Chem. Res.* **2012**, *45*, 814. b) Song, G.; Li, X. *Acc. Chem. Res.* **2015**, *48*, 1020.

[10] Roe, D. M.; Maitlis, P. M. *J. Chem. Soc. A* **1971**, 3173.

[11] Yoshino, T.; Ikemoto, H.; Matsunaga, S.; Kanai, M. *Angew. Chem. Int. Ed.* **2013**, *52*, 2207.

[12] Ikemoto, H.; Yoshino, T.; Sakata, K.; Matsunaga, S.; Kanai, M. *J. Am. Chem. Soc.* **2014**, *136*, 5424.

hydrogen/deuterium exchange experiments, kinetic isotope effect measurements, or the detection of cobalt intermediates using electrospray ionization mass spectrometry (ESI-MS).[13] However, since these data do not provide detailed structural information at the molecular level, the proposed catalytic cycles were based on analogous noble metal systems.[9] Challenged by the lack of fundamental understanding, our group aims to provide a more comprehensive mechanistic picture on these processes. Over the past years, we have designed different strategies to access and characterize relevant Cp*Co^{III} reactive intermediates in the context of C–H functionalization with electrophiles.[14] However, in this thesis, we have focused our attention on the intricacies of nucleophilic couplings. While hundreds of papers document the extraordinary capability of Cp*Co^{III} catalysts for facilitating the coupling with electrophiles, the use of nucleophilic coupling partners is extremely limited, with only three examples reported in the literature so far.[15]

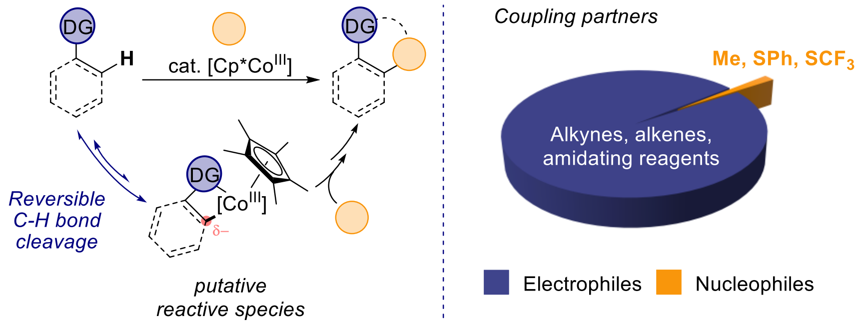

Scheme 2.2 Left: Formation of the polarized Co–C bond in the Co(III) intermediate. Right: A visual graph of the coupling partners nature from the reported Cp*Co(III) catalysis.

---

[13] a) Planas, O.; Chirila, P. G.; Whiteoak, C. J.; Ribas, X. *Adv. Organomet. Chem.* **2018**, *69*, 209. b) Gallego, D.; Baquero, D. A. *Open Chem.* **2018**, *16*, 1001.

[14] a) Sanjosé-Orduna, J.; Gallego, D.; Garcia-Roca, A.; Martin, E.; Benet-Buchholz, J.; Pérez-Temprano, M. H. *Angew. Chem. Int. Ed.* **2017**, *56*, 12137. b) Sanjosé-Orduna, J.; Sarria, J. M.; Pérez-Temprano, M. H. *Angew. Chem. Int. Ed.* **2018**, *57*, 11369. c) Sanjosé-Orduna, J.; Pérez-Temprano, M. H. *Inorg. Chem.* **2019**, *58*, 10569. d) Martinez de Salinas, S.; Sanjosé-Orduna, J.; Odena, C.; Barranco, S.; Benet-Buchholz, J.; Pérez-Temprano, M. H. *Angew. Chem. Int. Ed.* **2020**, *59*, 6139.

[15] a) T. Gensch, F. J. R. Klauck, F. Glorius, *Angew. Chem. Int. Ed.* **2016**, *55*, 11287. b) X.-G. Liu, Q. Li, H. Wang, *Adv. Synth. Catal.* **2017**, *359*, 1942. c) S. D. Friis, M. J. Johansson, L. Ackermann, *Nat. Chem.* **2020**, *12*, 511.

2.1.1. Nucleophlic C–H functionalizations catalyzed by Cp*Co^{III}

As mentioned in the previous section, it is particularly strikingly the scarcity of Cp*Co-catalyzed C–H functionalization reactions using nucleophiles as coupling partners. The three published examples, 2 two of them on C–S bond-forming reactions,[15a,b] and the third one targeting methylation processes,[15c] proposed a similar Co^{I}/Co^{III} catalytic cycle that involves 4 main steps (Scheme 2.3). Firstly, a Cp*Co^{III} triggeres the C–H activation step to to produce a metalacyclic Cp*Co^{III} intermediate. Secondly, a group transfer between the nucleophilic coupling partner and the cobalt(III) metal center takes place. Thirdly, the C–Nuc bond-forming rection is produced by the reductive elimination (RE) from the transmetallated Co^{III} intermediate. Finally, the resulting Co^{I} is re-oxidized with an external oxidant to regenerate the active Co^{III}.

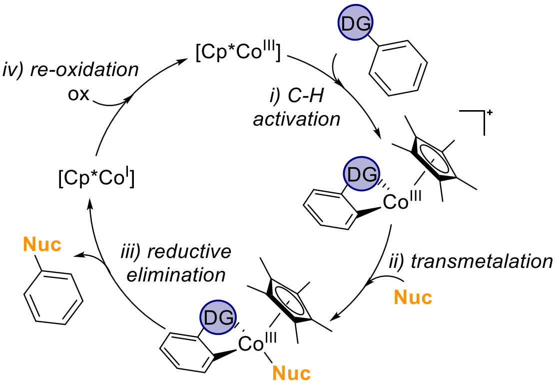

Scheme 2.3 Commonly proposed catalytic cycle for nucleophilic C–H functionalization by Cp*Co^{III} catalysts

The first example, reported by Glorius and co-workers in 2016.[15a] disclosed the functionalization of indole derivatives with thiols (Scheme 2.4). The authors proposed the *in situ* formation of the active thiolation agent, [Cu(SPh)$_2$], by using Cu(OAc)$_2$ and RSH (R = Ar, Alk). During the catalytic reaction, the authors detected by ESI-MS analysis the presence of three transient cobalt species that they assigned as the active catalyst that participates in the C–H activation step and the two metalacyclic Co^{III} intermediates .

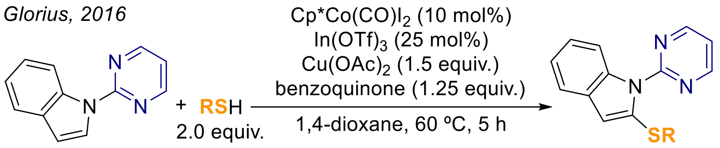

Scheme 2.4 Cp*Co-catalyzed C–H thiolation of indole derivatives

One year later, in 2017, Wang and co-workers described a trifluoromethylthiolation protocol of substrates containing strong directing groups such as pyridine or pyrimidine (Scheme 2.5). In this example, the authors employed a readily available silver reagent, $AgSCF_3$.

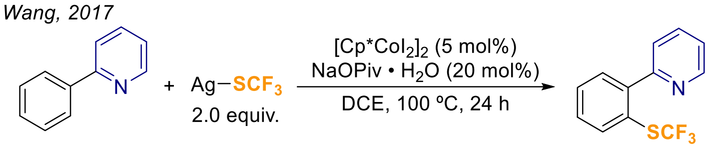

Scheme 2.5 Cp*Co-catalyzed C–H trifluoromethylthiolation

The final example, by the Ackermann group, shows a very elegant C–H methylation protocol using trimethylboroxine as nucleophilic source (Scheme 2.6). This work that exhibits an exceptional applicability in a wide range substrates containing,[15c] including the the late-stage functionalization (LSF) of more than 20 drug analogs.

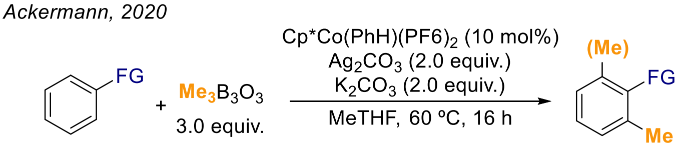

Scheme 2.6 Cp*Co-catalyzed C–H methylation

Although these methodologies provide exciting synthetic prospects, the mechanism by which these nucleophilic couplings operate is still unclear. Indeed, in similar Cp*Rh or Ir-catalyzed transformations by Chang and co-workers, the authors propose a more complex mechanistic scenario where the participation of high-valent organometallic species is key to promote the C–Nuc couplings.

2.1.2. Oxidatively induced reductive elimination events from Cp*TM systems.

In recent years, Chang and co-workers have extensively illustrated the remarkable potential of high valent Cp*TM catalysis involving group 9 metals. Their work has revealed the key role of oxidative induced reductive elimination steps from high-valent species to trigger otherwise inaccessible nucleophilic carbon–carbon and carbon–heteroatom bond-forming reactions[16]

In their seminal study,[16a] while attempting to develop a $\text{Cp*Ir}^{\text{III}}$-catalyzed C–H arylation protocol utilizing arylsilanes as coupling partners, the authors identified the reductive elimination step as a bottleneck within the traditional $\text{Ir}^{\text{I}}/\text{Ir}^{\text{III}}$ catalytic cycles (Scheme 2.7). To overcome this limitation, they modulated the electronic properties of the post-transmetallation $\text{Cp*Ir}^{\text{III}}$ intermediate through selective oxidation with silver salts to access high-valent Cp*Ir^{IV} or Cp*Ir^{V} species from which the challenging C–C bond-forming reaction takes place. Additional computational and electrochemical studies support the proposed high-valent catalysis.

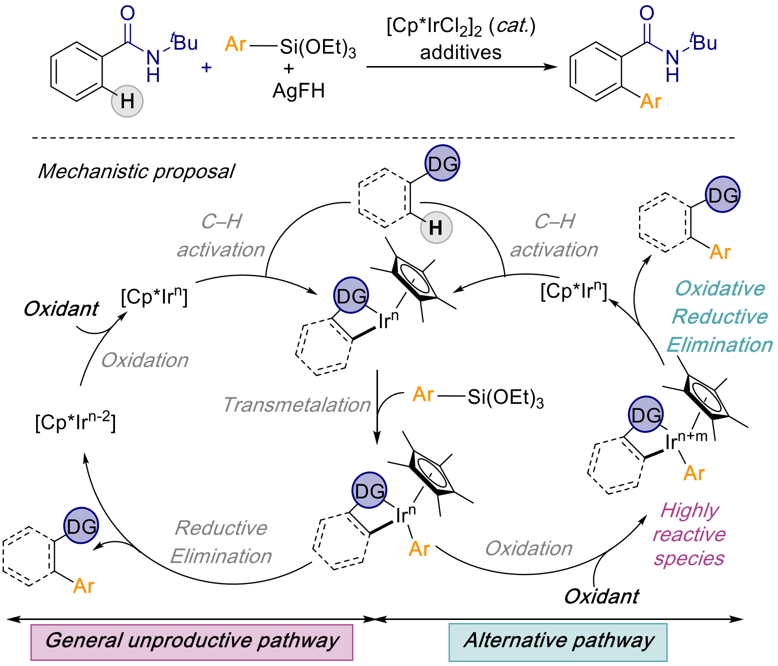

Scheme 2.7 Top: model reaction of Cp*Ir(III) catalyzed C–H arylation. Bottom: Mechanistic picture of the reaction, previous cycle involving Ir(III) and new alternative pathway involving high-valent species.

---

[16] a) K. Shin, Y. Park, M. H. Baik, S. Chang, *Nat. Chem.* **2018**, *10*, 218. b) J. Kim, K. Shin, S. Jin, D. Kim, S. Chang, *J. Am. Chem. Soc.* **2019**, *141*, 4137. c) J. Kim, D. Kim, S. Chang, *J. Am. Chem. Soc.* **2020**, *142*, 19052. d) J. Kim, S. Jin, D. Kim, S. Chang, *Bull. Korean Chem. Soc.* **2021**, *42*, 529. e) S. Jin, J. Kim, J.W. Park, S. Chang, *ACS Catal.* **2021**, *11*, 6590. f) Y. Kim, D. Kim, S. Chang, *Chem. Commun.* **2021**, *57*, 12309.

UNIVERSITAT ROVIRA I VIRGILI
UNCOVERING THE MECHANISTIC SCENARIOS OF NUCLEOPHILIC COUPLINGS IN CP*CO SYSTEMS
Sara López Resano

Building on these results, the group extended this approach to the development of C–H arylation reactions utilizing arylboronic esters,[16b] electrolytic C–H oxygenation,[16e] or intramolecular C–N bond-forming reactions.[16f]

2.2 Objectives

Over the past years, Cp*Co^{III} catalysts have shown their extraordinary capability to facilitate the functionalization of C–H bonds with a wide variety of electrophilic coupling partners. This stands in contrast to the scarce synthetic protocols that have examined the participation of nucleophiles in these transformations. In order to expand the utility and applicability of these transformations, it is timely to uncover the mechanistic intricacies of the reductive elimination step from Cp*Co-based systems.

The primary objectives of this chapter are as follows:

Design a strategy that enables the synthesis and characterization of a catalytically relevant transmetalated Cp*Co^{III} intermediate.

Perform reactivity studies to elucidate whether the target system participate in direct couplings or if the reductive elimination events are promoted under oxidative conditions, using chemical and electrochemical strategies.

Conduct DFT calculations to further assess the viability of the investigated reaction pathways.

By uncovering the principles that govern the underlying mechanisms of nucleophilic couplings by Cp*Co^{III} systems. We aim to foster the development of more efficient catalytic processes, along with broadening the scope of reactions that can be performed with these first-row TM catalysts.

2.3. Results and Discussion

2.3.1. Selection and Synthesis of a Model System

Several considerations went into the selection of a model system for elucidating the mechanistic insights associated to nucleophilic couplings mediated by Cp*Co-based systems. First, we aimed to synthesize one of the post-transmetalated Cp*Co^{III} complexes proposed in the literature as reactive intermediates in C–Nuc bond-forming reactions. Second, a nucleophile was targeted that would be well-defined and commercially available. Thus, we rule out the investigation of the system reported by Glorius. Finally, a system that would facilitate the investigation by NMR spectroscopy was sought. The catalytic system by Wang and co-workers fulfilled all our considerations (Scheme 2.8). We envision to access **1_{ppy}-SCF$_3$** through a transmetalation step between one of the cobaltacycles previously reported by our group,[14a] and AgSCF$_3$, a commercially available salt. Indeed, it is well-established the outstanding transmetalating ability of silver nucleophiles in TM catalysis.[17] Additionally, the installation of the SCF$_3$ moiety offers a distinctive chemical shift, facilitating the reaction monitoring and the potential identification of additional cobalt intermediates and/or the corresponding coupling product.

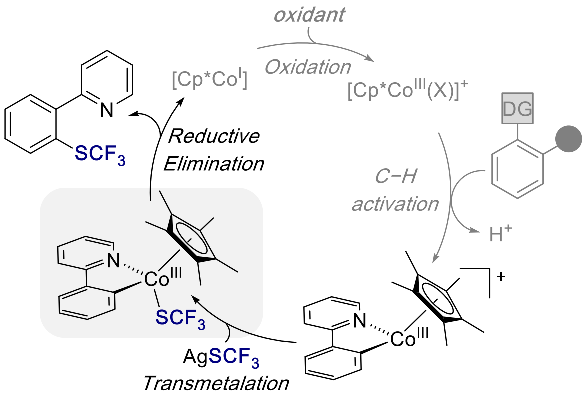

Scheme 2.8 Catalytic cycles proposed by Wang and co-workers.

Gratifyingly, complex **1_{ppy}-SCF$_3$** was obtained in 90% isolated yield by treatment of **1_{ppy}-I** with 1 equiv of AgSCF$_3$ in CH$_2$Cl$_2$ at room temperature for 15 min (Scheme

---

[17] Á. L. Mudarra, S. Martínez De Salinas, M. H. Pérez-Temprano, *Org. Biomol. Chem.* **2019**, *17*, 1655–1667.

2.9, entry 1). We also explored the synthesis of the post-transmelated compound an alternative nuceophilic source, NMe$_4$SCF$_3$ (Scheme 2.9, entry 2). However, in this case, the reaction required harsher reaction conditions, 80 ºC for 18 hours, provided lower yields (60%), the separation between the remaining **1$_{ppy}$-I** and **1$_{ppy}$-SCF$_3$** turned to be challeging challenging. Therefore, we opted to continue using the complex synthesized with AgSCF$_3$. 1$_{ppy}$-SCF$_3$ was fully characterized by 1D (^{1}H, ^{13}C and ^{19}F) and 2D NMR (^{1}H-^{1}H COSY, ^{1}H-^{13}C HSQC, ^{1}H-^{13}C HMBC) spectroscopy[18] and single-crystal X-ray diffraction (Scheme 2.9). Significantly, this complex was stable upon exposure to air for a few months, as after that time ^{1}H and ^{19}F NMR remained unchanged. It is worth mentioning that, to the best of our knowledge, it represents the first example of a Cp*Co metallacyclic species bearing a transmetalated nucleophile ligand.

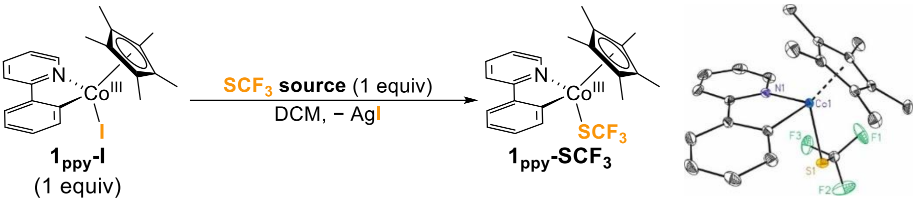

Entry	*SCF3 source*	*Temperature*	*Time*	*Yield*
1	AgSCF3	rt	15 min	90 %
2	NMe4SCF3	80 ºC	18 h	60 %

Scheme 2.9 Synthesis of **1$_{ppy}$-SCF$_3$** using AgSCF$_3$ or NMe$_4$SCF$_3$ as transmetalating agents. ORTEP drawing (thermal ellipsoids set at 50% probability) of the structure of **1$_{ppy}$-SCF$_3$**. Hydrogen atoms have been omitted for clarity.

2.3.2. Mechanistic Investigation on C–Bond-Forming Reductive Elimination

As mentioned above, in the C–H trifluoromethylthiolation protocol described by Wang in 2017 it is proposed that **1$_{ppy}$-SCF$_3$** directly produces de C–S coupling.[15b] We initiated our study by evaluating the intermediacy of this complex in catalysis by testing its catalytic competence. Gratifyingly, **1$_{ppy}$-SCF$_3$** probed not only to be a reactive intermediate but also a very active catalyst in the trifluoromethylthiolation of 2-

---

[18] See page 31 in the 2.5.1. Experimental appendix for the spectra

phenylpyridine, affording the coupling product in 81% yield (Scheme 2.10), and outperforming $[Cp^*CoI_2]_2$ used by Wang and co-workers (65% yield).

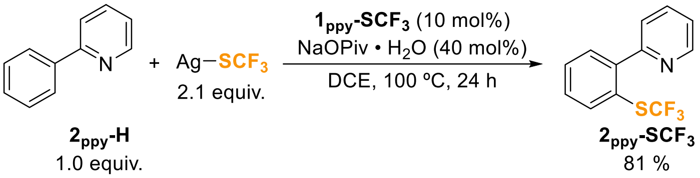

Scheme 2.10 Trifluoromethylthiolation of 2-phenylpyridine catalysed by complex $\mathbf{1_{ppy}\text{-}SCF_3}$.

Next, we sought to gain insights into the mechanism of the C–S coupling by combining a variety of experimental and computational studies. First, we investigated the direct participation of the post-transmetalated Co^{III} intermediate in the C–S reductive elimination upon thermolysis. In contrast to Wang's proposal, $\mathbf{1_{ppy}\text{-}SCF_3}$ only gives traces of the coupling product in dichloromethane or dichloroethane after heating for 1h at 100 ºC. To further confirm this experimental outcome, we performed DFT calculations at the M06-D3 level in CH_2Cl_2 solvent at 100 ºC (Scheme 2.12).[19] In alignment with the experimental results, the computational studies revealed a high energy barrier for the concerted C–S bond-forming reaction. Despite $\mathbf{1_{ppy}\text{-}SCF_3}$ is more stable in the singlet form, we found that the lowest energy barrier is in the triplet state (33.2 kcal mol^{-1}). Thus, to form the C–S bond, the singlet Co^{III} species should change the spin to triplet through a minimum-energy crossing point (MECP). Moreover, the reaction is thermodynamically unfeasible, due to the high energy of the resulting Co^{I} product (28.3 kcal·mol^{-1}). In agreement with the Hammond postulate, the TS is similar to the final Co(I) complex in respect to the C–S bond formation, whereas the Co–C bond has little elongation (see Scheme 2.12 for bond distances). These calculations along with the thermolysis of $\mathbf{1_{ppy}\text{-}SCF_3}$ confirmed that the direct reductive elimination pathway is not feasible.

---

[19] See Apendix for full computational details. All computational data are deposited in the ioChem-BD repository. M. Alvarez-Moreno, C. de Graaf, N. Lopez, F. Maseras, J. M. Poblet, C. Bo, *J Chem. Inf. Model.* **2015**, *55*, 95.
Follow the link for the structures of this collection: DOI: 10.19061/iochem-bd-1-193

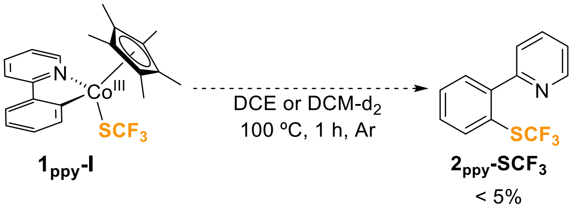

Scheme 2.11 Thermolysis of complex **1_{ppy}-SCF$_3$** to evaluate direct C–SCF$_3$ coupling.

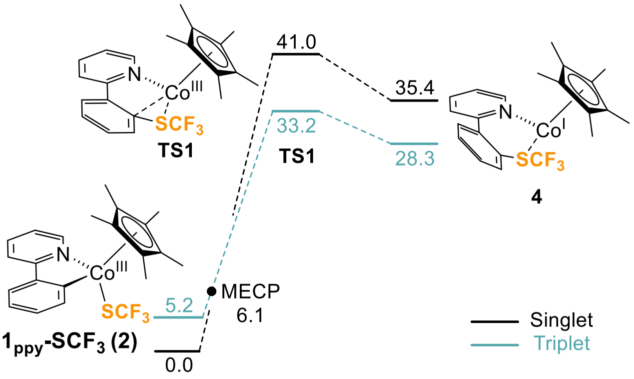

	Distances / Å			Angles / º
Structure	Co–C	Co–S	S–C	C-Co-S
2 (s)	1.92	2.28	2.85	84.9
TS1 (t)	1.99	2.37	2.06	55.6
4 (t)	3.02	2.33	1.80	36.5

Scheme 2.12 Computed free energy profile of the direct reductive elimination step from **1_{ppy}-SCF$_3$** (**2**). Energies are shown in kcal·mol^{-1}. Selected distances and bond angles for the structures involved in the reductive elimination from Co^{III} complex, **1_{ppy}-SCF$_3$** are shown on the table. The multiplicities of the structures are in parentheses, s for singlet and t for triplet.

In view of these results, we explored additional potential operative pathways. Inspired by the work by the Chang group, we aimed at investigating the feasibility of oxidatively induced reductive elimination events in Cp*Co-based systems. When we carried out the thermolysis **1_{ppy}-SCF$_3$**, but this time in the presence of 5 equiv of AgSCF$_3$, we were very pleased to observe quantitative formation of the coupling product after heating the reaction mixture for 1h at 100 ºC (Scheme 2.13). To probe the role of silver as oxidant in the reductive elimination step, we performed a similar experiment but replacing the silver salt by NMe$_4$SCF$_3$. After heating the reaction at 100 ºC for 7 h, we did not detect even traces of the C–S bond-forming reaction. This suggests strongly against an external nucleophilic attack from the SCF$_3$ anion directly to the carbon attached to the cobalt center. We also ruled out the participation of radical pathways by investigating the oxidative coupling in the presence of widely used radical scavengers such as TEMPO, butylated hydroxytoluene (BHT) or 4,4-dinitrobenzene. In these cases, we barely observed erosion on the yield of the organic product.

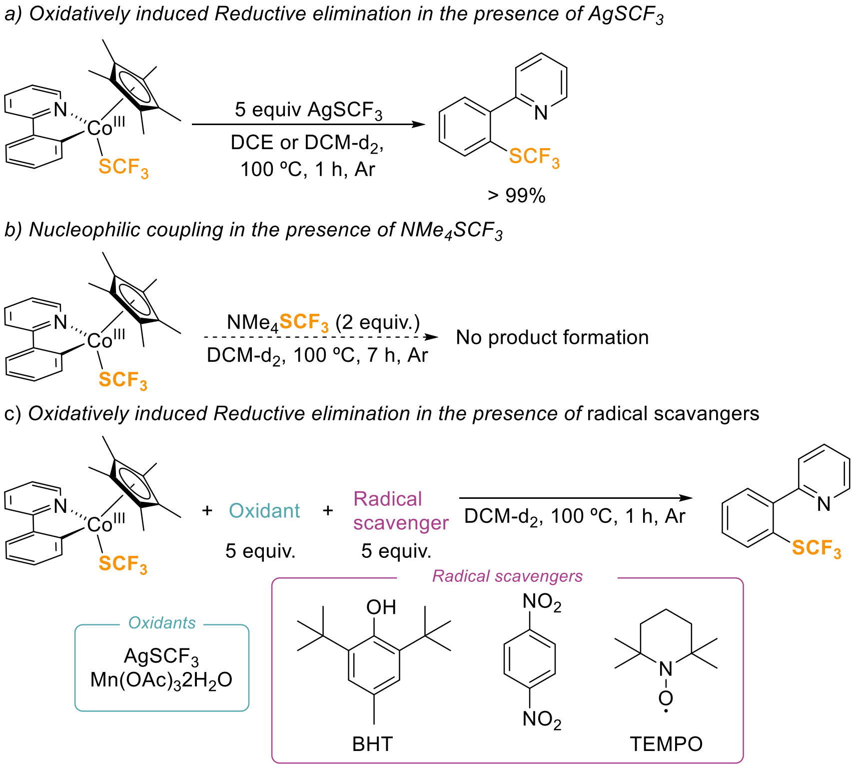

Entry	Chemical oxidant	Radical Scavenger	**2_{ppy}-SCF$_3$** (NMR yield / %)
1	AgSCF$_3$	BHT	>99
2	AgSCF$_3$	1,4 dinitrobenzene	>99
3	AgSCF$_3$	TEMPO	76

Scheme 2.13 Other possible pathways. On the table there are the yields of **2_{ppy}-SCF$_3$** obtained by ^{19}F NMR spectroscopy from the ORE with several radical scavengers.

Next, we tested whether additional oxidants could promote the targeted C–S coupling. We investigated the reactivity of **1_{ppy}-SCF$_3$** in the presence of different commonly used inorganic oxidants by ^{1}H and ^{19}F NMR spectroscopy (Scheme 2.14). Despite the tested silver and copper salts gave low yields, Mn(OAc)$_3$·2H$_2$O afforded **2_{ppy}-SCF$_3$** in quantitative yield.

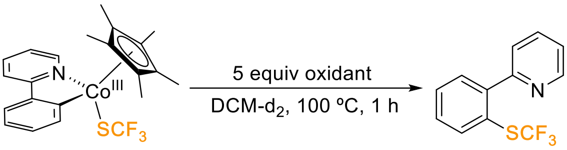

Oxidant	AgF	AgF_2	AgOTf	AgOAc	$Cu(OAc)_2$	$Mn(OAc)_3$ $2H_2O$
2_{ppy}-SCF_3 (NMR yield / %)	37	30	30	traces	12	Quantitative

Scheme 2.14 Oxidatively induced C–S bond-forming reductive elimination reaction from **1_{ppy}-SCF_3** in the presence of other 1-electron chemical oxidants. The reported yields were determined by ^{19}F NMR spectroscopy of the crude reaction mixture using 4,4'-difluorobiphenyl as internal standard.

With these promising experimental results on the involvement of ORE events in hand, we performed DFT calculations to assess the viability of the C–SCF_3 bond forming reaction from Cp*Co^{IV} and Cp*Co^{V} species (Scheme 2.15). As observed in related TM systems,[20] we have found that the oxidation state of metals centers is fundamental to promote otherwise inaccessible nucleophilic couplings, observing lower activation barriers at higher oxidation states of the cobalt metal center. In both cases, the reductive elimination events are kinetically and thermodynamically favorable. For Co^{IV}, both minima were calculated as a doublet and a quartet state, however the doublet states were always lower in energy. It has to be pointed out that the optimized structure of the Co^{V} complex (**7^{2+}**) in the singlet form was never achieve, and it always decayed to the product. Therefore, the energy of the singlet state of **7^{2+}** is an approximation using the geometry of the triplet state and performing a single-point calculation of the energy.[21]

---

[20] G. Song, X. Li, *Acc. Chem. Res.* **2015**, *48*, 1007.

[21] We did not calculate the activation barrier in the singlet state, because first as we observed for the calculation of the Co(V) it should be small and the starting and product complexes are more stable in triplet state, suggesting that in the TS the same would occur.

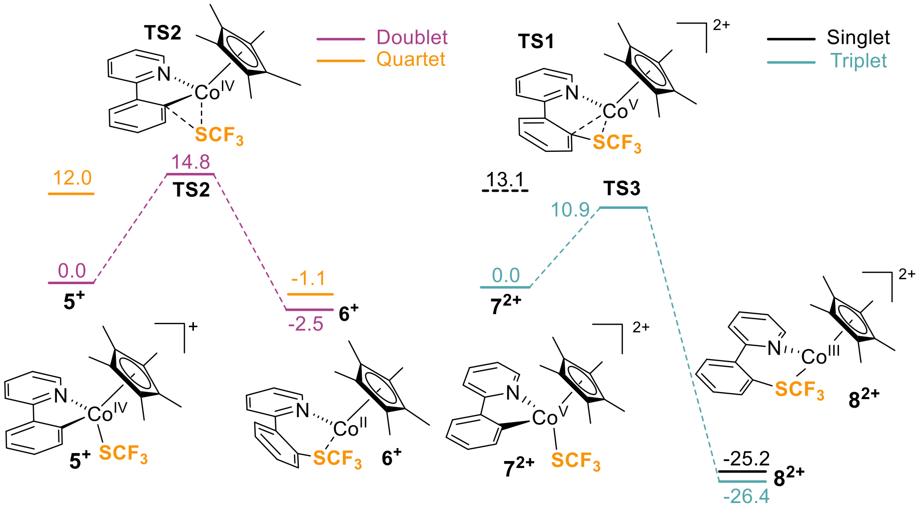

	Distances / Å			Angles / °
Structure	Co–C	Co–S	S–C	C-Co-S
5$^+$ (d)	1.95	2.18	3.13	98.2
TS2 (d)	1.98	2.20	2.25	64.9
6$^+$ (d)	3.05	2.26	1.79	35.5
7^{2+} (t)	1.89	2.17	3.00	95.0
TS3 (t)	1.92	2.23	2.61	77.5
8^{2+} (t)	2.86	2.31	1.80	38.9

Scheme 2.15 Computed free energy profile (kcal·mol^{-1}) of the reductive elimination step from complexes Co^{IV} (left) and Co^{V} (right) at 100 ºC. Selected distances and bond angles for the structures involved in the reductive elimination from complexes Co^{IV} and Co^{V} are shown on the table. The multiplicities of the structures are in parentheses, d for doublet and t for triplet.

Similarly, to what was observed for the reductive elimination from **1$_{ppy}$-SCF$_3$**, illustrating principles of the Hammond postulate, the transition state becomes much more reactant-like while oxidizing the metal center. And in the case of Co(IV) we observed longer distances for C–S bond of 2.25 Å and even larger with Co(V), 2.61 Å.

Mechanistic studies on the oxidation state of the high-valent Cp*Co species

While the shown experimental and computational results support that an oxidative induced reductive elimination step is responsible of promoting the targeted C–S bond-forming reaction, the gathered information do not allow to determine the exact oxidation state of the reactive intermediate (Scheme).

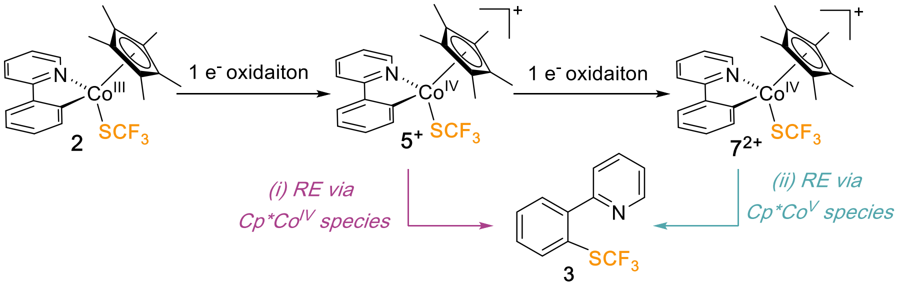

Scheme 2.16 Possible oxidation and subsequent C–SCF$_3$ bond-formation pathways

To gain more insight into the redox processes, we conducted cyclic voltammetry on **1_{ppy}-SCF$_3$**. Initially, we performed a scan with a wide potential range to obtain a comprehensive electronic profile (within the confines of DCM). The CV reveals an irreversible reduction peak at -1.6 V, and at least two irreversible oxidation peaks at 0.15 and 0.8 V. When we focused on the oxidation peak at 0.15 V, which we attributed to the Co$^{III/IV}$ couple, we observed that the oxidation was never reversible, even at fast scan rates,[22] indicating that a chemical reaction takes place after the electron transfer, transforming the formed Co^{IV} species into a different product. This suggests that once the cobalt (IV) intermediate is formed, the reductive elimination occurs faster than the second 1-electron oxidation to access a Co^{V} species.

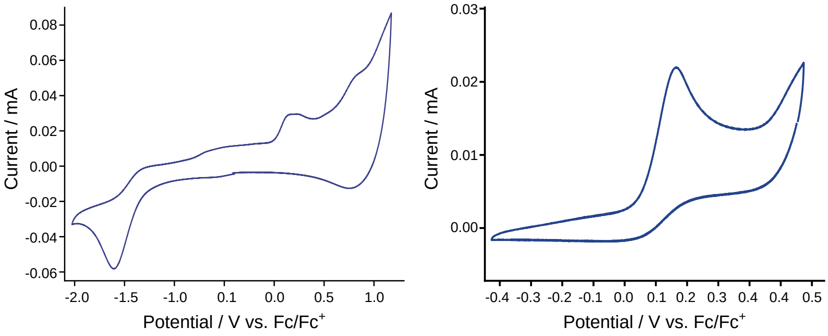

Scheme 2.17 Cyclic voltammogram of complex **1_{ppy}-SCF$_3$** vs Fc/Fc$^+$ in DCM/*n*NBu$_4$PF$_6$ at scan rate of 100 mV/s. On the left full potential window and on the right narrower window to isolate the peak.

To test this working hypothesis, we envisioned to promote the C–S bond forming reaction electrochemically. With the information gathered by CV and the DFT studies,

---

[22] Check appendix for the rest CVs at different scan rates

we performed a chronoamperometry (CA) technique to selectively **1_{ppy}-SCF_3** to Co(IV), applying 0.15 V vs Fc/Fc$^+$ and see if we obtained the desired organic product **2_{ppy}-SCF_3** (Scheme 2.18)

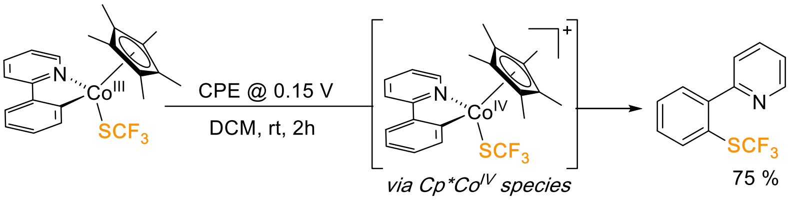

Scheme 2.18 Chronoamperometry experiments for the electrosynthesis of **2_{ppy}-SCF_3**

An average of 75 % yield was achieved in all the experiments with divided cells.[23] Unexpectedly, we observed a certain degree of mass transfer from anode to cathode and therefore collected both fractions. An undivided cell could also be used achieving 100 % conversion, however it as an inefficient way of performing the reaction due to the long reaction time (16 h) and low faraday efficiency (overall charge transferred 24 C). We followed the reaction current, as shown in Figure 2.1, and the reaction was stopped after 1 equivalent of electrons had been transferred from the Co^{III} complex.

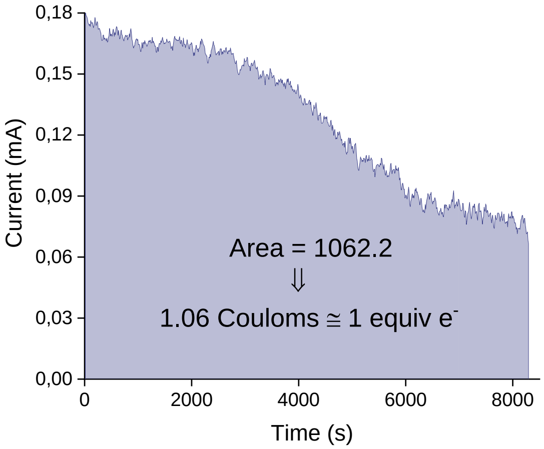

Figure 2.1 Transferred charge during a constant potential electrolysis experiment.

A clear color change was observed along the reaction, from orange, to grey and finally to a deep blue solution (Figure 2.2).

---

[23] Due to problems associated to the quantification of **3**, different internal standards were added at the end of each reaction: 4,4´-difluorobiphenyl, 3,5-bis(trifluoromethyl)benzoic acid and 4-(((trifluoromethyl)thio)oxy)benzaldehyde.

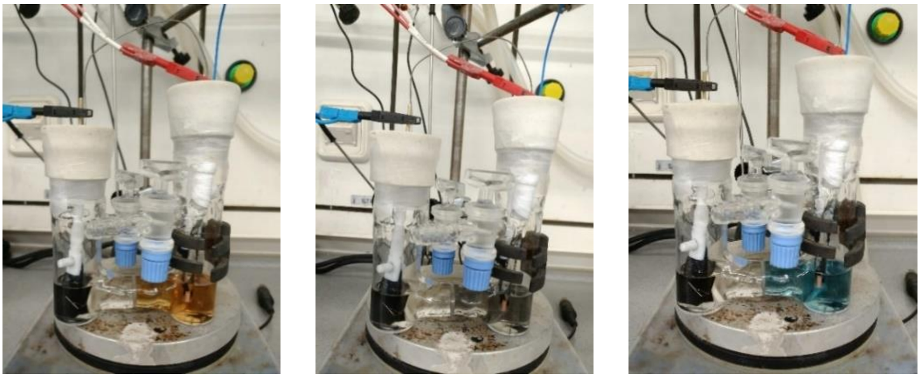

Figure 2.2 Reaction of entry 1 at 0 min, 1h and 2h (from left to right).

A similar result was obtained from the kinetic studies conducted to determine the order in $AgSCF_3$ (Scheme 2.19 Kinetic order in $AgSCF_3$Scheme 2.19). The C–S coupling shows a first-order kinetic dependence on [Ag] in THF at 70 ºC.[24] This finding provides compelling evidence supporting the occurrence of a single electron transfer oxidation, followed by reductive elimination step to form the new C–SCF_3 bond.

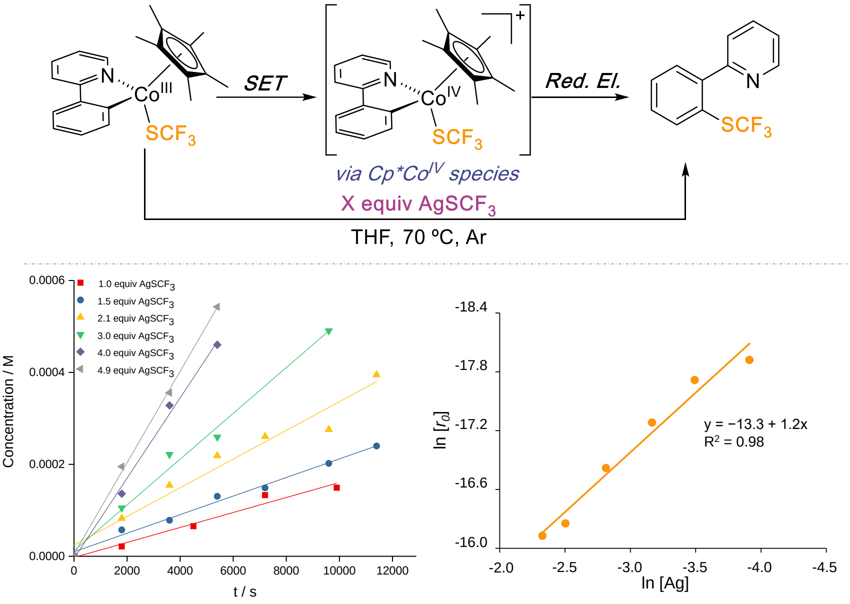

Scheme 2.19 Kinetic order in $AgSCF_3$

---

[24] The change of solvent to THF was required to guarantee that the silver is completely dissolved.

The energy required for 1 or 2 electron oxidations was also calculated computationally, in order to compare them with the experimental results. To do so, first, we computed the energy difference between complex **1_{ppy}-SCF$_3$ (2)** and **5^+**, obtaining a value of 4.87 V. This seems a large value, but it is an absolute value and redox potentials have to compared with a reference. In this case, the references are the standard hydrogen electrode (SHE) and ferrocene, as in the experiments (see equation 1). We calculated, in the same manner, the oxidation potential of Co(IV) to Co(V) oxidation equation 2. The calculated potential for the oxidation to Co(IV) (0.13 V) corresponds to the peak we observed in the CV. The potential required to oxidize the cobalt complex further is much larger.

$$\text{For Co}^{\text{III/IV}}\text{ oxidation: } 4.87\text{ V} - 4.28\text{ V (vs SHE)} - 0.46\text{ V}\left(\text{vs}\,\frac{\text{Fc}}{\text{Fc}^{+}}\right) = 0.13\text{ V} \tag{1}$$

$$\text{For Co}^{\text{IV/V}}\text{ oxidation: } 6.60\text{ V} - 4.28\text{ V (vs SHE)} - 0.46\text{ V}\left(\text{vs}\,\frac{\text{Fc}}{\text{Fc}^{+}}\right) = 1.86\text{ V} \tag{2}$$

As the value for oxidation to Co(V) is high, we hypothesize that under the reaction conditions, Co(IV) is the only high-valent species formed. Besides, in literature is reported that Ag (I) has a reduction potential of 0.65 V vs Fc/Fc$^+$ in DCM,[25] which would be enough to oxidize the Co(III) species to Co(IV).

The analysis of the natural orbitals of the Co(IV) and Co(V) complexes is shown in Figure 2.3 where for Co(IV) the orbital is centered between the Co and the S atoms. Besides, it has a spin density of 0.908 center in Co, which agrees with the oxidation state IV for the cobalt center. In case of the Co(V) species the orbital is a bit more localized on the Cp* ligand, and the spin density in the Co center is 1.87, in agreement with having two unpaired electrons.

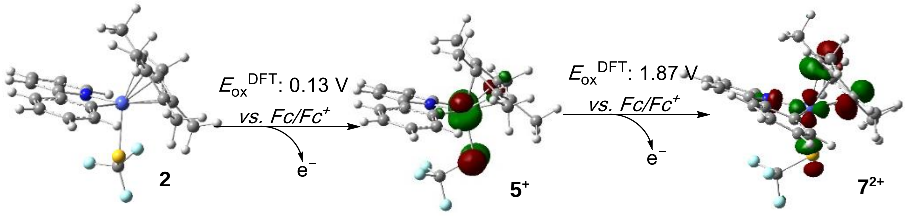

Figure 2.3 Oxidation of **1_{ppy}-SCF$_3$** by one electron Co(IV) complex (**5**$^+$) and next oxidation to the Co(V) complex (**7**$^{2+}$), their LUMO orbitals are shown with an isovalue of 0.06.

---

[25] Connelly and Geiger, *Chem. Rev.* **1996**, *96*, 877-910

DFT calculations of oxidation of [CpCo^{III}(2-ppy)(SCF_3)] with Ag*

In order to calculate the thermodynamic parameters of the oxidation of complex **1_{ppy}-SCF_3** by Ag(I), due to the involvement of a solid metal a thermodynamic cycle is required to estimate the energy for the reduction of Ag(I) to solid silver. By employing this methodology, it becomes possible to theoretically calculate the standard reduction potential (SRP), which is essential for estimating the thermodynamic parameters of this particular redox process.

The Standard Reduction Potential (SPR) is the thermodynamic parameter that the tendency of a chemical species to win or lose electrons. The theoretical calculation of SRP is achieved through the decomposition of the targeted reaction into different steps, in which the sum of all the contributions accomplish a simplified approach to the targeted parameter.[26] In 2007 Kobayashi and co-workers developed a thermodynamic cycle strategy, based on the Born-Haber cycle, to calculate the SRP of a reaction involving solid species, shown in Scheme 2.20.[27]

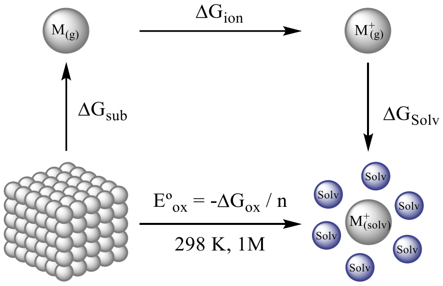

Scheme 2.20 Thermodynamic cycle to compute the Standard Redox Potential involving solid metals in solution.

The SRP of the metallic species in solution can be estimated through the sum of the free energies of sublimation (ΔG_{sub}), ionization (ΔG_{ion}), and solvation (ΔG_{solv}).

$$E^0_{red} = -E^0_{ox} = \frac{-\Delta G^0_{ox}}{n} = \Delta G^0_{sub} + \Delta G^0_{ion} + \Delta G^0_{solv} \qquad (3)$$

The sublimation energy, from solid to gas, corresponds to the cohesive energy, this value is taken from the experimental work by Friesner and co-workers.[28] The ionization

---

[26] Arumugam, K.; Becker, U. *Minerals* **2014**, 4, 345.

[27] Shimodaira, Y.; Miura, T-; Kudo, A.; Kobayashi, H. *J. Chem. Theory Comput.* **2007**, 3, 789.

[28] Baik, M.-H.; Friesner, R.A. *J. Phys. Chem. A* **2002**, 106, 7407

energy is also an experimental value from the work of Noodleman and co-workers.[29] Lastly, the solvation energy is calculated by DFT, introducing the solvent indirectly through the utilization of a self-consistent reaction field method (PCM). Our group reviewed this approach and improved the method, decreasing the absolute error from 0.23 V to 0.04 V. We found a systematic error due to the lack of entropic contributions in the cohesive and ionization energies which could be introduced obtaining the revised values: ΔG_{sub}^{corr} and ΔG_{ion}^{corr}.[30]

In our system, the silver(I) salt ($AgSCF_3$) is reduced to solid silver(0) therefore instead of having a metallic solid that oxidizes to a $M^+_{(solv)}$, the process occurs in reverse. The dissociation energy for the formation of Ag^+ and SCF_3^- must be included as well.

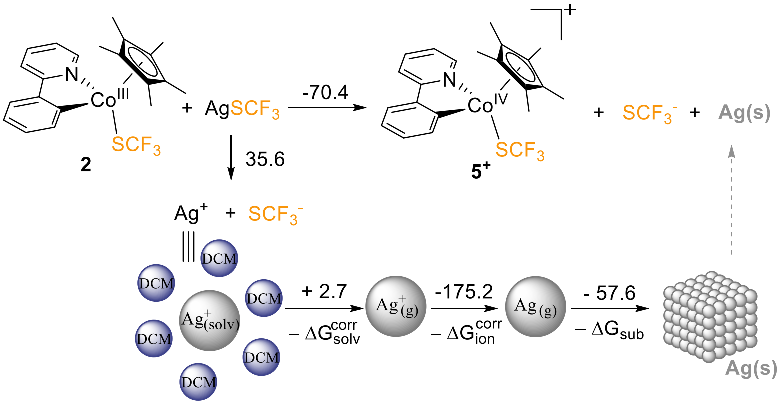

Scheme 2.21 Calculated energy for Co(III) oxidation together with Ag(I) reduction and solid silver formation. Energies in kcal·mol^{-1}.

Indeed, taking all the simpler smaller steps, including the dissociation of the $AgSCF_3$, the silver salt is able to oxidize the cobalt III centre to Co(IV) forming Ag(s) in an sl exergonic reaction, with an energy of -70.4 kcal·mol^{-1}.

2.3.3. Experiments to try to characterize the Co(IV) intermediates

a) EPR

Subsequently, we sought to provide additional experimental evidences for the transient formation of high-valent Co(IV) species. Our attempts to detect **5**$^+$ by electron paramagnetic resonance (EPR) were unclear. As shown in Figure 2.4, there is a small

---

[29] Han, W.-G.; Liu, T.; Lovell, T.; Noodleman, L. *Inorg. Chem.* **2006**, 45, 8533.

[30] F. Maseras, I. Funes-Ardoiz, *ChemPhysChem*. **2019**, 20, 159–162

EPR signal. However, the signal does not have the characteristic shape of a paramagnetic cobalt center, but as it was seen with the radical trappers, there are no organic radicals present in the reaction. Therefore, we cannot determine if it comes from the Co or maybe the formed Ag(0), which also has an unpaired electron.

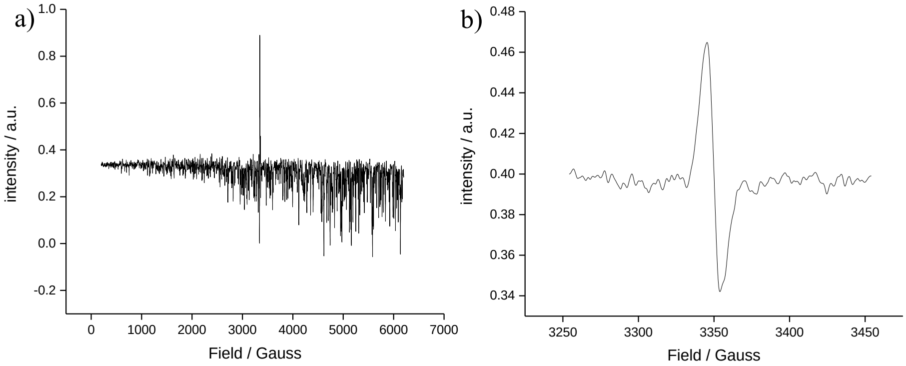

Figure 2.4 EPR spectra of the reaction of complex $\mathbf{1_{ppy}\text{-}SCF_3}$ with $AgSCF_3$, heated in the EPR tube for 15 min at 100 ºC. Left: Full window. Right: ampliation of the area where the signal appears.

c) EPR measurements during the electrochemical process

We also attempted to measure the reactions by EPR during the CA. However, no signal corresponding to a paramagnetic signal was observed. The reason behind no observed signal can be related to the manipulation process, that even if we had some paramagnetic species, it would have decomposed. The experiments were carried out at 77 K (liquid nitrogen temperature), it could be that the paramagnetic cobalt species are not observed at this temperature and lower temperatures (5 K, helium temperature) are required. As in these experiments there is no Ag is present, we did not observe any paramagnetic signal, we cannot conclude if the signal we observed in Figure 2.4 corresponds to the cobalt complex or not.

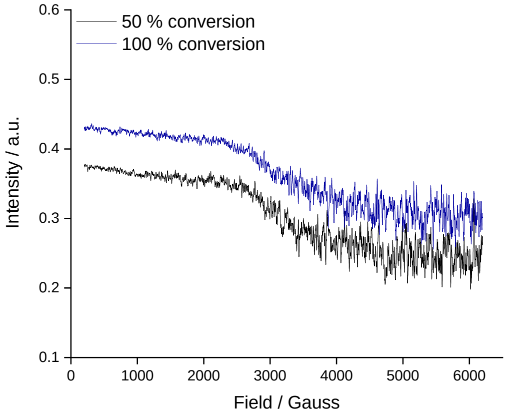

Figure 2.5 EPR spectra during the electrochemical oxidation of **1_{ppy}-SCF_3** at 50 % conversion (20 scans, black) and after, 100 % conversion (15 scans, blue).

b) UV-vis following the reaction

We followed the electrochemical reaction by UV-vis (Figure 2.6). The black line corresponds to the first point of the reaction, of the complex **2**. During the reaction we can observe a disappearance of the absorption peak at 400nm, while a peak at 600 nm appears. At 525 nm there is an isosbestic point which can indicate the conversion of complex **1_{ppy}-SCF_3** to another short-lived cobalt complex.

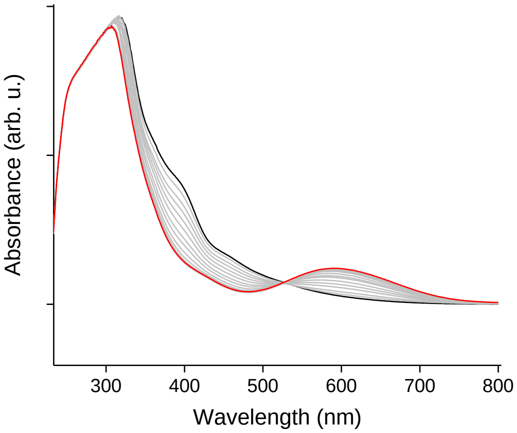

Figure 2.6 UV-vis analysis of the electrochemical generation of **2_{ppy}-SCF_3** (red line) using **1_{ppy}-SCF_3** (black line) as starting material.

c) Magnetic measurements - SQUID

Finally, we looked for other alternatives trying to characterize the high valent Co(IV) elusive species. However, the calculations suggest that once the high valent

Co(IV) species is formed, it reacts fast. Thus, it would be a real challenge to isolate or characterize it. Therefore, we focused our attention on detecting the Co(II) species that would result from the reductive elimination step, gaining indirect evidence of the presence of the high-valent Co(IV) species.

We performed magnetism measurements with a superconducting quantum interference device (SQUID). We focused our attention on the electrochemical transformation because using AgSCF$_3$ as oxidant could lead to inconclusive results as five equivalents of the silver salt are used, which could result in Co(II) being reoxidized (as it is shown by the DFT calculations in the appendixes, on page 92).

For detecting the Co(II) species after the reductive elimination step using electrochemistry, three measurements are required: 1) the crude mixture after the chronoamperometry experiment, which consists on first fully oxidizing complex **1$_{ppy}$-SCF$_3$** by passing 1 C, then the solution is collected and the solvent is evaporated under reduced pressure, and without any other purification. 2) the supportive electrolyte used in the CA (TBAPF$_6$) and 3) the starting complex [Cp*Co(PPy)(SCF$_3$)]. The last two samples are done to make sure that the signals comes from the Co(II) complex, and there is no signal in the starting material or electrolyte.

Next, the data obtained by the SQUID is shown:

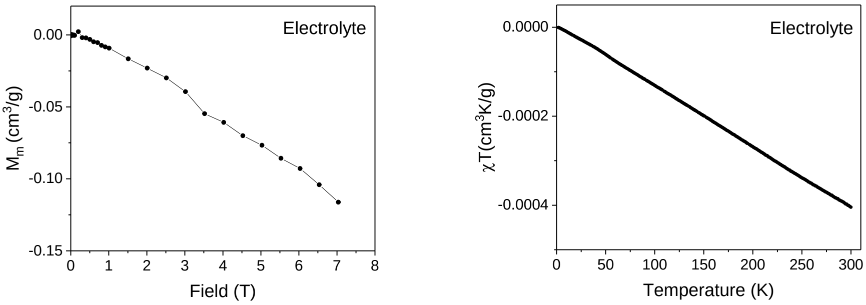

Figure 2.7 Left: Magnetization vs magnetic field plot at 2 K for the electrolyte. Right: Thermal dependence of the $\chi_T T$ product for the electrolyte within 300 – 2 K temperature range.

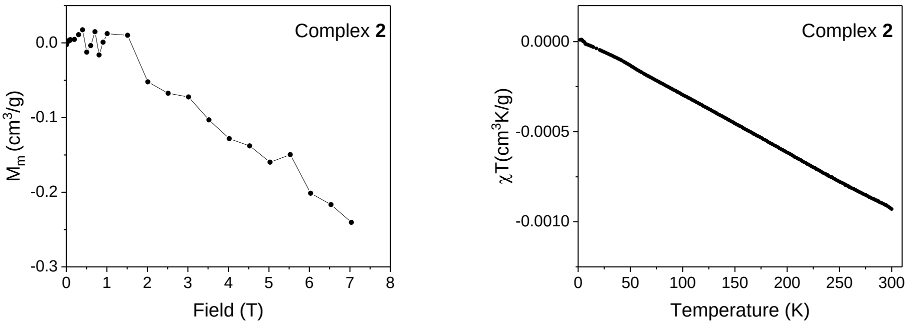

Figure 2.8 Left: Magnetization vs magnetic field plot at 2 K for **1$_{ppy}$-SCF$_3$**. Right: Thermal dependence of the $\chi_T T$ product for complex **1$_{ppy}$-SCF$_3$** within 300 – 2 K temperature range.

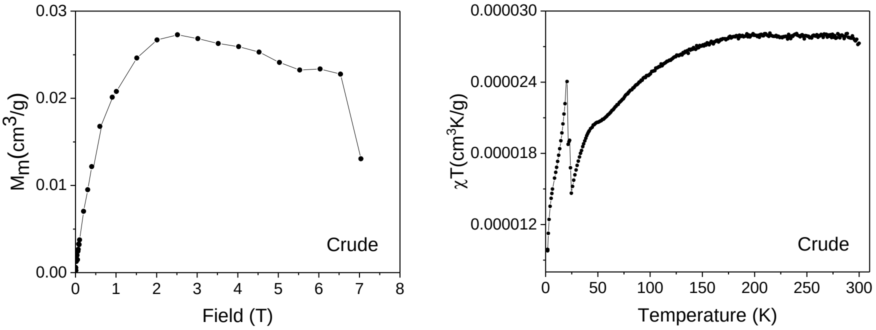

Figure 2.9 Left: Magnetization vs magnetic field plot at 2 K for the crude. Right: Thermal dependence of the $\chi_T T$ product for the crude within 300 – 2 K temperature range.

While the electrolyte and complex **1$_{ppy}$-SCF$_3$** showed diamagnetic response (Figure 2.7 and Figure 2.8), the crude sample (Figure 2.9) revealed paramagnetic species, suggesting a presence of a Co(II) species. The data of the field-dependence magnetization at 2 K showed in small magnetic fields a rise in the magnetization value, indicative of a major paramagnetic behavior of the crude sample.

These results confirm that at the end of the electrochemical oxidation of **1$_{ppy}$-SCF$_3$**, we obtained a paramagnetic cobalt species. We assigned it to be a Co(II) species, formed after the reductive elimination from a Co(IV) species. Hence, we have indirect proof of the involvement of a high-valent cobalt species for the formation of the C–SCF$_3$ bond.

2.4. Conclusion

In summary, in this chapter we were able to synthesize a proposed intermediate to study the mechanism of the C–S bond formation. We demonstrated that the previously proposed mechanism was incorrect, and instead of direct reductive elimination form Co(III) an oxidatively induced reductive elimination mechanism takes place. For the first time, we provide experimental and computational evidence on the involvement of a high-valent Co(IV) species. Additionally, we could promote the reaction not only with chemical oxidants, but also by electrochemical methods.

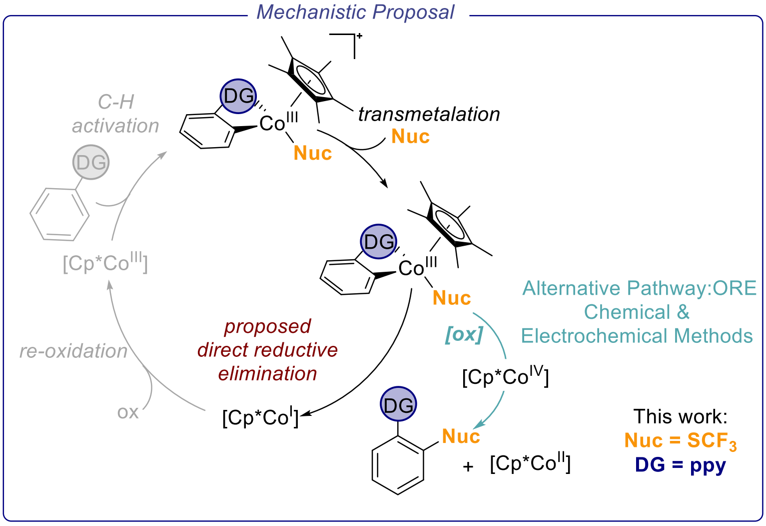

Scheme 2.22 Final mechanistic proposal

2.5. Appendixes

2.5.1. Experimental appendix

General procedures

All reactions were conducted in an argon-filled glovebox (mBraun Unilab 4420) with concentrations of O_2 and H_2O < 0.1 ppm or oven-dried glassware (at 100 ºC overnight and cooled under vacuum prior use) using Schlenk techniques under argon atmosphere (otherwise mentioned). NMR spectra were obtained on a Bruker 400 MHz, a 500 MHz or a 500 MHz with cryoprobe spectrometers equipped with probeheads capable of producing gradients in the z direction with a maximum strength of 53.5 G/cm. ^{1}H, ^{13}C and ^{19}F NMR chemical shifts are reported in parts per million (ppm), relative to tetramethylsylane (TMS) for ^{1}H and ^{13}C with the residual solvent peak used as an internal reference and relative to $CFCl_3$ (Freon) for ^{19}F. Multiplicities are reported as follows: s (singlet), dd (doublet of doublets), td (triplet of doublets), quadruplet (q) and multiplet (m). ^{19}F and ^{1}H NMR yields for reductive elimination studies were obtained on a Bruker 400 MHz or 500 MHz spectrometer using 4,4´- difluorobenzene (–116.65 ppm) as an internal standard with 8 scans for data acquisition. All electrochemical experiments were performed with a Biologic SP–150 potentiostat at rt. UV-Vis measurements were carried out on a Shimadzu UV-1800PC spectrophotometer equipped with a photomultiplier detector, double beam optics and D2 and W light sources. Continuous wave (CW) EPR spectra were acquired on a Bruker EMX X-band Micro EPR spectrometer with an ER 4116 HS cavity. A 150 mL Suprasil offset liquid nitrogen dewar flask (Wilmad-LabGlass) was used for low-temperature measurements (77 K). Magnetic measurements were carried out with a Quantum Design MPMS-XL SQUID magnetometer (Quantum Design, Inc, San Diego, CA, USA).

Materials and methods

Commercially available reagents 2-iodobenzaldehyde, 2-phenylpyridine, N-iodosuccinimide, $Pd(OAc)_2$, 1,2,3,4,5-pentamethylcyclopenta-1,3-diene, $CoCl_2$, nBuLi, Zn powder, (Trifluoromethyl)trimethylsilane, sulfur, tetramethylammonium fluoride, $AgSCF_3$, AgOTf, $Mn(OAc)_3•2H_2O$, AgOAc, AgF, AgF_2, $Cu(OAc)_2$, (2,2,6,6-Tetramethylpiperidin-1-yl)oxyl (TEMPO), 2,6-Di-tert-butyl-4-methylphenol (BHT), 1,4 dinitrobenzene, 4,4´-difluorobiphenyl, 3,5-bis(trifluoromethyl)benzoic acid, 4-(((trifluoromethyl)thio)oxy)benzaldehyde and $(nBu)_4NPF_6$ were used without further purification directly as received from the commercial supplier, and stored under inert gas and/or low temperature when required. 1,2-dichloroethane (DCE) was stored under argon with activated 4 Å molecular sieves. If necessary, the solvents (Hexane, THF, CH_2Cl_2) were used from a solvent purification system pure-solv (SPS-400, Innovative Technology) and stored under argon over activated 4 Å molecular sieves. CD_2Cl_2 and $CDCl_3$ were stored under argon over activated molecular sieves 4 Å. The compounds [Cp*Co(VTMS)$_2$],[1] [Cp*Co^{III}(2-ppy)(I)] (**1**),[1] and NMe_4SCF_3[2] were synthesized according to previous literature procedures.

*Isolation and characterization of [Cp*Co^{III}(2-ppy)(SCF$_3$)] (**1$_{ppy}$-SCF$_3$**)*

Scheme 2.23 Sythesis of complex [Cp*Co^{III}(2-ppy)(SCF$_3$)] (**1$_{ppy}$-SCF$_3$**)

In an argon atmosphere glovebox, **1$_{ppy}$-I** (25 mg, 0.053 mmol) and $AgSCF_3$ (11 mg, 0.053 mmol) were added to an oven-dried Schlenk containing a magnetic stir bar. CH_2Cl_2 (3 mL) was added and the mixture was stirred at room temperature for 15 min. The red suspension was then filtrated using a PTFE 13 mm 0.2 µm NSTR syringe filter and the solution was evaporated under vacuum. Hexane (10 mL) was directly added, the solution was removed and the red solid was dried under vacuum. Yield (90%, 22 mg). Crystals of [Cp*Co^{III}(2-ppy)(SCF$_3$)] (**1$_{ppy}$-SCF$_3$**) were obtained in a mixture of CH_2Cl_2/hexane at room temperature.

^{1}H NMR (CD_2Cl_2, 298 K, 500 MHz): δ 9.06 – 8.78 (m, 1H), 7.89 (dd, $^3J_{H,H} = 7.7$, 1.1 Hz, 1H), 7.81 – 7.64 (m, 2H), 7.62 (dd, $J = 7.7$, 1.5 Hz, 1H), 7.28 (td, $J = 7.4$, 1.5 Hz, 1H), 7.21 – 6.93 (m, 2H), 1.32 (s, 15H).

^{13}C NMR (CD_2Cl_2, 298 K, 126 MHz): δ 179.31 (C_{ipso}), 166.70 (C_{ipso}), 153.75, 153.73, 145.70 (C_{ipso}), 140.0, 138.69, 137.04, 136.4 (q, $^1J_{C,F} = 307$ Hz, SCF_3), 129.96, 123.62, 123.21, 121.40, 118.69, (C_{ipso}, Cp*), 9.02 (CH_3, Cp*) ppm

---

[1] J. Sanjosé-Orduna, D. Gallego, A. García-Roca, E. Martin, J. Benet-Buchholz, M. H. Pérez-Temprano, *Angew. Chem., Int. Ed.* **2017**, *56*, 12137.

[2] T. Scattolin, F. Schoenebeck, *e-EROS* **2018**, DOI: 10.1002/047084289X.rn02228.

^{19}F NMR (CD_2Cl_2, 298 K, 471 MHz): δ –21.07 ppm

NMR spectra of complex ***1$_{ppy}$-SCF$_3$***

^{1}H NMR spectrum of **1_{ppy}-SCF$_3$** at 25 ºC (CD_2Cl_2)

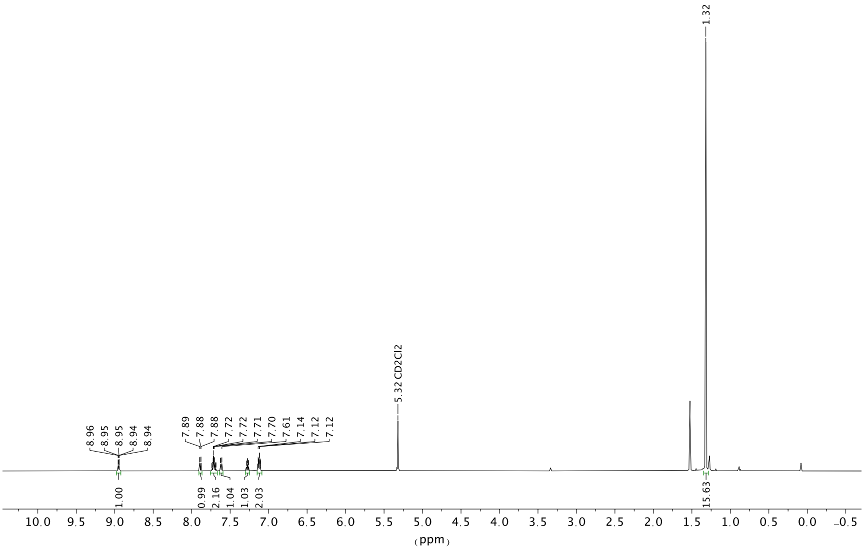

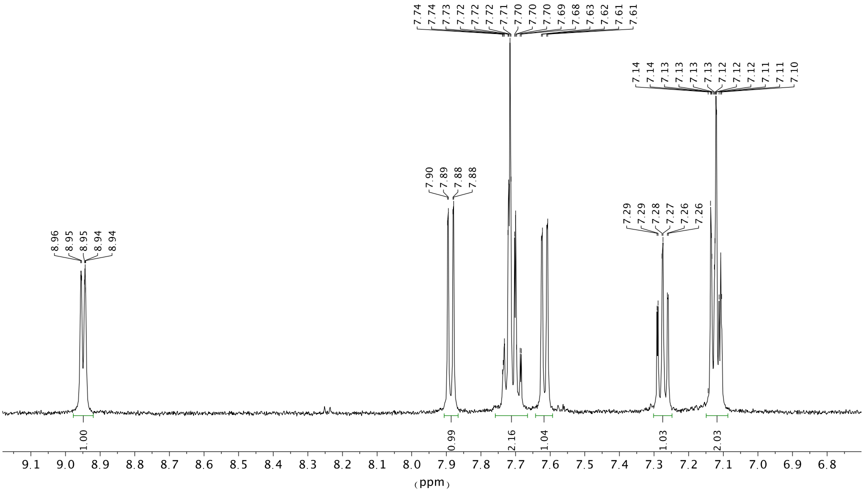

^{13}C $\{^{1}$H$\}$ NMR spectrum of **1_{ppy}-SCF$_3$**at 25 ºC (CD$_2$Cl$_2$)

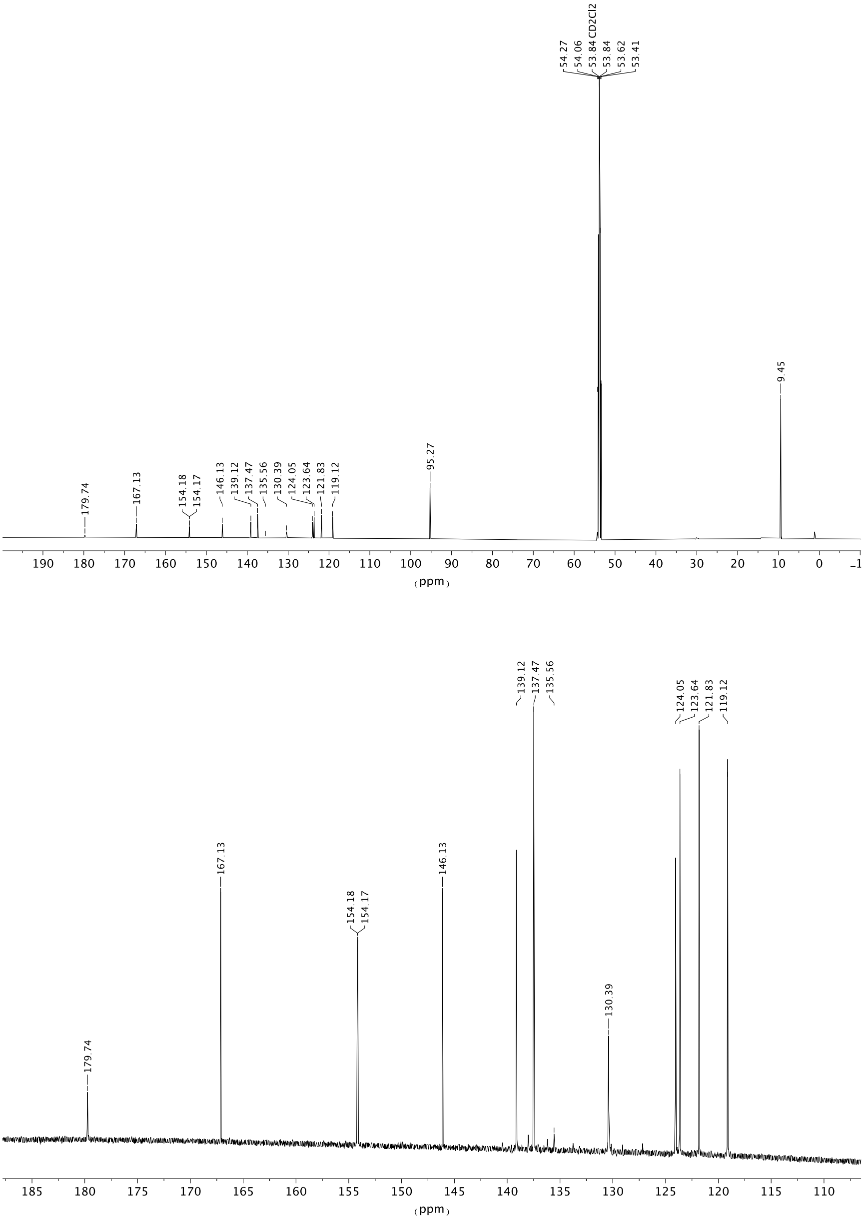

^{1}H-^{1}H COSY NMR spectrum of $\mathbf{1_{ppy}}$**-**$\mathbf{SCF_3}$ at 25 ºC (CD_2Cl_2)

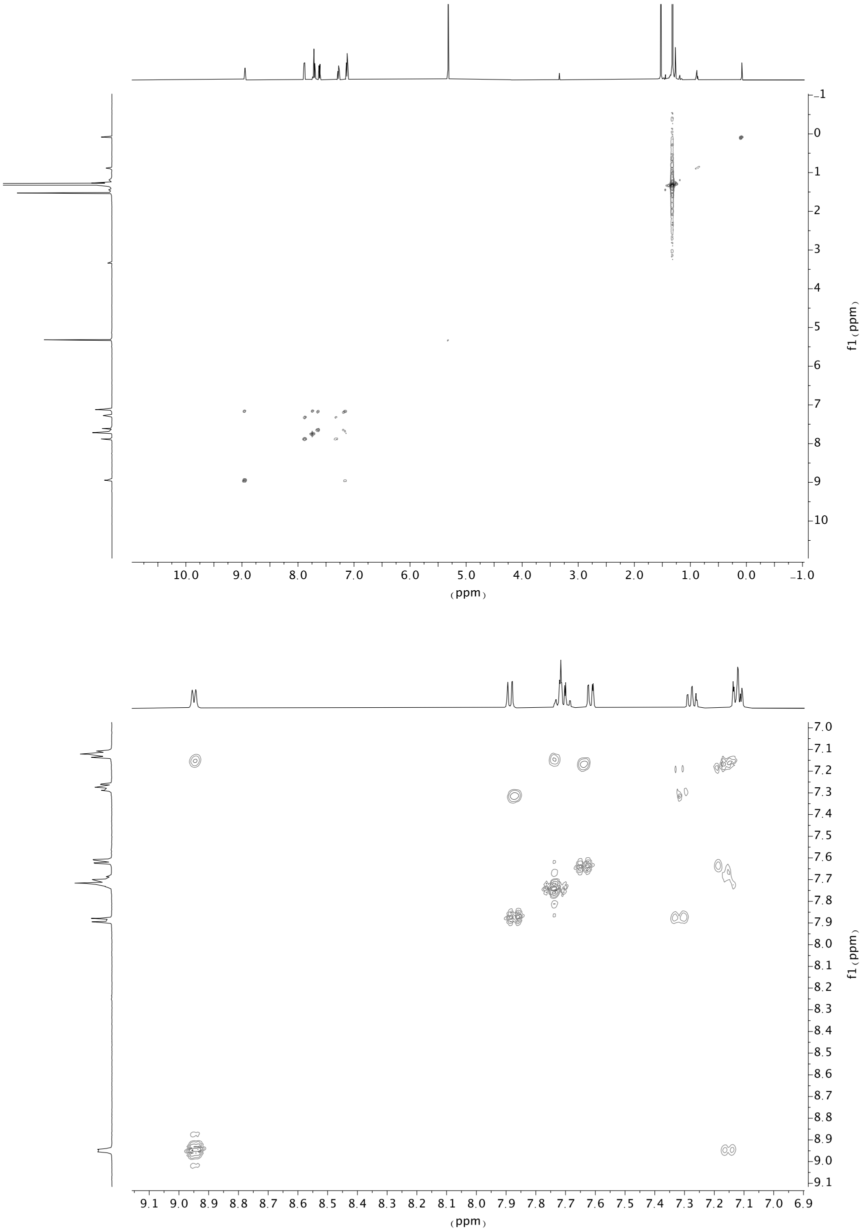

^{1}H-^{13}C HSQC NMR spectrum of **1_{ppy}-SCF$_3$** at 25 ºC (CD$_2$Cl$_2$)

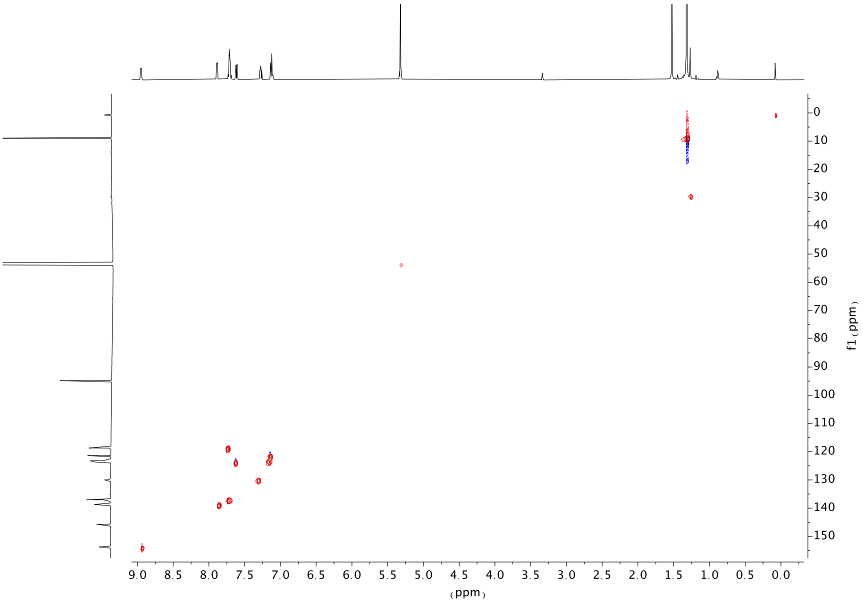

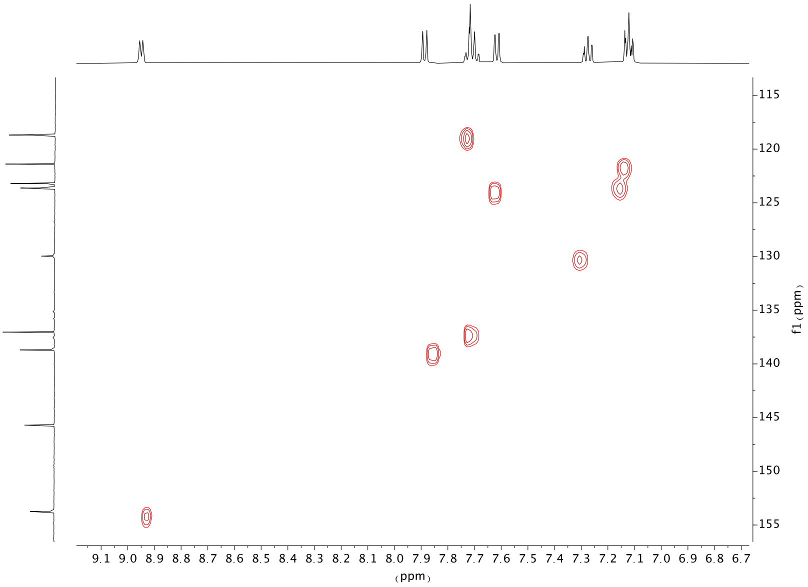

^{1}H-^{13}C HMBC NMR spectrum of **1_{ppy}-SCF$_3$** at 25 ºC (CD$_2$Cl$_2$)

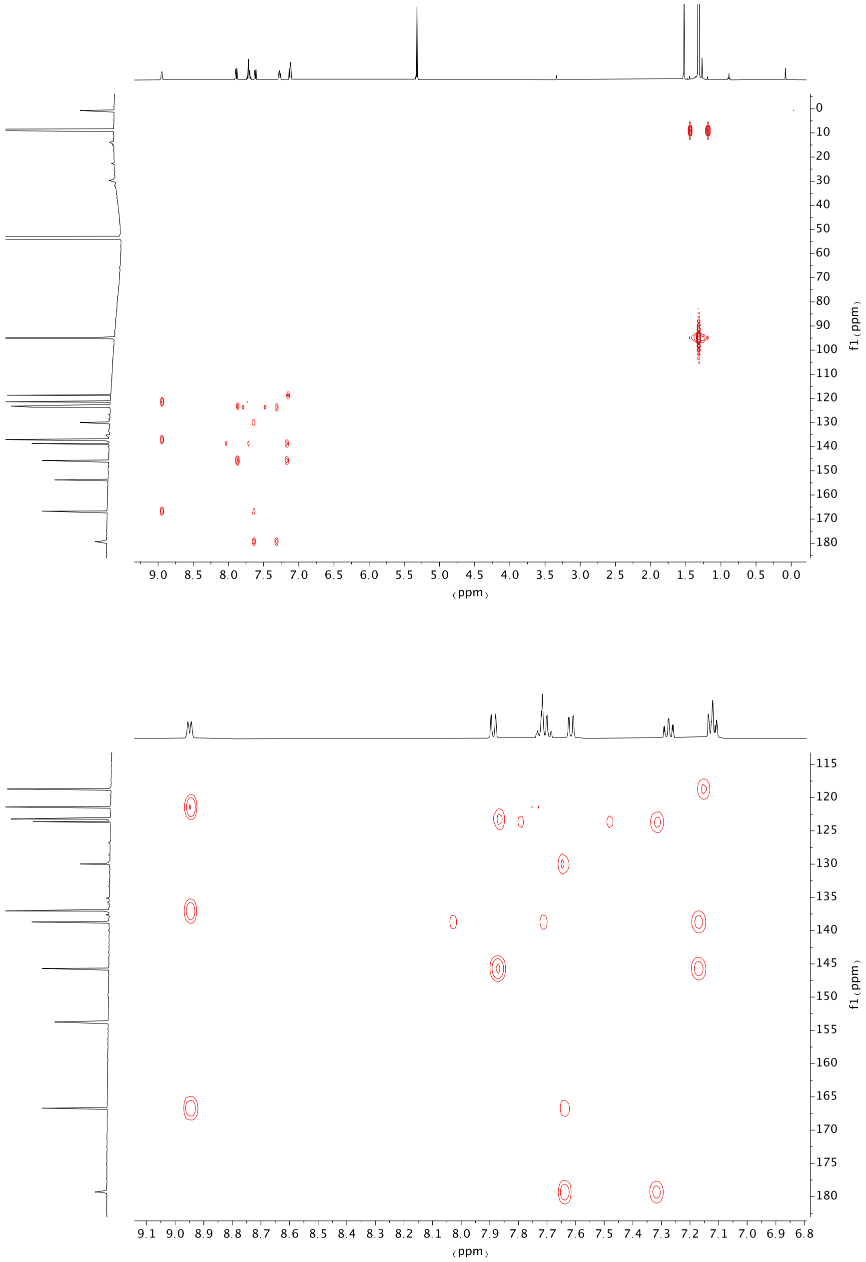

^{19}F NMR spectrum of **1_{ppy}-SCF$_3$** at 25 °C (CD$_2$Cl$_2$)

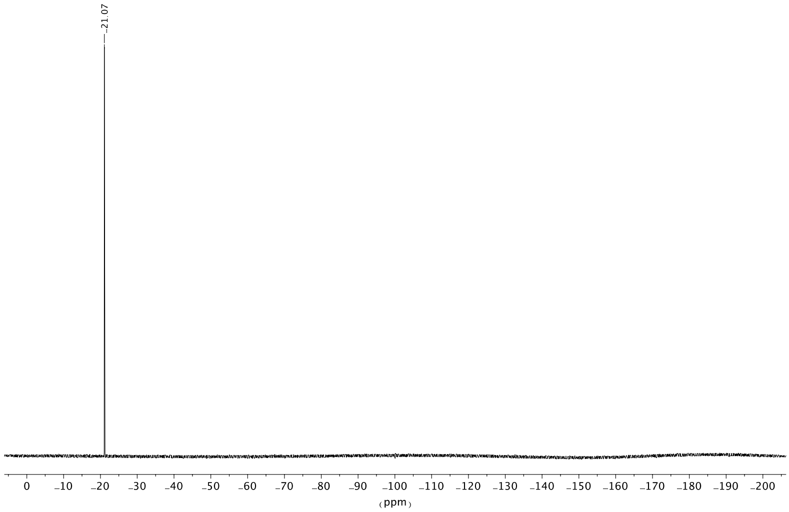

*Catalytic experiment using **1_{ppy}-SCF$_3$** as catalyst*

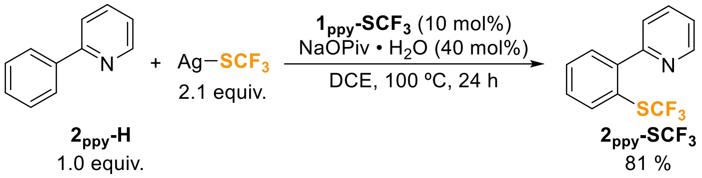

Scheme 2.24 Catalytic competence of complex **1_{ppy}-SCF$_3$.**

A crimped vial with a magnetic stir bar was charged with 2-phenylpyridine (14.3 mg, 0.1 mmol), AgSCF$_3$ (41.7 mg, 0.2 mmol), NaOPiv·H$_2$O (5.7 mg, 0.04 mmol), **1_{ppy}-SCF$_3$** (8.9 mg, 0.02 mmol) and 0.5 mL DCE under an argon atmosphere in the glovebox. The reaction mixture was stirred at 100 ºC for 22h. After cooling down to room temperature, the reaction was filtered through a silica and celite plug using a mixture of diethyl ether: ethyl acetate 20:1 to afford the crude mixture. The yield of **2_{ppy}-SCF$_3$** was determined by ^{1}H and ^{19}F NMR using 4,4´-difluorobiphenyl as internal standard.

*Reactivity of **1_{ppy}-SCF$_3$** in the presence of inorganic chemical oxidants*

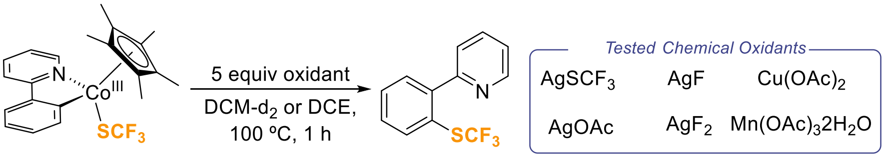

Scheme 2.25 Reactivity of different chemical oxidants with complex **1$_{ppy}$-SCF$_3$**.

In an argon atmosphere glovebox, a screw-cap NMR tube was charged with 0.4 mL of a stock solution with a molarity of 25 mM of **1$_{ppy}$-SCF$_3$** and 4,4´-difluorobiphenyl as the internal standard in CD_2Cl_2 or DCE, which corresponds to 0.01 mmol of **1$_{ppy}$-SCF$_3$** and 4,4´-difluorobiphenyl for each experiment. The corresponding oxidant (5 equiv) was added to each NMR tube and ^{1}H and ^{19}F NMR, spectra were acquired. Afterward, the reactions were heated at 100 ºC for 1 hour and the NMR spectra were recorded again. Then, all reactions were filtrated using a PTFE 13 mm 0.2 µm NSTR syringe filter and the resulting solution was checked by ^{1}H NMR spectroscopy.

Entry	Oxidant	Amount / mg	2ppy-SCF$_3$ NMR yield / %
1	AgF	6.4	37
2	AgOTf	12.9	30
3	AgOAc	8.3	0
4	AgF2	7.3	30
5	Cu(OAc)2	9.1	12
6	Mn(OAc)3•2H2O	13.4	quantitative

Reactions for discarding the involvement of radical pathways

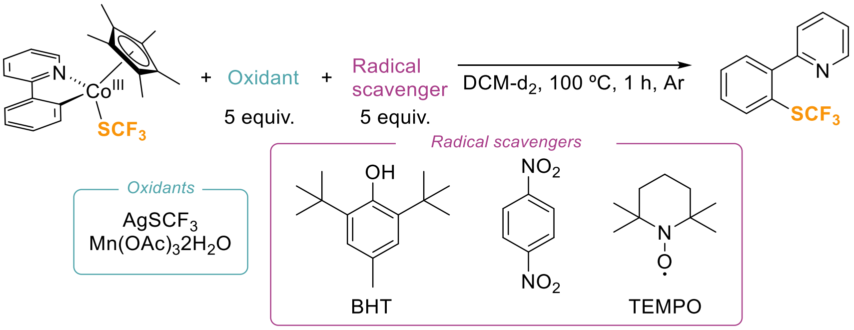

Scheme 2.26 Radical scavenger experiments in presence of complex **1$_{ppy}$-SCF$_3$** and oxidants, wither $AgSCF_3$ or $Mn(OAc)_32H_2O$.

In an argon atmosphere glovebox, a screw-cap NMR tube was charged with 0.4 mL of a stock solution with a molarity of 25 mM of **1$_{ppy}$-SCF$_3$** and 4,4´-difluorobiphenyl as the internal standard in DCM-d$_2$, which corresponds to 0.01 mmol of **1$_{ppy}$-SCF$_3$** and 4,4´-difluorobiphenyl for each experiment. To each tube the corresponding oxidant (13.4 mg, 0.05 mmol of $Mn(OAc)_3$•$2H_2O$ or 10.5 mg, 0.05 mmol of $AgSCF_3$) and the radical scavenger (5 equiv) were added and subsquentely, we recorded the corresponding ^{1}H and ^{19}F NMR spectra. Next, the reactions were heated at 100 ºC for 1 hour and the NMR spectra were recorded again. In case of the reactions with $Mn(OAc)_3•2H_2O$, the solutions were filtrated using a PTFE 13 mm 0.2 µm NSTR syringe filter and then the resulting solution was checked by ^{1}H and ^{19}F NMR spectroscopy.

Entry	Chemical oxidant	Radical Scavenger	Amount/ mg	$2ppy-SCF_3$ (NMR yield / %)
1	$AgSCF_3$	BHT	11.0	100
2	$AgSCF_3$	1,4 dinitrobenzene	8.4	100
3	$AgSCF_3$	TEMPO	7.8	76
4	$Mn(OAc)_3•2H_2O$	BHT	11.0	100
5	$Mn(OAc)_3•2H_2O$	1,4 dinitrobenzene	8.4	100
6	$Mn(OAc)_3•2H_2O$	TEMPO	7.8	100

Cyclic voltammetry analysis

Cyclic voltammetry analysis of the isolated $[Cp*Co(PPy)(SCF_3)]$ cobaltacycle (**1_{ppy}-SCF_3**) was performed in a 3-electrode cell consisting of a glassy carbon disk as working and counter electrodes (0.07 cm^2 of surface area) and SCE (Saturated Calomel electrode) as the reference electrode. The electrodes were previously polished with diamond abrasive slurries (DIAPAT-M, 39-321-M, Netkon) in an order of 3 µm and 1 µm diameter particle based slurries (2 minutes in each) to obtain mirror surfaces. Synthetic nap based polishing pads (METAPO-B, polishing cloth, self- adhesive back, diamond 3-1 µm, Netkon) were used for diamond polishing.

Solutions of **1_{ppy}-SCF_3** (0.003 M) in DCM with $(n\mathrm{Bu})_4NPF_6$ (0.3 M) as electrolyte were added to the electrochemical cell. CV measurements were made between –1.5 V and +1.5 V vs SCE. Scans were performed at 25, 50, 100, 200, 400 and 600 mV/s. Between every scan, the solution was stirred in order to remove the species close to the surface. All potentials reported in this manuscript were converted to the couple Fc/Fc^+, taking account the redox peak from ferrocene during the electrochemistry.

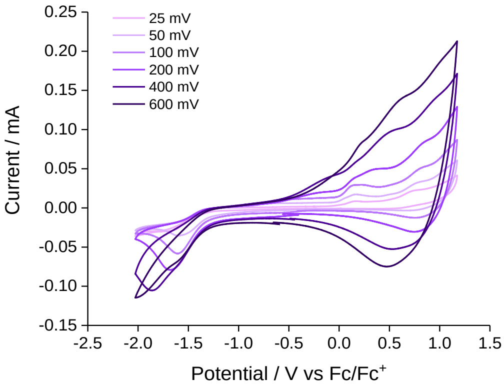

Figure 2.10 Full potential window CV of complex **1ppy-SCF3** vs Fc/Fc$^+$ at several scan rates. Solutions 0.003M of **1ppy-SCF3** and 0.3 M of (*n*Bu)$_4$NPF$_6$, in DCM, were added to the cell.

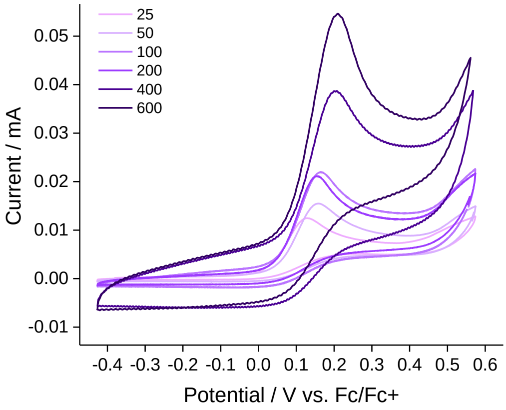

Figure 2.11 Narrow potential window CV of complex **1ppy-SCF3** vs Fc/Fc$^+$ at various scan rates for solutions of **1ppy-SCF3** (0.003 M) in 0.3 M of (*n*Bu)$_4$NPF$_6$ DCM electrolyte.

Chronoamperometry experiments for the ORE

We used a SCE (Saturated Calomel electrode) reference electrode and carbon felt as high-surface area counter (12 x 12 x 30 mm) and working (4 x 3 x 40 mm) electrodes in a two-compartment cell to separate cathode and anode.

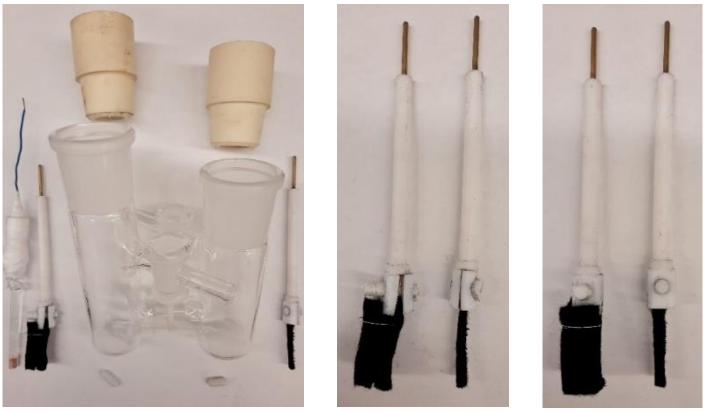

Figure 2.12 Pictures of the H electrolytic cell and the Carbon felt electrodes.

The cell was charged with **1_{ppy}-SCF$_3$** in the anode (5 mg, 0.01 mmol) and tetra-N-butylammonium hexafluorophosphate, [(*n*Bu)$_4$N]PF$_6$, as supporting electrolyte (30 mg in each compartment, 0.15 mmol), and DCM as solvent (15 mL x 2). A potential of 0.15 V vs Fc/Fc$^+$ was applied until the necessary charge was transferred in order to fully oxidize cobaltacycle (**1_{ppy}-SCF$_3$**) to cobalt(IV) species, (for 0.01 mmol 0.96 Coulombs). Subsequently, the solution was filtered using a 0.2 mm PTFE filter and transferred to a Schlenk flask to evaporate the solvent. A known amount of 4,4´-difluorobiphenyl as internal standard was added and the final product was analyzed by ^{1}H and ^{19}F NMR spectroscopy.

Chronoamperometry experiment followed by UV-Vis spectroscopy

A H electrolytic cell was charged with **1_{ppy}-SCF$_3$** (5 mg, 0.01 mmol) and tetra-N-butylammonium hexafluorophosphate ,(*n*Bu)$_4$NPF$_6$, as supporting electrolyte (30 mg x 2, 0.15 mmol) in DCM (15 mL x 2). A potential of 0.15 V vs Fc/Fc$^+$ was applied until the necessary charge was transferred in order to oxidize all the Co(III) cobaltacycle (**1_{ppy}-SCF$_3$**) to Co(IV), 1116 Coulombs. Every 15 min an aliquot of 1 mL was taken from the anodic cell and measured by UV-Vis, once measured it was transferred back to the cell.

Electron Paramagnetic Resonance (EPR) experiments

The spectral data was collected with the following spectrometer settings: microwave frequency = 9.38e^9; microwave power = 0.5606 mW; center field = 3200 G, sweep width = 6000 G, sweep time = 60 s, modulation frequency = 100 KHz, modulation amplitude = 4 G, power attenuation = 25 dB, time constant = 10.24 ms.

Individual EPR tubes were filled with the sample and were placed at the same position of the resonant cavity for EPR spectral acquisition.

A solution of complex **1_{ppy}-SCF_3** and $AgSCF_3$ in DCE were added to a Young-lock EPR tube and heated at 100 ºC for 15 min, before measuring it by EPR at 77 K.

Magnetic measurements

Magnetic measurements were carried out on grained solid powders of the electrolyte, **1_{ppy}-SCF_3** and the resulting crude after the CA experiment once we have removed the solvent, which we will call it **crude**, with a Quantum Design MPMS-XL SQUID magnetometer (Quantum Design, Inc, San Diego, CA, USA). Variable temperature magnetic susceptibility measurements were carried out under an applied field of 1000 Oe at 1 K·min^{-1} between 300 and 2 K. Variable field magnetization measurements were carried out at 2 K from 0 to 7 T.

Experimental magnetic susceptibilities for the crude were corrected of the extra-diamagnetic contribution. This contribution was experimentally obtained by fitting the high temperature data (above 20 K) to a Curie law with addition of a diamagnetic term:

$$\chi_T = \chi_{PARA} + \chi_{DIA} = \frac{C}{T} + \chi_{DIA} \qquad \text{(eq. 3)}$$

*X-ray structural determination for [Cp*Co(2-ppy)(SCF_3)] (**1_{ppy}-SCF_3**)*

Crystal preparation: Crystals of **1_{ppy}-SCF_3** were grown at room temperature by liquid/liquid diffusion of n-hexane into a solution of the corresponding compound in CH_2Cl_2. The crystals used for structure determination were selected using a Zeiss stereomicroscope using polarized light and prepared under inert conditions immersed in perfluoropolyether as protecting oil for manipulation.

Data collection: Crystal structure determination for sample **1_{ppy}-SCF_3** was carried out using a Apex DUO Kappa 4-axis goniometer equipped with an APPEX 2 4K CCD area detector, a Microfocus Source E025 IuS using MoK$_\alpha$ radiation, Quazar MX multilayer Optics as monochromator and an Oxford Cryosystems low temperature device Cryostream 700 plus (T = -173 °C). Crystal structure determination for samples Full-sphere data collection was used with ω and φ scans. *Programs used:* Data collection APEX-2,[3] data reduction Bruker Saint[4] V/.60A and absorption correction SADABS.[5]

Structure Solution and Refinement: Crystal structure solution was achieved using the computer program SHELXT.[6] Visualization was performed with the program SHELXle.[7] Missing atoms were subsequently located from difference Fourier synthesis and added to the atom list. Least-squares refinement on F^2 using all measured intensities was carried out using the program SHELXL 2015.[8] All non-hydrogen atoms were refined including anisotropic displacement parameters.

Comments to the structures:

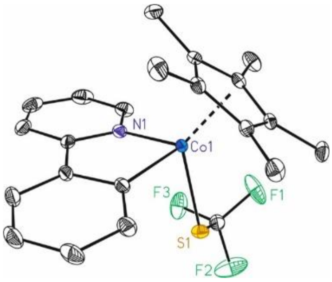

Figure 2.13 ORTEP drawing (thermal ellipsoids set at 50% probability) of the structure of $\mathbf{1_{ppy}}$-$\mathbf{SCF_3}$. Hydrogen atoms have been omitted for clarity.

This sample crystallizes with one molecule of the metal complex in the asymmetric unit. The structure is of excellent quality (no A- or B-alerts) and publishable with a R1 value of 2.75 %.

---

[3] Data collection with APEX II version v2013.4-1. Bruker (2007). Bruker AXS Inc., Madison, Wisconsin, USA.

[4] Data reduction with Bruker SAINT version V8.30c. Bruker (2007). Bruker AXS Inc., Madison, Wisconsin, USA.

[5] SADABS: V2012/1 Bruker (2001). Bruker AXS Inc., Madison, Wisconsin, USA. Blessing, Acta Cryst. **1995**, A51, 33.

[6] SHELXT; V2014/4 (Sheldrick 2014). Sheldrick, G.M. *Acta Cryst*. **2015**, A71, 3.

[7] SHELXle; C.B. Huebschle, G.M. Sheldrick & B. Dittrich; J. Appl. Cryst. **2011**, *44*, 1281.

[8] SHELXL; SHELXL-2014/7 (Sheldrick 2014). Sheldrick, G.M. *Acta Cryst*. **2015**, C71, 3.

2.5.2. Computational appendix

Computational details

All the computational data are deposited in the ioChem-BD repository.[9] DFT calculations were performed using the Gaussian09[10] package with the M06-D3 (where D3 stands for GD3[11] empirical dispersion) functional.[12] All geometry optimizations were carried out in solution without symmetry restrictions with LANL2DZ as the basis set for cobalt and silver,[13]and 6-31G(d)[14] for the remaining atoms. Unless otherwise stated, the reported energies were obtained from single point calculations with a larger basis set, LANL2TZ plus pseudopotential for cobalt and silver,[15] and 6-311++G(d,p)[16] for the remaining atoms. Implicit solvent was modeled through the SMD method.[17] Calculations were carried out in DCM ($\varepsilon = 8.93$). All the energies reported in the main text and the Supporting Information are free energies at 100 ˚C[18] and in $kcal\cdot mol^{-1}$. The nature of the stationary point was verified using frequency analyses.

---

[9] M. Alvarez-Moreno, C. de Graaf, N. Lopez, F. Maseras, J. M. Poblet, C. Bo, *J Chem. Inf. Model*. **2015**, *55*, 95.

[10] Gaussian 09, Revision D.01, M. J. Frisch, G. W. Trucks, H. B. Schlegel, G. E. Scuseria, M. A. Robb, J. R. Cheeseman, G. Scalmani, V. Barone, B. Mennucci, G. A. Petersson, H. Nakatsuji, M. Caricato, X. Li, H. P. Hratchian, A. F. Izmaylov, J. Bloino, G. Zheng, J. L. Sonnenberg, M. Hada, M. Ehara, K. Toyota, R. Fukuda, J. Hasegawa, M. Ishida, T. Nakajima, Y. Honda, O. Kitao, H. Nakai, T. Vreven, J. A. Montgomery, Jr., J. E. Peralta, F. Ogliaro, M. Bearpark, J. J. Heyd, E. Brothers, K. N. Kudin, V. N. Staroverov, T. Keith, R. Kobayashi, J. Normand, K. Raghavachari, A. Rendell, J. C. Burant, S. S. Iyengar, J. Tomasi, M. Cossi, N. Rega, J. M. Millam, M. Klene, J. E. Knox, J. B. Cross, V. Bakken, C. Adamo, J. Jaramillo, R. Gomperts, R. E. Stratmann, O. Yazyev, A. J. Austin, R. Cammi, C. Pomelli, J. W. Ochterski, R. L. Martin, K. Morokuma, V. G. Zakrzewski, G. A. Voth, P. Salvador, J. J. Dannenberg, S. Dapprich, A. D. Daniels, O. Farkas, J. B. Foresman, J. V. Ortiz, J. Cioslowski, D. J. Fox, Gaussian, Inc., Wallingford CT, 2013.

[11] S. Grimme, Semiempirical GGA-type density functional constructed with a long-range dispersion correction, *J. Comput. Chem.* **2006**, *27*, 1787.

[12] Y. Zhao, D. G. Truhlar, *Theor. Chem. Account.* **2008**, *120*, 215.

[13] LANL2DZ T. H. Dunning Jr. and P. J. Hay, in *Modern Theoretical Chemistry*, Ed. H. F. Schaefer III, Vol. 3 (Plenum, New York, **1977**) 1.

[14] (a) W. J. Hehre, R. Ditchfield, J. A. Pople, *J. Chem. Phys.* **1972**, *56*, 2257; (b) J. D. Dill, J. A. Pople, *J. Chem. Phys.* **1975**, *62*, 2921; (c) M. M. Francl, W. J. Petro, W. J. Hehre, J. S. Binkley, M. S. Gordon, D. J. DeFrees, A. J. Pople, *J. Chem. Phys.* **1982**, *77*, 3654.

[15] L. E. Roy, P. J. Hay, R. L. Martin, *J. Chem. Theory Comput.* **2008**, *4*, 1029.

[16] (a) R. Krishnan, J. S. Binkley, R. Seeger, J. A. Pople, *J. Chem. Phys.* **1980**, *72*, 650–654; (b) A. D. McLean, G. S. Chandler, *J. Chem. Phys.* **1980**, *72*, 5639–5648.

[17] S. A. V. Marenich, C. J. Cramer, D. G. Truhlar, *J. Phys. Chem. B* **2009**, *113*, 6378.

[18] G. Luchini, J. V. Alegre-Requena, I. Funes-Ardoiz, R. S. Paton, GoodVibes: Automated Thermochemistry for Heterogeneous Computational Chemistry Data. *F1000Research*, **2020**, *9*, 291.

Benchmarking of functionals

We performed a small benchmarking of DFT methods through comparison of the calculated optimized structure to the X-ray structure for complex **1_{ppy}-SCF_3**. The basis set used was 6-31G(d) for C, N, S, F and H and LANL2DZ for Co. We compared the distances from the cobalt center to the S, the N and C atoms in the phenylpyridine and to the Cp* centroid. Selected angular parameters, C1─Co─N and N─Co─S bond angles and C1─C2─C3─N C2─C1─Co─S torsion angles were also compared. The best geometry was obtained with M06-D3, which was thus chosen for the rest of the calculations.

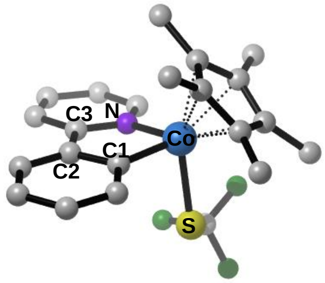

Figure 2.14 Optimized geometry of **1_{ppy}-SCF_3** with M06-D3 functional. Hydrogen atoms have been omitted for clarity.

Table 2.1 Benchmark of several functionals. Comparison of the energy, distances, bond angles, and torsion angles of importance between the X-ray structure and the optimized ones.

	Energy / a.u.		Bond Length / Å				Angle / Å		Torsion angle / °	
Method	potential	free energy	Co─S	Co─N	Co─Cp*	Co─C1	C–Co–N	N–Co–S	C1–C2–C3–N	C2–C1–Co–S
Crystal Structure			2.25	1.95	1.71	1.94	83.09	97.10	1.61	-108.61
ωB97X-D	-1749.4303585	-1749.081707	2.29	1.96	1.75	1.91	83.54	95.25	0.92	-102.97
B3LYP-D3	-1749.8788107	-1749.533450	2.30	1.97	1.79	1.92	83.65	95.48	0.92	-102.58
B97D	-1749.3839921	-1749.049559	2.30	1.97	1.76	1.92	83.54	96.49	0.93	-103.68
M06-D3	-1749.0273017	-1748.679362	2.28	1.97	1.72	1.92	83.34	95.40	0.69	-106.17
BP86-D3	-1750.0205426	-1749.687984	2.28	1.94	1.75	1.91	83.82	95.74	0.40	-105.29
TPSSh	-1749.8346767	-1749.491629	2.29	1.96	1.75	1.92	83.44	94.83	0.91	-101.19
B3LYP	-1749.8025156	-1749.459884	2.32	1.98	1.82	1.93	83.47	95.40	1.02	-101.33
M06-2x-d3	-1749.2496344	-1748.900265	2.33	2.00	1.82	1.92	83.27	95.41	1.64	-102.08
M06L-d3	-1749.7276387	-1749.381281	2.31	1.98	1.72	1.93	83.17	95.09	1.63	-102.2
M06-2x	-1749.2444783	-1748.895098	2.33	2.00	1.82	1.92	83.27	95.39	1.61	-101.98
M06-L	-1749.7217618	-1749.375412	2.31	1.98	1.72	1.93	83.16	95.07	1.61	-102.12

Calculations including $AgSCF_3$

Our fist idea was to introduce explicitly $AgSCF_3$ explicitly in the calculations, but we had to discard it for reasons we explain below.

Structure of $AgSCF_3$

We found a crystal structure of $AgSCF_3$ salt with an ACN coordinated.[19] Here we see that at least we should have two Ag in our model. The coordination of Ag in the crystal structure is larger than in our system, with 4 SCF_3 coordinated vs 2. The SCF_3 is making a bridge between two silvers.

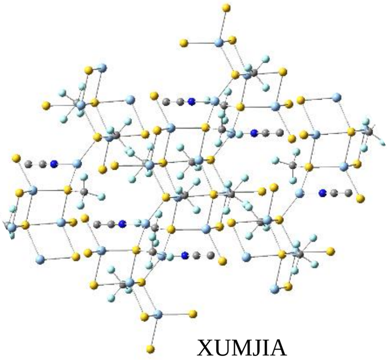

Figure 2.15 X-ray structure of $AgSCF_3$ACN

Another issue with this system is the description of salts and metal clusters. In one hand, $AgSCF_3$ is not a dimer but a salt; the structure is repeated through space. We computed several geometries with different $AgSCF_3$ units, from 1 to 4. Each addition of one unit stabilizes the structure, in agreement with the behavior of a salt.

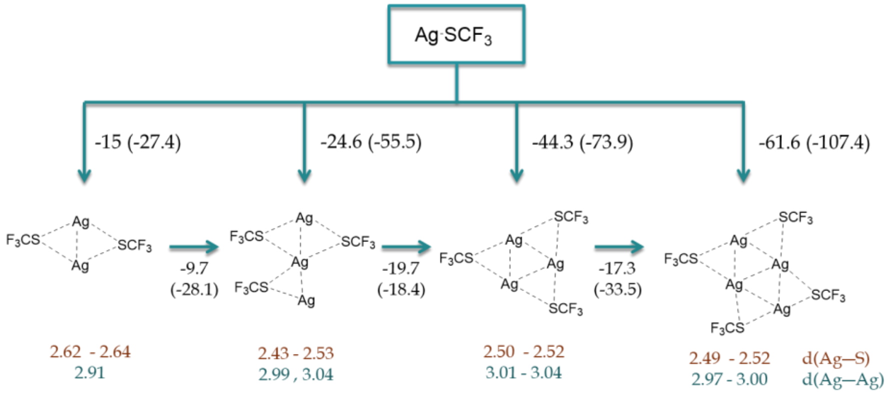

Scheme 2.27 Adducts of $AgSCF_3$. Energies in kcal·mol^{-1}.

---

[19] H. Wu, Z. Xiao, J. Wu, Y. Guo, J. C. Xiao, C. Liu, Q. Y. Chen, *Angew. Chemie - Int. Ed.* **2015**, *54*, 4070–4074.

In the calculations we need to add at least a dimer of $AgSCF_3$ to be able to match with the reality.

Direct reductive elimination from Co(III with coordinated $AgSCF_3$

However, adding a dimer of the silver salt in the calculations did not help to solve the problem. The adducts of $\mathbf{2}_{\mathbf{Ag}}$ and $\mathbf{4}_{\mathbf{Ag}}$ are stabilized, but the activation energy is also 32 kcal·mol^{-1}. We thought that we could see the transfer of an electron to silver from the cobalt, nonetheless, if looking at spin densities for the triplet states, the unpaired electrons are always in the cobalt center and no Ag(0) is observed. No cooperation between the metals is observed.

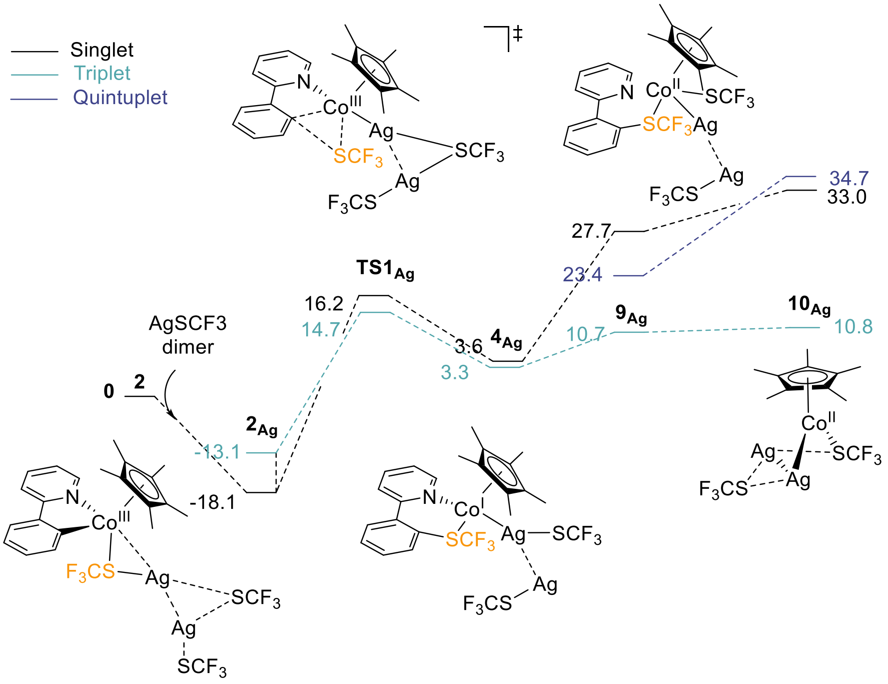

Scheme 2.28 Energy profile of reductive elimination form OC(III) with $AgSCF_3$ dimer coordinated. Energies in kcal·mol^{-1}.

We tried other approaches to lower the energy of the complexes after reductive elimination, such as formation of cobalt complex dimers or different doublet or quartet structures, although, none of them were stable enough.

Solid Silver formation

The solution we found was to compute the thermodynamic cost of the reduction of silver through a thermodynamic cycle, with the method described within the chapter.

The energy of the solid formation can be calculated by a thermodynamic cycle, it is -54.9 kcal·mol^{-1} for each Ag atom.

Last steps after the reductive elimination step

Once we obtained the Co(IV) species, the reductive elimination occurs, with a activation barrier of 10.3 kcal·mol^{-1}. The **5^+** compound is a Co(II) complex which is 9 kcal·mol^{-1} lower in energy than **4^+**. Then the previously formed $^-$SCF$_3$ can coordinate to the compound to create H. the discoordination of the product is not favourable at this point. First, the cobalt has to be oxidized again now to Co(III) by the silver salt, followed by product discoordination to form **14^+**. Then again the $^-$SCF3 gets coordinated to form **15**, a Co(III) species. In this case, the reaction is thermodynamically favoured, due in part to reduction of Ag$^+$ and formation of solid silver.

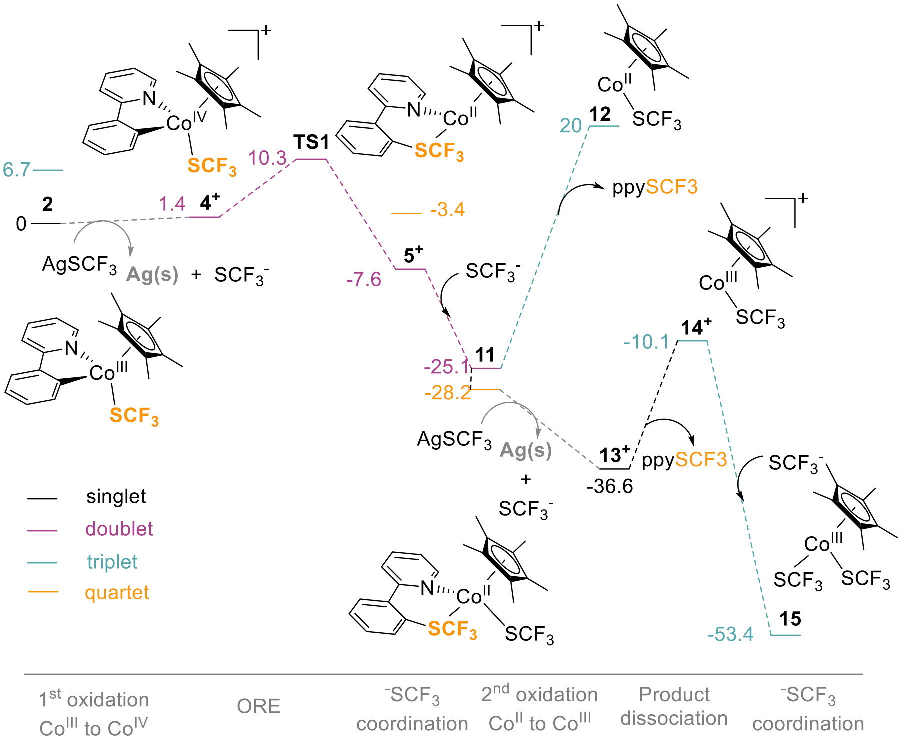

Scheme 2.29 Energy profile of the stoichiometric reaction of complex **1_{ppy}-SCF$_3$** (**2**) with AgSCF$_3$. Energies in kcal·mol^{-1}.

We consider that this is the mechanism for the stoichiometric reaction. There is an alternative in catalysis that another SCF_3 unit may come in other steps, such as after the oxidation, the C-H activation, or in the last step. We consider however that these nuances will not affect significantly the global picture.

UNIVERSITAT ROVIRA I VIRGILI
UNCOVERING THE MECHANISTIC SCENARIOS OF NUCLEOPHILIC COUPLINGS IN CP*CO SYSTEMS
Sara López Resano

*Chapter 3. Study on the Mechanism of the Oxidatively Induced C–I Reductive Elimination from high-valent Cp*Co species with F^+ oxidants*

UNIVERSITAT ROVIRA I VIRGILI
UNCOVERING THE MECHANISTIC SCENARIOS OF NUCLEOPHILIC COUPLINGS IN CP*CO SYSTEMS
Sara López Resano

3.1. Introduction

As mentioned in the previous chapter, we have recently discovered the intermediacy of high-valent Co species in C–H functionalization reactions. In that particular case, we use as chemical oxidants inorganic salts that are prevalent additives in catalysis. However, there are other type of oxidants that over the past years have demonstrated their tremendous capability to trigger otherwise inaccessible bond-forming reactions: F^+ oxidants.

The final step in catalytic cycles for many carbon-carbon and carbon-heteroatom bond-forming reactions involves reductive elimination from transition metal centers. One of the most prominent transformations of this kind is the low-valent Pd(0/II) catalytic cycle, where reductive elimination from square-planar [L_2Pd(II)R^1Y] or [L_2Pd(II) R^1R^2](R^1, R^2 = alkyl or aryl, Y= heteroatom) intermediates typically create a new C–Y or C–C bond.[1] To accelerate these reactions, phosphine and N-heterocyclic carbene ligands are often used. They facilitate oxidative addition and promote reductive elimination, leading to the oversight of the fundamental reductive elimination step.[2]

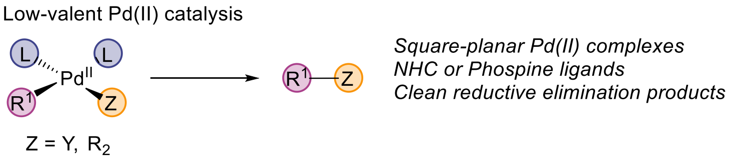

Scheme 3.1 Reductive elimination from a square-planar Pd(II) species

However, the aforementioned ligands are typically not compatible with the high-valent Pd(II)-mediated C–H cleavage step.[3] Therefore, to enable Pd(II)-catalyzed C–H functionalization reactions, new oxidants have been developed to induce reductive elimination by oxidizing Pd(II) to a Pd(III) or Pd(IV) species. The formation of an

---

[1] a) A. Gillie, J. K. Stille, *J. Am. Chem. Soc.* **1980**, *102*, 4933–4941. b) K. Tatsumi, R. Hoffmann, A. Yamamoto, J. K. Stille, *Bull. Chem. Soc. Jpn.* **1981**, *54*, 1857–1867. c) J. F. Hartwig, *Acc. Chem. Res.* **1998**, *31*, 852–860. d) J. F. Hartwig, *Nature* **2008**, *455*, 314–322.

[2] a) W. A. Herrmann, *Angew. Chemie - Int. Ed.* **2002**, *41*, 1290–1309. b) A. F. Littke, G. C. Fu, *Angew. Chemie - Int. Ed.* **2002**, *41*, 4176–4211. c) R. Martin, S. L. Buchwald, *Acc. Chem. Res.* **2008**, *41*, 1461–1473. d) J. F. Hartwig, *Acc. Chem. Res.* **2008**, *41*, 1534–1544.

[3] a) K. Muñiz, *Angew. Chemie - Int. Ed.* **2009**, *48*, 9412–9423. b) L. M. Xu, B. J. Li, Z. Yang, Z. J. Shi, *Chem. Soc. Rev.* **2010**, *39*, 712–733. c) P. Sehnal, R. J. K. Taylor, L. J. S. Fairlamb, *Chem. Rev.* **2010**, *110*, 824–889. d) A. J. Hickman, M. S. Sanford, *Nature* **2012**, *484*, 177–185.

octahedral Pd(IV) intermediate becomes a fundamental challenge to control the reductive elimination process. All three ligands cis to the alkyl or aryl group could potentially participate in the reductive elimination, leading to a mixture of products.[4]

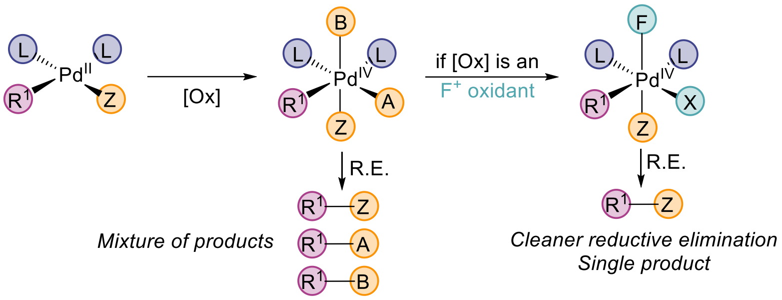

Scheme 3.2 Reductive elimination from Pd(IV) species

A widely used strategy to achieve selective C–C and C–heteroatom bond formation and suppress undesired products is the use of F^+ oxidants.[4] These oxidants have also been known to react with various organometallic reagents to form C–F bonds.[5] Nevertheless, several mechanistic studies[6] revealed that reductive elimination for C–F bond formation is slow, promoting a wide variety of C–Y[7] and C–C[8] reductive elimination reactions. These types of electrophilic oxidants are also widely use with first row metals, specifically in high-valent Ni chemistry, as seen in the selected examples of the introduction.

Since their establishment, the mechanism behind the oxidation with F^+ reagents has been a topic of debate. While many examples in the literature describe F^+ oxidants as 2 e^- oxidants that proceed through the transfer of a F^+ atom. Nonetheless, it has been

---

[4] K. M. Engle, T. S. Mei, X. Wang, J. Q. Yu, *Angew. Chemie - Int. Ed.* **2011**, *50*, 1478–1491.

[5] a) G. S. Lal, G. P. Pez, R. G. Syvret, *Chem. Rev.* **1996**, *96*, 1737–1755. b) A. W. Kaspi, I. Goldberg, A. Vigalok, *J. Am. Chem. Soc.* **2010**, *132*, 10626–10627. c) N. Rozatian, D. R. W. Hodgson, *Chem. Commun.* **2021**, *57*, 683–712.

[6] a) T. Furuya, T. Ritter, *J. Am. Chem. Soc.* **2008**, *130*, 10060–10061. b) A. W. Kaspi, A. Yahav-Levi, I. Goldberg, A. Vigalok, *Inorg. Chem.* **2008**, *47*, 5–7. c) N. D. Ball, M. S. Sanford, *J. Am. Chem. Soc.* **2009**, *131*, 3796–3797. d) T. Furuya, D. Benitez, E. Tkatchouk, A. E. Strom, P. Tang, W. A. Goddard, T. Ritter, *J. Am. Chem. Soc.* **2010**, *132*, 3793–3807. e) H. Park, P. Verma, K. Hong, J. Q. Yu, *Nat. Chem.* **2018**, *10*, 755–762. f) C. Testa, J. Roger, P. Fleurat-Lessard, J. C. Hierso, *Eur. J. Org. Chem.* **2019**, *2019*, 233–253.

[7] a) T. Mei, X. Wang, J.-Q. Yu, *J. Am. Chem. Soc.* **2009**, *131*, 10806–10807. b) X. Wang, Y. Lu, H. Dai, J. Yu, **2010**, 12203–12205.

[8] a) A. Yahav, I. Goldberg, A. Vigalok, *J. Am. Chem. Soc.* **2003**, *125*, 13634–13635. b) N. D. Ball, J. W. Kampf, M. S. Sanford, *J. Am. Chem. Soc.* **2010**, *132*, 2878–2879.

found that N-fluorobenzenesulfonimide (NFSI) can react as a single electron oxidant in Ni-catalyzed fluorination reaction.[9] Therefore, there are two potential pathways: single-electron transfer (SET) followed by F radical addition or 2e$^-$ nucleophilic S_N2 substitution. Differentiating between these mechanisms is a challenging task due to the formation of identical products.[5a,10]

3.2. Objectives

In an effort to broaden our understanding of nucleophilic coupling using the Cp*Co(III) catalyst, we sought to explore whether alternative oxidants commonly used in transition metal catalysis can trigger oxidatively induced reductive elimination (ORE) events from high-valent Cp*Co species, as the one proposed in Chapter 2. After establishing their feasibility, we will investigate the mechanism involved in those transformations.

---

[9] a) J. Ding, Y. Zhang, J. Li, *Org. Chem. Front.* **2017**, *4*, 1528–1532. b) P. Song, S. Zhu, *ACS Catal.* **2020**, *10*, 13165–13170.

[10] P. T. Nyffeler, S. G. Durón, M. D. Burkart, S. P. Vincent, C. H. Wong, *Angew. Chem. Int. Ed.* **2004**, *44*, 192–212.

3.2. Results and Discussion

3.2.1. Model system selection and initial experimental and computational studies

For this chapter, we have selected the metallacycle **1$_{\text{ald}}$-I** as touchstone to evaluate the potential involvement of high-valent Cp*Co species in additional C–X bond-forming reactions. This compound, previously reported by our group (Scheme 3.3) and stable in DCM solution at rt for several weeks,[11] contains an aldehydic proton that provides a distinctive chemical shift in ^{1}H NMR spectroscopy, facilitating the mechanistic study.

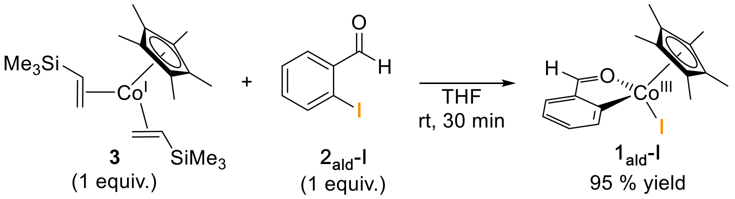

Scheme 3.3 Synthesis of **1$_{\text{ald}}$-I** through oxidative addition from Co(I)-VTMS

Following a similar procedure than in the previous chapter, first, we evaluated whether **1$_{\text{ald}}$-I** directly undergoes C–I reductive elimination upon thermolysis. In alignment with our previous results, we did not observe the targeted reductive elimination process by ^{1}H NMR spectroscopy after heating a solution of the complex in CD_2Cl_2 at 100 ºC for 24 h. Gratifyingly, DFT calculations (Scheme 3.4) are consistent with the experimental data, as we observed a large activation barrier (54.2 kcal mol^{-1}) for the C–I bond formation.

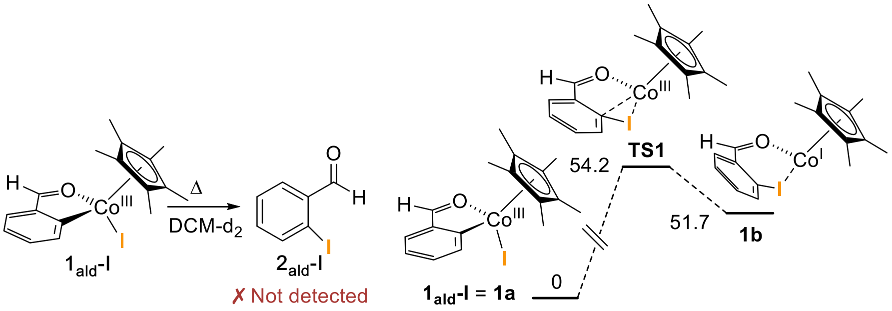

Scheme 3.4 Thermolysis of **1$_{\text{ald}}$-I** to evaluate direct C–I reductive elimination. Right: Computed free energy profile of the direct reductive elimination step from complex **1$_{\text{ald}}$-I**. Energies are shown in kcal·mol^{-1}.

---

[11] S. Martínez de Salinas, J. Sanjosé-Orduna, C. Odena, S. Barranco, J. Benet-Buchholz, M. H. Pérez-Temprano, *Angew. Chem. Int. Ed.* **2020**, *59*, 6239–6243.

3.2.2. Chemical Oxidation Studies with Complex $\mathbf{1_{ald}}$-I and Preliminary Experimental Studies

Encouraged by these promising experimental and computational results and inspired by our previous trifluoromethylthiolated system, next we investigate whether complex **$\mathbf{1_{ald}}$-I** can undergo reductive elimination to form 2-iodobenzaldehyde in the presence of different chemical oxidants. The involvement of oxidative induced reductive elimination processes was first examined using 1-electron inorganic oxidants with different redox potentials (Scheme 3.6), which are often used as additives in transition metal-catalyzed reactions.[12] None of the tested inorganic oxidants yielded promising results after monitoring the reactions by ^{1}H NMR spectroscopy at different reactions times and temperatures.[13]

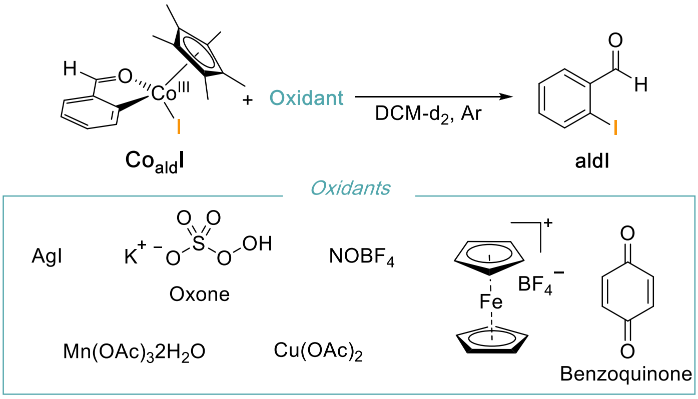

Scheme 3.5 Reaction of different oxidants with **$\mathbf{1_{ald}}$-I**.

Next, we explored the chemical oxidation of **$\mathbf{1_{ald}}$-I** with different inner-sphere oxidants that are known to trigger ORE reactions with other transition metals (Scheme 3.7). The reactions between **$\mathbf{1_{ald}}$-I** and the corresponding oxidants were monitored at different reaction time at room temperature or 50 ºC by ^{1}H NMR spectroscopy.[14] First, we tested widely used hypervalent iodine oxidants, such as PIDA or PIFA. With the first one, we observed the formation of the targeted organic product in moderate yields (30%) after 16 h, while the second afforded the desired product along with a complex mixture of unidentified complexes. The reaction with the Umemoto reagent did not promote the

---

[12] T. Dalton, T. Faber, F. Glorius, *ACS Cent. Sci.* **2021**, *7*, 245–261.

[13] In certain cases, as mentioned in the text, the reaction was heated.

[14] ^{19}F NMR experiments were also performed when required.

C–I bond-forming product, yet we observed the formation of a new compound by ^{19}F NMR spectroscopy (–5 ppm). Finally, we tested different electrophilic F^+ oxidants. While with selectfluor we only detected traces of reductive elimination compound, presumably due to its low solubility in the reaction conditions,[15] the reaction with 1.2 equivalentes of 1-Fluoro-2,4,6-trimethylpyridinium triflate (NFTPT) or NFSI resulted in high conversion of complex **1_{ald}-I** into the organic product (85% and 90% respectively) within minutes at room temperature. Indeed, when we used 2 equivalents of these F^+ oxidants, we obtained, in both cases, quantitative conversion.

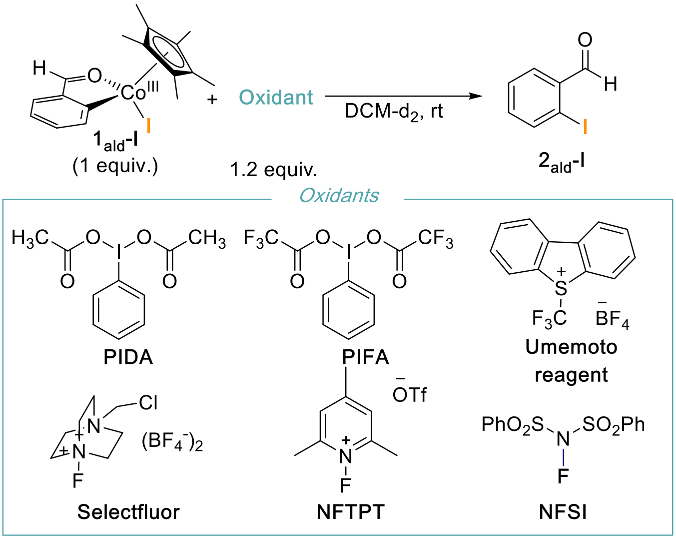

Scheme 3.6 Reactivity of different chemical oxidants with **1_{ald}-I**.

Inspired by the promising results obtained with NFTPT and NFSI, we focused our attention towards gaining a fundamental understanding on the observed reactivity and the organometallic species formed during and after the ORE event. Gratifyingly, X-ray quality crystals of the resulting cobalt complexes after the C–I bond-forming reactions with NFTPT and NFSI were obtained via vapor diffusion at low temperature using different solvent mixtures.

---

[15] P. T. Nyffeler, S. G. Durón, M. D. Burkart, S. P. Vincent, C. H. Wong, *Angew. Chem. Int. Ed.* **2004**, *44*, 192–212.

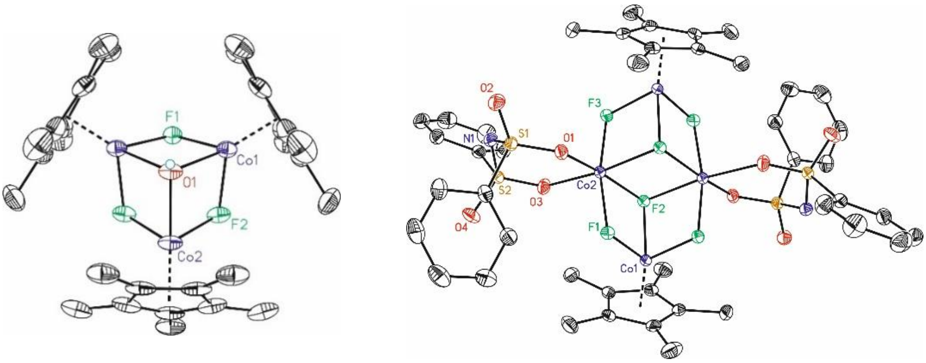

Bond	Distance / Å
Co1–Co2	3.055
Co–F	1.934 –1.941
Cp*–Co	2.022 – 2.063
Co–OH	2.029

Bond	Distance / Å
Co1–Co2	8.769
Co1–F	1.932 – 2.001
Cp*–Co	2.022 – 2.063
Co2–F	1.976 – 2.124
Co2–O1/O3	2.088 and 2.094

Figure 3.1 ORTEP structures of the final cobalt complexes from the reaction with the F+ oxidants NFTPT (left) and NFSI (right). Thermal ellipsoids are drawn at 50% of probability. For the right structure, only one hydrogen attached to the O is shown, the rest of the hydrogen atoms have been omitted for clarity. The structure contained two OTf anions, which have also been omitted. For the structure on the left, hydrogen atoms have been omitted for clarity. Selected distances are shown on the tables for each compound.

For NFTPT ($CHCl_3$/pentane), the solid-state structure consists of trimeric species, a Co_3F_3OH cluster, where all the cobalt metal centers are coordinated to one Cp* ligand. The presence of two triflate anions in the structure indicates that the oxidation state of the cobalt metal centers is +3. The formation of this trimeric species suggests that NFPTP is capable to promote the access to Co^V species that reductive eliminates to give the desired organic product and a Co^{III} structure that finally collapses to give the obtained crystal structure.

Interestingly, for NFSI (CH_2Cl_2/hexane), the X-ray structure is completely different. This compound crystallizes in the monoclinic space *P*2_1/n with half metal-complex molecule in the asymmetric unit showing *C*i-symmetry. The central core of the metal-complex is formed by a Co_4F_6 cluster surrounded by two ligand molecules (without flour atom at the nitrogen atom) and two Cp* molecules, all coordinated to the cobalt atoms. A thorough check of the nitrogen atoms present in the molecule did not confirm the presence in the electron density for hydrogen atoms attached to them. The bond distances N–S are shorter (1.585 and 1.591 Å) than the expected for a S–N single bond which should be around 1.690 Å. The short distances confirm the lack of hydrogen

UNIVERSITAT ROVIRA I VIRGILI
UNCOVERING THE MECHANISTIC SCENARIOS OF NUCLEOPHILIC COUPLINGS IN CP*CO SYSTEMS
Sara López Resano

atoms at the nitrogen atoms and pointing towards a charge delocalization. In this case, the X-ray crystal structure contains cobalt metal centers with more than one oxidation state. While the first two Co (Co1) atoms are in oxidation state +3, the former two (Co2) are +2.

Intrigued by the obtained X-ray structures, we performed a preliminary NMR study of the reaction of complex **1$_{ald}$-I** in the presence of NFTPT and NFSI to examine whether any high-valent cobalt intermediates are detectable and determine the presence of paramagnetic species. Interestingly, when we conducted the paramagnetic ^{1}H NMR experiments after 10 minutes at room temperature, with both oxidants, we observed a mixture of paramagnetic and diamagnetic resonances. It should be mentioned that, in alignment with the crystallographic analysis, significantly different ^{1}H NMR chemical shifts were observed in the paramagnetic regions.

While for NFTPT several sharper signals were observed at both upshift and downshift ppm (Figure 3.2), for NFSI we observed a major paramagnetic broad signal at 33 ppm and a shoulder around 15-20 ppm (Figure 3.2, bottom). The observation of paramagnetic signals was particularly surprisingly when using NFTPT, since as mentioned above, after the measurement of the corresponding X-ray structure of the cobalt(III) dimeric product, we hypothesized the reductive elimination step may take place from a Co^{V} compound. The observed NMR spectrum could suggest that if formed, the Co^{V} intermediate species was not a singlet state.[16]

---

[16] There is a possibility that with NFTPT a Co(IV) is also formed which undergoes reductive elimination to a Co(II), which then is re-oxidized by the oxidant, explaining the Co(III) complex obtained in the X-ray structure.

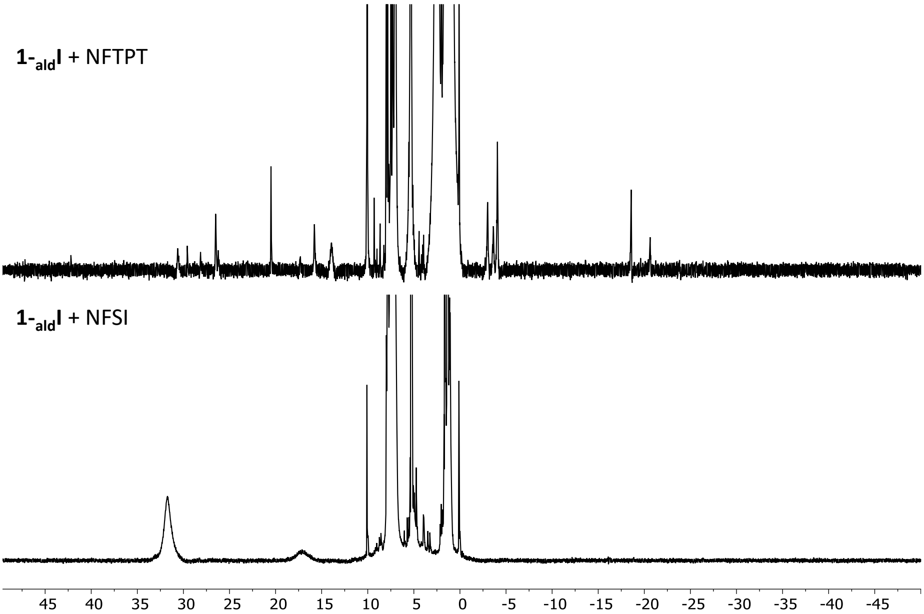

Figure 3.2 Paramagnetic ^{1}H NMR during the reaction of **Co$_{ald}$I** and NFTPT (top) and NFSI (bottom).

These preliminary experimental studies demonstrate not only the feasibility of ORE events with F$^+$ oxidants (NFTPT and NFSI) in the context of Cp*Co-based systems but also that different mechanisms may be involved. Additionally, the presence of Co–F bonds in the obtained X-ray structures suggests the transfer of the F moiety to the cobalt metal center during the oxidation processes.

3.2.3. Further Mechanistic Investigation on the ORE Process of Complex 1$_{ald}$-I in the Presence of F$^+$ Oxidants

As shown in the previous section, the F$^+$ oxidants NFTPT and NFSI are the only tested oxidants that afford the desired reductive elimination. Preliminary crystallographic and spectroscopic data suggest that the oxidants do not promote the same type of ORE event. Indeed, in the literature, it is known that both oxidants can go through 1 or 2-electron oxidation processes with and without transferring the F ligand. The oxidation mechanism with electrophilic F$^+$ oxidants can go through multiple reaction pathways: (i) single electron transfer (SET), (ii) single electron F· oxidation, or (iii) conventional two-electron oxidation by transferring a F$^+$ moiety. In this section, we will perform a wide variety of experimental and computational studies to elucidate the most plausible mechanistic proposals.

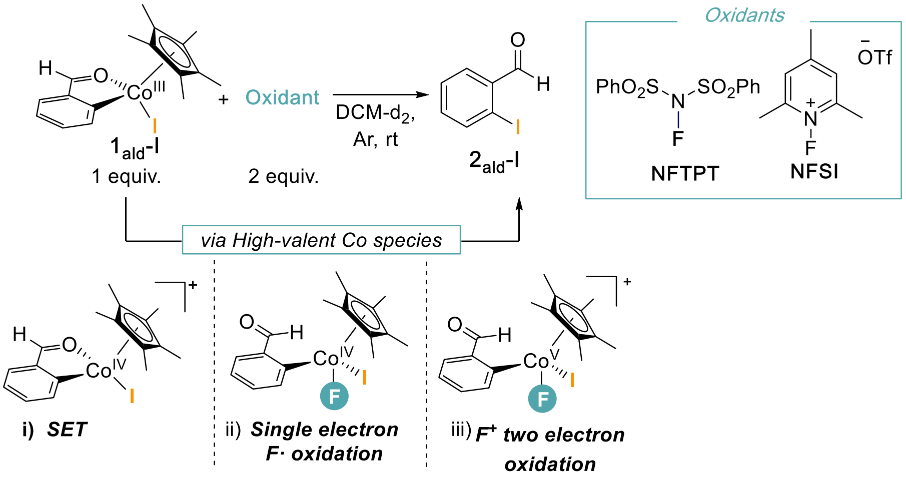

Scheme 3.7 Possible mechanistic scenarios involving high-valent Cp*Co species.

Despite the presence of Co–F bonds in the resulting cobalt products may rule out the involvement of SET events, we have evaluated this scenario, by using cyclic voltammetry (CV). As shown in Figure 3.1, complex **1_{ald}-I** shows quasi-irreversible oxidation peaks, being the most relevant at $E_{1/2} = 0.4$ vs Fc/Fc^+ which is assigned to Co(III)/Co(IV) oxidation. We hypothesized that the other observed waves may correspond to Co(IV)/Co(V) and I^- oxidations.[17]

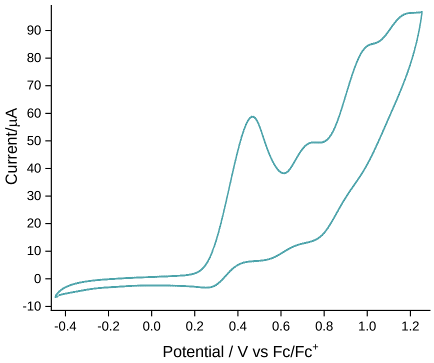

Figure 3.3 Cyclic voltammogram of complex **1_{ald}-I** vs Fc/Fc^+ in DCM/$n$$NBu_4PF_6$ at scan rate of 200 mV/s.

---

[17] X. Wang, D. M. Stanbury, *Inorg. Chem.* **2006**, *45*, 3415–3423.

We decided to investigate in more detail the oxidation at 0.4 V vs Fc/Fc$^+$, assigned to Co(III) to Co(IV) oxidation. At low scan rates (25 - 200 mV/s) an irreversible peak is observed at $E_{p,a}$ = 0.41 V, increasing the potential some reversibility is observed and at high scan rates (6000 – 8000 mV/s) it becomes reversible.

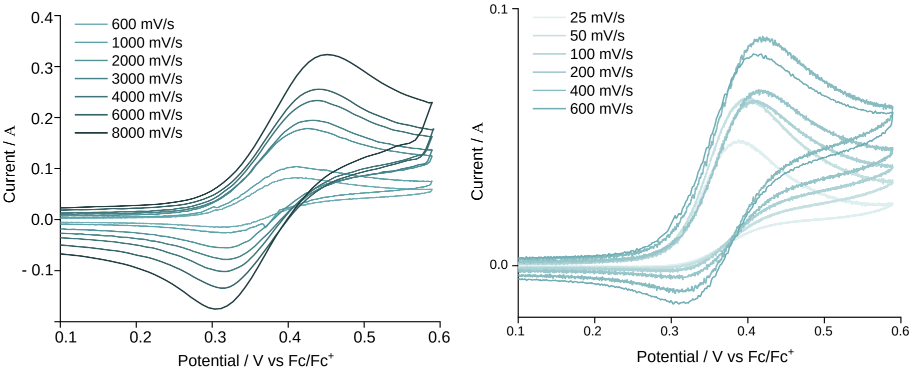

Figure 3.4 Cyclic voltammogram of complex **1_{ald}-I** vs Fc/Fc+ in DCM/*n*NBu$_4$PF$_6$ at different scan rates, for the first redox process.

To determine the feasibility of reaching the Co(IV) species through SET using NFTPT (**ox3**) and NFSI (**ox5**), we conducted a electrochemical study on these oxidants. The reduction potential (E_{pc}) was measured through cyclic voltammetry, as illustrated in Scheme 3.5.

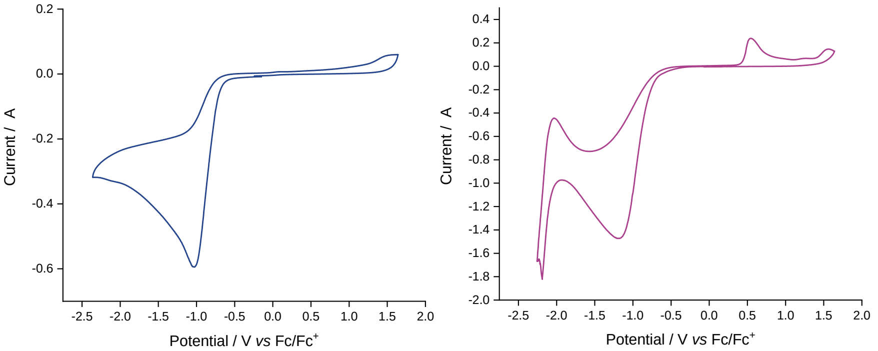

Figure 3.5 Cyclic voltammogram of **NFTPT** (left, blue) and **NFSI** (right, purple) *vs* Fc/Fc$^+$ in DCM/*n*NBu$_4$PF$_6$ at a scan rate of 200 mV s^{-1}.

Both oxidants revealed an irreversible reduction peak around -1.0 V Fc/Fc$^+$. These results suggest that the F^+ oxidants lack the sufficient potential to perform a SET to the

Co(III) center (scenario I, in Scheme 3.7) and that a chemical reaction is required to oxidize the Co(III) center, in this case, F transfer.

Mechanistic insights by NMR spectroscopy

In order to get further insights into the mechanism of the oxidatively induced reductive elimination step triggered NFTPT and NSFI from **1**$_{\mathbf{ald}}$**-I** and the nature of the transient cobalt intermediates involved in these oxidative processes, we performed multiple 1D and 2D NMR experiments. Due to the fast product formation observed at room temperature with the selected F^+ oxidants, we conducted a variable temperature (VT) ^{1}H NMR study to optimize the analysis of the reaction mixture by this technique (Figure 3.6 andFigure 3.7). After careful consideration, we selected 253 K as the ideal temperature for the study.

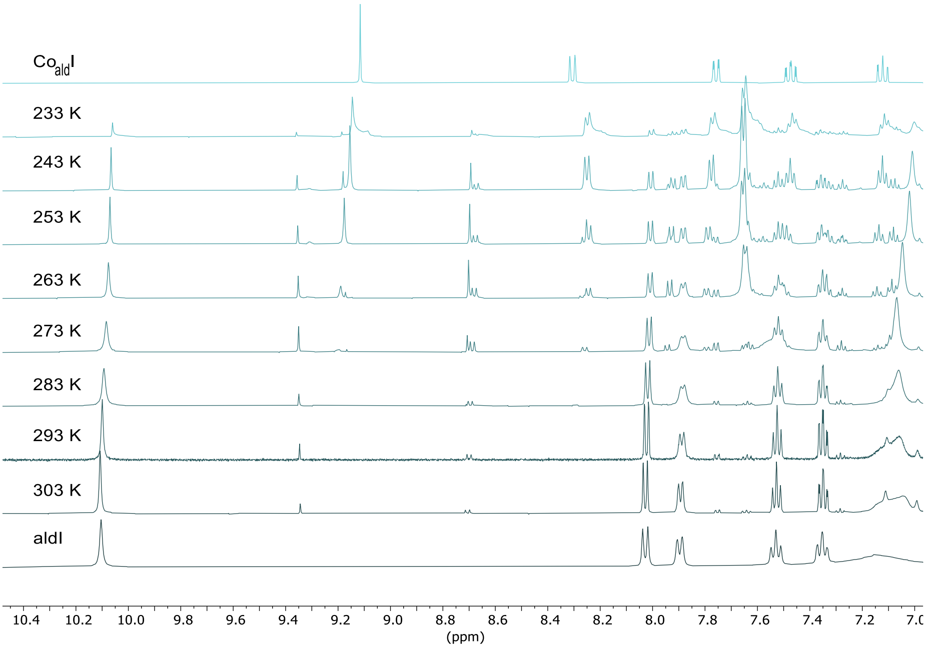

Figure 3.6 Aromatic region of the ^{1}H VT-NMR of the reaction with NFTPT.

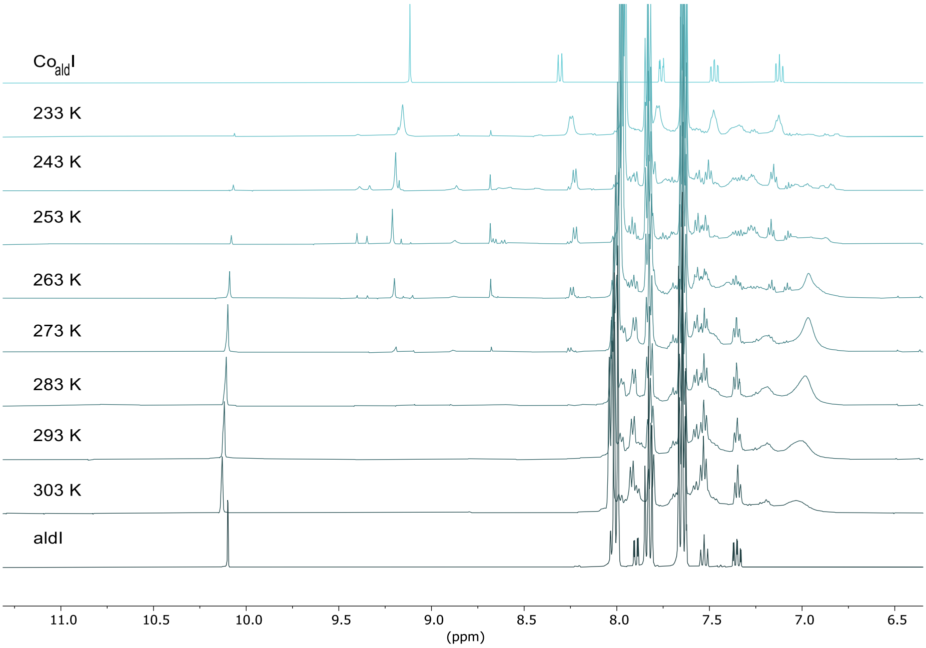

Figure 3.7 Aromatic region of the ^1H VT-NMR of the reaction with NFSI.

In a closer comparison between reactions in the presence of NFTPT or NFSI at 253 K (Figure 3.8), different species can be detected in the reaction media. In both cases, we observe the presence of **1_{ald}-I** and the organic product.[18] Additionally, the reaction with NFTPT yielded a new cobaltacycle species, **$Co_{ald}OTf$**[19] (highlighted in purple), where the oxidant's counterion displaced the I atom. Furthermore, there was another unidentified cobaltacycle (highlighted in orange) that was common to both oxidants.

---

[18] The ^1H NMR spectra of **$Co_{ald}I$** and **aldI** were done at 298 K, which accounts for the slight shifts observed in the signals.

[19] Its synthesis and characterization are included in Chapter 4 of this thesis.

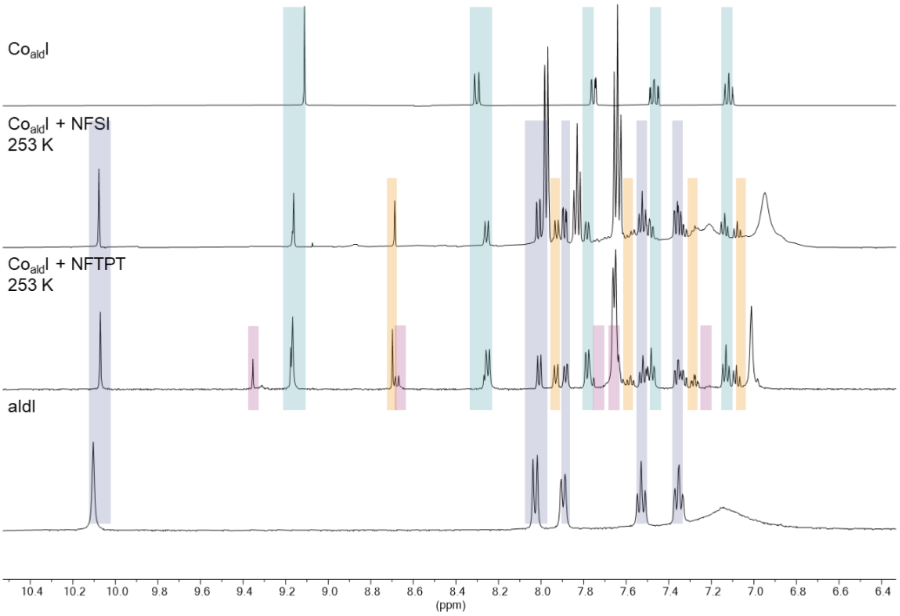

Figure 3.8 Comparison of the reaction at 253 K with both oxidants.

As mentioned above, upon examining the paramagnetic region at different temperatures, we observed a complex scenario, where multiple unidentified species are formed (Figure 3.9 and Figure 3.10). For NFSI (Figure 3.10), we observed dynamic processes involving the two sets of paramagnetic signals around 18 and 35 ppm.

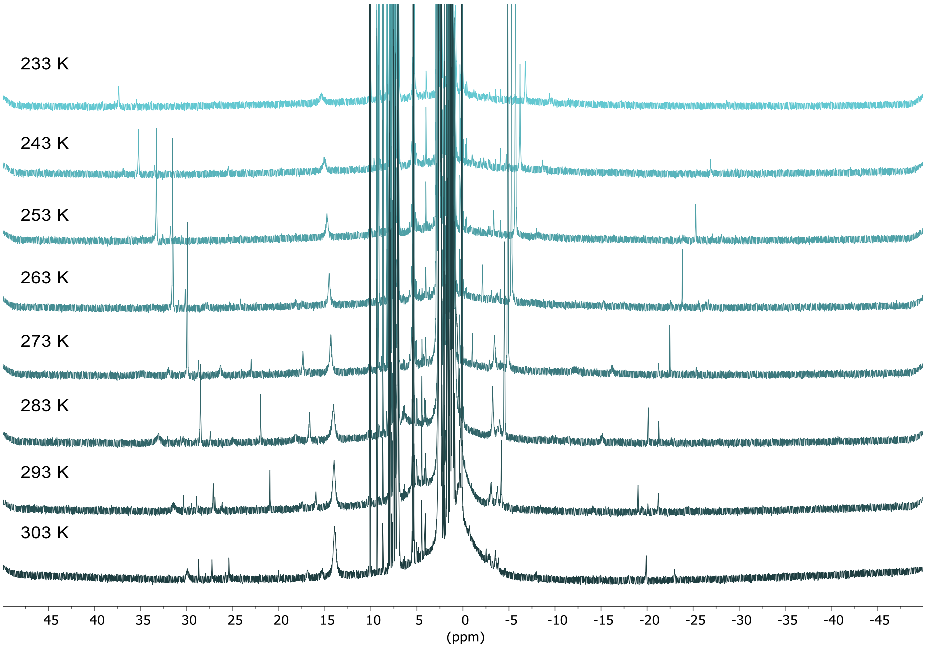

Figure 3.9 Paramagnetic region of the ^{1}H VT-NMR of the reaction with NFTPT.

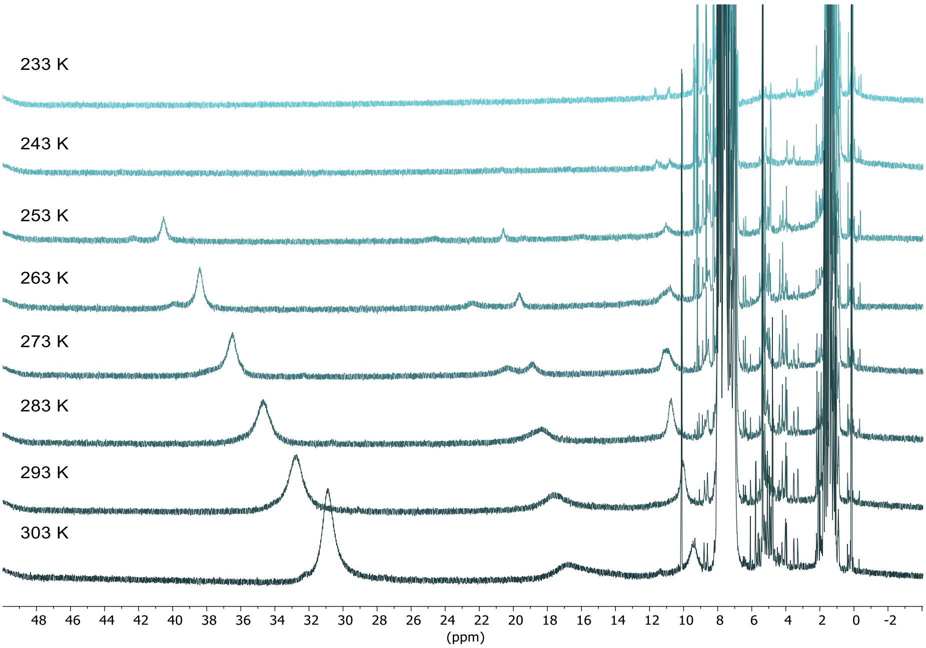

Figure 3.10 Paramagnetic region of the ^{1}H VT-NMR of the reaction with NFSI.

As observed in the VT study, the monitoring of the oxidative reactions along time at 253 K afforded a complex mixture of compounds that along a broad spectral window,[20] with some of the peaks disappearing along time, highlighted in the circles, indicating the transient nature of those species.

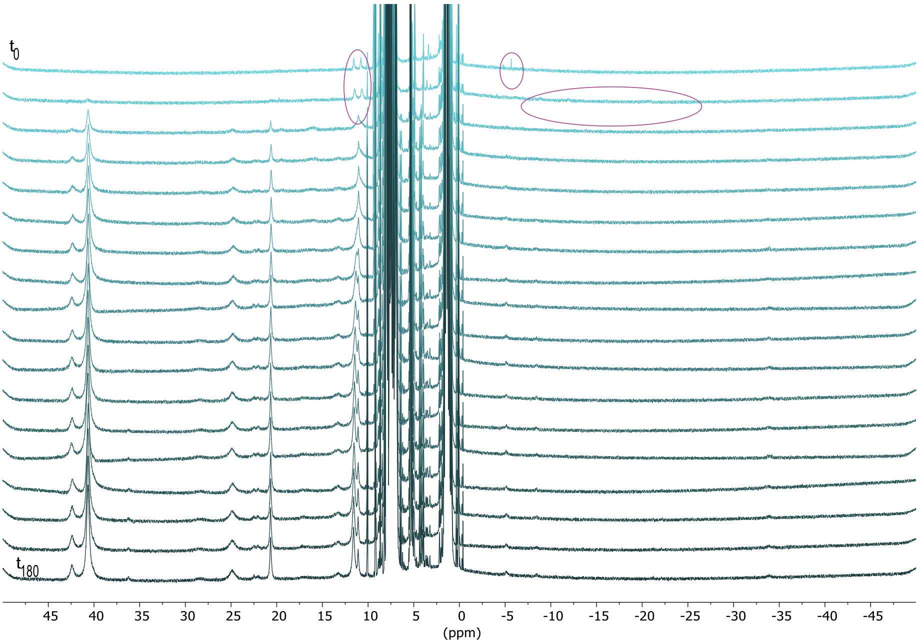

Figure 3.11 ^{1}H paramagnetic NMR, **Co$_{ald}$I** and NFSI reaction monitoring over 3 h. The darkening of the spectra corresponds to the progression of the reaction with darker spectra representing later time points. The purple cycles point out the signals that disappear over time.

---

[20] The ^{1}H and ^{19}F NMR spectra are included in the experimental appendix.

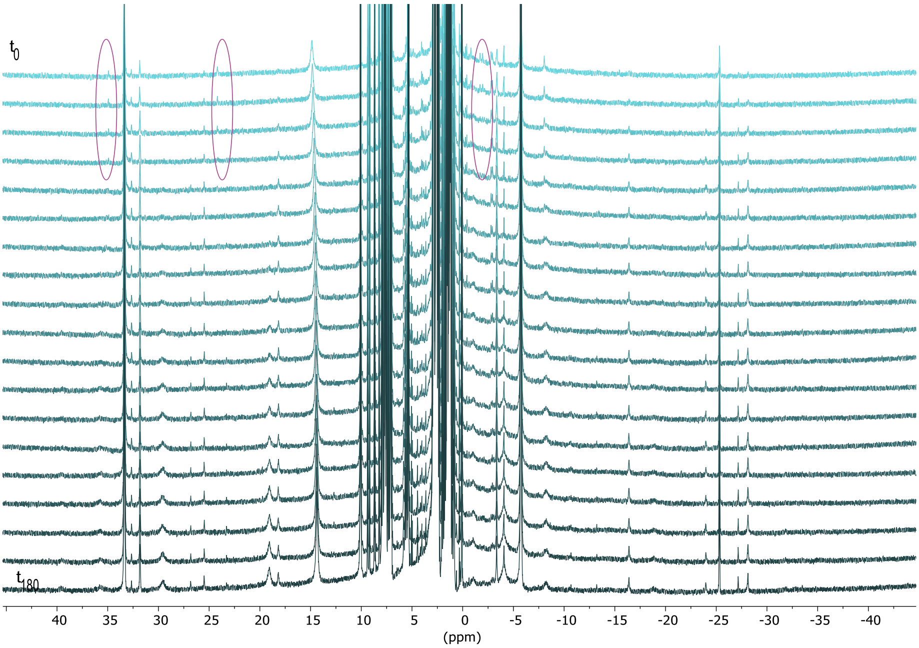

Figure 3.12 ^{1}H param NMR, **Co$_{ald}$I** and NFTPT reaction monitoring over 3h. The darkening of the spectra corresponds to the progression of the reaction with darker spectra representing later time points. The purple cycles point out the signals that disappear over time.

To gain deeper insights into the role of fluorine atoms in the reactions, we employed ^{19}F NMR spectroscopy (Figure 3.13). This analysis was particularly significant considering our previous observation of a fluorine atom attached to the cobalt center through X-ray analysis. The ^{19}F NMR spectra revealed the presence of several small peaks ranging from -400 to -600 ppm, suggesting the potential presence of fluorine atoms attached to the cobalt center.

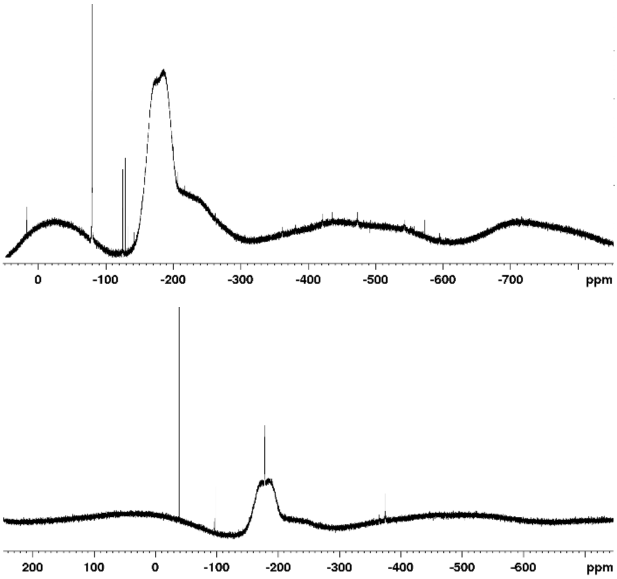

Figure 3.13 ^{19}F NMR of the reaction of **Co$_{\text{ald}}$I** with NFTPT (top) and NFSI (bottom) at 253K.

The complex mechanistic scenario observed in the shown 1D NMR experiments led us to explore additional alternatives to gather relevant mechanistic information. For example, we conducted a series of 2D NMR experiments (NOESY, ^{1}H-^{19}F HMBC, ^{19}F-^{19}F EXSY) in collaboration with Dr. Teodor Parella at the Autonomous University of Barcelona, but unfortunately any clear correlation could be extracted from the spectra (see experimental section). We also conducted a series of kinetic experiments to determine the reaction order with respect to the initial cobalt compounds and the corresponding oxidants NFTPT and NFSI. Unfortunately, NFTPT is not fully soluble neither in the reaction conditions or in alternative solvent mixtures, which precluded the kinetic study. For NSFI, while the reaction rate exhibits a first-order on complex **1$_{\text{ald}}$-I**, we observed a minus first-order with respect to the oxidant. We attribute this unexpected outcome to the coordinating properties of the remaining fragment of the oxidant after the oxidation process, as it can be observed in the X-ray structure shown in Figure 3.1.

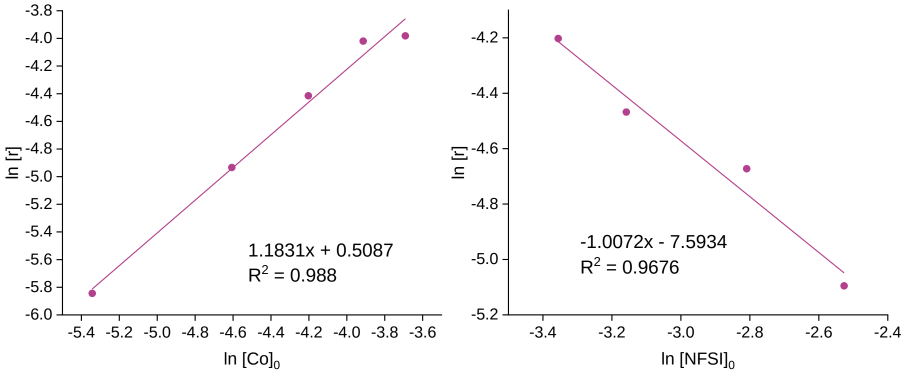

Figure 3.14 Kinetic order in **1ald-I** (right) and NFSI (left).

Additional attempts to detect or isolate any transient high-valent cobalt intermediate by mass spectroscopy or X-ray crystallography have been so far unsuccessful. Due to the presence of paramagnetic species confirmed by NMR spectroscopy, we have carried out different EPR measurements at 77 K, but unfortunately, we have not observe any signal (Figure 3.15).[21]

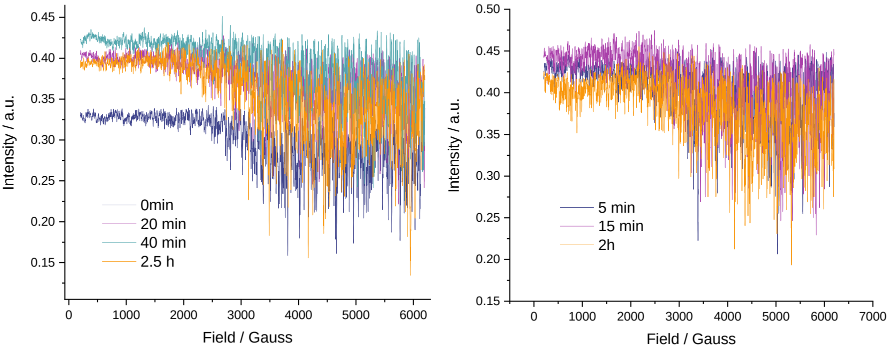

Figure 3.15 EPR spectra at 77 K in DCM at different reaction times. Left reaction with NFTPT (**ox3**) and right reaction with NFSI (**ox5**).

---

[21] Measurements at 4 K are still pending.

UNIVERSITAT ROVIRA I VIRGILI
UNCOVERING THE MECHANISTIC SCENARIOS OF NUCLEOPHILIC COUPLINGS IN CP*CO SYSTEMS
Sara López Resano

Computational study

Given the experimental difficulties encountered in studying the oxidative C–I bond formation from complex **1_{ald}-I**, we have undertaken a computational study to explore the different mechanistic scenarios that we could confirm or rule out experimentally: 2e- nucleophilic S_N2 substitution or SET followed by F radical addition. First, we calculated the aforementioned mechanism with both oxidants, using M06-D3 level of theory.[22]

From the thermodynamic perspective, both reaction pathways are feasible with the NFTPT oxidant, Scheme 3.8. The formation of **i2,** a Co(V) species and 2,4,6-trimethylpyridine, being the most favored with a relative energy of 2.5 kcal·mol^{-1}. The Co(V) is favored because the formation of a stable neutral pyridine instead of the more unstable pyridinium cation species with a N-centered radical.

The formation of Co(IV) and Co(V) species goes through a halide abstraction alike transition state, with differences on the electron distribution. The one-electron oxidation (**3a**) occurs in the open shell singlet surface, with a spin density of 0.68 in the Co center and has an energy of 33.5 kcal·mol^{-1}. The two-electron oxidation (**i2**) occurs on the triplet spin state and has a spin density of 1.93 in the metal center and is found at 38.8 kcal·mol^{-1} above reactants. The structure and energy of both the singlet and quintuplet states were computed; yet, they exhibited higher energies of 43.4 and 46.1 kcal·mol^{-1}, respectively.

---

[22] See page 67 for full computational details.

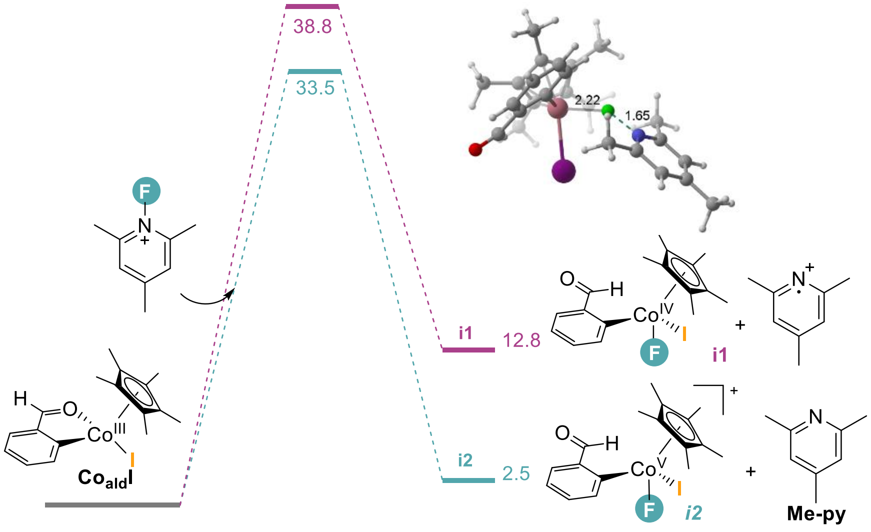

Scheme 3.8 Free energy profile of the oxidation of **Co$_{ald}$I** with NFTPT. The geometry on the top corresponds to the TS to form the Co(V). Energies in kcal·mol^{-1} and selected distances are shown in Å.

In the presence of the NFSI oxidant, both high-valent cobalt species are thermodynamically possible (Scheme 3.9). However, in contrast to the NFTPT oxidant, a distinct predilection is observed for Co(IV) (**i1**) and a neutral N-radical N-sulfonamide species, with a relative energy of -2.4 kcal·mol^{-1}. This preference can be attributed to the creation of a stable radical on the oxidant moiety, supported by electron delocalization on the sulfonyl groups.

The transition states with this oxidant are similar to those with NFTPT. The formation of the Co(IV) species is through an open-shell singlet, with a spin density of 0.47 in the cobalt center and an energy of 32.7 kcal·mol^{-1}. And the Co(V) (**i2**) formation has a lower barrier of 28.4 kcal·mol^{-1}, occurring in a triplet state with 1.96 spin density on cobalt. The singlet and quintuplet states were also calculated, but they exhibited higher energies of 36.9 and 37.6 kcal·mol^{-1}, respectively.

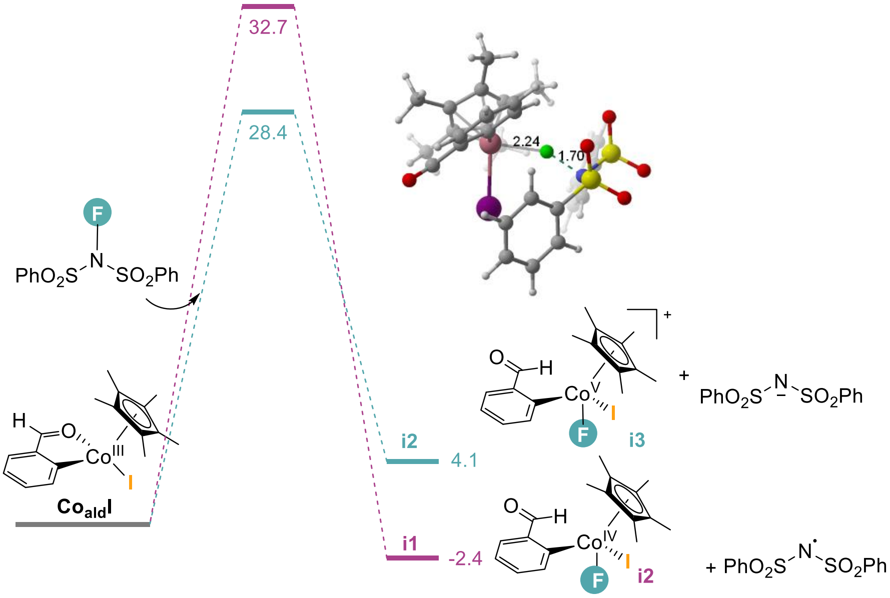

Scheme 3.9 Free energy profile of the oxidation of **Co**$\mathbf{Co_{ald}I}$ with NFSI. The geometry on the top corresponds to the TS to form the Co(V).Energies in kcal·mol^{-1} and selected distances are shown in Å.

However, due to the large barriers, neither pathway occurs at the experimental conditions, which are 25 ºC for 30 min. Consequently, we sought to find other alternative mechanisms.

Given the intricacy of the X-ray structure obtained with NFSI (Figure 3.1, in page 103) and the potential engagement of various mechanisms, particularly due to the observation of two distinct cobalt oxidations, our research focus shifted towards the reaction employing NFTPT as the oxidant. This choice is motivated by the exclusive observation of Co(III) species in the X-ray analysis.

In previous work from the group, a cationic cobaltacycle with ACN or THF coordinated could be isolated. Furthermore, experimental observations indicated the feasibility of I dissociation. Hence, the possibility of a dissociative pathway for the oxidation process of $\mathbf{Co_{ald}I}$ with NFTPT was studied in Scheme 3.10. Upon examining the thermodynamics of the reaction, it becomes evident that the dissociation of iodide followed by the addition of a fluorine radical is unfavorable. The relative energy of the Co(IV) intermediate (**i4**) incorporating the fluorine atom is significantly high, 20.0 kcal·mol^{-1}.

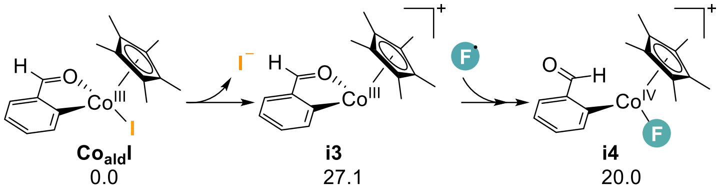

Scheme 3.10 Dissociative oxidation of **1$_{ald}$-I** with NFTPT. Free energies in kcal·mol^{-1}

An alternative pathway in which NFTPT can facilitate a 2e$^-$ oxidation by transfer of the F$^+$ moiety, resulting in the formation of a stable pyridine, involves the oxidation of two cobalt centers to Co(IV) simultaneously, with each site receives one electron (Scheme 3.11). The oxidation leads to the formation of a dimer (**i5**), where the F atom acts as a bridge connecting both Co centers.

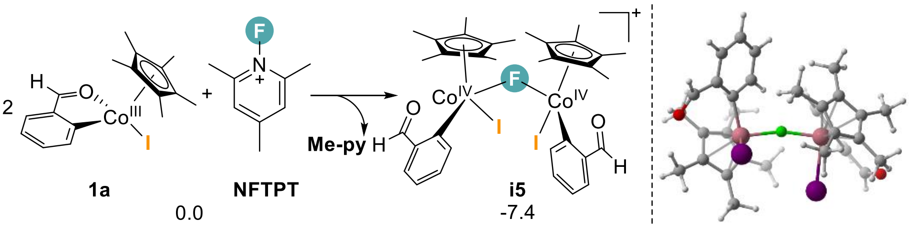

Scheme 3.11 A 2e$^-$ oxidation reaction to form a dimer with two Co(IV) centers. On the right is the geometry of **i5**. Free energies in kcal·mol^{-1}

Thermodynamically the formation of the **i5** intermediate is favorable, with an energy of -7.4 kcal·mol^{-1}.[23] It is a triplet state with 1.5 spin densities in both Co centers and -0.5 in the Cp*. This observation aligns with the X-ray structures, which revealed the presence of a cluster consisting of three cobalt atoms bridged by fluorine. In order to find the TS for this reaction, we conducted a scan calculation (Figure 3.16) on the N–F distance, starting from an adduct between **i5** and 2,4,6-trimethylpyridine and ending at the initial reactants, two **1$_{ald}$-I** species and NFTPT.[24]

---

[23] Gaussian16 was required to perform the calculations for the dimers, as Gaussian09 was causing frequency errors, thus, it was not possible to obtain the free energies. From here on Gaussian16 was use, unless otherwise stated.

[24] As the system is large, this scan is a loose scan without fully optimized structures and the dihedral between 4 atoms of the oxidant (F, N, and two C) frozen.

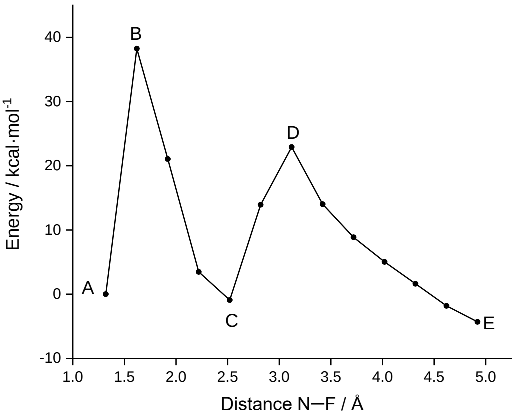

Figure 3.16 Scan for the formation of the dimer **i5** from two **Co$_{ald}$I** and **NFTPT**.

Initially, two separate cobaltacycles show no interaction, while NFTPT was oriented towards one cobalt center (structure A, in Figure 3.17). Next, a high-energy barrier (38 kcal·mol^{-1}, potential energy) hinders the transfer of F$^+$ to the metal center, oxidizing it to Co(V), simultaneously the two cobalt centers slightly approach each other (structure B, in Figure 3.17). The energy then decreases, leading to an intermediate state where the F atom is transferred to the cobalt center while still maintaining some interactions with N (structure C, in Figure 3.17). In the following step, the other cobalt(III) center gets oxidized to Co(IV), resulting in the formation of a Co-F bond and complete dissociation of the N–F bond, (structure D, in Figure 3.17) with a lower energy barrier (23 kcal·mol^{-1}, potential energy), to ultimately, form the Co(IV) dimer, **i5**, (structure E, in Figure 3.17).

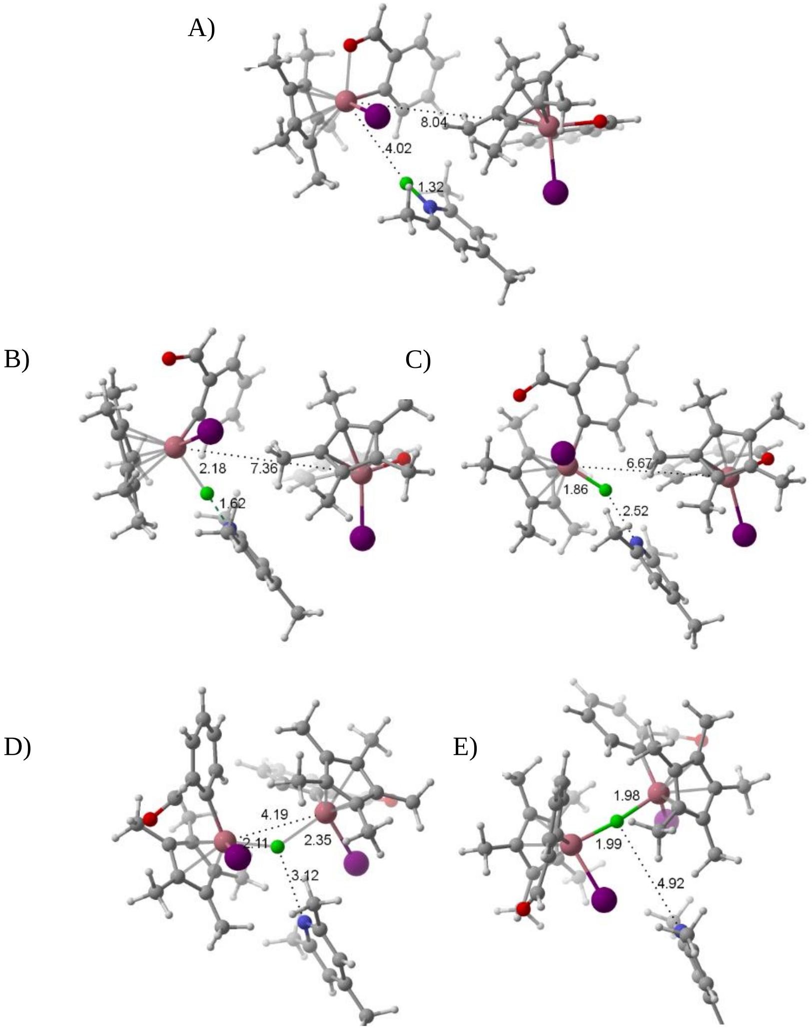

Figure 3.17 Geometries of the relevant points of the scan for oxidation of Co(III) to form **i5**. Selected distances are shown in Å.

The determination of the energy barrier for this step is challenging due to the inability to obtain the accurate transition state structure despite our efforts to optimize structure B. Nevertheless, it is evident that the barrier for this transformation is expected to be excessively high. [25]

Another possible mechanism for a dimer formation involves the oxidant attacking a cobalt center from the side, followed by electron transfer from this cobalt to the

---

[25] Also we have to considered that it is potential energy and is relative to the adduct formed with the two Co(III) centers and the oxidant.

adjacent cobalt through an I atom, as shown in Figure 3.18. Unfortunately, the energy barrier for this transformation is also exceedingly high, 53.7 kcal·mol^{-1}.

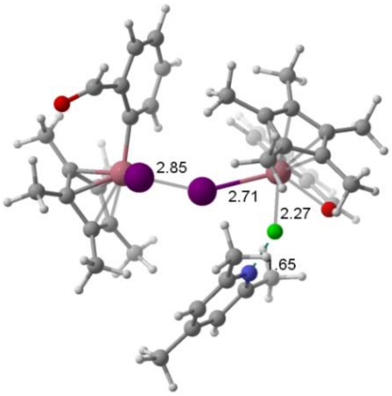

Figure 3.18 Oxidation of Co(III) to make a dimer. Selected distances are shown in Å.

Next, we explored the possibility of a Co(II) center as a potential candidate for oxidation. Indeed, this Co(II) species can be oxidized by two electrons using NFTPT, with a relatively low barrier of 13.1 kcal·mol^{-1}.

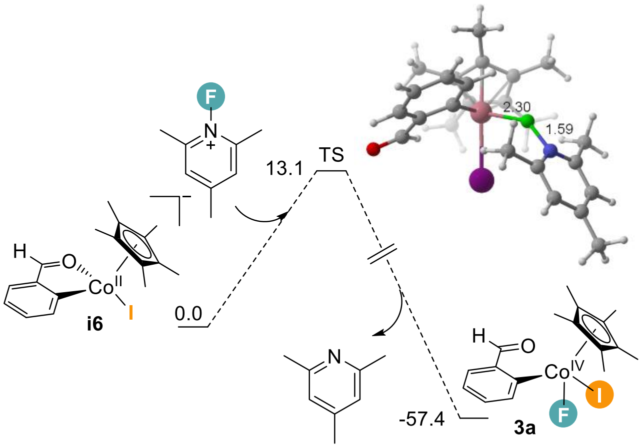

Scheme 3.12 Oxidation of a Co(II) to a Co(IV) species by NFTPT. Free energies in kcal·mol^{-1} and selected distances are shown in Å.

Nevertheless, the challenge remained in determining how to obtain the Co(II) species. We hypothesized that a disproportionation reaction involving two Co(III) species could potentially yield a Co(II) and a Co(IV) species, even in trace amounts, thus initiating the reaction. However, it was discovered that the energy of the Co(II) and Co(IV) species relative to the starting Co(III) complex is prohibitively high, (Scheme 3.13).

Given the presence of charge separation and the potential significance of ion pairs, an adduct between the Co(II) species and NFTPT was computationally assessed. However, the resulting adduct was only stabilized by 3.3 kcal·mol^{-1}.

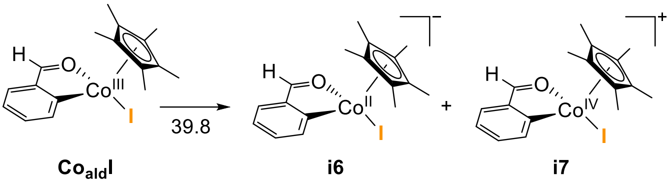

Scheme 3.13 Disproportionation of the **Co$_{ald}$I**. Free energies in kcal·mol^{-1}

A Co(II) species (**i8**) can also be achieved by the dissociation of the I radical, as depicted in Scheme 3.14, although it is thermodynamically unfavorable. We hypothesized that the unstable radical formation might be a contributing factor and speculated the possibility of the recombination of two iodine radicals to form more stable molecular iodide. Unfortunately, even with this stabilization, the reduction of Co(III) to Co(II) accompanied by the formation of molecular iodide remains an endothermic reaction, requiring an energy input of 25.2 kcal·mol^{-1}.

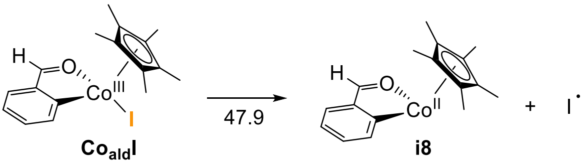

Scheme 3.14 Co(II) formation from dissociation of I radical. Free energies in kcal·mol^{-1}

We also examined the remote possibility of the triflate counterion facilitating the reduction of the Co(III) complex by one electron to form **i4** and a triflate radical, but the thermal energy required for this step is prohibitively high, 80.1 kcal·mol^{-1}.

Despite exploring various pathways to obtain a Co(II) species for oxidation, none proved successful. Consequently, our attention returned to the X-ray structures, particularly the cluster formed with NFTPT, which includes an OH group attached to the three cobalt centers. Considering the potential relevance of water traces during the reaction, we investigated the possibility of OH-F exchange and the formation of a new electrophilic "OH$^+$ oxidant" (**ox3-OH**) found it to be thermodynamically favorable. Despite that, the energy barrier for the oxidation of the Co(III) species using the new oxidant remains excessively high.

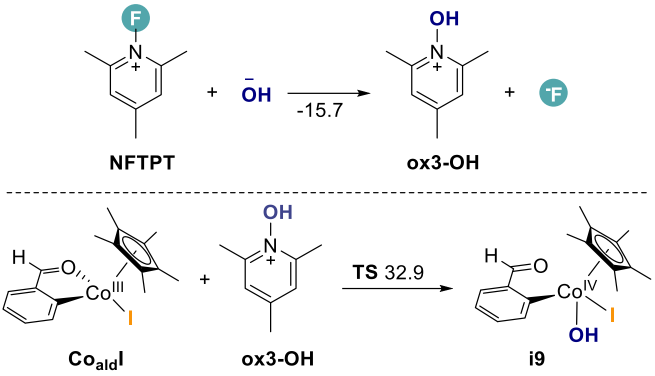

Scheme 3.15 Insolvent of $^{-}$OH in the reaction. Top: formation of the new OH+ oxidant. Bottom: oxidation of **Co$_{ald}$I** by **ox3-OH**. Free energies in kcal·mol^{-1}

Upon the oxidation of the metal center, the reductive elimination reaction becomes more exergonic, as seen in Chapter 2 of this thesis and in the work by Chang and co-workers on similar Cp*Ir systems.[26] Building upon this knowledge, we proposed that if the driving force behind the reductive elimination is significant enough, it might potentially overcome the high oxidation barrier. Following the reductive elimination from the Co(V) species (**i2**), we performed calculations on the resulting Co(III) species (**i10**). While the singlet form **i10** exhibited a relative energy of only -9.9 kcal·mol^{-1}, which is insufficient to outdo the barrier, the triplet state proved significantly more stable, with an energy of - 45.8 kcal·mol^{-1}.

---

[26] K. Shin, Y. Park, M. H. Baik, S. Chang, *Nat. Chem.* **2018**, *10*, 218–224.

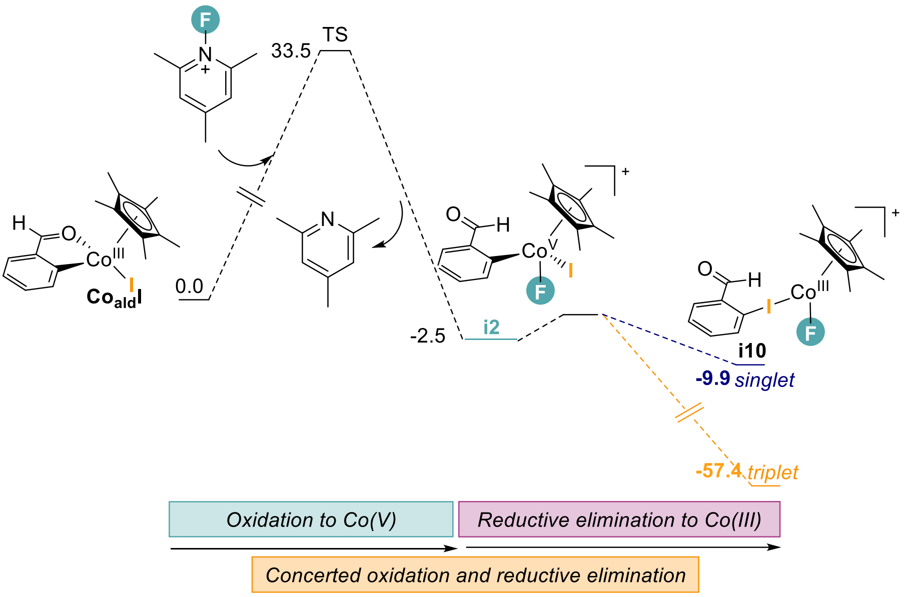

Scheme 3.16 Possibility of a concerted oxidation and reductive elimination taking advantage of the low energy of the triplet Co(III) to overcome the high oxidation barrier.

The remarkable stability of the triplet Co(III) species allows for the possibility of a concerted oxidation-reductive elimination process (Scheme 3.17), where the oxidation to a high-valent species occurs simultaneously with the reductive elimination.

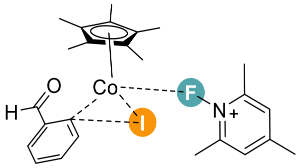

Scheme 3.17 Concerted oxidation and reductive elimination

Extensive efforts were made to locate a transition state for this transformation. Given the presence of multiple reaction coordinates, we conducted a loose scan along the C–I bond coordinate while keeping the N–F and Co–F bonds fixed in the TS geometry of the oxidation reaction, shown in Figure 3.19.

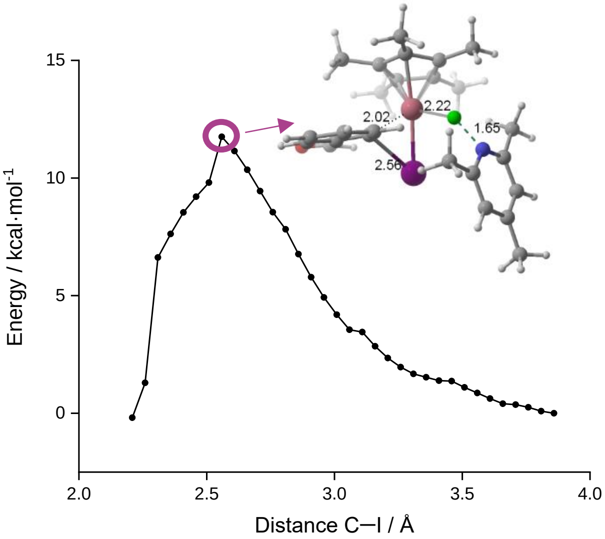

Figure 3.19 Scan performed on the C–I coordinate to find the concerted TS.

The optimization of the highest point, did not lead to the desired TS, and lead either to the reductive elimination product or the initial starting point, the TS for the oxidation to Co(V). We also performed a scan calculation along the F–N bond coordinate, while keeping the C–I bond frozen in the geometry of the TS for the reductive elimination. Unfortunately, we were unable to obtain the TS for the concerted mechanism through these attempts. Furthermore, we employed the QST3 method in several iterations, but also failed finding the TS.

In light of the unsuccessful search for a viable oxidation pathway for the experimental conditions, and considering the high energy barriers encountered in all other calculated pathways, a benchmark study was conducted to assess the possibility that the M06 method may not be suitable for accurately predicting the barriers in our system and potentially overestimating them. We selected the mechanisms on Scheme 3.8 and Scheme 3.9 (pages 117 and 118) to calculate the energy barriers, as the remaining tested mechanisms exhibited comparatively higher energy barriers.

We evaluated the performance of eleven density functionals across all rungs of Jacob's ladder. We also used a larger basis set with M06.[22] The results obtained are depicted in Table 3.1.

Some functionals did not calculate properly the electron distribution for the Co(IV) transition states, resulting in a triplet state with ωB97XD, M06-2X, and M06-HF methods, and a closed singlet state with PBE0 and B2PLYP methods.

We employed the BP86 functional, a generalized gradient approximation (GGA) functional, at the lowest rung of the ladder, which resulted in lower energy barriers. Surprisingly, the Co(IV) states were even lower than the Co(V) states in this case. As we ascended the ladder, we explored Meta-GGA functionals, specifically the Minnesota 06 series with varying degrees of Hartree-Fock (HF) exchange. These functionals incorporate additional exchange-correlation terms beyond the GGA level, providing a more accurate description of electronic properties. The energy barriers for Co(IV) formation were consistently higher than those for Co(V) formation when using these functionals. Notably, the spin density on Co(IV) increased with increasing HF exchange, and when M06-2X was employed, the Co(IV) state manifested as a triplet state. Conversely, increasing the HF exchange led to a decrease in the energy barrier for Co(V) complex formation. Additionally, employing a larger basis set alongside M06 resulted in slight reductions in all barriers.

Several hybrid GGA functionals were tested, including non-empirical PBE0 and TPSSh, as well as empirical functionals such as, B3PW91, B3LYP and ωB97XD. With the exception of TPSSh, all the tested functionals yielded higher energy barriers for the formation of Co(IV) species compared to Co(V) species. When TPSSh was employed with the NFTPT oxidant, it exhibited a similar trend, but the energy differences were smaller. However, when using NFSI, the barrier for Co(IV) formation was slightly lower. The energy barriers for Co(IV) formation ranged from 25-30 kcal·mol^{-1}across the tested functionals in this group, except for ωB97XD, which had the highest energy barrier of 34.9 kcal·mol^{-1}for the formation of Co(V) with NFTPT.

Finally, we also examined the double-hybrid GGA functional B2PLYP. Remarkably, this functional yielded particularly low energy barriers for the formation of Co(V) species, with a value of 17.5 kcal·mol^{-1} observed for both oxidants.

Table 3.1 Benchmark study on the oxidation of $\mathbf{1_{ald}}$**-I**. Free energy barriers to form the corresponding high-valent species are in kcal·mol^{-1}. ^{a}Single point calculations with a larger basis set.

		NFTPT			*NFSI*		
	Method	*Co(IV)*	*Spin*	*Co(V)*	*Co(IV)*	*Spin*	*Co(V)*
GGA	**BP86**	23.7	0.259	25.5	19.0	0.311	22.0
Meta-GGA	**M06-L**	32.5	0.3	29.1	31.4	0.01	27.9
	M06	**38.8**	**0.68**	**33.5**	**32.7**	**0.47**	**28.4**
	M06-2X	38.7	1.98	22.9	40.6	1.98	21.0
	M06-HF	43.3	2.2	12.7	40.7	1.9	10.7
	^{a}**M06**	37.3	0.98	30.3	32.9	0.38	24.8
Hybrid GGA	**PBE0**	43.3	0.0	31.4	37.8	-0.18	28.3
	TPSSh	29.7	0.33	28.5	26.5	0.37	27.1
	B3PW91	37.0	0.165	29.8	31.6	0.296	25.4
	B3LYP	34.6	0.12	26.7	30.9	0.28	24.0
	ωB97XD	46.6	1.61	34.9	41.6	1.63	31.6
Double-Hybrid GGA	**B2PLYP**	32.3	0.0	17.6	30.4	0.0	17.5

After careful consideration, we selected B3LYP-D3 as the appropriate method for our system. We conducted reoptimization of all structures including starting materials, transition states, and products. To obtain more precise energies, we performed single point calculations using a larger basis set (Scheme 3.18 and Scheme 3.19). Encouragingly, this approach yielded reduced energy barriers for oxidizing Co(III) to a Co(V) species, 25.1 and 21.0 kcal·mol^{-1} with NFTPT and NFSI oxidants, respectively.

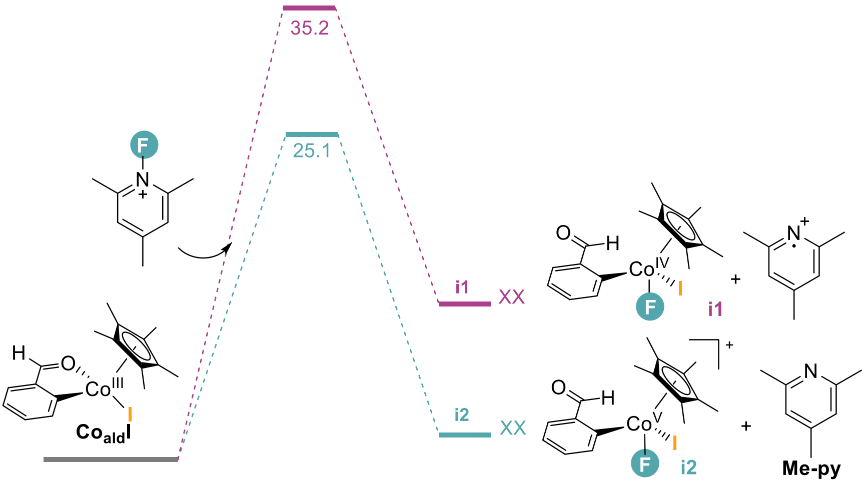

Scheme 3.18 Free energy profile of the oxidation of $\mathbf{1_{ald}}$**-I** with NFTPT calculated with B3LYP-D3. Energies in kcal·mol^{-1}.

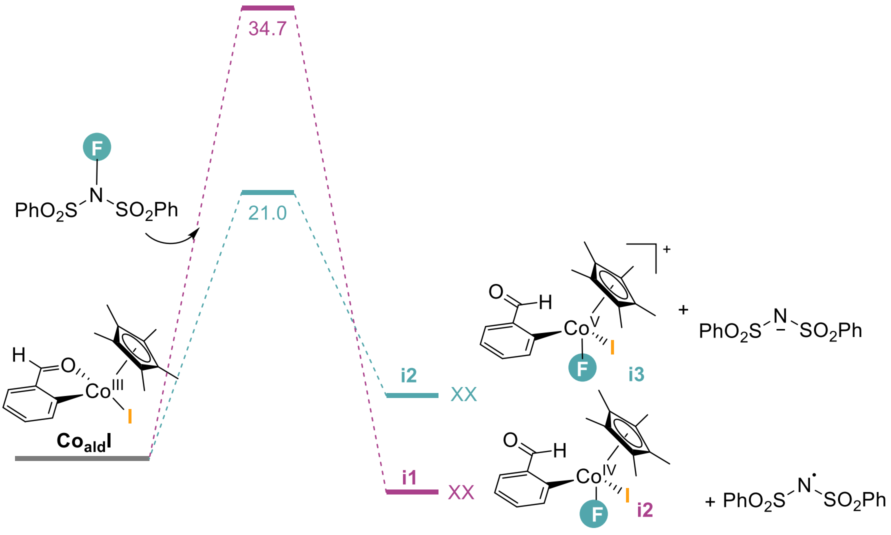

Scheme 3.19 Free energy profile of the oxidation of **1ald-I** with NFSI calculated with B3LYP-D3. Energies in kcal·mol^{-1}.

The observed discrepancies in X-ray structures and paramagnetic signals between the two systems, despite both proceeding through the same Co(V) transition state, raise an intriguing question. To shed light on this, we must evaluate the stabilities of the oxidants after the 2e- redox process (Scheme 3.8 and Scheme 3.9). In the case of NFTPT, where the oxidant forms a stable pyridine, the Co(V) undergoes reductive elimination to Co(III), thus explaining the corresponding X-ray structure.

Conversely, with NFSI, the negatively charged species is less stable and exhibits a preference for oxidation while simultaneously reducing the Co(V) to Co(IV), resulting in the formation of a more stable nitrogen radical. In this case, once the Co(V) species is formed, two competing pathways emerge: i) reductive elimination to Co(III) and ii) reduction of the remaining oxidant by Co(IV), leading to the formation of a Co(II) species. This finding aligns with the observed X-ray structure, which reveals the presence of these two distinct oxidation states of cobalt.

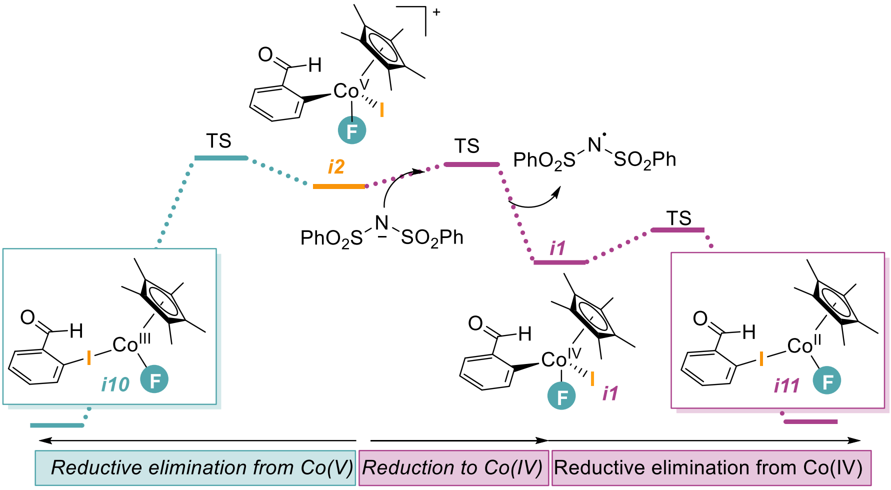

Scheme 3.20 Possible reductive elimination mechanisms, after obtaining Co(V) with NFSI oxidant.

3.3. Conclusion

In summary, this chapter focused on the investigation of the nucleophilic coupling of CpCo(III) with F+ oxidants, namely NFTPT and NFSI. Our primary objective was to understand the reductive elimination process from a well-defined CpCo(III) species, resulting in the formation of a C-I bond.

Through our comprehensive study, we successfully demonstrated that this nucleophilic coupling reaction follows an oxidative reductive elimination mechanism. Through a combination of experimental techniques, including NMR, X-ray, and EPR spectroscopic studies, and computational DFT calculations, we unraveled the intricacies of the oxidation process.

Specifically, our findings revealed that the reactions proceed via a Co(V) species, with the NFSI oxidant allowing for the formation of a more stable Co(IV) intermediate. This resulted in a final mixture of Co(II) and Co(III) centers after the reductive elimination step.

Overall, our study provided valuable insights into the mechanism and nature of the nucleophilic coupling reaction, shedding light on the complexities of the oxidation process and expanding our understanding of these chemical transformations.

3.4. Appendixes

3.4.1. Experimental appendix

General procedures

All reactions were conducted in an argon-filled glovebox (mBraun Unilab 4420) with concentrations of O_2 and H_2O < 0.1 ppm or oven-dried glassware (at 100 ºC overnight and cooled under vacuum prior use) using Schlenk techniques under an argon atmosphere (otherwise mentioned). NMR spectra were obtained on a Bruker 400 MHz, a 500 MHz or a 500 MHz with cryoprobe spectrometers equipped with probeheads capable of producing gradients in the z direction with a maximum strength of 53.5 G/cm. ^{1}H, ^{13}C and ^{19}F NMR chemical shifts are reported in parts per million (ppm), relative to tetramethylsylane (TMS) for ^{1}H and ^{13}C with the residual solvent peak used as an internal reference and relative to $CFCl_3$ (Freon) for ^{19}F. Multiplicities are reported as follows: s (singlet), dd (doublet of doublets), td (triplet of doublets), quadruplet (q) and multiplet (m). ^{19}F and ^{1}H NMR yields for reductive elimination studies were obtained on a Bruker 400 MHz or 500 MHz spectrometer using 4,4´- difluorobenzene (–116.65 ppm) as an internal standard with 8 scans for data acquisition. All electrochemical experiments were performed with a Biologic SP–150 potentiostat at rt. UV-Vis measurements were carried out on a Shimadzu UV-1800PC spectrophotometer equipped with a photomultiplier detector, double beam optics and D2 and W light sources. Continuous wave (CW) EPR spectra were acquired on a Bruker EMX X-band Micro EPR spectrometer with an ER 4116 HS cavity. A 150 mL Suprasil offset liquid nitrogen dewar flask (Wilmad-LabGlass) was used for low-temperature measurements (77 K). Mass spectra were acquired on a Bruker Daltonics - micrOTOF II – High performance TOF-MS system.

Materials and methods

Commercially available reagents 2-iodobenzaldehyde, 2-phenylpyridine, N-iodosuccinimide, $Pd(OAc)_2$, 1,2,3,4,5-pentamethylcyclopenta-1,3-diene, $CoCl_2$, nBuLi, Zn powder, (Trifluoromethyl)trimethylsilane, sulfur, tetramethylammonium fluoride, $AgSCF_3$, AgOTf, $Mn(OAc)_3 \cdot 2H_2O$, AgOAc, AgF, AgF_2, $Cu(OAc)_2$, (2,2,6,6-Tetramethylpiperidin-1-yl)oxyl (TEMPO), 2,6-Di-tert-butyl-4-methylphenol (BHT), 1,4 dinitrobenzene, 4,4´-difluorobiphenyl, 3,5-bis(trifluoromethyl)benzoic acid, 4-(((trifluoromethyl)thio)oxy)benzaldehyde and $(nBu)_4NPF_6$ were used without further purification directly as received from the commercial supplier, and stored under inert gas and/or low temperature when required. 1,2-dichloroethane (DCE) was stored under argon with activated 4 Å molecular sieves. If necessary, the solvents (Hexane, THF, CH_2Cl_2) were used from a solvent purification system pure-solv (SPS-400, Innovative Technology) and stored under argon over activated 4 Å molecular sieves. CD_2Cl_2 and $CDCl_3$ were stored under argon over activated molecular sieves 4 Å. The compounds [Cp*Co(VTMS)$_2$],[27] [Cp*Co^{III}(2-ppy)(I)] (**1**),[1] and NMe_4SCF_3[28] were synthesized according to previous literature procedures.

*Isolation and characterization of [Cp*Co^{III}(ald)(I)] (**2**)*

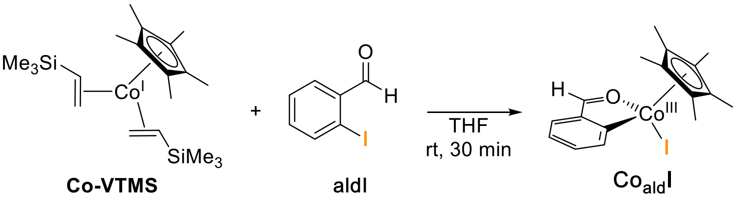

In an argon atmosphere glovebox, Co-VTMS (1000 mg, 2.6 mmol) and **aldI** (587.8 mg, 1 equiv.) were added to an oven-dried Schlenk containing a magnetic stir bar. THF (10 mL) was added and the mixture was stirred at room temperature for 30 time. The solvent and the vinyltrimethylsilane were removed under reduced pressure. The reaction was dissolved in DCM and filtered. Then the residue was dried under vacuum and washed with hexane. Finally, the residue was dried under vacuum until a solid is obtained, 990 mg, 89 % yield. The complex is stable under air and was stored in the desiccator. The complex was characterized by ^1H NMR which fits with the reported spectra.**Error! Bookmark not defined.**

^{1}H NMR (CD_2Cl_2, 298 K, 500 MHz): δ 9.08 (s, 1H, CHO), 8.27 (d, 1H, $^3J_{H,H}$ = 7.8 Hz), 7.72 (dd, 1H, $^3J_{H,H}$ = 7.6 Hz, $^4J_{H,H}$ = 1.5 Hz), 7.43 (td, 1H, $^3J_{H,H}$ = 7.5 Hz, $^4J_{H,H}$ = 1.5 Hz), 7.08 (td, 1H, $^3J_{H,H}$ = 7.5 Hz, $^4J_{H,H}$ = 1.5 Hz), 1.56 (s, 15H, Cp*) ppm

*Thermolysis of **Co$_{ald}$I***

In an argon atmosphere glovebox, a screw-cap NMR tube was charged with **Co$_{ald}$I** (4.26 mg, 0.01 mmol) and 0.4 mL of DCM-d_2. The reactions were monitored at 20 min,

---

[27] J. Sanjosé-Orduna, D. Gallego, A. García-Roca, E. Martin, J. Benet-Buchholz, M. H. Pérez-Temprano, *Angew. Chem., Int. Ed.* **2017**, *56*, 12137.

[28] T. Scattolin, F. Schoenebeck, *e-EROS* **2018**, DOI: 10.1002/047084289X.rn02228.

2 h, and overnight by ^{1}H NMR spectroscopy, if no change was observed the reaction was heated for 2 h at 50 ºC.

ORE with different oxidants

In an argon atmosphere glovebox, a screw-cap NMR tube was charged with **Co$_{ald}$I** (4.26 mg, 0.01 mmol) and the corresponding oxidant (0.012 mmol), and 0.4 mL of DCM-d$_2$. The reactions were monitored at 20 min, 2 h, and overnight by ^{1}H NMR spectroscopy, if no change was observed the reaction was heated for 2 h at 50 ºC.

Quantification with NFTPT and NFSI

In an argon atmosphere glovebox, a screw-cap NMR tube was charged with **Co$_{ald}$I** (4.26 mg, 0.01 mmol) and the corresponding oxidant (0.02 mmol) and 0.4 mL of DCM-d$_2$. The reaction mixture was stirred a couple of times manually and was left to react at room temperature and monitored by ^{1}H NMR. The next day around 1 mg of internal standard (1,3,5-Trimethoxybenzene) was added to the NMR tube. The yield of **aldI** was determined by 1H NMR using 1,3,5-Trimethoxybenzene as internal standard.

Oxidant	*mg of oxidant*	*mg of IS*	*NMR Yield*
1,Fluoro-2,4,6-trimethylpyridinium	5.7	0.99	95 %
N-Fluorobenzenesulfonimide	6.3	1.10	96.5 %

^{1}H NMR spectrum of reaction of **Co$_{ald}$I** and NFSI at 25 ºC (CD$_2$Cl$_2$)

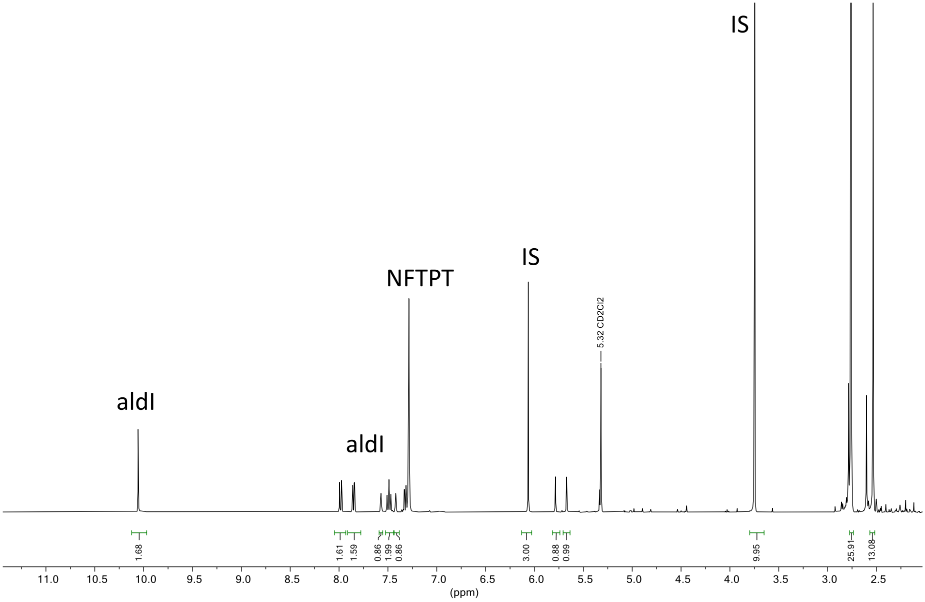

^{1}H NMR spectrum of reaction of **Co$_{ald}$I** and NFSI at 25 ºC (CD$_2$Cl$_2$)

UNIVERSITAT ROVIRA I VIRGILI
UNCOVERING THE MECHANISTIC SCENARIOS OF NUCLEOPHILIC COUPLINGS IN CP*CO SYSTEMS
Sara López Resano

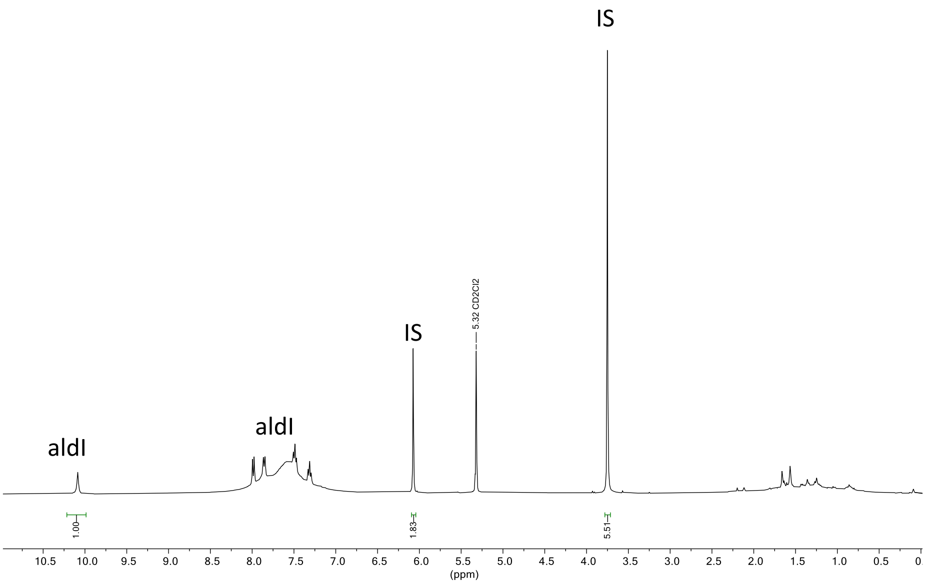

Solvent screening with NFTPT and NFSI

With the two best oxidants in hand, a solvent screening was carried out to get more information about the mechanism (Scheme 3.21). In an argon atmosphere glovebox, a screw-cap NMR tube was charged with **Co$_{ald}$I** (4.26 mg, 0.01 mmol) and the corresponding oxidant (0.02 mmol) and 0.4 mL of the corresponding deuterated solvent. The reaction mixture was stirred a couple of times manually and was left to react at room temperature and monitored by ^{1}H NMR.

With **ox3** the only solvents that worked are DCM and CHCl$_3$, Benzene gave decomposition at 30 min, and the reactions were slow in THF and ACN, due to the formation of **Co$_{ald}$THF**/**Co$_{ald}$ACN** inhibiting the product formation. Therefore, it is difficult to draw a conclusion.

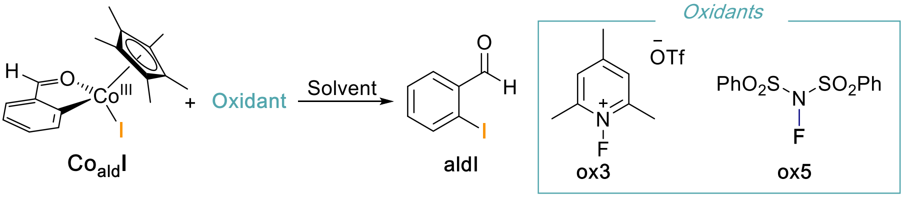

Solvent	*Conversion with ox3*	*Conversion with ox5*
DCM	100 %	100 %
ACN	46 % (72 h)	25 % (96 h)
Benzene	Decomposition (30 min)	100 % (30 min)

$CHCl_3$	100% (24 h)	100 % (24 h)
THF	Slow – after 5 days some Co$_{ald}$THF	Fast – not clean spectra. 100% conversion, then more things appear

Scheme 3.21 Solvent screening for C–I bond-forming reductive elimination from **Co$_{ald}$I**. The reported conversions were determined by ^{1}H NMR spectroscopy of the crude reaction mixture.

Cyclic voltammetry analysis

Cyclic voltammetry analysis of the isolated **Co$_{ald}$I** and the two oxidants, NFTPT and NFSI were performed in a 3-electrode cell consisting of a glassy carbon disk as working and counter electrodes (0.07 cm^2 of surface area) and SCE (Saturated Calomel electrode) as the reference electrode. The electrodes were previously polished with diamond abrasive slurries (DIAPAT-M, 39-321-M, Netkon) in an order of 3 μm and 1 μm diameter particle-based slurries (2 minutes in each) to obtain mirror surfaces. Synthetic nap based polishing pads (METAPO-B, polishing cloth, self- adhesive back, diamond 3-1 μm, Netkon) were used for diamond polishing.

Solutions of **Co$_{ald}$I** (0.003 M) in DCM with $(n\mathrm{Bu})_4\mathrm{NPF}_6$ (0.3 M) as electrolyte were added to the electrochemical cell. Between every scan, the solution was stirred in order to remove the species close to the surface. In some cases, the electrodes had to be polished between each scan. All potentials reported in this thesis were converted to the couple Fc/Fc^+. To achieve this, measurements were performed either by adding Fc/Fc^+ to the solution mixture or by preparing a new DCM $(n\mathrm{Bu})_4\mathrm{NPF}_6$ solution and subsequently measuring the desired CVs.

X-ray structural determination for

Crystal preparation: Crystals of **the final Co cluster of the reaction of Co$_{ald}$I with NFTPT (cryst1)** were grown at -35 ºC, under Ar, by vapor diffusion of pentene into a solution of the reaction in CH_3Cl. The crystals of **the final Co cluster of the reaction of Co$_{ald}$I with NFSI (cryst2)** were grown at -35 ºC, under Ar, by vapor diffusion of hexane into a solution of the reaction in CH_2Cl_2. The crystals used for structure determination were selected using a Zeiss stereomicroscope using polarized light and prepared under inert conditions immersed in perfluoropolyether as protecting oil for manipulation.

Data collection: Crystal structure determination for **cryst1** and **cryst2** were carried out using a Apex DUO Kappa 4-axis goniometer equipped with an APPEX 2 4K CCD area detector, a Microfocus Source E025 IuS using MoK_α radiation, Quazar MX multilayer Optics as monochromator and an Oxford Cryosystems low temperature device Cryostream 700 plus (T = -173 °C). Crystal structure determination for samples Full-sphere data collection was used with ω and φ scans. *Programs used:* Data collection APEX-2,[29] data reduction Bruker Saint[30] V/.60A and absorption correction SADABS.[31]

Structure Solution and Refinement: Crystal structure solution was achieved using the computer program SHELXT.[32] Visualization was performed with the program SHELXle.[33] Missing atoms were subsequently located from difference Fourier synthesis and added to the atom list. Least-squares refinement on F^2 using all measured intensities was carried out using the program SHELXL 2015.[34] All non-hydrogen atoms were refined including anisotropic displacement parameters.

Comments on the structures:

Cryst1

The asymmetric unit contains half molecule of the metal complex located on a mirror plane, 1 1/8 molecules of chloroform and one triflate anion. Once the symmetry operations are applied, this is equivalent to one molecule of metal complex, 2 ¼ molecules of chloroform and two triflate anions. One of the triflate anions is disordered in three orientations and the second triflate anions shows some disorder in the Oxygen atoms. The chloroform molecule with an occupation of 1/4 is disordered in four orientations along a 4-fold rotation axis. The structure obtained is of good quality (no A- or B-alerts) and publishable with a R1 value of 5.44 %.

Cryst2

This compound crystallizes in the monoclinic space $P2_1$/n with half metal-complex molecule in the asymmetric unit showing Ci-symmetry. Additionally, the asymmetric

---

[29] Data collection with APEX II version v2013.4-1. Bruker (2007). Bruker AXS Inc., Madison, Wisconsin, USA.

[30] Data reduction with Bruker SAINT version V8.30c. Bruker (2007). Bruker AXS Inc., Madison, Wisconsin, USA.

[31] SADABS: V2012/1 Bruker (2001). Bruker AXS Inc., Madison, Wisconsin, USA. Blessing, Acta Cryst. **1995**, A51, 33.

[32] SHELXT; V2014/4 (Sheldrick 2014). Sheldrick, G.M. *Acta Cryst*. **2015**, A71, 3.

[33] SHELXle; C.B. Huebschle, G.M. Sheldrick & B. Dittrich; J. Appl. Cryst. **2011**, *44*, 1281.

[34] SHELXL; SHELXL-2014/7 (Sheldrick 2014). Sheldrick, G.M. *Acta Cryst*. **2015**, C71, 3.

UNIVERSITAT ROVIRA I VIRGILI
UNCOVERING THE MECHANISTIC SCENARIOS OF NUCLEOPHILIC COUPLINGS IN CP*CO SYSTEMS
Sara López Resano

unit contains a disordered dichloromethane molecule (ratio 63:37). The central core of the metal-complex is formed by a Co_4F_6 cluster surrounded by two ligand molecules (without flour atom at the nitrogen atom) and two Cp* molecules, all coordinated to the cobalt atoms. One of the benzene rings at the ligand is disordered in two orientations with a ratio of 91:09. At the central nitrogen atom of the ligand no electron densities were detected, thus no hydrogen atoms could be localized. The structure of **cryst2** is of excellent quality (no A- or B-alerts) and publishable with a R1 value of 2.84 %.

NMR

Variable temperature NMR

In order to gain more information about the paramagnetic species we performed some variable temperature ^{1}H and ^{19}F NMR. We added the Co(III) complex (4.26 mg, 0.01 mmol) and the corresponding oxidant (0.02 mmol) under Ar, and cooled down the NMR tube to – 75 ºC, then we added the DCM under Ar, to make sure that the reaction does not start. Then the tube was brought to the NMR and after careful mixing was measured, starting at 233 K. Two spectra were done at each temperature, one just when the desired temperature was reached and the next one after 10 min at the corresponding temperature. We repeated the reaction, and the same procedure to obtain the ^{19}F NMR of the reactions, in this case only four temperatures were used: 253, 263, 273 and 293 K.

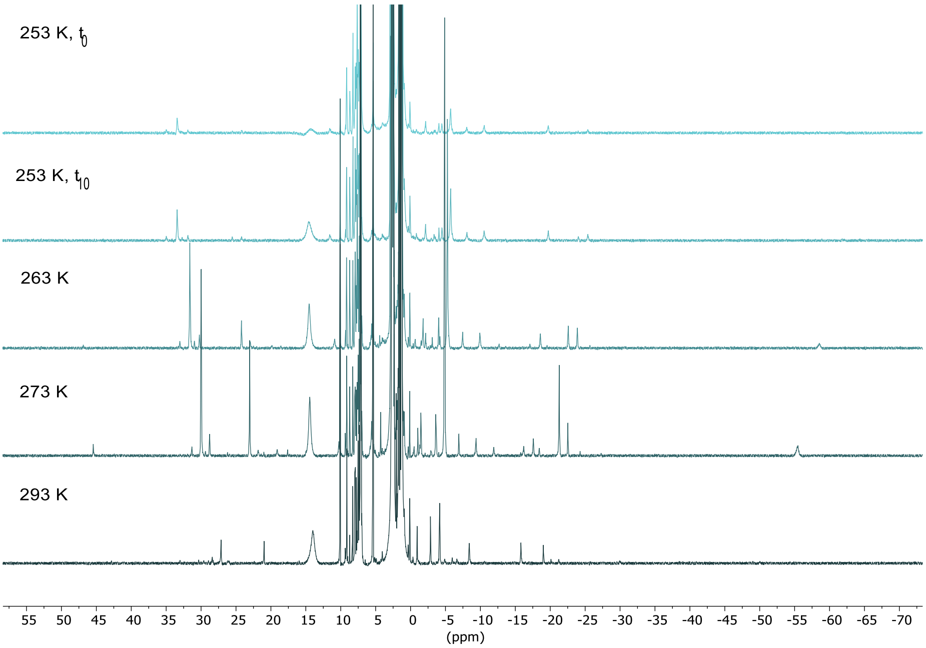

Figure 3.20 Paramagnetic region of the ^{1}H VT-NMR of the reaction with NFTPT.

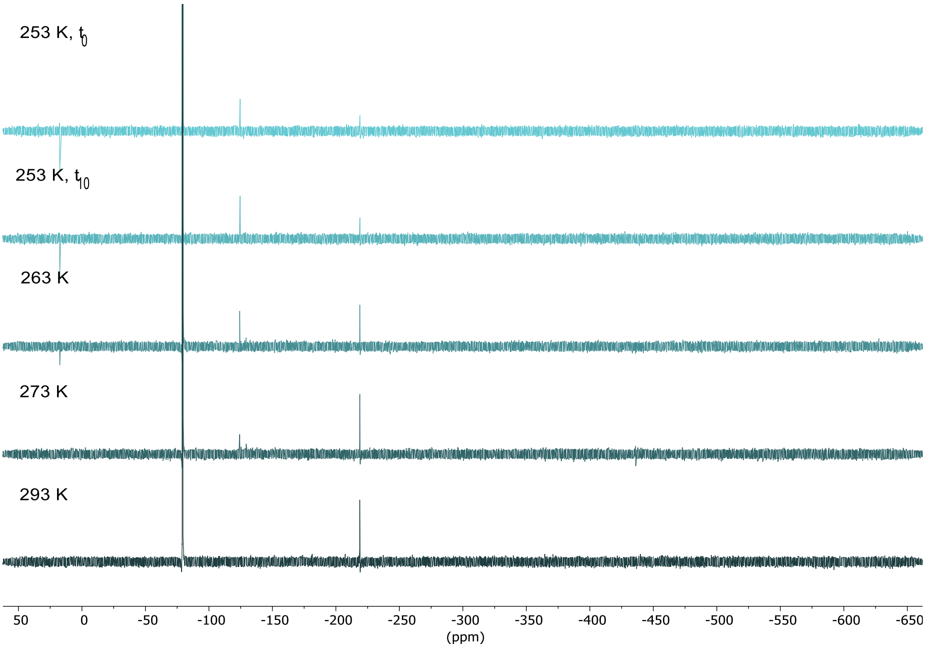

Figure 3.21 ^{19}F VT-NMR of the reaction with NFTPT.

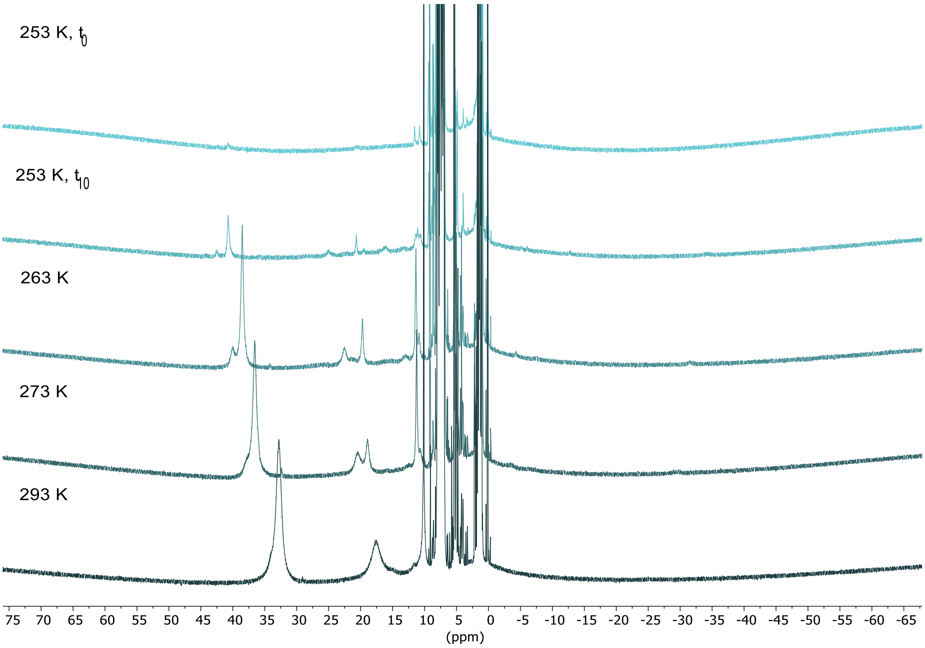

Figure 3.22 Paramagnetic region of the ^{1}H VT-NMR of the reaction with NFSI.

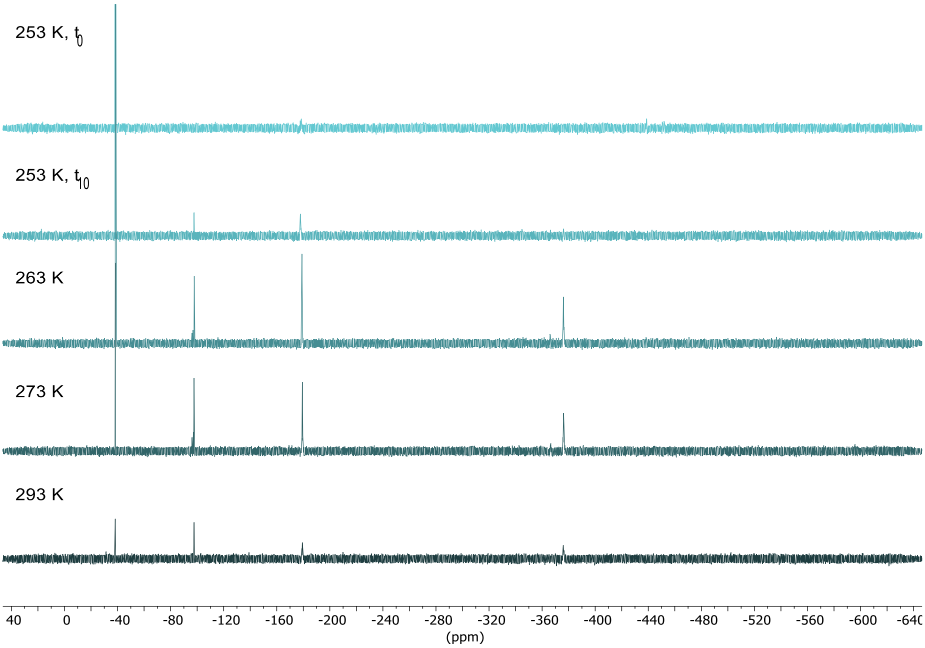

Figure 3.23 ^{19}F VT-NMR of the reaction with NFSI.

To investigate the reversibility of the paramagnetic species formation, we conducted a ^1H variable temperature NMR experiment.[35] The experiment involved starting at a low temperature of 233 K, increasing it to 263 K, then lowering it again to 233 K and finally raising the temperature to 263 K. At low temperatures, some small signals appeared at negative chemical shifts, which decreased at higher temperatures, suggesting some degree of reversibility. However, it is difficult to interpret these signals as they may correspond to intermediate species due to the ongoing reaction. A similar phenomenon was observed with the two small signals around 22 ppm. The signals between 35-45 ppm were challenging to interpret due to the progress of the reaction and the significant increase in the signal over time.

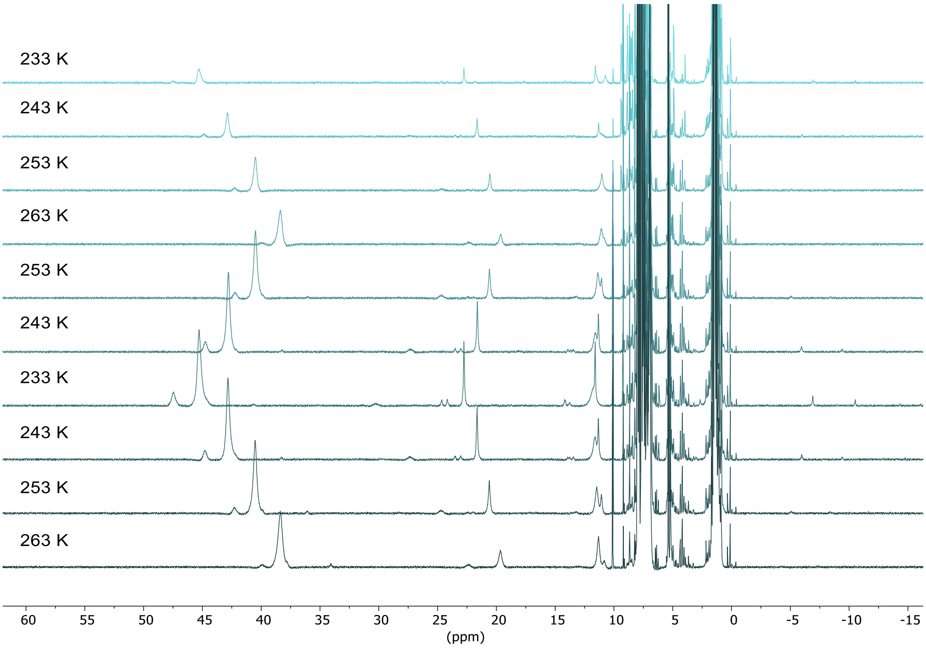

Figure 3.24 ^1H VT-NMR of the reaction with NFSI to check the reversibility of a reaction involving the paramagnetic species.

In the case of the reaction with NFTPT we only observed the increase of the paramagnetic signals over time.

---

[35] The VT-NMR with the NFTPT oxidant is in the experimental appendix.

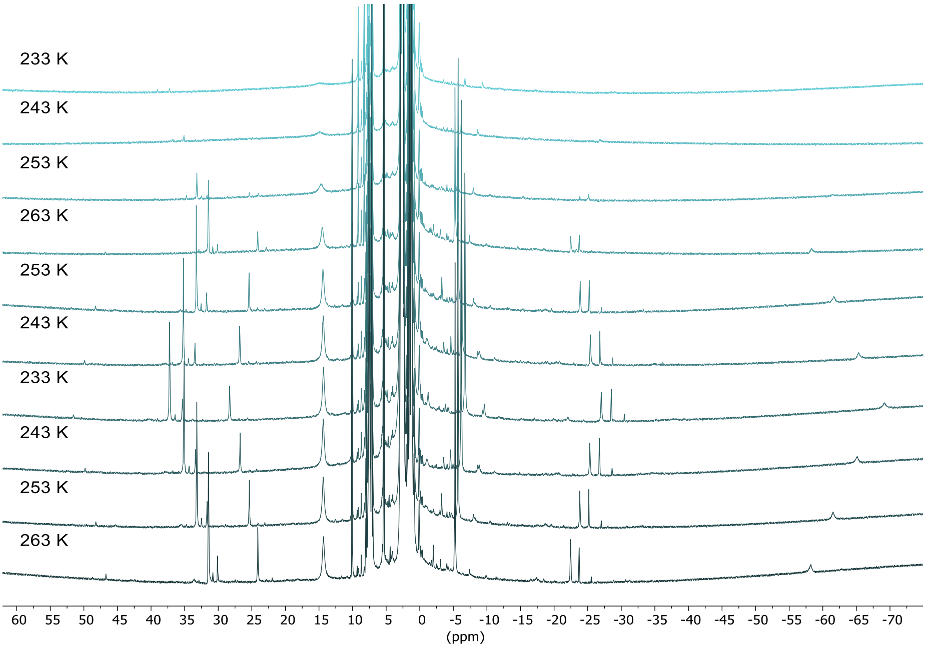

Figure 3.25 ^{1}H VT-NMR of the reaction with NFTPT (**ox3**) to check the reversibility of a reaction involving the paramagnetic species.

Monitoring the reactions at 253 K

We added the Co(III) complex (4.26 mg, 0.01 mmol) and the corresponding oxidant (0.02 mmol) under Ar, and cooled down the NMR tube to – 75 ºC, then we added the DCM under Ar, to make sure that the reaction does not start. Then the tube was brought to the NMR and after careful mixing was measured, starting at 253 K, ^{1}H, ^{1}H-paramagnetic and ^{19}F NMR spectra were taken every 10 min.

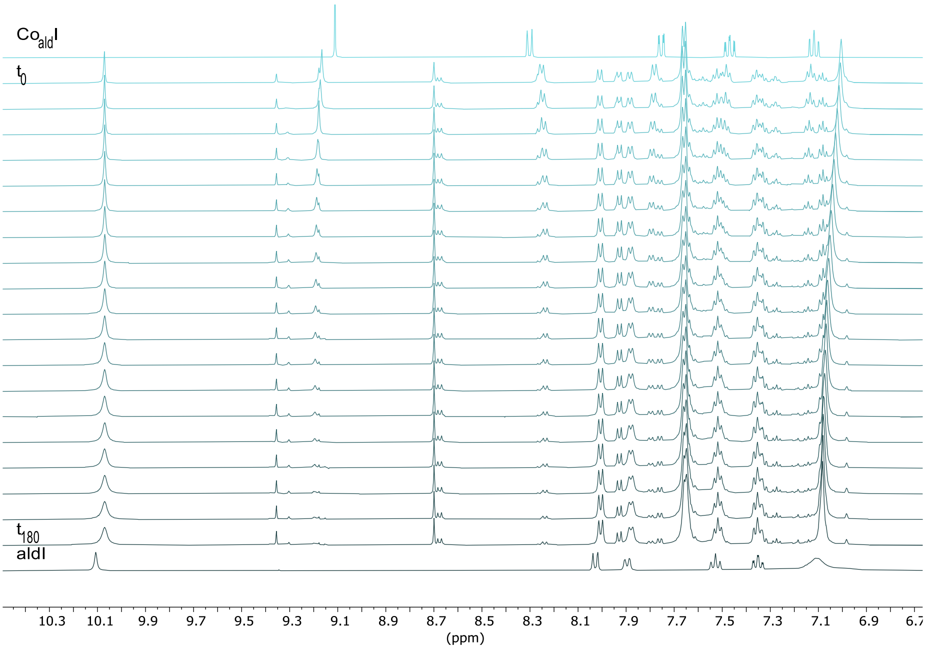

Figure 3.26 Aromatic region of ^{1}H NMR, of the **Co$_{ald}$I** and NFTPT reaction monitoring over 3h.

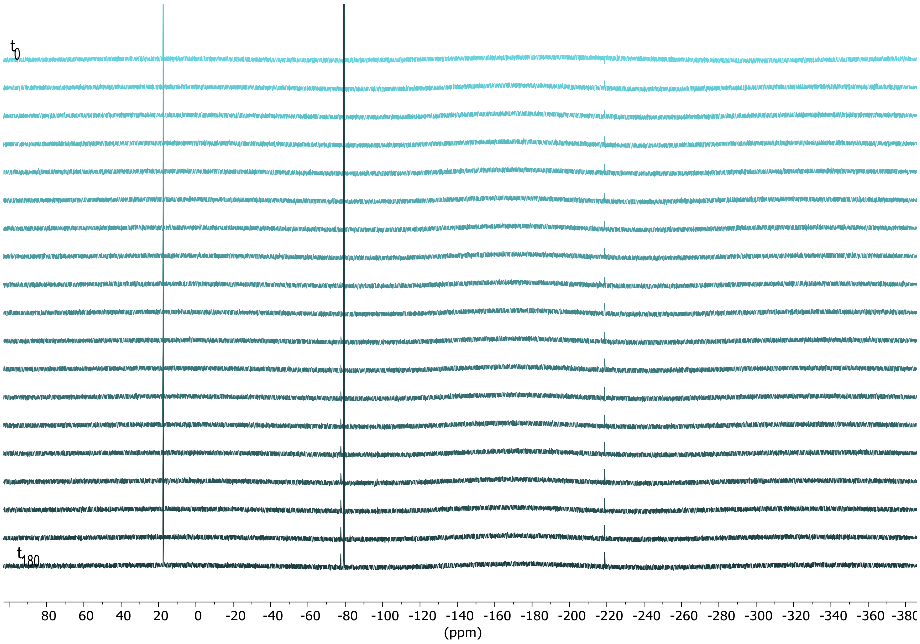

Figure 3.27 ^{19}F NMR, of the **Co$_{ald}$I** and NFTPT reaction monitoring over 3h.

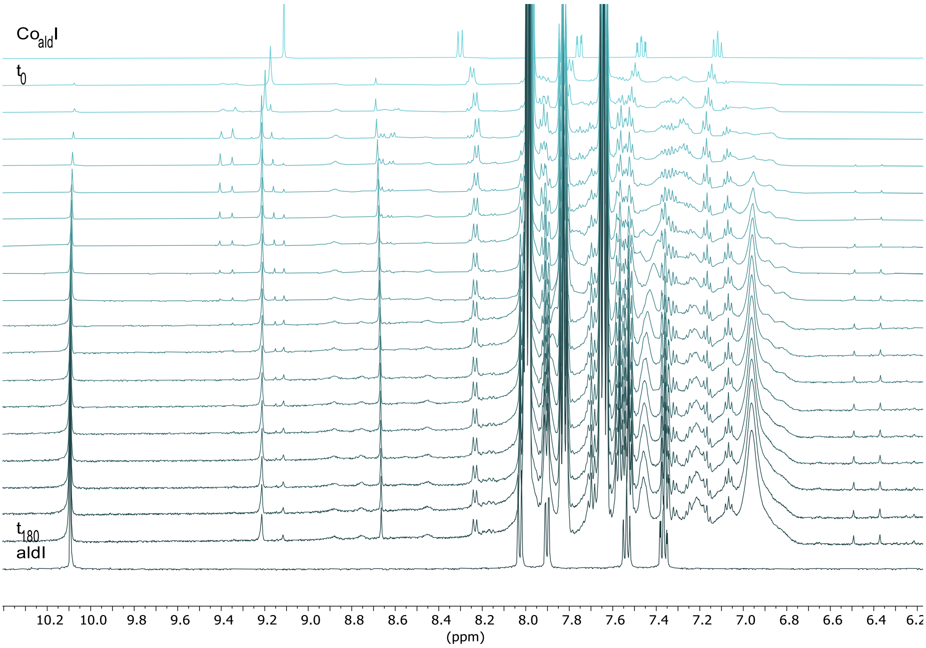

Figure 3.28 Aromatic region of ^{1}H NMR, of the **Co$_{ald}$I** and NFSI reaction monitoring over 3h.

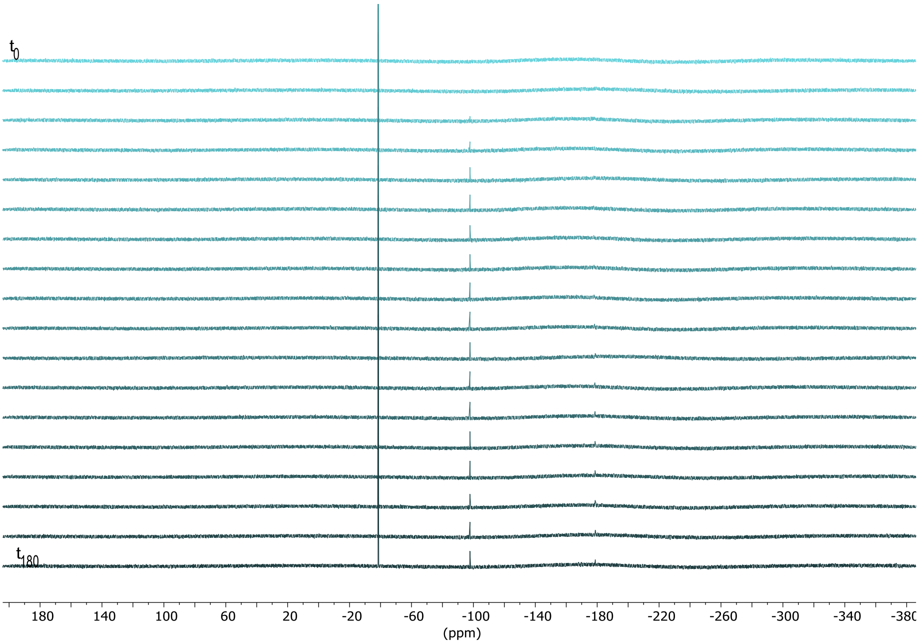

Figure 3.29 ^{19}F NMR, of the **Co$_{ald}$I** and NFSI reaction monitoring over 3h.

2D experiments

We added the Co(III) complex (4.26 mg, 0.01 mmol) and the corresponding oxidant (0.02 mmol) under Ar, and cooled down the NMR tube to – 75 ºC, then we added the DCM under Ar, to make sure that the reaction does not start. Then the tube was brought to the NMR and after careful mixing was measured at 253 K. The acquisition parameters for each spectrum are shown in the text on the right of the spectra.

Oxidant: NFSI

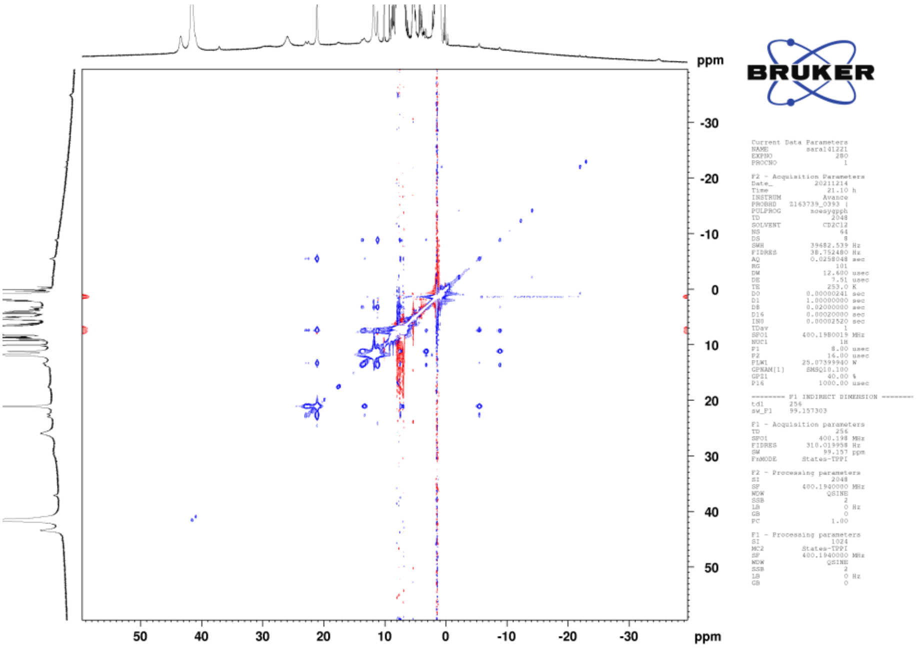

```
Current Data Parameters
NAME          sara141221
EXPNO                280
PROCNO                 1

F2 - Acquisition Parameters
Date_           20211214
Time               21.10 h
INSTRUM           Avance
PROBHD   Z163739_0393 (
PULPROG        noesygpph
TD                  2048
SOLVENT           CD2Cl2
NS                    64
DS                     8
SWH            39682.539 Hz
FIDRES         38.752480 Hz
AQ             0.0258048 sec
RG                   101
DW                12.600 usec
DE                  7.51 usec
TE                 253.0 K
D0            0.00000241 sec
D1            1.00000000 sec
D8            0.02000000 sec
D16           0.00020000 sec
IN0           0.00002520 sec
TDav                   1
SFO1         400.1980019 MHz
NUC1                  1H
P1                  8.00 usec
P2                 16.00 usec
PLW1         25.07399940 W
GPNAM[1]      SMSQ10.100
GPZ1               40.00 %
P16              1000.00 usec

======== F1 INDIRECT DIMENSION ========
td1        256
sw_F1      99.157303

F1 - Acquisition parameters
TD                   256
SFO1             400.198 MHz
FIDRES        310.019958 Hz
SW                99.157 ppm
FnMODE       States-TPPI

F2 - Processing parameters
SI                  2048
SF           400.1940000 MHz
WDW                QSINE
SSB                    2
LB                     0 Hz
GB                     0
PC                  1.00

F1 - Processing parameters
SI                  1024
MC2          States-TPPI
SF           400.1940000 MHz
WDW                QSINE
SSB                    2
LB                     0 Hz
GB                     0
```

Figure 3.30 ^{1}H-^{1}H NOESY of the reaction between **Co$_{ald}$I** and NFSI at 253K.

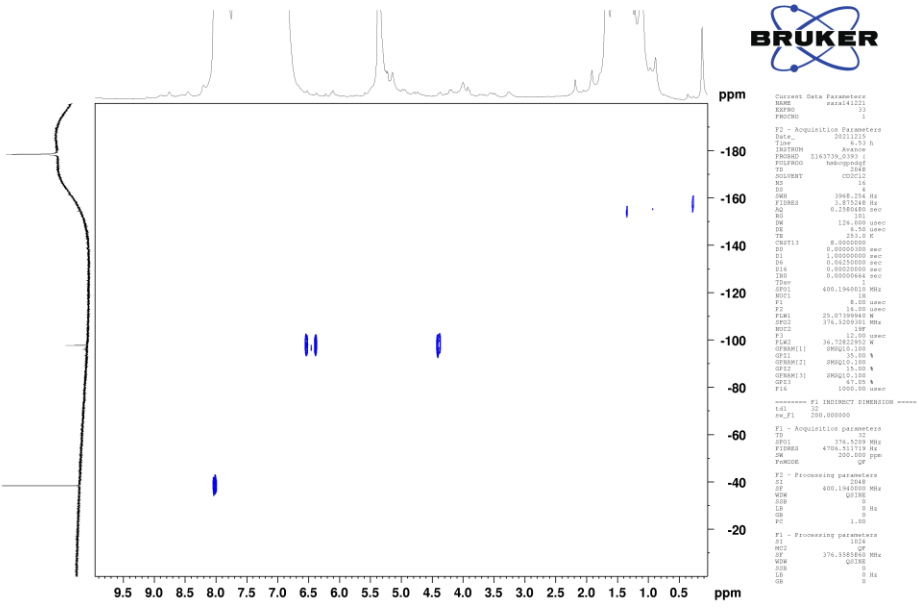

Figure 3.31 ^{1}H-^{19}F HMBC of the reaction between **Co$_{\mathbf{ald}}$I** and NFSI at 253K.

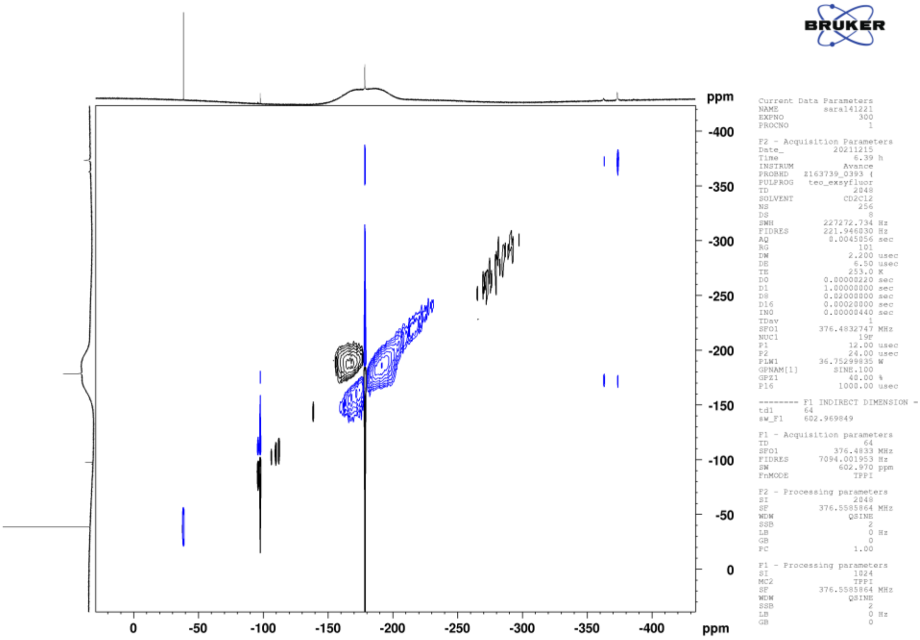

Figure 3.32 ^{19}F-^{19}F EXSY NMR of the reaction between **Co$_{\mathbf{ald}}$I** and NFSI at 253K.

*Oxidant: NFTPT (**ox3**)*

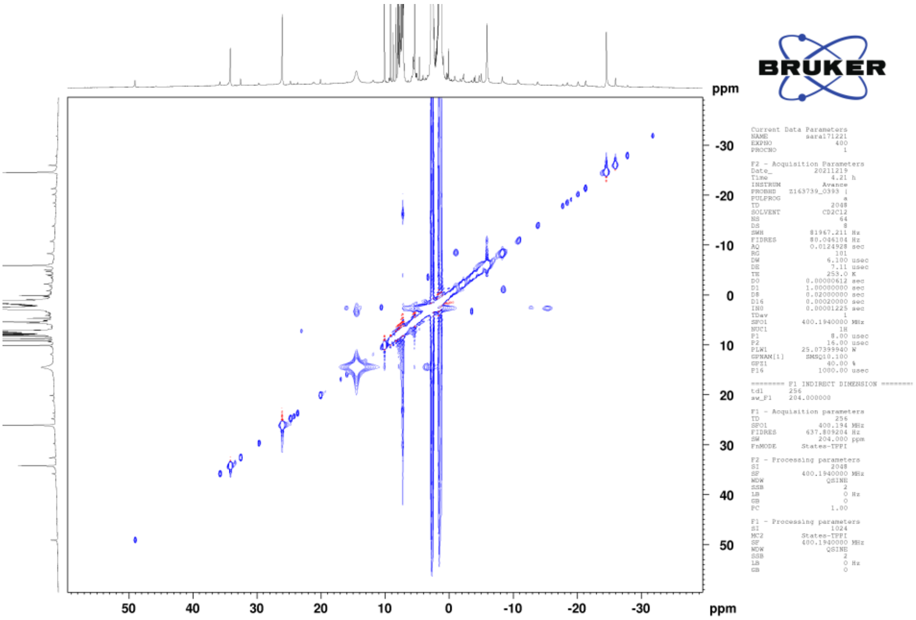

Figure 3.33 ^{1}H-^{1}H NOESY of the reaction between **Co**$_{\text{ald}}$**I** and NFTPT at 253K.

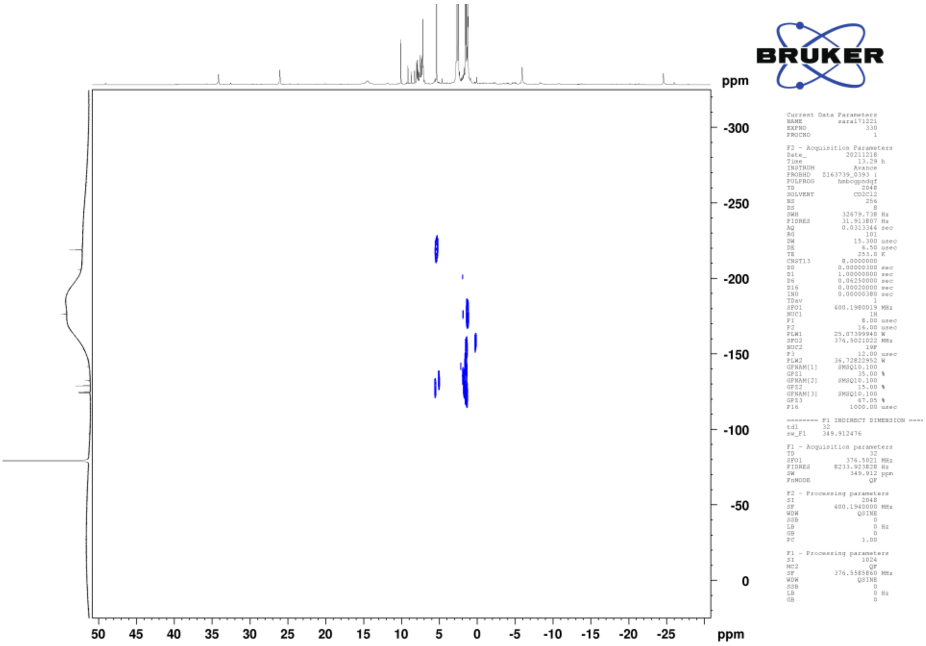

Figure 3.34 ^{1}H-^{19}F HMBC of the reaction between **Co**$_{\text{ald}}$**I** and NFTPT at 253K.

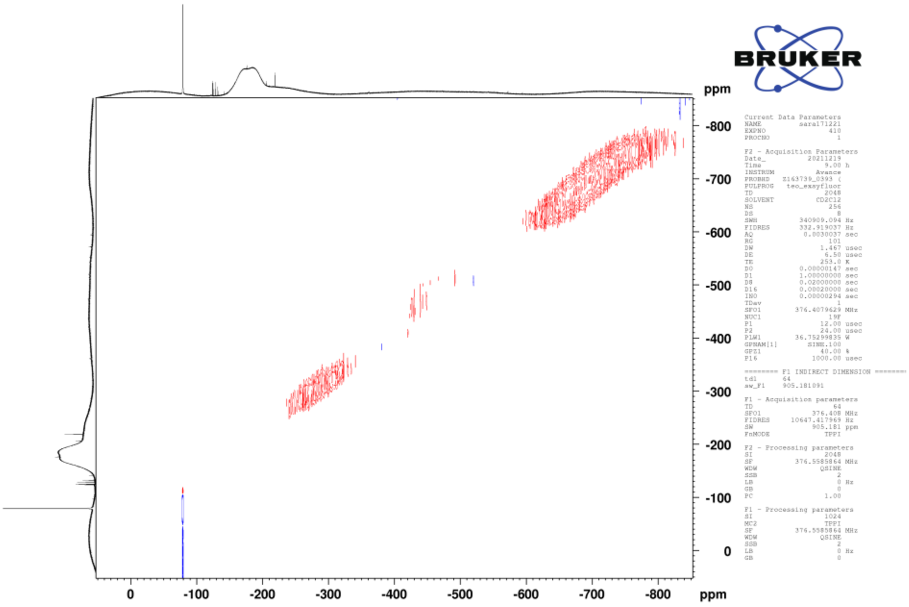

Figure 3.35 ^{19}F-^{19}F EXSY NMR of the reaction between **Co$_{ald}$I** and NFTPT at 253K.

Electron Paramagnetic Resonance (EPR) experiments

The spectral data was collected with the following spectrometer settings: microwave frequency = 9.38e^{9}; microwave power = 0.5606 mW; center field = 3200 G, sweep width = 6000 G, sweep time = 60 s, modulation frequency = 100 KHz, modulation amplitude = 4 G, power attenuation = 25 dB, time constant = 10.24 ms. Individual EPR tubes were filled with the sample and placed at the same position of the resonant cavity for EPR spectral acquisition.

General procedure

A solution of **Co$_{ald}$I** (0.01 mmol) and each oxidant (0.02 mmol) in the corresponding solvent was added to an EPR tube at the corresponding temperature for the selected time, before measuring it by EPR at 77 K or 10 K.

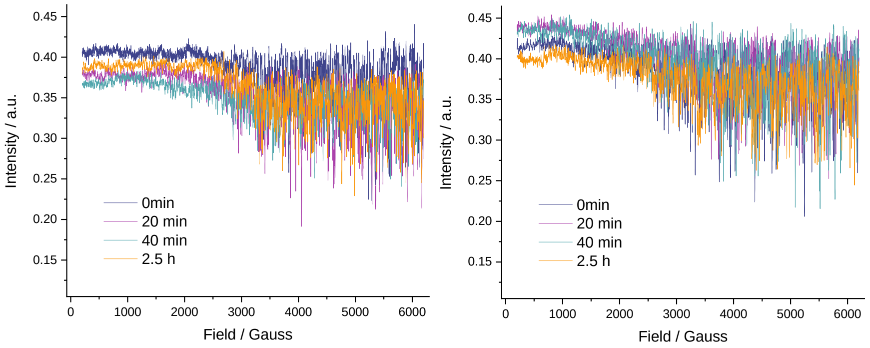

Figure 3.36 EPR spectra at 77 K in THF at different reaction times. Left reaction with NFTPT and right reaction with NFSI.

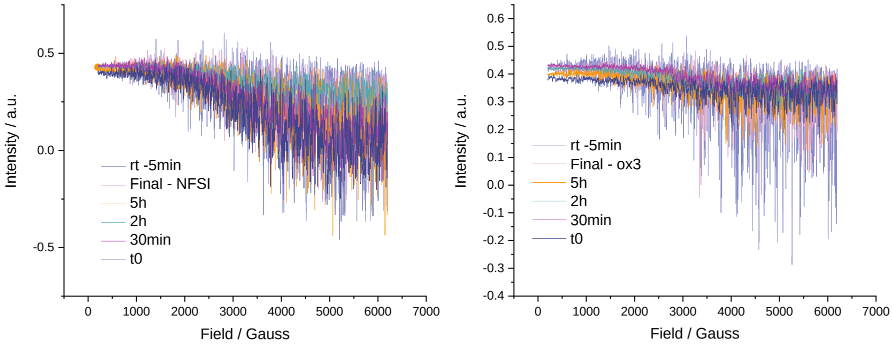

Figure 3.37 EPR spectra at 77 K in DCM at different reaction times. Left reaction with NFTPT and right reaction with NFSI. Reaction done at 253 K.

Mass spectroscopic studies

Mass spectrometry is a powerful analytical tool that can be used to detect and identify intermediates in chemical reactions. It is particularly useful for detecting reactive intermediates that are involved in fast or complex reactions.

However, in our case we did not observe the desired intermediates in any case, we observed the starting material, **Co$_{\text{ald}}$I** and the cobalt complex with the I ion dissociated.

A solution of **Co$_{\text{ald}}$I** (0.01 mmol) and each oxidant (0.02 mmol) in the corresponding solvent was added to a vial with 0.4 mL of DCM, inside the glovebox. After 5 min the reaction was diluted to 5 μg/mL and brought to the MicroTOF II mass spectroscopy machine. The sample was injected under Ar and ESI + ionization mode was used.

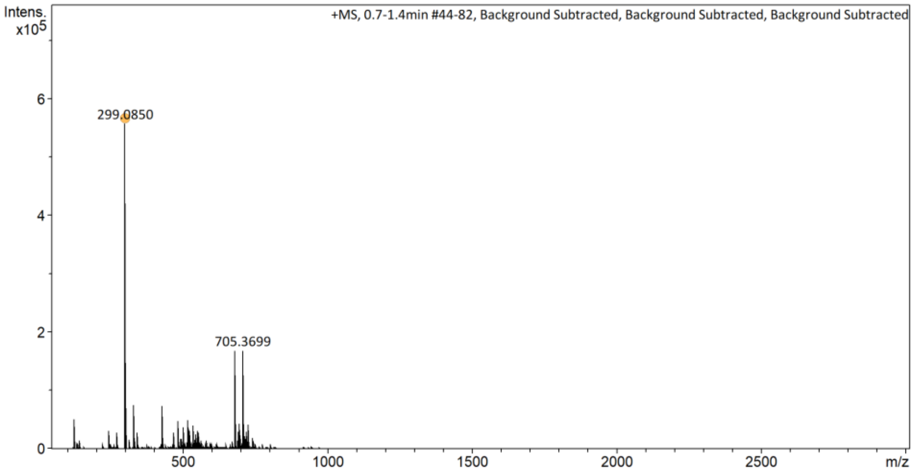

Figure 3.38 ESI-MS full spectra of the reaction of **Co$_{ald}$I** and NFTPT.

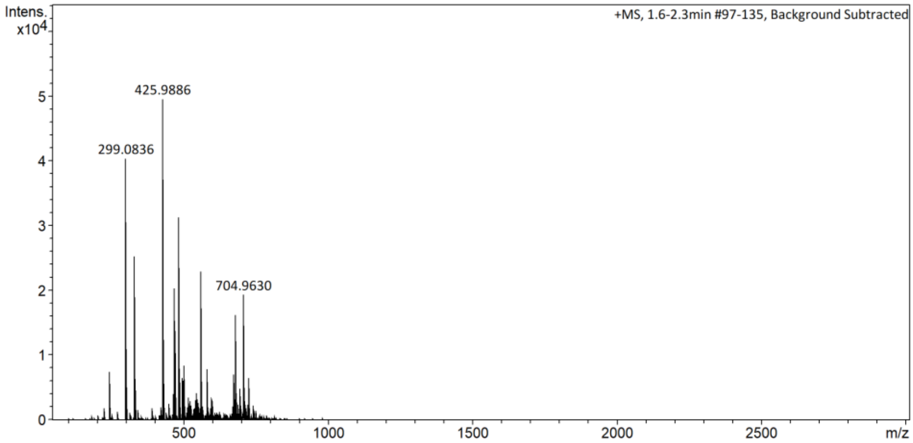

Figure 3.39 ESI-MS full spectra of the reaction of **Co$_{ald}$I** and NFSI.

Kinetic experiments

We added the Co(III) complex and the corresponding oxidant in different amounts to fit he corresponding concentrations under Ar, and cooled down the NMR tube to – 75 ºC, then we added 0.4 mL of DCM-d_2 under Ar, to make sure that the reaction does not start. Then the tube was brought to the NMR and after careful mixing was measured as soon as possible at 273 K, taking the time when the first spectra was measured. A ^{1}H NMR spectra was taken every 60s. By inputting the collected data into GEPASI, we calculated the reaction rate for each system.

Table 3.2 Data used to calculate the order in Co with NFTPT as oxidant. Initial concentration of NFTPT (constant) and **Co$_{ald}$I** with the corresponding calculated rates from GEPASI.

$[NFTPT]_0$	$[Co]_0$	r_1	$\ln [Co]_0$	$\ln r_1$
0.04	0.00483	0.02416	-5.33291	-3.72306
0.04	0.007644	0.02894	-4.87389	-3.54253
0.04	0.01	0.03265	-4.60517	-3.42191
0.04	0.015	0.03769	-4.19971	-3.27836
0.04	0.02	0.04659	-3.91202	-3.06637

Table 3.3 Data used to calculate the order in Co with NFSI as oxidant. Initial concentration of NFSI (constant) and **Co$_{ald}$I** with the corresponding calculated rates from GEPASI.

$[NFTPT]_0$	$[Co]_0$	r_1	$\ln [Co]_0$	$\ln r_1$
0.04	0.004783	0.002896	-5.34266	-5.84442
0.04	0.009988	0.007196	-4.60634	-4.93423
0.04	0.014959	0.01209	-4.20244	-4.41538
0.04	0.019977	0.01796	-3.9132	-4.01961
0.04	0.024947	0.01865	-3.69099	-3.98191

Table 3.4 Data used to calculate the order in NFSI. Initial concentration of NFTPT and **Co$_{ald}$I** (constant) with the corresponding calculated rates from GEPASI.

$[Co]_0$	$[NFSI]_0$	r_1	$\ln [Co]_0$	$\ln r_1$
0.02	0.03488	0.01496	-3.35562	-4.20237
0.02	0.04249	0.01147	-3.15826	-4.46802
0.02	0.06026	0.009347	-2.80908	-4.67269
0.02	0.07992	0.006981	-2.52668	-4.96456

UNIVERSITAT ROVIRA I VIRGILI
UNCOVERING THE MECHANISTIC SCENARIOS OF NUCLEOPHILIC COUPLINGS IN CP*CO SYSTEMS
Sara López Resano

3.4.2. Computational appendix

Computational details

DFT calculations were performed using the Gaussian09[36] or Gaussian16[37] package with the M06-D3[38] (where D3 stands for GD3[39] empirical dispersion) functional. For the initial studies, geometry optimizations were carried out in solution without symmetry restrictions with the LANL2DZ[40] basis set, along with its associated ECP[41] was employed for Co and I and 6-31+G(d)[42] for the remaining atoms. Then to continue, as we had problems with Gaussian09 to calculate the dimers we change to Gaussian16 and in order to reduce the computational cost we also removed the diffuse functions. Finally, to do the method benchmark we used the first basis set combination: LANL2DZ and the corresponding ECP for Co and I, and 6-31+G(d) for the remaining atoms. The single point calculations were calculated with a larger basis set, LANL2TZ

---

[36] Gaussian 09, Revision D.01, M. J. Frisch, G. W. Trucks, H. B. Schlegel, G. E. Scuseria, M. A. Robb, J. R. Cheeseman, G. Scalmani, V. Barone, B. Mennucci, G. A. Petersson, H. Nakatsuji, M. Caricato, X. Li, H. P. Hratchian, A. F. Izmaylov, J. Bloino, G. Zheng, J. L. Sonnenberg, M. Hada, M. Ehara, K. Toyota, R. Fukuda, J. Hasegawa, M. Ishida, T. Nakajima, Y. Honda, O. Kitao, H. Nakai, T. Vreven, J. A. Montgomery, Jr., J. E. Peralta, F. Ogliaro, M. Bearpark, J. J. Heyd, E. Brothers, K. N. Kudin, V. N. Staroverov, T. Keith, R. Kobayashi, J. Normand, K. Raghavachari, A. Rendell, J. C. Burant, S. S. Iyengar, J. Tomasi, M. Cossi, N. Rega, J. M. Millam, M. Klene, J. E. Knox, J. B. Cross, V. Bakken, C. Adamo, J. Jaramillo, R. Gomperts, R. E. Stratmann, O. Yazyev, A. J. Austin, R. Cammi, C. Pomelli, J. W. Ochterski, R. L. Martin, K. Morokuma, V. G. Zakrzewski, G. A. Voth, P. Salvador, J. J. Dannenberg, S. Dapprich, A. D. Daniels, O. Farkas, J. B. Foresman, J. V. Ortiz, J. Cioslowski, D. J. Fox, Gaussian, Inc., Wallingford CT, 2013.

[37] Gaussian 16, Revision C.01, M. J. Frisch, G. W. Trucks, H. B. Schlegel, G. E. Scuseria, M. A. Robb, J. R. Cheeseman, G. Scalmani, V. Barone, G. A. Petersson, H. Nakatsuji, X. Li, M. Caricato, A. V. Marenich, J. Bloino, B. G. Janesko, R. Gomperts, B. Mennucci, H. P. Hratchian, J. V. Ortiz, A. F. Izmaylov, J. L. Sonnenberg, D. Williams-Young, F. Ding, F. Lipparini, F. Egidi, J. Goings, B. Peng, A. Petrone, T. Henderson, D. Ranasinghe, V. G. Zakrzewski, J. Gao, N. Rega, G. Zheng, W. Liang, M. Hada, M. Ehara, K. Toyota, R. Fukuda, J. Hasegawa, M. Ishida, T. Nakajima, Y. Honda, O. Kitao, H. Nakai, T. Vreven, K. Throssell, J. A. Montgomery, Jr., J. E. Peralta, F. Ogliaro, M. J. Bearpark, J. J. Heyd, E. N. Brothers, K. N. Kudin, V. N. Staroverov, T. A. Keith, R. Kobayashi, J. Normand, K. Raghavachari, A. P. Rendell, J. C. Burant, S. S. Iyengar, J. Tomasi, M. Cossi, J. M. Millam, M. Klene, C. Adamo, R. Cammi, J. W. Ochterski, R. L. Martin, K. Morokuma, O. Farkas, J. B. Foresman, and D. J. Fox, Gaussian, Inc., Wallingford CT, 2016.

[38] Y. Zhao, D. G. Truhlar, *Theor. Chem. Account.* **2008**, *120*, 215.

[39] S. Grimme, *J. Comput. Chem.* **2006**, *27*, 1787.

[40] LANL2DZ T. H. Dunning Jr. and P. J. Hay, in *Modern Theoretical Chemistry*, Ed. H. F. Schaefer III, Vol. 3 (Plenum, New York, **1977**) 1.

[41] J. Hay, W. R. Wadt, *J. Chem. Phys.* **1985**, *82*, 270–283.

[42] a) W. J. Hehre, R. Ditchfield, J. A. Pople, *J. Chem. Phys.* **1972**, *56*, 2257. b) J. D. Dill, J. A. Pople, *J. Chem. Phys.* **1975**, *62*, 2921. c) M. M. Francl, W. J. Petro, W. J. Hehre, J. S. Binkley, M. S. Gordon, D. J. DeFrees, A. J. Pople, *J. Chem. Phys.* **1982**, *77*, 3654.

plus pseudopotential for cobalt and iodine[43] and 6-311++G(d,p)[44] for the remaining atoms. Implicit solvent was modeled through the SMD method.[45] Calculations were carried out in DCM (ε = 8.93). For all calculations, vibrational frequency calculations were computed to establish the nature of all stationary points (zero imaginary frequencies for minima and one for transition states). All the calculations have been carried out at 298.15K and 1 atm.

---

[43] L. E. Roy, P. J. Hay, R. L. Martin, *J. Chem. Theory Comput*. **2008**, *4*, 1029.

[44] a) R. Krishnan, J. S. Binkley, R. Seeger, J. A. Pople, *J. Chem. Phys.* **1980**, *72*, 650–654. b) A. D. McLean, G. S. Chandler, *J. Chem. Phys.* **1980**, *72*, 5639–5648.

[45] S. A. V. Marenich, C. J. Cramer, D. G. Truhlar, *J. Phys. Chem. B* **2009**, *113*, 6378.

UNIVERSITAT ROVIRA I VIRGILI
UNCOVERING THE MECHANISTIC SCENARIOS OF NUCLEOPHILIC COUPLINGS IN CP*CO SYSTEMS
Sara López Resano

*Chapter 4. Reactivity Studies on C–X and C–C bond forming reactions from cyclometalated Cp*Co complexes*

UNIVERSITAT ROVIRA I VIRGILI
UNCOVERING THE MECHANISTIC SCENARIOS OF NUCLEOPHILIC COUPLINGS IN CP*CO SYSTEMS
Sara López Resano

4.1. Introduction

In our previous chapters, we have highlighted the limited number of investigations into nucleophilic couplings with Cp*Co systems. Notably, we have established that the formation of C–SCF3 and C–I bonds requires oxidatively induced reductive elimination. These discoveries have sparked our curiosity and motivated us to delve deeper into the fundamental principles governing these reactions.

To date, there has been a lack of systematic investigation into the role of the directing group in the reductive elimination step of nucleophilic coupling reactions involving Cp*Co complexes. Understanding the directing group's and nucleophile's impact is of paramount importance for gaining insights into the underlying factors that govern reaction selectivity and efficiency.

4.2. Objectives

In order to expand the scope of nucleophiles that can serve as coupling partners in Cp*Co-catalyzed C–H functionalization reactions, it is necessary to gain a fundamental understanding of the relative reactivity and mechanisms of reductive eliminations mediated by Cp*Co complexes. Thus, this chapter focuses on the following primary objectives:

- Synthesis and isolation of well-defined cobaltacycles containing different nucleophilic moieties and/or directing groups
- Experimental reactivity studies towards catalytically relevant carbon–heteroatom and carbon–carbon bond-forming reactions under thermal or oxidative reaction conditions (electrochemically or in the presence of chemical oxidants)
- Computational investigation on the distinct behaviors exhibited by the targeted Cp*Co-based systems.

By achieving these objectives, we aim to gain a comprehensive understanding of the underlying mechanisms that govern the reactions of Cp*Co(III) systems with nucleophiles, which can ultimately improve the development of more efficient catalytic processes, along with broadening the scope of reactions that can be performed with Cp*Co(III) catalysts.

4.3. *Results and Discussion*

4.3.1. Carbon–Heteroatom Couplings from metalacyclic Cp*Co-based systems

*Synthesis and characterization of Cp*Co^{III}(ald)X complexes*

In order to study the fundamental reactivity of Cp*Co^{III} compounds towards a wide variety of C–X bond-forming reactions, and inspired by the promising results detailed in Chapter 3, we targeted as model systems well-defined and isolable metalacyclic Cp*Co^{III} compounds of general structure **1$_{ald}$-X**, that contain the benzaldehyde fragment and different X-based nucleophiles (Figure 4.1).[1]

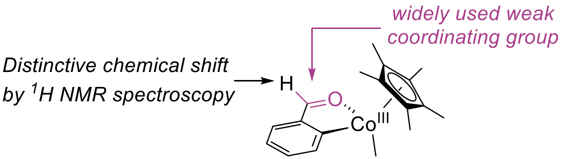

1$_{ald}$-X

Figure 4.1 General structure of the Cp*Co(III) complexes under study

To access these cobaltacycles, we followed two different synthetic routes. For X = Br, the complex was synthesized via a ligand-assisted oxidative addition of 2-bromobenzaldehyde to Cp*Co^{I}(VTMS)$_2$, following the procedure reported previously by our group (Scheme 4.1, top).[2] Attempts to synthesize the Co^{III}-Cl analogue via oxidative addition were unsuccessful.[2] Instead, **1$_{ald}$-Cl** was obtain in 78% isolated yield via metathesis by the treatment of **1$_{ald}$-I** with 3 equiv of AgCl in THF at room temperature for 4 days. A similar strategy was followed to access the corresponding cobaltacycles containing SCF$_3$, OTFA and OTf.[3] The reaction of **1$_{ald}$-I** with 1 equiv of the corresponding silver salt (AgSCF$_3$, AgOTFA or AgOTf) at room temperature for 1

---

[1] The synthesis and characterization of some of the targeted cobaltacycles belong to the MSc Thesis carried out in our group by Carlota Odena (unpublished results). My work in this chapter focused on the experimental and computational mechanistic study of the systems.

[2] S. Martínez de Salinas, J. Sanjosé-Orduna, C. Odena, S. Barranco, J. Benet-Buchholz, M. H. Pérez-Temprano, *Angew. Chem. Int. Ed.* **2020**, *59*, 6239–6243.

[3] Following the metathesis approach, we have been able to access the corresponding cobaltacycle containing OAc. However, due to its inherent instability, it has not been possible to isolate it. We have included their characterization in the experimental section, but we have not investigated their reactivity.

hour afforded the desired organometallic compounds in very good yields.[4] The complexes have been fully characterized by ^{1}H and ^{13}C NMR spectroscopy.

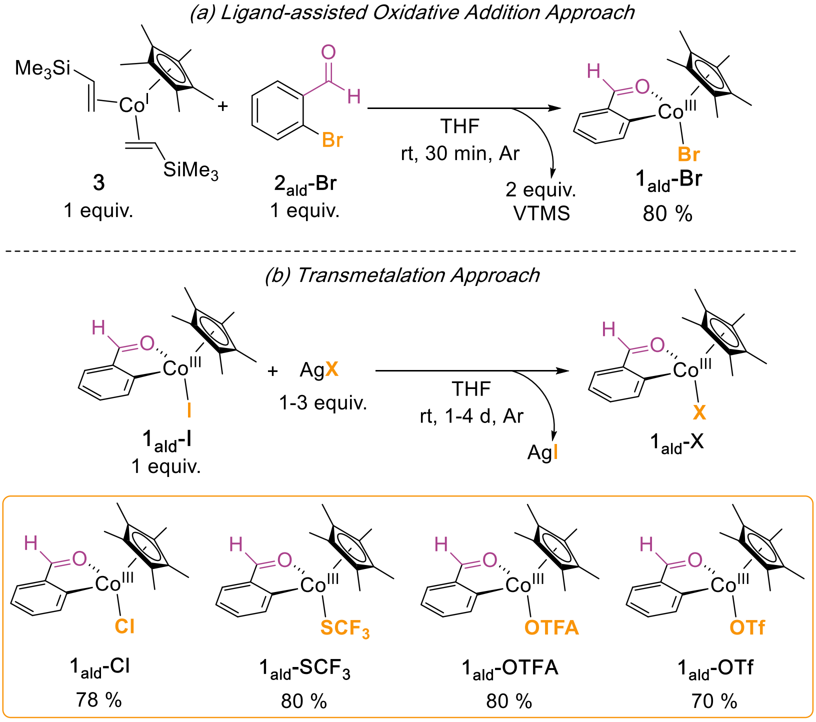

Scheme 4.1 Synthesis of $\mathbf{1}_{\mathbf{ald}}$-**X**.

---

[4] We have conducted preliminary attempts to synthesize cobaltacycles containing N-based moieties using AgNMeTs, $AgNTf_2$, or LiNHAc. However, any of these reactions afforded the desired organometallic compounds. Indeed, the reaction with $AgNTf_2$ afforded an unexpected outcome, a crystal structure where the triflimide anion is coordinated through the oxygen atom. See the experimental section for further details.

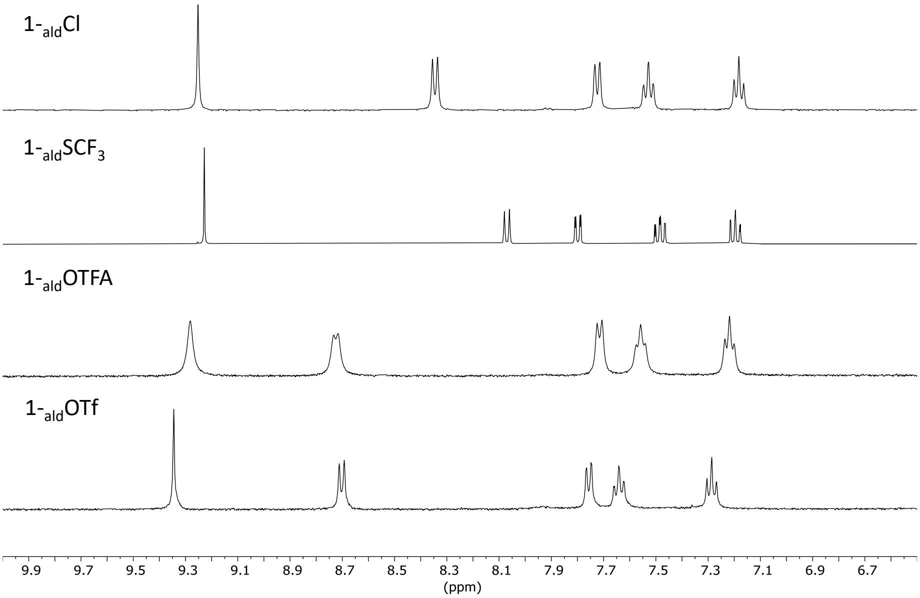

Figure 4.2 ^{1}H NMR of the aromatic region of the new **1$_{ald}$-X** complexes

X-ray quality crystals of **1$_{ald}$-Cl**, **1$_{ald}$-SCF$_3$** and **1$_{ald}$-OTFA** were grown at room temperature by liquid/liquid diffusion of n-hexane into a solution of the corresponding complex in CD_2Cl_2 (Figure 4.3). As previously observed for compound **1$_{ald}$-I** and **1$_{ald}$-Br**, the new cobaltacycles show a three-legged piano-stool geometry. As expected, the solid-state structures show different Co–X distances, as function of the nature of the nucleophilic fragment. Subtle variations are observed for the other selected values, yet without a clear trend.

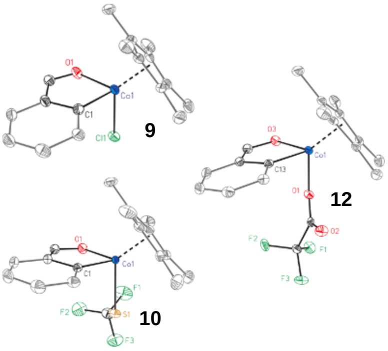

Selected distances [Å] / angle [deg]

X	Co–X	Co–C	Co–O	C–Co–X[b]
I (**5**)[a]	2.569	1.925	1.982	88.54
Br (**8**)[a]	2.393	1.938	1.981	89.63
Cl (**9**)	2.285	1.924	2.002	89.14
SCF_3 (**10**)	2.252	1.910	1.963	87.49
OTFA (**12**)	1.956	1.929	1.995	88.20

Figure 4.3 ORTEP structures of **1$_{ald}$-Cl**, **1$_{ald}$-SCF$_3$** and **1$_{ald}$-OTFA**. Thermal ellipsoids are drawn at 50 % probability, H atoms have been omitted for clarity. Selected bond distances in Å and angles in degrees for the shown structures. [a]From reference 2. [b]Angle between the carbon of the metallacycle, cobalt and the corresponding X moiety.

Mechanistic investigation on C–X bond-forming reactions

With the synthesis of a variety of metallyclic Cp*Co^{III}-X complexes in hand, we next evaluated whether these compounds are susceptible to participate in C–X bond-forming reactions. As in the previous chapters, we investigated two different scenarios: (i) direct bond formation from Cp*Co^{III} or (ii) oxidative induced reductive elimination reactions via 1- or 2-electron processes.

As observed in the previous chapters, compounds **1$_{ald}$-Br, 1$_{ald}$-Cl** and **1$_{ald}$-SCF$_3$** were inert to reductive elimination processes upon thermolysis in CD_2Cl_2 for 2 hours,[5] just observing traces of the corresponding protodemetalation products (Figure 4.4 and Figure 4.6). This is in accordance with the calculated activation barriers for the reductive elimination from **1$_{ald}$-Br, 1$_{ald}$-Cl** and **1$_{ald}$-SCF$_3$**, being 51.2, 53.8 and 34.7 kcal·mol^{-1}, respectively.[6] For **1$_{ald}$-Br** and **1$_{ald}$-Cl**, we also did not detected the direct reductive elimination event. Instead, we observed an unidentifiable complex mixture.

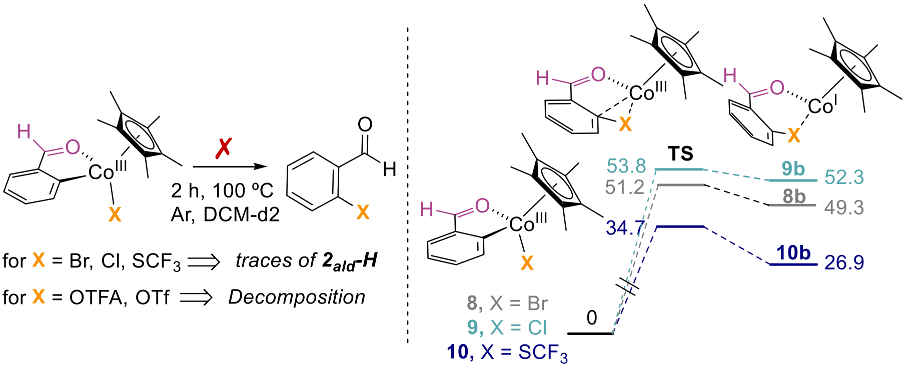

Scheme 4.2 Direct reductive elimination from Co(III)(Nuc) complexes,. Right: DFT calculation on **1$_{ald}$-Br, 1$_{ald}$-Cl** and **1$_{ald}$-SCF$_3$**. Energies are shown in kcal·mol^{-1}.

---

[5] First hour the reaction was heated at 75 ºC and the following hour the temperature was increased to 100 ºC.

[6] We have tried to calculate the barriers for **1$_{ald}$-OTFA** and **1$_{ald}$-OTf** without success.

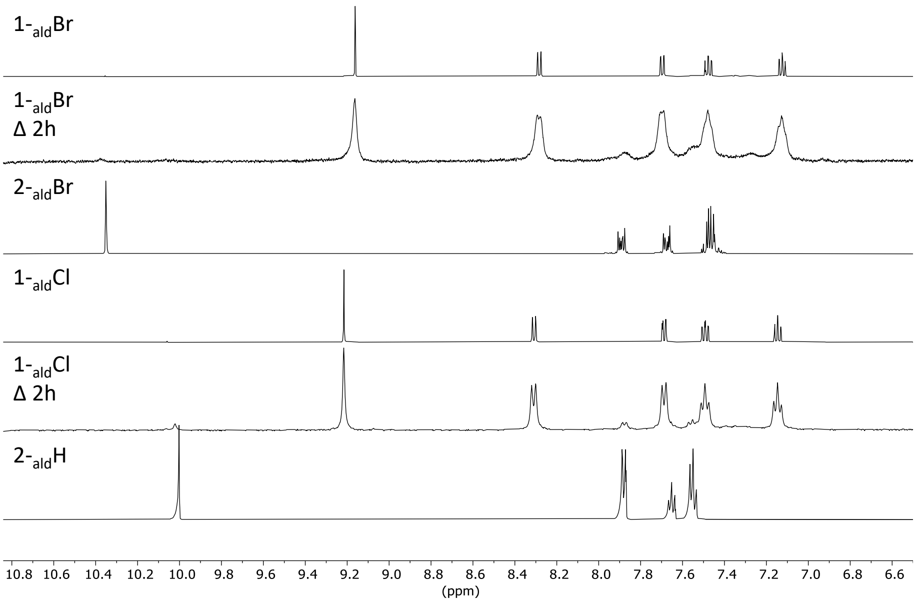

Figure 4.4 5 Aromatic region of ^{1}H NMR Spectra of the thermolysis of **1_{ald}-Br** and **1_{ald}-Cl**.

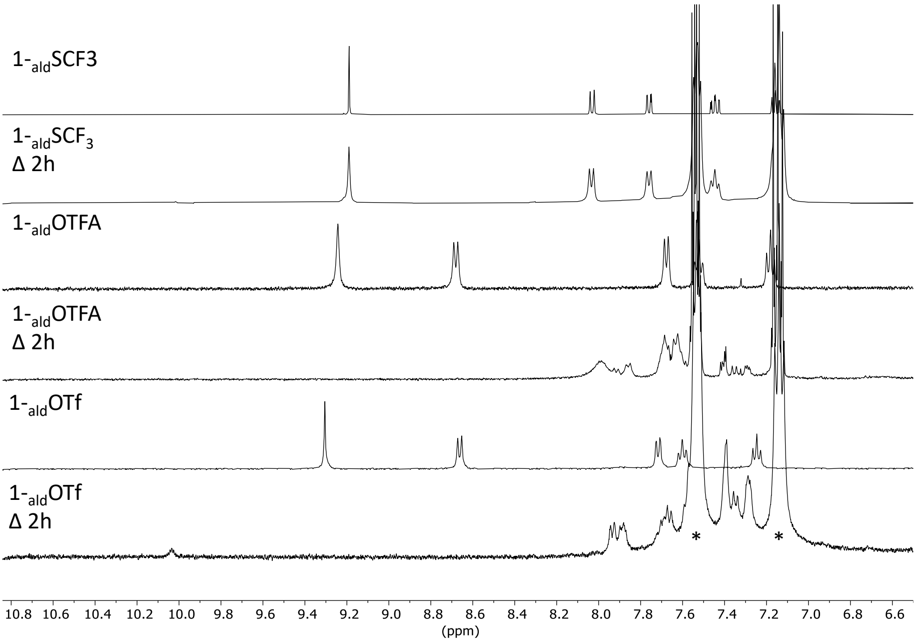

Figure 4.6 Aromatic region of ^{1}H NMR Spectra of the thermolysis of **1_{ald}-SCF$_3$** and **1_{ald}-OTFA** and **1_{ald}-OTf.** The IS is marked with asterisks.

In view of the lack of C–X reductive elimination products upon heating, we next carried out electrochemical analyses to further assess the accessibility to high-valent Co. Similarly, to the findings observed in Chapter 3 (page 107) with **1_{ald}-I**, the cyclic voltammograms for X = Br (**1_{ald}-Br**), Cl (**1_{ald}-Cl**) revealed a quasi-reversible oxidation process. Both complexes exhibited oxidation peaks at $E_{1/2}$ = 0.41 V and 0.40 V, respectively, that we assigned to the $Co^{III/}Co^{IV}$ couple. The observed oxidation peaks are slightly higher when compared to **1_{ald}-I**, which exhibited an oxidation wave at 0.36 V vs Fc/Fc^+. Significantly, the reduction peaks are detectable even at slower scan rates, indicating that the electrochemically formed Co^{IV} for **1_{ald}-Br** and **1_{ald}-Cl** are more stable than the one formed with **1_{ald}-I**.

For the chalcogen-based cobaltacycles, **1_{ald}-SCF$_3$** and **1_{ald}-OTf** exhibited a similar oxidation potential to **1_{ald}-Br** and **1_{ald}-CL**, featuring a quasi-reversible peak at 0.4 V vs Fc/Fc^+. However, the oxidation process of **1_{ald}-SCF$_3$** was found to be irreversible. In contrast, complex **1_{ald}-OTFA** displayed a more positive irreversible oxidation potential of 0.56 V vs Fc/Fc^+. This suggests that complex **1_{ald}-SCF$_3$** requires a higher energy input to undergo oxidation, indicating a less favorable electron transfer process compared to the other cobaltacycles under investigation. Notably, the irreversibility persisted even at higher scan rates, indicating a possible chemical reaction after the electron transfer.

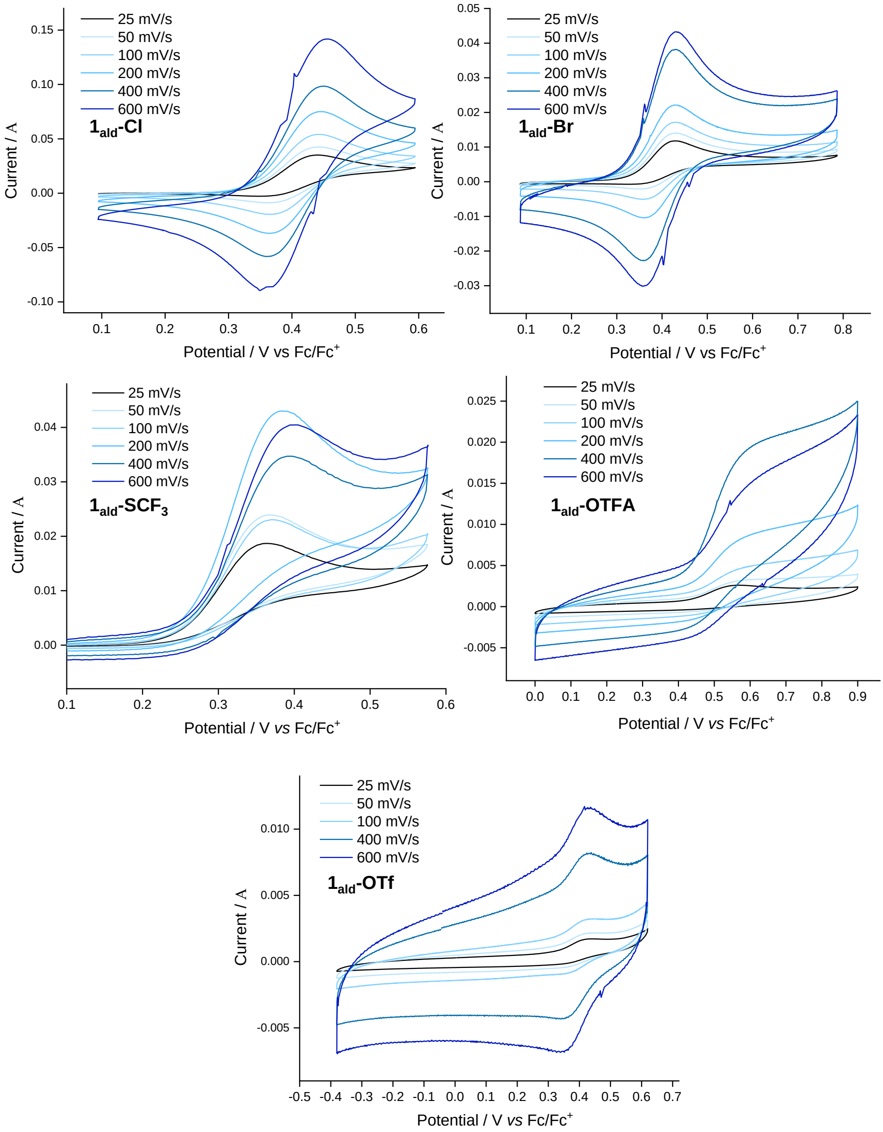

Figure 4.7 Cyclic Voltammograms of **1**$_{\text{ald}}$-**X** complexes recorded at different scan rates.

Indeed, preliminary chronoamperometry studies have already shown promising results for triggering the formation of C–I and C–SCF_3 coupling products, albeit not as efficiently as desired. No product formation was observed for the remaining nucleophilic coupling (Table 4.1).

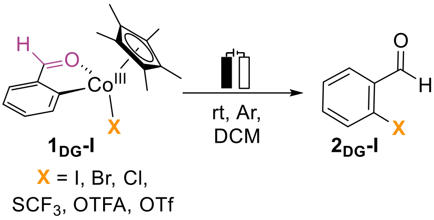

1_{ald}-X	*E_{ca} (V)*	*Q (equiv.)*	*NMR yield of the coupled product*
I	0.37	1.1	10 %
Br	0.43	0.7	-
Cl	0.46	1.0	-
SCF_3	0.34	0.6	32 %
OTFA	0.56	1.3	-
OTf	0.36	0.5	-

Table 4.1 Electrochemical oxidation of the Co(III) complexes. Applied potential values are referenced to Fc/Fc^+.

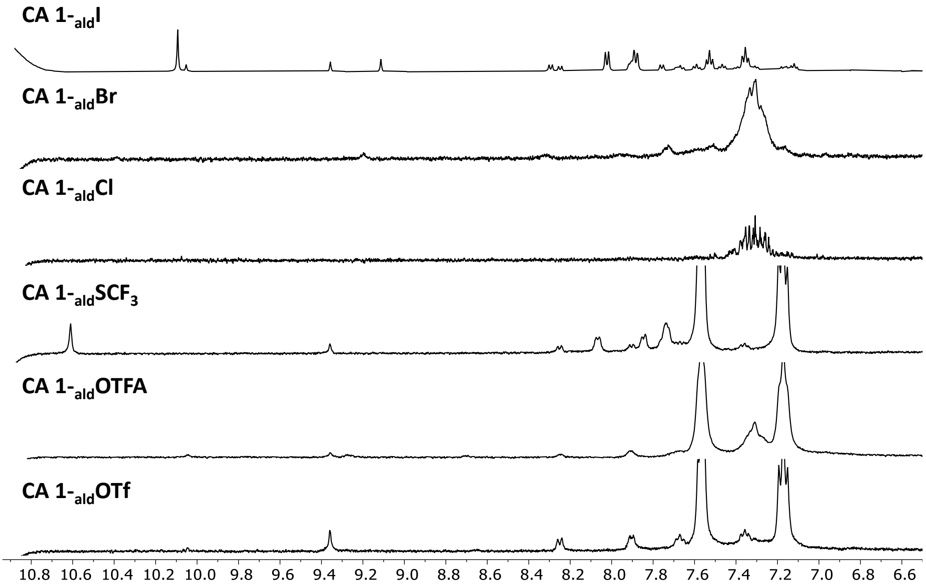

Figure 4.8 Aromatic region of ^1H NMR Spectra of the chronoamperometry studies of **1_{ald}-X**.

These trends are in alignment with the calculated activation barriers for the reductive elimination event from the corresponding oxidized Co(IV) species (Figure 4.9). We observed that the formation of C–O bonds is particularly challenging, with activation barriers of 22.0 kcal·mol^{-1} for C–OTFA formation and 29.6 kcal·mol^{-1} for OTf coupling.

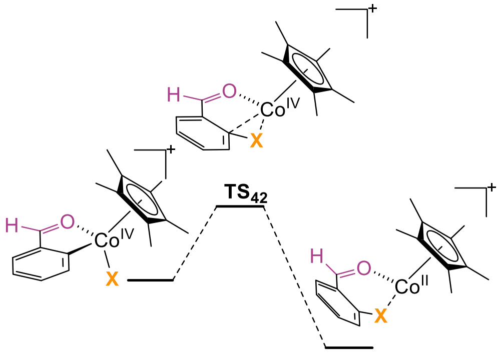

1_{ald}-X	*Activation Energy*
I	8.5
Br	12.8
Cl	14.4
SCF_3	11.7
OTFA	22
OTf	29.6

Figure 4.9 Calculated activation energy barriers for the reductive elimination step from an oxidized Co(IV) species in kcal·mol^{-1}.

Next, the chemical oxidation of the different Co(III) complexes was examined with the F$^+$ oxidants previously used in Chapter 3 (Table 4.2).[7] As expected, **1_{ald}-SCF_3** is proven to be the complex that undergo more facile C–X reductive elimination under our reaction conditions, along with complex **1_{ald}-I**.[8] The oxidation of **1_{ald}-Br** with NFTPT or NFSI resulted in low yields of the desired reductive elimination product, along with the formation of benzaldehyde and unreacted starting material. **1_{ald}-Cl**, **1_{ald}-OTFA** and **1_{ald}-OTf** did not lead to product formation.

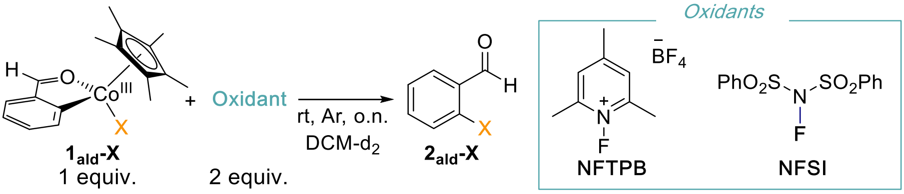

NMR yield of the coupled product

X (1_{ald}-X)	*NFTPB*	*NFSI*
I	84 %	[a]96 %
Br	17 %	24 %
Cl	0 %	0 %
SCF_3	60 %	97 %
OTFA	0 %	0%
OTf	0 %	Decomposition

Table 4.2 Reactivity towards F$^+$ oxidants forming C–X bonds. [a]NMR yield obtained from previous chapter.

---

[7] Due to the no longer commercialization of the 1-Fluoro-2,4,6-trimethylpyridinium triflate used in Chapter 3, we employed the tetrafluoroborate salt for the set of experiments carried out in this chapter.

[8] See Chapter 3.

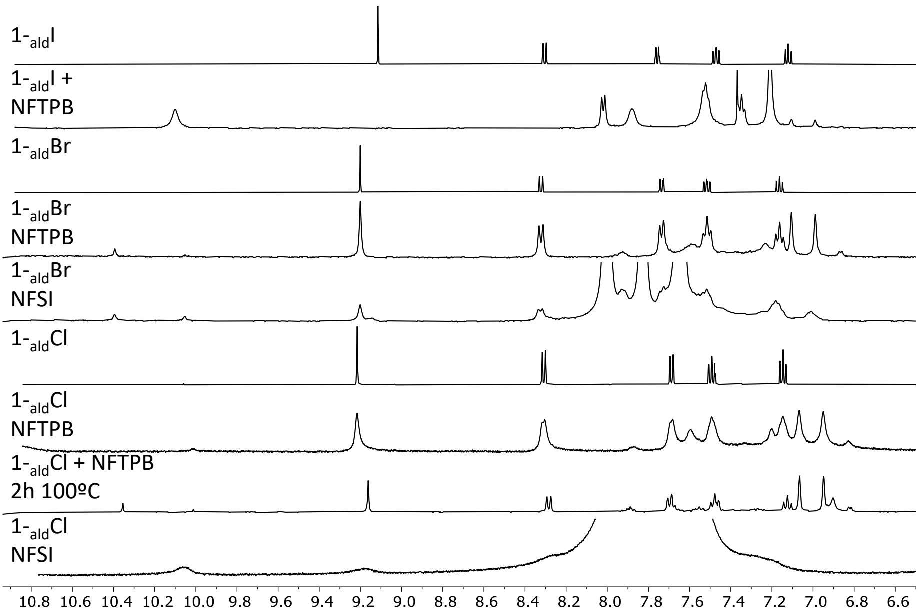

Figure 4.10 Aromatic region of ^{1}H NMR Spectra of the reaction of **1_{ald}-I**, **1_{ald}-Br** and **1_{ald}-Cl** with NFTPB and NFSI.

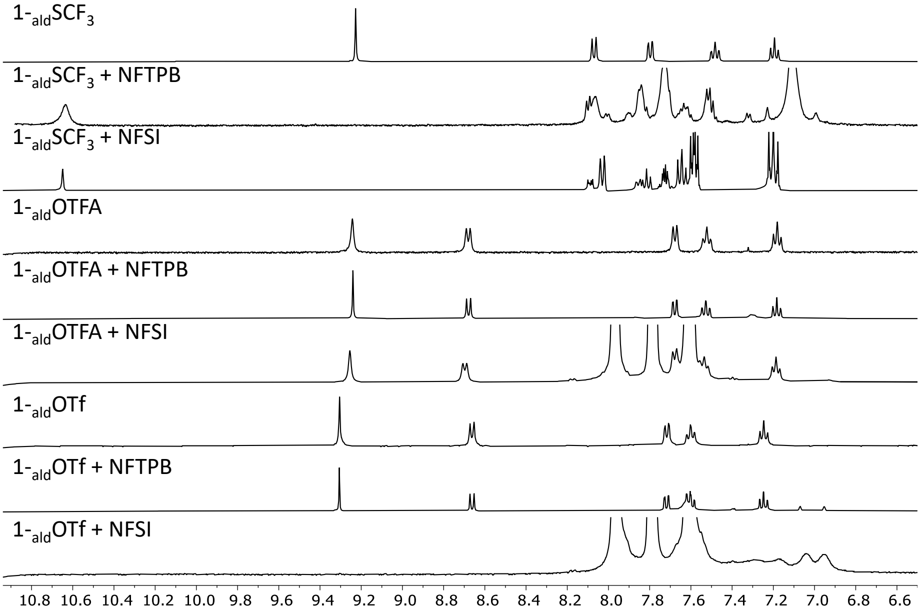

Figure 4.11 Aromatic region of ^{1}H NMR Spectra of the reaction of **1_{ald}-SCF$_3$** and **1_{ald}-OTFA** and **1_{ald}-OTf** with NFTPB and NFSI..

Our initial findings regarding nucleophilic C–X couplings from Cp*Co-based systems show the difficulties associated to triggering certain reductive elimination events. This is in agreement with the scarcity of nucleophilic reports disclosed in the literature, currently limited to C–S bond-forming reactions.[9] However, our preliminary experimental and computational studies show promising prospects for exploring the formation of C–halogen bonds under catalytic conditions using nucleophilic sources.

4.3.2. Directing group effect on C–I bond-forming reactions

Aiming to gather further fundamental knowledge on C–X bond-forming reactions from Cp*Co-based systems, we next investigated whether the nature of the directing group present in the metalacyclic species plays a key role on promoting C–X reductive elimination events. To explore this variable, we targeted C–I bond-forming reactions by taking advantage of the library of cobaltacyles previously reported by our group (Figure 4.12),[2,10] **1**$_{\mathbf{DG}}$**-I**, which comprises cobaltacycles with strong (**1**$_{\mathbf{imi}}$**-I** and **1**$_{\mathbf{ppy}}$**-I**) and weakly directing groups (**1**$_{\mathbf{tBu\text{-}amd}}$**-I,** **1**$_{\mathbf{amd}}$**-I** and **1**$_{\mathbf{acm}}$**-I**). Following the same procedure than in previous sections, we investigated both, the direct reductive elimination from Cp*Co^{III} and the C–I bond-formation via high-valent coabalt species.

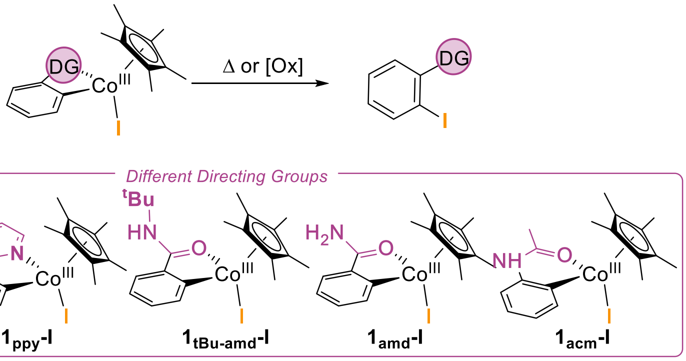

Figure 4.12 Scope of **1**$_{\mathbf{DG}}$**-I** used in the study on the effect of the directing groups on C–I bond-forming reactions.

As expected, we did not observe the formation of the C–I reductive elimination products by ^{1}H NMR spectroscopy (Figure 4.14 and Figure 4.15), upon thermolysis

---

[9] a) T. Gensch, F. J. R. Klauck, F. Glorius, *Angew. Chem. Int. Ed.* **2016**, *55*, 11287. b) X.-G. Liu, Q. Li, H. Wang, *Adv. Synth. Catal.* **2017**, *359*, 1942.

[10] J. Sanjosé-Orduna, D. Gallego, A. Garcia-Roca, E. Martin, J. Benet-Buchholz, M. H. Pérez-Temprano, *Angew. Chem. Int. Ed.* **2017**, *56*, 12137–12141.

1_{DG}-I in CD_2Cl_2 at 100 ºC at different time intervals (1, 2, 5, and 16 hours). It is worth-mentioned that heating the cobaltacycles containing O-based chelating moieties, **$1_{tBu\text{-}amd}$-I**, **1_{amd}-I** and **1_{acm}-I**, led to complete decomposition while **1_{imi}-I** and **1_{ppy}-I**, exhibited greater stability, with 86% and 45% of unreacted cobaltacycles remaining, respectively.

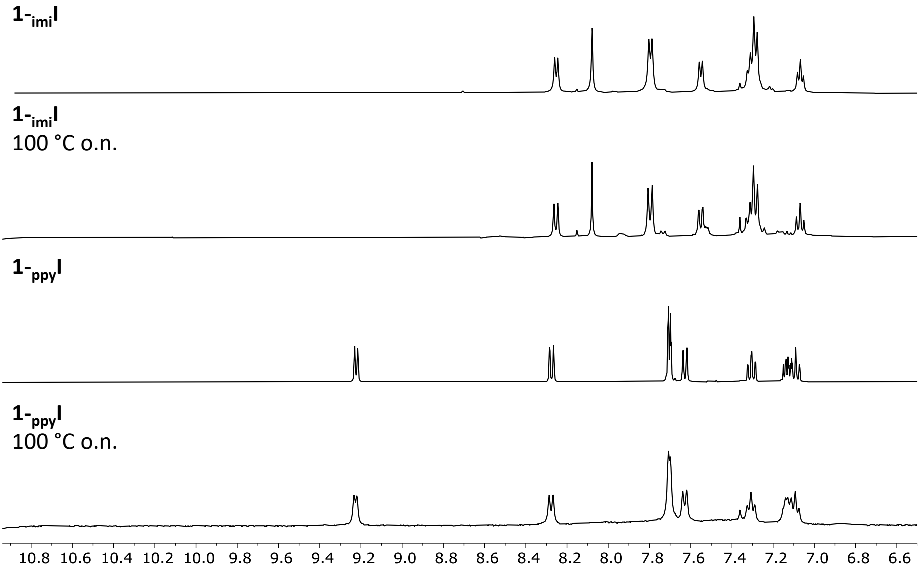

Figure 4.13 Aromatic region of ^{1}H NMR Spectra of the thermolysis of **1_{imi}-I** and **1_{ppy}-I.**

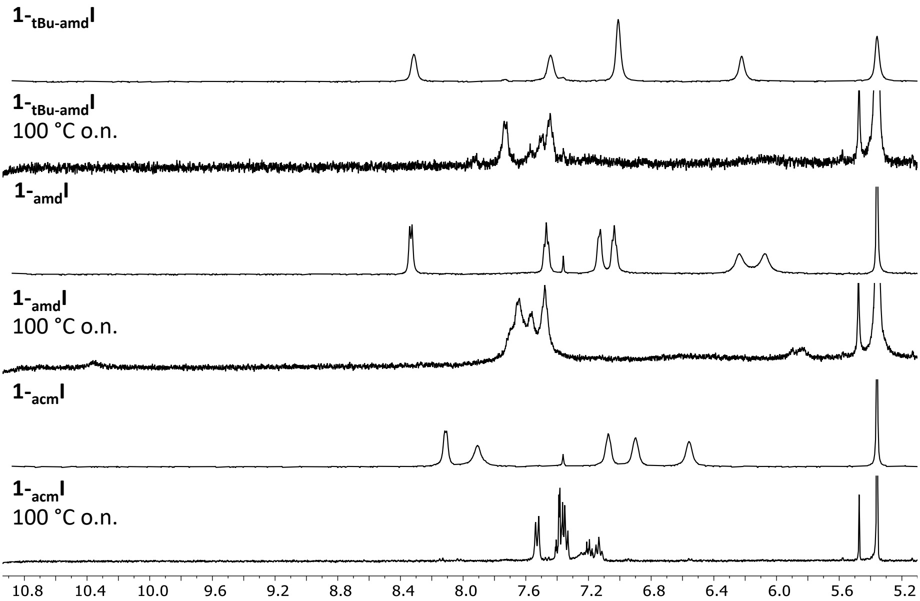

Figure 4.14 Aromatic region of ^{1}H NMR Spectra of the thermolysis of $\mathbf{1_{tBu\text{-}amd}\text{-}I}$, $\mathbf{1_{amd}\text{-}I}$ and $\mathbf{1_{acm}\text{-}I}$.

Computational studies with selected $\mathbf{1_{DG}\text{-}I}$ are consistent with the experimental data, showing high barriers for the reductive elimination from cobalt(III). Interestingly, the activation energies observed in Figure 4.15 are higher than those observed in Scheme 4.2 when using the aldehyde as a directing group.

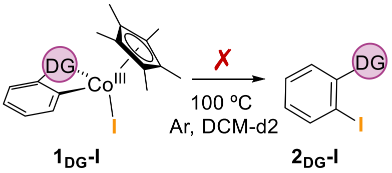

Cobaltacycle	*DFT calculated activation energy*
$\mathbf{1_{imi}\text{-}I}$	53.4
$\mathbf{1_{amd}\text{-}I}$	60.0
$\mathbf{1_{acm}\text{-}I}$	59.7

Figure 4.15 Direct reductive elimination from $\mathbf{1_{DG}\text{-}I}$ complexes. The calculated DFT activation energies are shown in kcal·mol^{-1}.

Electrochemical analyses of $\mathbf{1_{DG}\text{-}I}$ were carried out to further assess the accessibility and stability of high-valent cobalt species. As shown in Figure 4.16, the reversible nature of the oxidation peaks varied among the cobaltacycles.[11] While, $\mathbf{1_{imi}\text{-}I}$ exhibits a single irreversible oxidation peak at 0.34 V vs Fc/Fc$^+$, the three cobaltacycles

---

[11] The cyclic voltammogram of $\mathbf{1_{ppy}\text{-}I}$ is still pending.

containing amide moieties display similar cyclic voltammograms (CV) with two oxidation peaks. The first peak occurred at a slightly lower potential than that **1$_{ald}$-I**, approximately around 0.23 V vs Fc/Fc$^+$, while the second peak appeared at higher potentials, specifically at 0.74 V for complexes **1$_{tBu\text{-}amd}$-I** and **1$_{acm}$-I**, and 0.71 V vs Fc/Fc$^+$ for **1$_{amd}$-I**. Indeed, the latter shows quasi-reversible peaks at high scan rates, indicating a partial reversibility of the oxidation process. For **1$_{tBu\text{-}amd}$-I**, only the peak at 0.23 V demonstrated quasi-reversibility, while both oxidations were found to be irreversible for **1$_{acm}$-I**.

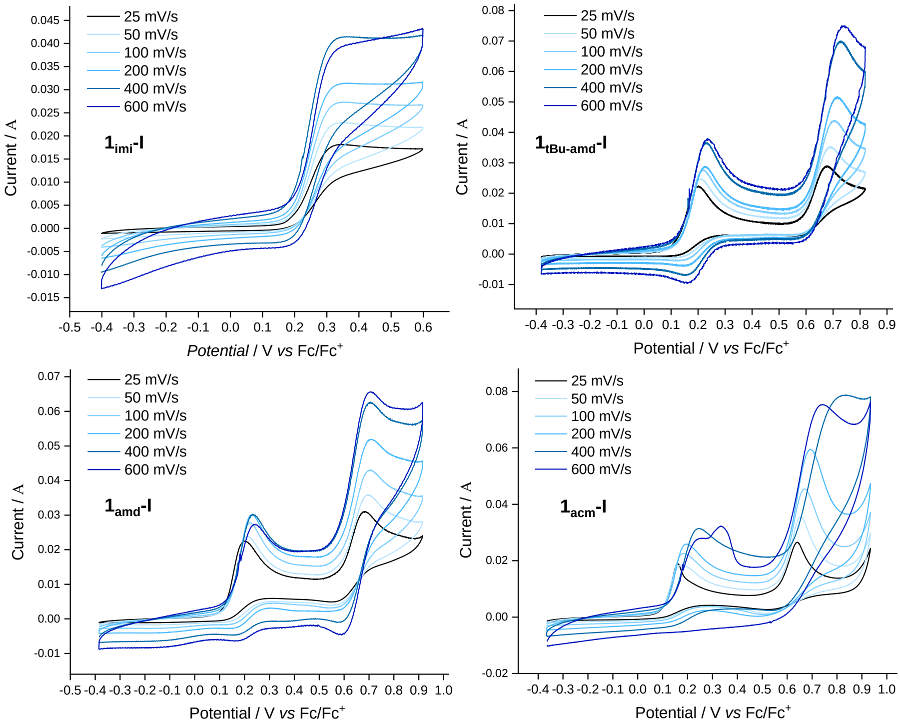

Figure 4.16 Cyclic voltammogram of **1$_{imi}$-I**, **1$_{tBu\text{-}amd}$-I**, **1$_{amd}$-I** and **1$_{acm}$-I** recorded at different scan rates.

Next, the reactivity of our family of **1$_{DG}$-I** complexes was evaluated in the presence of 2 equiv of F$^+$ oxidants to test the feasibility of the formation of C–I bonds via oxidatively induced reductive elimination events (Table 4.3). As observed for **1$_{ald}$-I**, the oxidative reactions with **1$_{imi}$-I** and **1$_{tBu\text{-}amd}$-I** led to high yields of the corresponding coupling product in CD_2Cl_2 after 30 minutes at room temperature, see Figure 4.17. Despite **1$_{amd}$-I** and **1$_{acm}$-I** also afforded the reductive elimination product as the major product, the reactions did not proceed cleanly, hampering their quantification, Figure 4.18. Surprisingly, the oxidative coupling of **1_{ppy}-I** in the presence of NFTPB and NFSI is low yielding in both cases, Figure 4.19. This result is in marked contrast to entry 2, where the presence of an alternative N-based strong DG, such as imine, provides the C(sp^2)–I bond-forming reductive elimination in almost quantitative yields. Thus, the experimental outcomes suggest that the nature of the directing group affects the feasibility of OREs event with F$^+$ oxidants in Cp*Co-based systems. The fundamental knowledge can be exploited for designing more efficient systems that could be translated to catalysis.

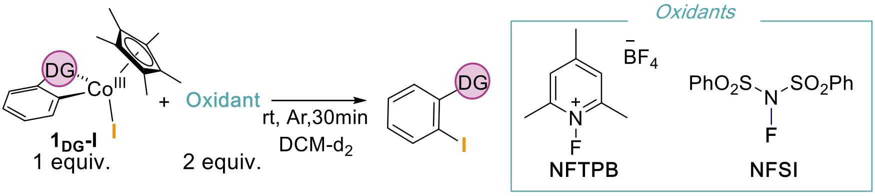

		NMR yield of the coupled product	
Entry	***Cobaltcycle***	***NFTPB***	***NFSI***
1	**1_{ald}-I**	84 %	96 % [a]
2	**1_{imi}-I**	97 %	91 %
3	**$1_{tBu\text{-}amd}$-I**	98 %	80 %
4	**1_{amd}-I**	[b]	[b]
5	**1_{acm}-I**	[b]	[b]
6	**1_{ppy}-I**	4 %	16 %

Table 4.3 Reactivity of **1_{DG}-I** towards F$^+$ oxidants to promote C–I bond-forming reactions from high-valent cobalt species. [a]NMR yield obtained from previous chapter. [b]The corresponding organic product was observed but the quantification by NMR spectroscopy was hampered due to the poor quality of the NMR spectrum.

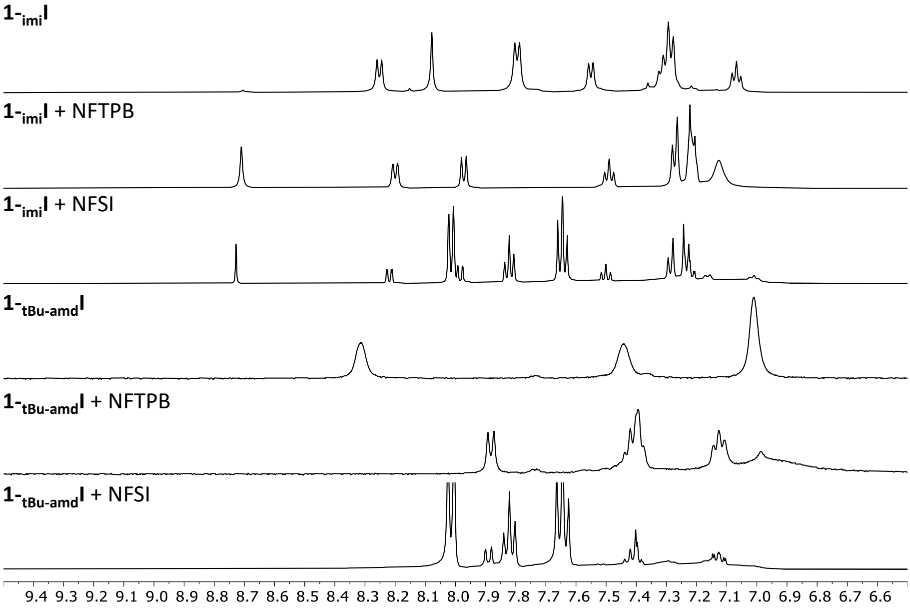

Figure 4.17 Aromatic region of ^{1}H NMR Spectra of the reaction of **1_{imi}-I** and **$1_{tBu\text{-}amd}$-I** with NFTPB and NFSI.

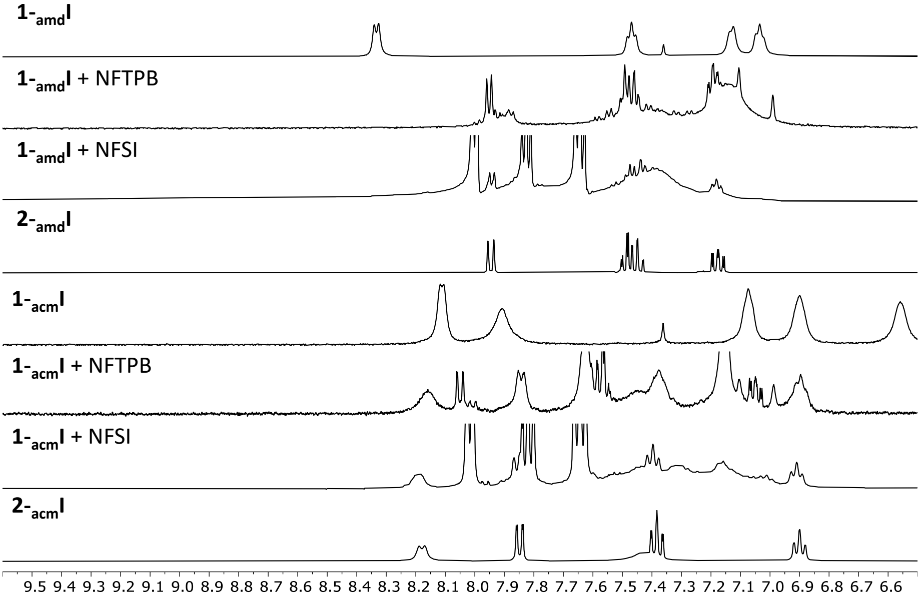

Figure 4.18 Aromatic region of ^{1}H NMR Spectra of the reaction of **1_{amd}-I** and **$1_{tBu\text{-}acm}$-I** with NFTPB and NFSI.

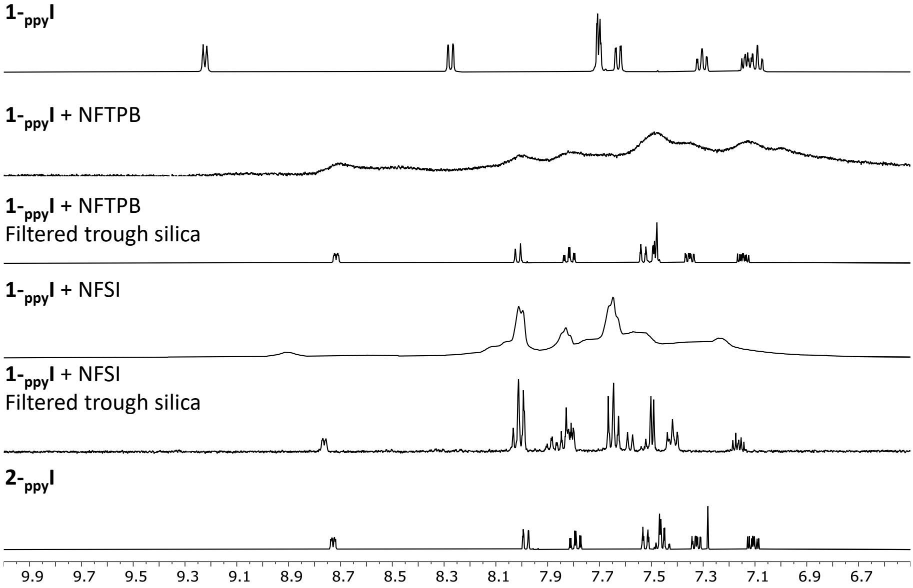

Figure 4.19 Aromatic region of ^{1}H NMR Spectra of the reaction of $\mathbf{1_{ppy}}$**-I** with NFTPB and NFSI.

4.3.3. Synthesis and reactivity of Cp*Co(ald)(R) complexes

As explained above, there are very limited examples of nucleophilic C–H functionalization reactions catalyzed by Cp*Co^{II} complexes. Apart from the two examples of C–S bond-forming reactions reported by the groups of Glorius[12] and Wang[13] in 2016 and 2017, respectively, Ackermann and co-workers disclosed in 2020 a very elegant methylation protocol using as nucleophilic coupling partner trimethylboroxine (Scheme 4.3).[14] As part of our interest on uncovering the mechanistic insights of reductive elimination events from Cp*Co species, in the last section of this thesis we will explore nuclophilic C–C couplings. Our goal is to establish if, Cp*Co^{III} can directly promote these transformations or on the contrary, ORE events are crucial as disclosed in the previous section for C–X bond-forming reactions.

---

[12] T. Gensch, F. J. R. Klauck, F. Glorius, *Angew. Chem. Int. Ed.* **2016**, *55*, 11287.

[13] X.-G. Liu, Q. Li, H. Wang, *Adv. Synth. Catal.* **2017**, *359*, 1942.

[14] S. D. Friis, M. J. Johansson, L. Ackermann, *Nat. Chem.* **2020**, *12*, 511.

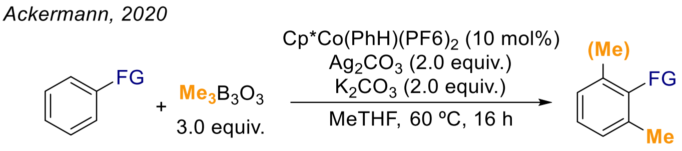

Scheme 4.3 Ackermann’s cobalt-catalyzed methylation of aryls and drugs

Inspired by the report by the Ackermann group, our initial investigations focused on accessing a direct analogue of the methylated Cp*Co^{III} complex proposed as reactive intermediate in their synthetic protocol. Unfortunately, attempts to access $\mathbf{1_{ald}}$**-Me** via the treatment of $\mathbf{1_{ald}}$**-I** with 1 equiv of $Me_3B_3O_3$ in CD_2Cl_2 resulted unsuccessful. The initial cobaltacycle remains intact, even after heating the reaction at 80 ºC for 3 hours, see Figure 4.21.[15] Inspired by the efficient transmetalation reactions between $\mathbf{1_{DG}}$**-I** and nucleophiles based on coinage metals developed by our group,[16] we explored the employment of a commercially available methylated gold source. While the reaction with 1 equiv of $MeAuPPh_3$ at room temperature for 3 hours did not lead to desired organometallic compound, we were very pleased to detect the formation of the corresponding organic product, upon heating the reaction at 80 ºC, along with the formation of $\mathbf{1_{ald}}$**-Cl** as main by-product of the reaction[17] Despite the coupling product is only observed in low yields by ^{1}H NMR spectroscopy, its presence in the reaction media suggests that C–C reductive eliminations may not require the involvement of high-valent cobalt species, and can occur directly from Cp*Co^{III} species. This finding contrasts with the previous studies disclosed in this thesis, where we have established experimentally and computationally that similar Cp*Co^{III}-based systems are not able to promote on C–X bond-forming reactions.

---

[15] Further ongoing mechanistic studies are being carried out in our group to unravel the intricacies associated to the methylated protocol reported by Ackermann.

[16] S. López-Resano, S. Martínez de Salinas, F. A. Garcés-Pineda, A. Moneo-Corcuera, J. R. Galán-Mascarós, F. Maseras, M. H. Pérez-Temprano, *Angew. Chem. Int. Ed.* **2021**, *60*, 11217–11221.

[17] No reaction was observed when $\mathbf{Co_{ald}Cl}$ was treated with 1 equivalent of $MeAuPPh_3$ at room temperature. Heating the reaction at 50 ºC for 1 hour resulted in the formation of only decomposition products.

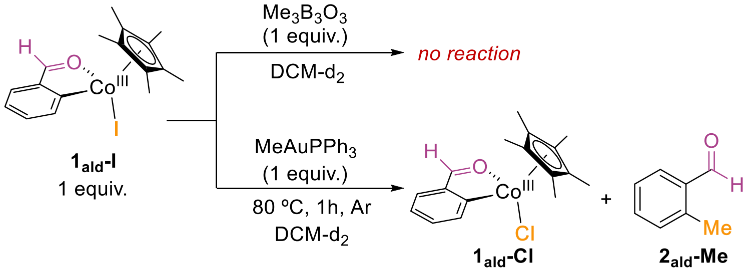

Figure 4.20 Attempts to synthesize **1_{ald}-Me**.

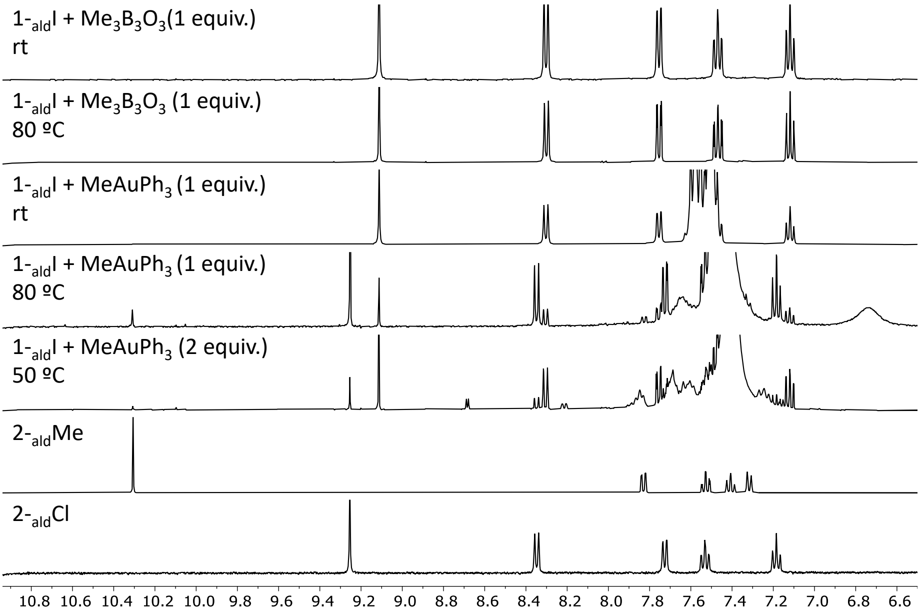

Figure 4.21 Aromatic region of ^{1}H NMR spectra of the reactions between **1_{ald}-I** and trimethylboroxine or $MeAuPPh_3$ in CD_2Cl_2 under different reaction conditions.

In order to confirm that participation of cobalt(III) intermediates in carbon–carbon couplings, we aimed to investigate the access to alternative isolable **1_{ald}-R** complexes. In particular, we explored the installation of perfluorinated organic groups such as CF_3 or C_6F_5 (Scheme 4.4). These groups possess a unique combination of electron-donating[18] and electron-accepting[19] properties, which contribute to the stabilization of highly reactive organometallic species. Gratifyingly, when we employed as transmetalating agent (Cs)[Ag(CF$_3$)$_2$], an effective CF$_3$ shuttle previously reported by our research group,[20] in combination with AgBF$_4$, **1$_{\text{ald}}$-CF$_3$** was isolated in 78% yield. For **1$_{\text{ald}}$-C$_6$F$_5$**, we used AgC$_6$F$_5$·EtCN as the arylated source, affording the desired cobaltacycle in good yield.

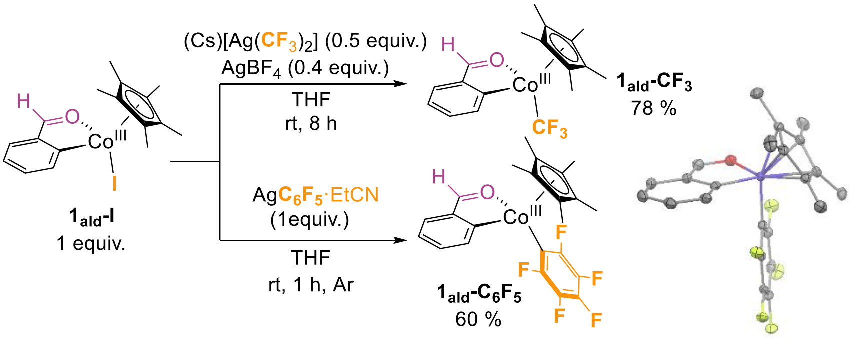

Scheme 4.4 Synthesis of **1$_{\text{ald}}$-CF$_3$** and **1$_{\text{ald}}$-C$_6$F$_5$** with silver nucleophiles. ORTEP structures of **1$_{\text{ald}}$-C$_6$F$_5$**. Thermal ellipsoids are drawn at 50 % probability, H atoms have been omitted for clarity.

The direct participation of these cobaltacycles in C–C bond-forming reactions was next evaluated by ^{19}F NMR spectroscopy. While **1$_{\text{ald}}$-CF$_3$** did not undergo reductive elimination, heating **1$_{\text{ald}}$-C$_6$F$_5$** overnight at 100 ºC in DCM, provided the coupling product in 98 % yield. We hypothesize that increasing the electron density of the carbon facilitates the C–C reductive elimination process from cobalt(III) species (Scheme 4.5).

---

[18] a) T. G. Appleton, M. H. Chisholm, H. C. Clark, L. E. Manzer, *Inorg. Chem.* **1972**, *11*, 1786–1794. b) S. A. Holmes, T. D. Thomas, *J. Am. Chem. Soc.* **1975**, *97*, 2337–2341.

[19] a) C. Hansch, A. Leo, R. W. Taft, *Chem. Rev.* **1991**, *91*, 165–195. b) K. Uneyama (2006) *Organofluorine Chemistry*. Blackwell Publishing Ltd., Oxford.

[20] a) S. Martínez de Salinas, Á. L. Mudarra, J. Benet-Buchholz, T. Parella, F. Maseras, M. H. Pérez-Temprano, *Chem. Eur. J.* **2018**, *24*, 11805–11805. b) S. Martínez de Salinas, Á. L. Mudarra, C. Odena, M. Martínez Belmonte, J. Benet-Buchholz, F. Maseras, M. H. Pérez-Temprano, *Chem. Eur. J.* **2019**, *25*, 9343–9343.

UNIVERSITAT ROVIRA I VIRGILI
UNCOVERING THE MECHANISTIC SCENARIOS OF NUCLEOPHILIC COUPLINGS IN CP*CO SYSTEMS
Sara López Pesano

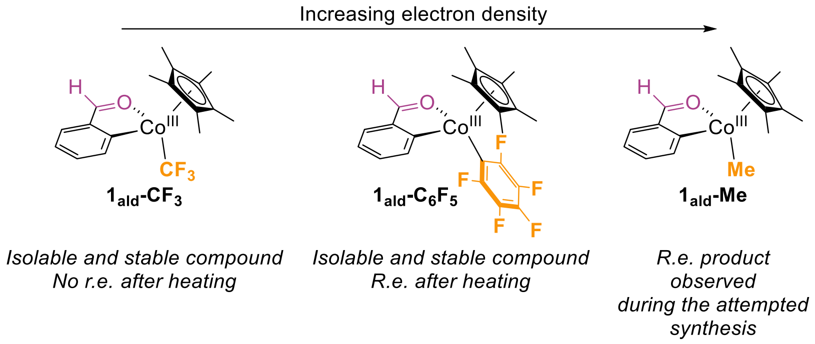

Scheme 4.5 Experimental trend for C–C reductive eliminations from **1_{ald}-R** complexes.

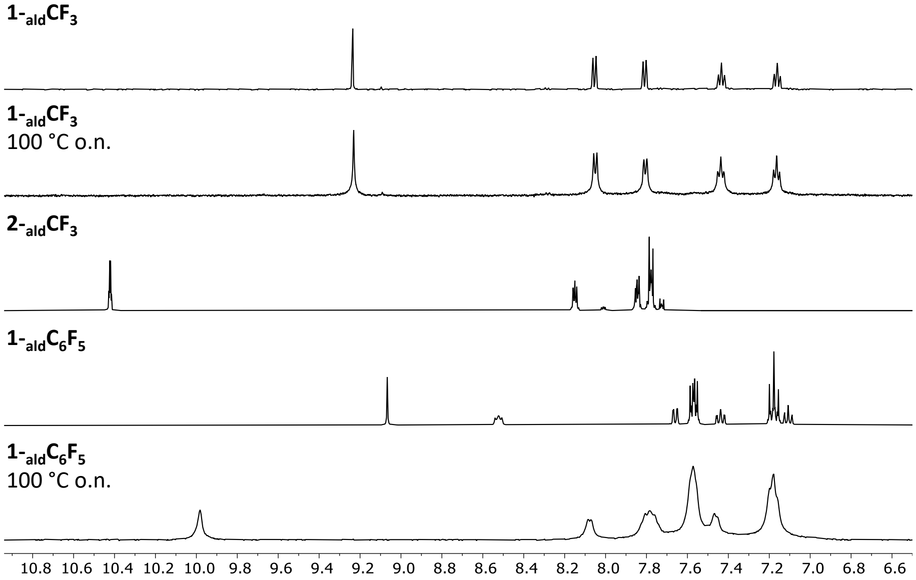

Figure 4.22 Aromatic region of ^{1}H NMR Spectra of the thermolysis of **1_{ald}-CF_3** and **1_{ald}-C_6F_5**.

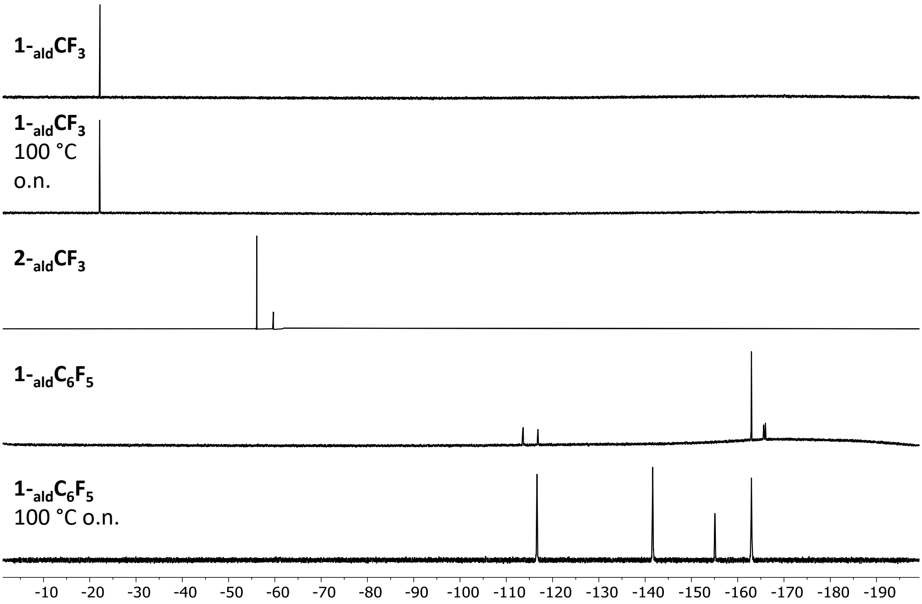

Figure 4.23 ^{19}F NMR Spectra of the thermolysis of **1_{ald}-CF$_3$** and **1_{ald}-C$_6$F$_5$**.

Consistent with our experimental observations, DFT calculations show a clear influence on the activation barrier of the C–C coupling via Cp*Co^{III} depending on the organic fragment. The computational study shows low activation barriers for **1_{ald}-Me** and **1_{ald}-Ph**, followed by **1_{ald}-C$_6$F$_5$**. The high barrier computed for the C–CF$_3$ coupling supports the lack of reactivity from **1_{ald}-CF$_3$**.

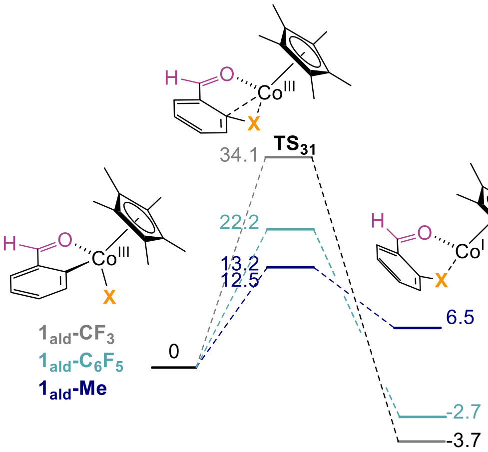

Scheme 4.6 DFT calculated energies for direct reductive elimination from Co(III) complexes to form C–C bonds. Energies are shown in kcal·mol^{-1}.

Overall, these experimental and computational studies demonstrate that metallyclic Cp*Co^{III} complexes can undergo Csp^2–Csp^2 and Csp^2–Csp^3 couplings. This reactivity contrasts with the observed behavior reported by Chang and co-workers in analogous Cp*Rh^{III} and Cp*Ir^{III} systems (Figure XX). These reports established the necessity to induced C–C reductive elimination events in the presence of chemical oxidants such as coinage metal salts or triggered electro- or photochemically. Therefore, our work reinforces that Cp*Co-based systems are not just a cost-effective alternative to rhodium or iridium and can exhibit unique features.

4.4. Conclusion

In summary, in this chapter we embarked on an exploration of the reactivity of a family of metalacyclic Cp*Co^{III} complexes, which encompassed various heteroatom- and carbon-based nucleophilic moieties. Our primary objective was to investigate the reductive elimination reactions of these complexes, aiming to unravel the diverse reactivity patterns exhibited by different nucleophiles and directing groups.

Remarkably, oxidatively induced reductive elimination successfully delivered C–I and C–S bonds, while the formation of C–Br, C–Cl, and C–O bonds posed greater challenges. Furthermore, the impact of directing groups on the feasibility of oxidative reductive eliminations (OREs) was unveiled, with weakly directing amides and the robust imine exhibiting favorable reactivity for C–I bond formation, while the widely employed phenylpyridine moiety displayed inferior performance.

Notably, contrary to what observed by Chang and co-workers in analogous Cp*Rh^{III} and Cp*Ir^{III} systems, our finding revealed the feasibility of direct reductive elimination from Cp*Co^{III} species to form Csp^2–Csp^2 and Csp^2–Csp^3 bonds. This discovery shows the unique features of Cp*Co-based systems.

This fundamental understanding serves as a solid foundation for the design of highly efficient systems that can be readily translated into catalytic applications, thereby advancing the field of synthetic chemistry.

4.5. Appendixes

4.5.1. Experimental appendix

General Procedures

All reactions were conducted in an argon-filled glovebox (mBraun Unilab 4420) with concentrations of O_2 and H_2O < 0.1 ppm or using Schlenk techniques under argon atmosphere. All the glassware was oven-dried at 100 ºC overnight and cooled under vacuum prior use.

NMR spectra were obtained on a Bruker 400 MHz or a 500 MHz cryoprobe spectrometers. ^{1}H, ^{13}C and ^{19}F NMR chemical shifts are reported in parts per million (ppm), relative to tetramethylsylane (TMS) for ^{1}H and ^{13}C with the residual solvent peak used as an internal reference and relative to $CFCl_3$ (Freon) for ^{19}F. In the ^{19}F spectra registered in non-deuterated solvents, a coaxial tube containing acetone-d_6 was used to maintain the lock ^{2}H signal. Multiplicities are reported as follows: singlet (s), broad singlet (bs), doublet (d), doublet of doublets (dd), triplet (t), triplet of doublets (td) and multiplet (m).

High Resolution Mass Spectrometry (HRMS) data was recorded on a LCT-Premier (Waters) or a MicroTOF Focus (Bruker Daltonics) mass spectrometers using ESI ionization technique and dichloromethane as solvent.

Materials and methods

Commercially available reagents AgOAc, AgOTf, AgOTFA, $AgSCF_3$, AgCl, $AgBF_4$, CsF, Me_3SiCF_3, pentamethylcyclopentadiene, nBuLi, $CoCl_2$, Zn, vinyltrimethylsilane, 2-iodobenzaldehyde, 2-bromobenzaldehyde, 2-iodobenzamide, 1-fluoro-2,4,6-trimethylpyridinium tetrafluoroborate, N-fluorobenzenesulfonimide, were used without further purification directly as received from the commercial supplier and stored under inert gas and/or low temperature when required. Dichloromethane-d_2 (CD_2Cl_2) and tetrahydrofurane-d8 (THF-d_8) were stored under argon with activated 4 Å molecular sieves.

If necessary, the solvents (THF, CH_2Cl_2, hexane, MeCN) were used from a solvent purification system pure-solv (SPS-400, Innovative Technology) and stored under argon with activated molecular sieves 4 Å.

The complexes [Cp*CoI(VTMS)2] (**3**),[21] [Cp*Co(ald)Br],[22] [Cp*Co(WDG)I],[22] [Cp*Co(ppy)I][21] (**19**), (Cs)[Ag(CF3)2][23] AgC_6F_5ref were synthesized according to previous literature procedures.

Synthesis and characterization of $\mathbf{1_{ald}}$***-X***

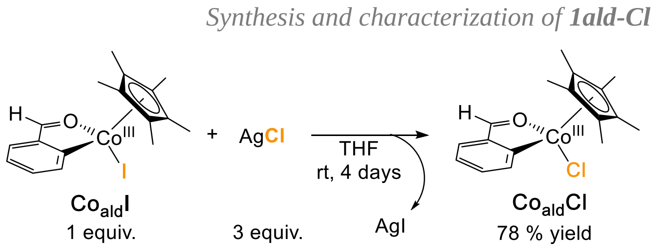

In an argon atmosphere glovebox, $\mathbf{1_{ald}}$**-I** (50.0 mg, 0.12 mmol) and AgCl (50.5 mg, 0.35 mmol) were added to an oven-dried Schlenk containing a magnetic stir bar. THF (5 mL) were added and the mixture was stirred at room temperature for 4 days. After that, the solution was filtered through cannula and the solvent was removed under reduced pressure. The solid/oily residue was washed with hexane (2 x 10 mL) and the black solid was dried under vacuum to afford $\mathbf{1_{ald}}$**-Cl** (30.6 mg, 78 %). The complex was stored inside the glovebox at –32 ºC.

^{1}H NMR (THF-d_8, 298 K, 500 MHz): δ 9.16 (s, 1H, CHO), 8.25 (d, 1H, $^3J_{H,H}$ = 7.7 Hz), 7.65 (dd, 1H, $^3J_{H,H}$ = 7.6 Hz, $^4J_{H,H}$ = 1.5 Hz), 7.39 (td, 1H, $^3J_{H,H}$ = 7.5 Hz, $^4J_{H,H}$ = 1.5 Hz), 7.05 (td, 1H, $^3J_{H,H}$ = 7.5 Hz, $^4J_{H,H}$ = 1.5 Hz), 1.37 (s, 15H, Cp*) ppm

^{13}C NMR (THF-d_8, 298 K, 126 MHz): δ 206.82 (CHO), 198.37 (Cipso), 151.56, 140.51, 133.54, 132.33, 123.18, 93.27 (Cipso, Cp*), 9.40 (CH_3, Cp*) ppm

---

[21] Sanjosé-Orduna, J.; Gallego, D.; Garcia-Roca, A.; Martin, E.; Benet-Buchholz, J.; Pérez-Temprano, M. H. *Angew. Chem. Int. Ed.* **2017**, *56*, 12137

[22] S. Martínez de Salinas, J. Sanjosé-Orduna, C. Odena, S. Barranco, J. Benet-Buchholz, M. H. Pérez-Temprano, *Angew. Chemie - Int. Ed.* **2020**, *59*, 6239–6243.

[23] Martínez de Salinas, S.; Mudarra, A. L.; Benet-Buchholz, J.; Parella, T.; Maseras, F.; Pérez-Temprano, M. H. *Chem. Eur. J.* **2018**, *24*, 11895

*Synthesis and characterization of **1$_{ald}$-OTFA**, **1$_{ald}$-OTf** and **1$_{ald}$-SCF$_3$***

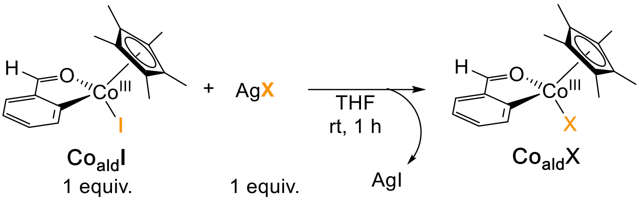

In an argon atmosphere glovebox, **1$_{ald}$-I** (50.0 mg, 0.12 mmol) and AgL (1 equiv) were added to an oven-dried Schlenk containing a magnetic stir bar. THF (5 mL) were added and the mixture was stirred at room temperature for 1 hour. After that, the solution was filtered through cannula and the solvent was removed under reduced pressure. The solid/oily residue was washed with hexane (2 x 10 mL) and the solid was dried under vacuum to afford **1$_{ald}$-X**. All the complexes were stored inside the glovebox at –32 ºC.

Entry	1$_{ald}$-X	AgX	Obtained (mg/yield)	Color
1	**1$_{ald}$-OTFA**	26.0 mg	38.6 / 81 %	Black
2	**1$_{ald}$-OTf**	30.2 mg	36.8 / 70 %	Black
3	**1$_{ald}$-SCF$_3$**	24.6 mg	38.1 / 81 %	Reddish

[Cp*Co$_{ald}$OTFA]

^{1}H NMR (CD$_2$Cl$_2$, 298 K, 500 MHz): δ 9.24 (s, 1H, CHO), 8.68 (d, 1H, $^3J_{H,H}$ = 7.7 Hz), 7.68 (d, 1H, $^3J_{H,H}$ = 7.5 Hz), 7.53 (t, 1H, $^3J_{H,H}$ = 7.5 Hz), 7.18 (t, 1H, $^3J_{H,H}$ = 7.4 Hz), 1.37 (s, 15H, Cp*) ppm

^{13}C NMR (CD$_2$Cl$_2$, 298 K, 126 MHz): δ 206.90 (CHO), 194.09 (Cipso), 151.70, 140.95, 133.71, 132.48, 124.12, 93.06 (Cipso, Cp*), 9.47 (CH$_3$, Cp*) ppm[24]

^{19}F NMR (DCM-d$_2$, 298 K, 471 MHz): δ - 75.84 ppm

HRMS-electrospray (+) in methylene chloride (m/z): Calc. for $C_{17}H_{20}CoO^+$ [M–CF$_3$COO]$^+$: 299.0841; found: 299.0852

[Cp*Co$_{ald}$OTf]

---

[24] In the ^{13}C NMR spectrum, the peak corresponding to the O–C=O should appear around 150-160 ppm and the one of the SCF$_3$ around 110-120 ppm.

^{1}H NMR (CD_2Cl_2, 298 K, 500 MHz): δ 9.31 (s, 1H, CHO), 8.67 (d, 1H, $^{3}J_{H,H}$ = 7.7 Hz), 7.73 (dd, 1H, $^{3}J_{H,H}$ = 7.5 Hz, $^{4}J_{H,H}$ = 1.5 Hz), 7.61 (td, 1H, $^{3}J_{H,H}$ = 7.5 Hz, $^{4}J_{H,H}$ = 1.5 Hz), 7.26 (td, 1H, $^{3}J_{H,H}$ = 7.3 Hz, $^{4}J_{H,H}$ = 1.0 Hz), 1.33 (s, 15H, Cp*) ppm

^{13}C NMR (CD_2Cl_2, 298 K, 126 MHz): δ 208.62 (CHO), 190.28 (Cipso), 152.87, 140.80, 134.83, 132.85, 124.91, 93.43 (Cipso, Cp*), 9.57 (CH_3, Cp*) ppm[25]

^{19}F NMR (CD_2Cl_2, 298 K, 471 MHz): δ - 79.28 ppm

[Cp*Co$_{ald}$SCF$_3$]

^{1}H NMR (CD_2Cl_2, 298 K, 400 MHz) δ 9.19 (d, *J* = 0.4 Hz, 1H, CHO), 8.05 – 8.01 (m, 1H), 7.76 (ddd, $^{3}J_{H,H}$ = 7.6, $^{4}J_{H,H}$ = 1.5 Hz, $^{5}J_{H,H}$ = 0.5 Hz, 1H), 7.44 (ddd, $^{3}J_{H,H}$ = 7.8, 7.2, $^{4}J_{H,H}$ = 1.5 Hz, 1H), 7.16 (ddd, $^{3}J_{H,H}$ = 7.6, 7.2, $^{4}J_{H,H}$ = 1.0 Hz, 1H), 1.39 (s, 15H, Cp*) ppm

^{13}C NMR (CD_2Cl_2, 298 K, 126 MHz): δ 205.63 (CHO), 198.08 (Cipso), 150.03, 139.83, 137.13, 133.56, 132.80, 123.28, 94.48 (Cipso, Cp*), 9.34 (CH_3, Cp*) ppm

^{19}F NMR (CD_2Cl_2, 298 K, 471 MHz): δ - 21.67 ppm

Synthesis and characterization of ***1$_{ald}$-CF$_3$***

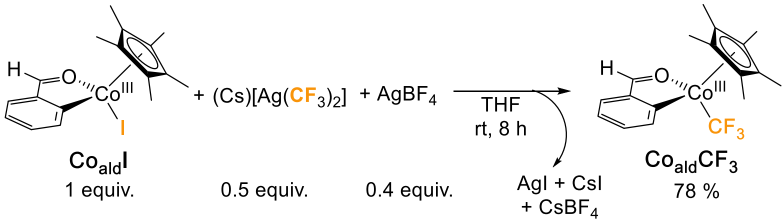

In an argon atmosphere glovebox, **1$_{ald}$-I** (50 mg, 0.12 mmol), (Cs)[Ag(CF_3)$_2$] (22.3 mg, 0.06 mmol) and $AgBF_4$ (9.2 mg, 0.05 mmol) were added to an oven-dried Schlenk containing a magnetic stir bar. The solids were dissolved in 5 mL of THF and the mixture was stirred at room temperature until all the signals related with **1$_{ald}$-I** disappeared by ^{1}H NMR (normally around 8 h). After that, the solution was filtered through cannula and the solvent was removed under reduced pressure. The solid/oily residue was washed with hexane (2 x 10 mL) and the reddish solid was dried under

---

[25] The peak corresponding to the carbon of the OTf group should appear around 120 ppm in the ^{13}C NMR spectrum.

vacuum to afford **3_{ald}-CF_3** (33.5 mg, 78 % yield). The complex was stored inside the glovebox at –32 ºC.

^{1}H NMR (THF-d_8, 298 K, 500 MHz): δ 9.22 (s, 1H, CHO), 8.01 (dd, 1H, $^3J_{H,H}$ = 7.7 Hz, $^4J_{H,H}$ = 0.8 Hz), 7.78 (dd, 1H, $^3J_{H,H}$ = 7.5 Hz, $^4J_{H,H}$ = 1.5 Hz), 7.35 (td, 1H, $^3J_{H,H}$ = 7.4 Hz, $^4J_{H,H}$ = 1.5 Hz), 7.08 (td, 1H, $^3J_{H,H}$ = 7.3 Hz, $^4J_{H,H}$ = 1.0 Hz), 1.50 (s, 15H, Cp*) ppm

^{13}C NMR (THF-d_8, 298 K, 126 MHz): δ 207.78 (CHO), 202.13 (Cipso), 151.12, 139.31, 133.15, 133.06, 130.70, 123.30, 95.64 (Cipso, Cp*), 9.48 (CH_3, Cp*) ppm

^{19}F NMR (THF-d_8, 298 K, 471 MHz): δ - 22.68 ppm

*Synthesis and characterization of **$Co_{ald}C_5F_5$***

A crimp vial was charged with **3_{Ald}-I** (100 mg, 0.23 mmol, 1.0 eq.) and transferred to the glove box where AgC_6F_5 (83 mg, 0.30 mmol, 1.3 eq.) and THF (3 mL) was added. The crimp vial was sealed and stirred inside the glove box for 2.5 hours. After the reaction was completed, the suspension was filtered through a large 0.2 mm Teflon syringe filter in the glove box. The solvent was removed under reduced pressure, the residue was dissolved in hexane and filtered through a large 0.2 mm Teflon syringe filter for a second time. The hexane was removed under reduced pressure to obtain **3_{Ald}-C_6F_5** (45 mg, 42%) as a dark solid. **$3_{ald}C_6F_5$** was stored under air in a desiccator at room temperature.

^{1}H NMR (500 MHz, CD_2Cl_2) δ = 9.03 (s, 1H), 8.49 (t, J = 6.6 Hz, 1H), 7.62 (dd, J = 7.6, 1.5 Hz, 1H), 7.40 (ddd, J = 7.9, 7.1, 1.6 Hz, 1H), 7.07 (ddd, J = 7.8, 7.2, 1.0 Hz, 1H), 1.38 (s, 15H).

^{19}F NMR ^{19}F NMR (471 MHz, CD_2Cl_2) δ -113.60 (d, *J* = 32.9 Hz), -116.79 (d, *J* = 30.5 Hz), -162.96 (t, *J* = 20.1 Hz), -165.61, -165.99.

*NMR characterization of Cp*Co$_{ald}$X complexes*

NMR characterization of complex ***1$_{ald}$-Cl***

^{1}**H NMR** spectrum of **1$_{ald}$-Cl** at 298 K in THF-d_8

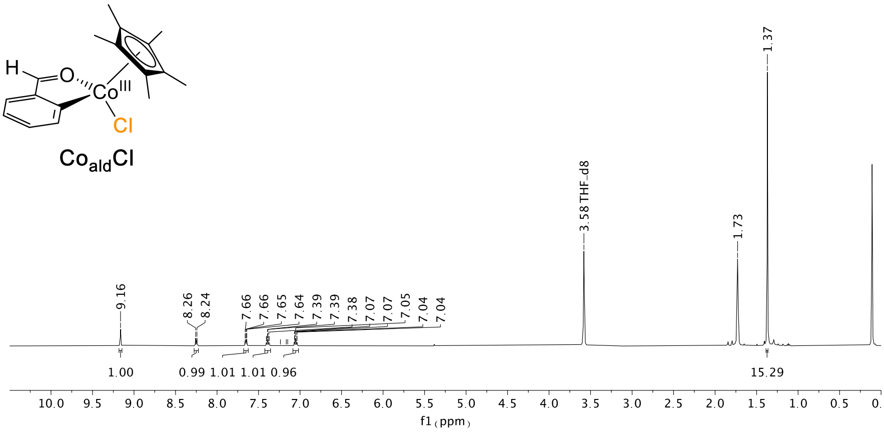

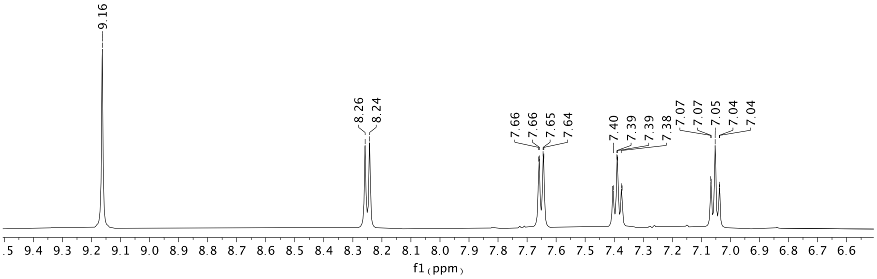

^{13}**C NMR** spectrum of **3$_{ald}$-Cl** at 298 K in THF-d_8

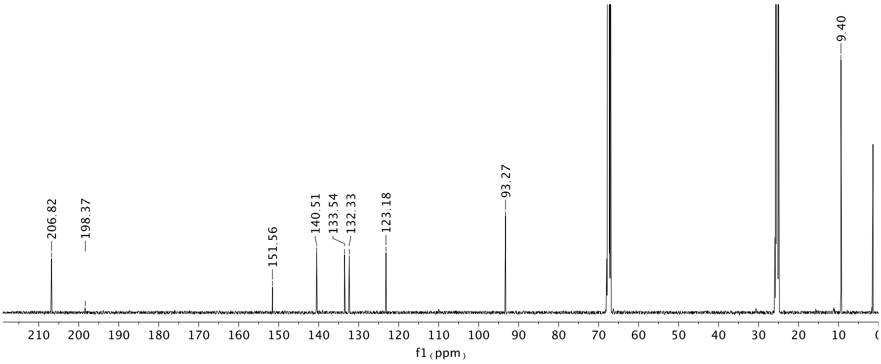

NMR characterization of complex ***1_{ald}-OAc***

^{1}**H NMR** spectrum of **1_{ald}-OAc** at 243 K in CD_2Cl_2

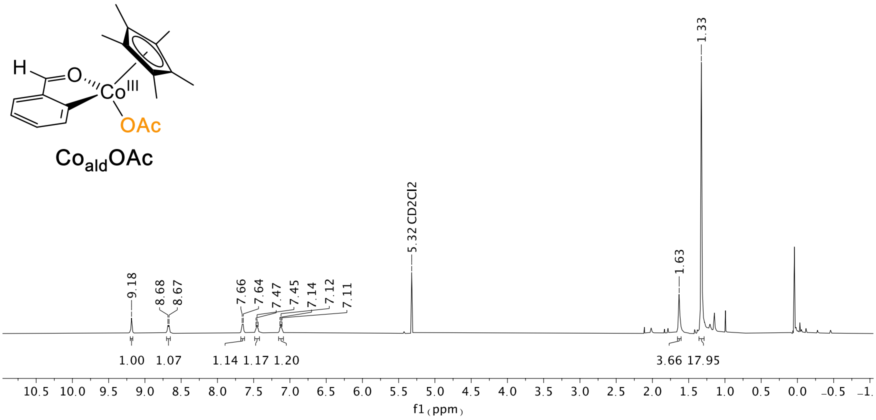

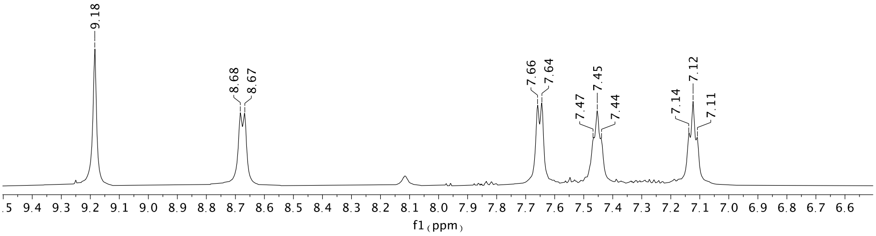

^{13}**C NMR** spectrum of **1_{ald}-OAc** at 243 K in CD_2Cl_2

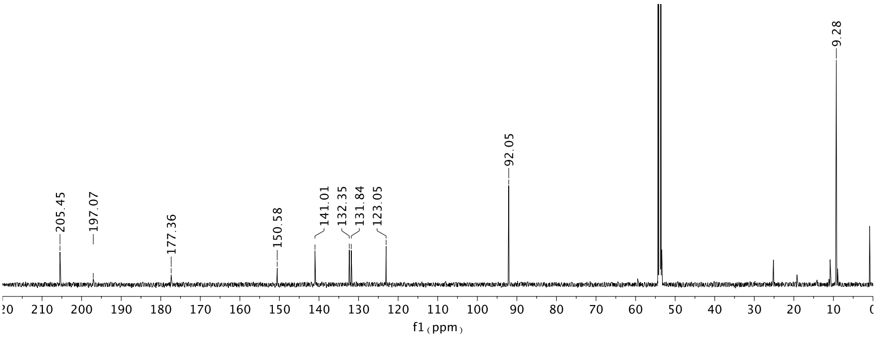

NMR characterization of complex ***1_{ald}-OTFA***

^{1}**H NMR** spectrum of **1_{ald}-OTFA** at 298 K in CD_2Cl_2

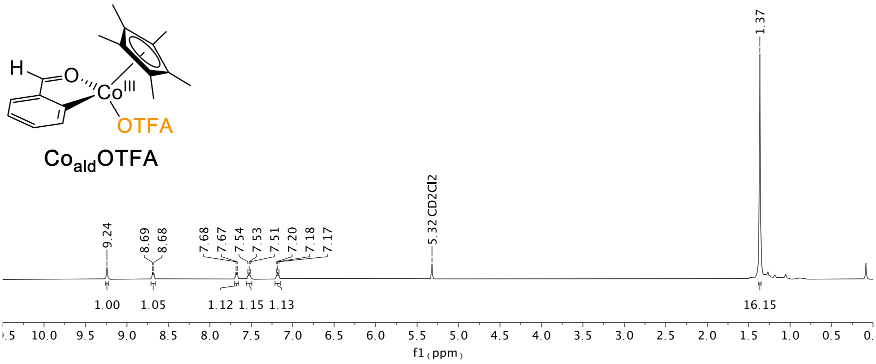

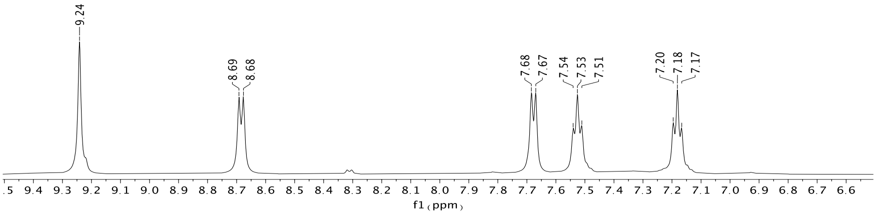

^{19}**F NMR** spectrum of **1_{ald}-OTFA** at 298 K in CD_2Cl_2

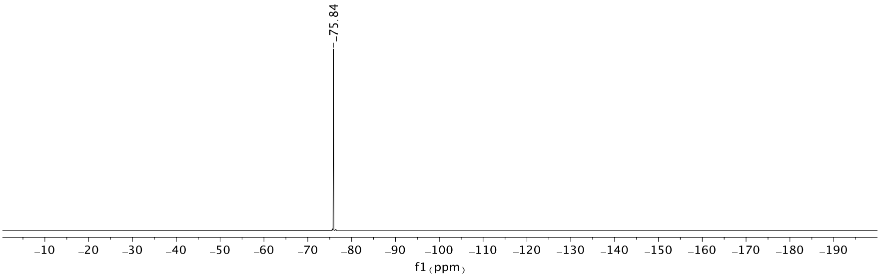

^{13}**C NMR** spectrum of **1_{ald}-OTFA** at 298 K in CD_2Cl_2

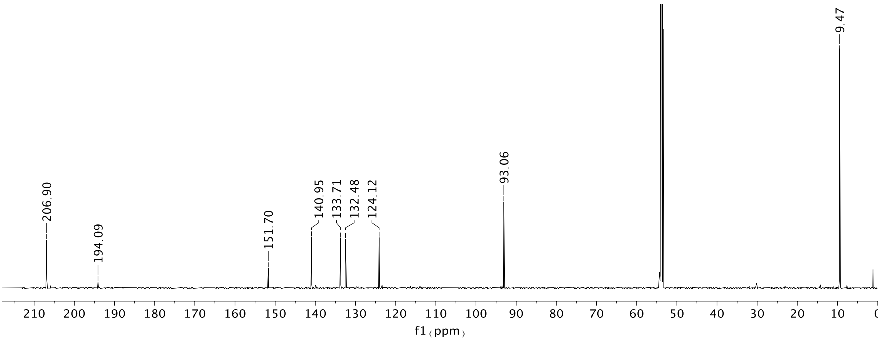

*NMR characterization of complex **1_{ald}-OTf***

^{1}**H NMR** spectrum of **1_{ald}-OTf** at 298 K in CD_2Cl_2

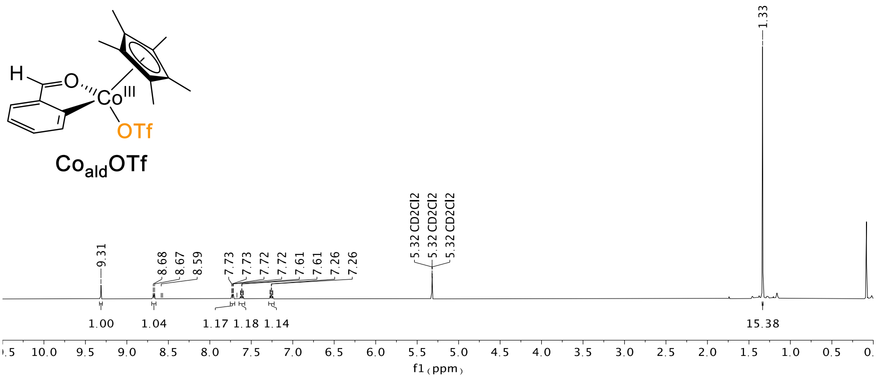

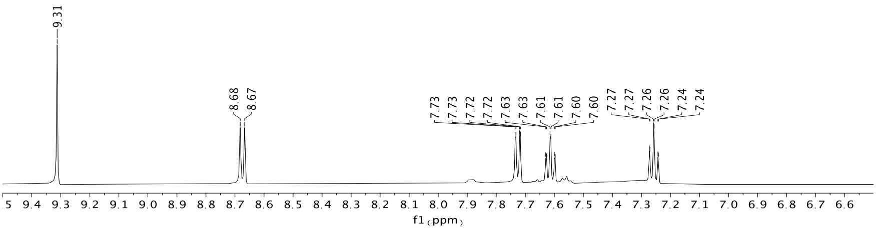

^{19}**F NMR** spectrum of **1_{ald}-OTf** at 298 K in CD_2Cl_2

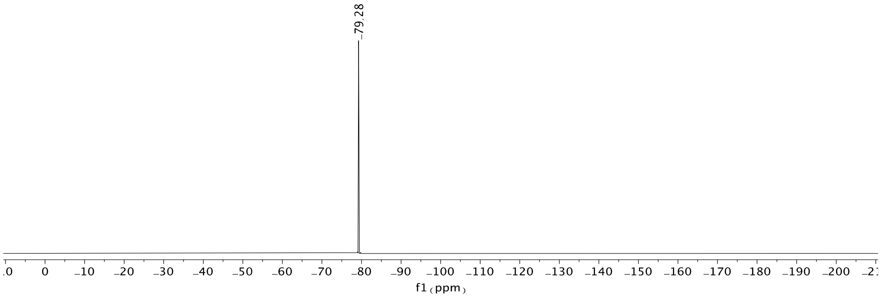

^{13}**C NMR** spectrum of **1_{ald}-OTf** at 298 K in CD_2Cl_2

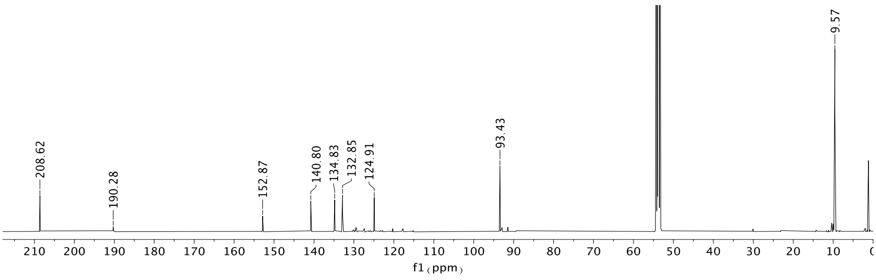

NMR characterization of complex $\mathbf{1_{ald}}$-SCF$_3$

^{1}H NMR spectrum of $\mathbf{1_{ald}}$-SCF$_3$ at 298 K in CD$_2$Cl$_2$

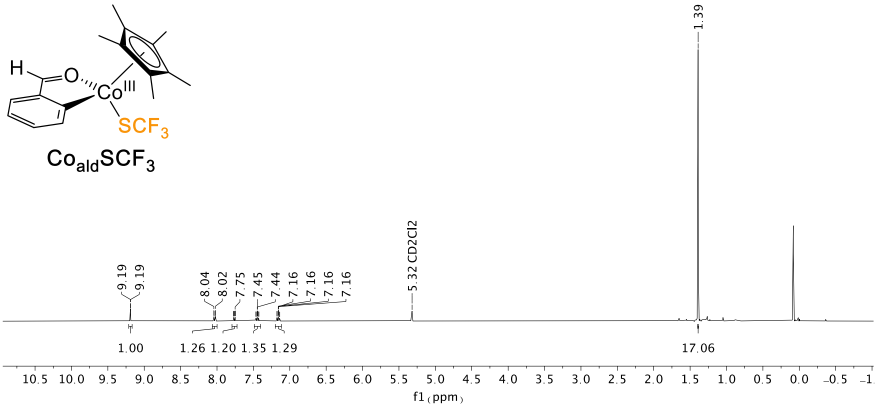

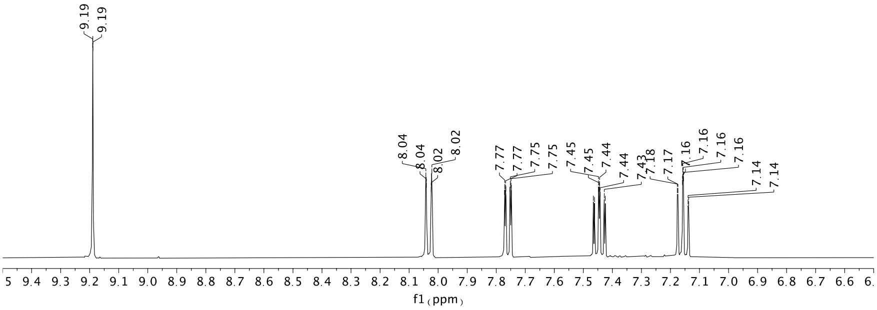

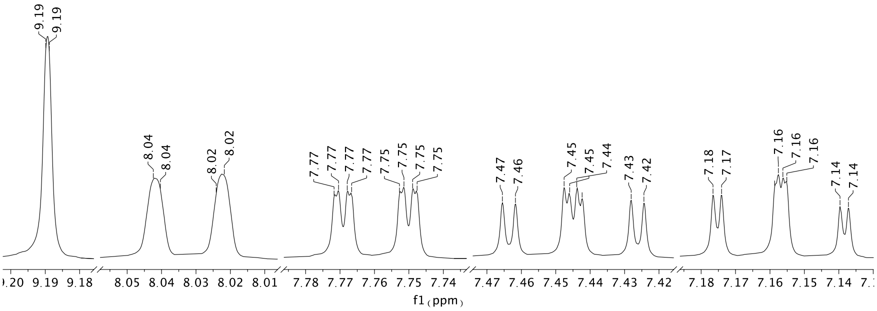

^{19}F NMR spectrum of $\mathbf{1_{ald}}$-SCF$_3$ at 298 K in CD$_2$Cl$_2$

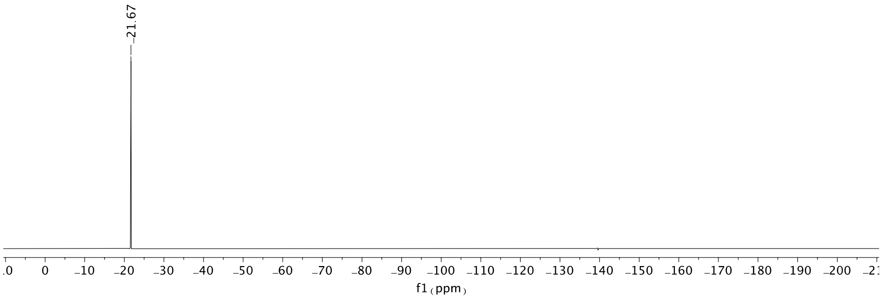

^{13}C NMR spectrum of 1_{ald}-SCF$_3$ at 298 K in CD$_2$Cl$_2$

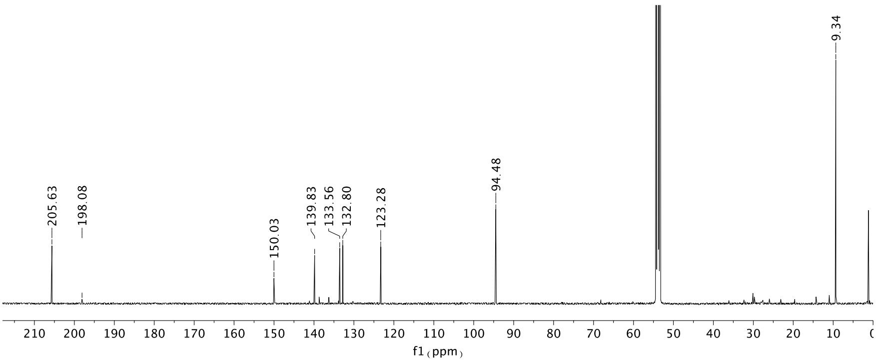

NMR characterization of complex 1_{ald}-CF$_3$

^{1}H NMR spectrum of 1_{ald}-CF$_3$ at 298 K in THF-d$_8$

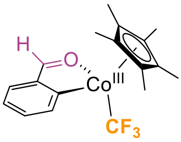

15

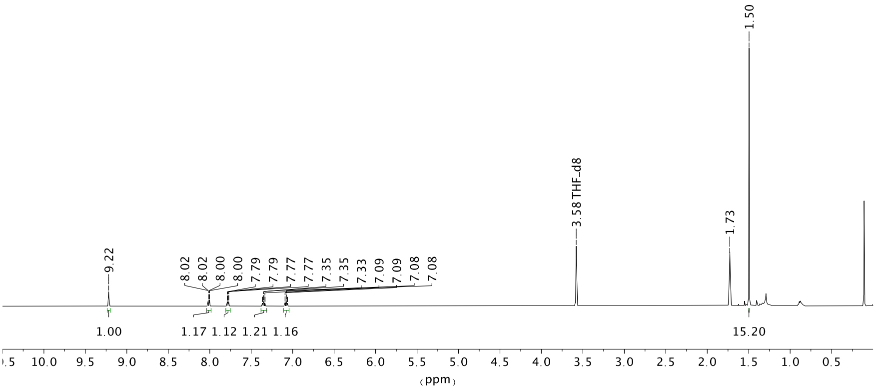

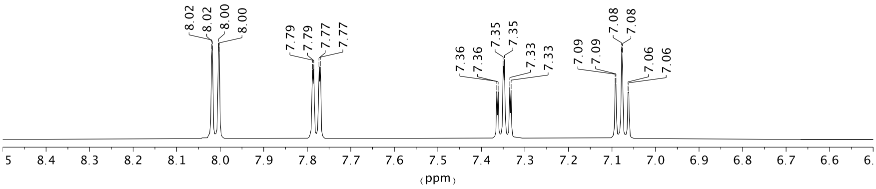

^{19}**F NMR** spectrum of **1**$_{\mathbf{ald}}$**-CF**$_3$ at 298 K in THF-d$_8$

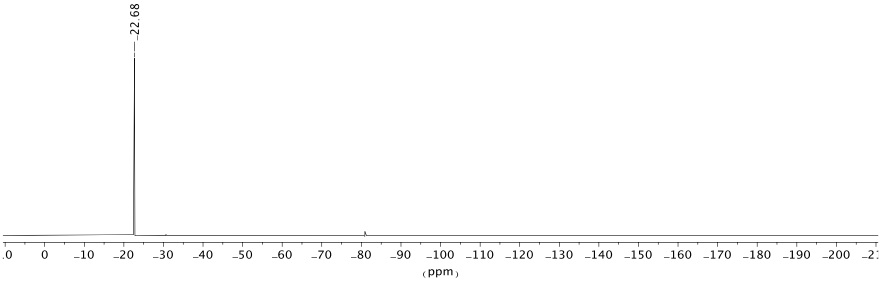

^{13}**C NMR** spectrum of **1**$_{\mathbf{ald}}$**-CF**$_3$ at 298 K in THF-d$_8$

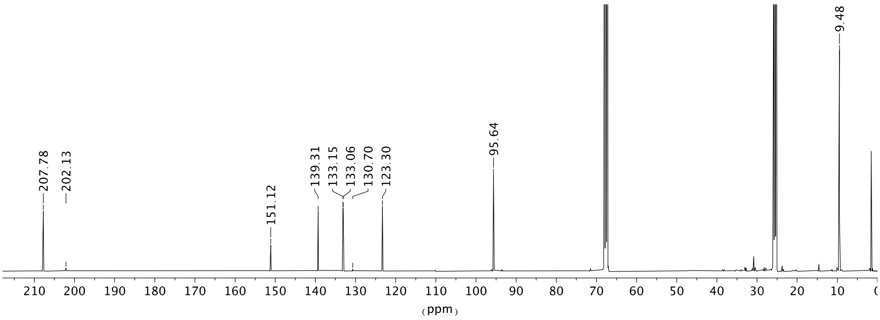

*NMR characterization of complex **1ald-C$_6$F$_5$***

^{1}**H NMR** spectrum of **1**$_{ald}$**-C$_6$F$_5$** at 298 K in CD$_2$Cl$_2$

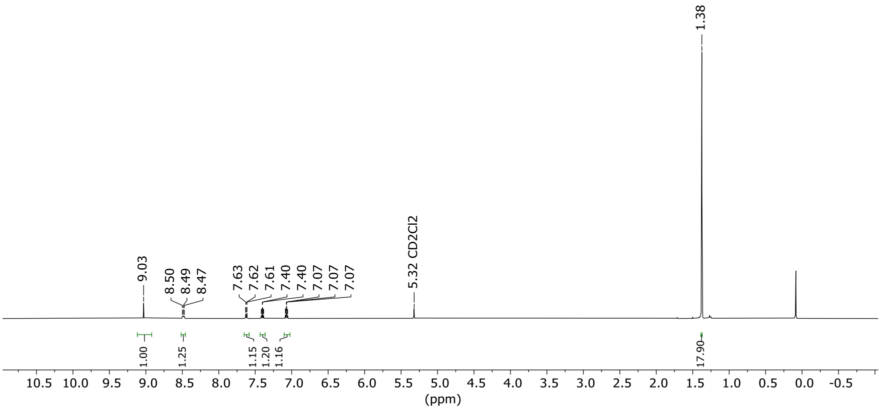

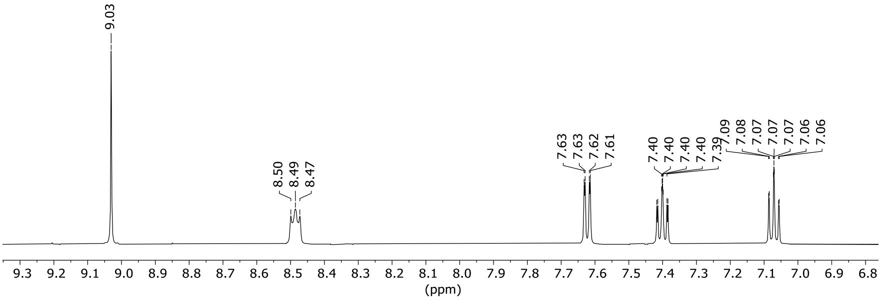

Single Crystal X-Ray Structure Determination

Crystal preparation: **1$_{ald}$-Cl**, **1$_{ald}$-OTFA**, **1$_{ald}$-SCF$_3$** and **1$_{ald}$-C_6F_5** were grown at room temperature by liquid/liquid diffusion of n-hexane into a solution of the corresponding complex in CD_2Cl_2. The crystals used for structure determination were selected using a Zeiss stereomicroscope using polarized light and prepared under inert conditions immersed in perfluoropolyether as protecting oil for manipulation.

Data collection: Crystal structure determination for samples **1$_{ald}$-Cl, 1$_{ald}$-OTFA, 1$_{ald}$-SCF$_3$** and **1$_{ald}$-C_6F_5** and were carried out using a Apex DUO Kappa 4-axis goniometer equipped with an APPEX 2 4K CCD area detector, a Microfocus Source E025 IuS using MoK$_\alpha$ radiation, Quazar MX multilayer Optics as monochromator and an Oxford Cryosystems low temperature device Cryostream 700 plus (T = - 173 °C). Crystal structure determination for samples Full-sphere data collection was used with ω and φ

scans. *Programs used:* Data collection APEX-2,[26] data reduction Bruker Saint[27] V/.60A and absorption correction SADABS.[28]

Structure Solution and Refinement: Crystal structure solution was achieved using the computer program SHELXT[29]. Visualization was performed with the program SHELXle.[30] Missing atoms were subsequently located from difference Fourier synthesis and added to the atom list. Least-squares refinement on F^2 using all measured intensities was carried out using the program SHELXL 2015.[31] All non-hydrogen atoms were refined including anisotropic displacement parameters.

Comments to the structures: Structure Structure $\mathbf{3_{ald}}$-Cl: The asymmetric unit contains one molecule of the metal complex. The structure is of good quality (no A- and commented B-alert) and publishable with a R1 value of 4.26 %. **Structure $\mathbf{3_{ald}}$-OTFA**: The asymmetric unit contains one molecule of the metal complex. The structure is of good quality (no A- and B-alerts) and publishable with a R1 value of 4.10 %. **Structure $\mathbf{3_{ald}}$-SCF$_3$**: The asymmetric unit contains one molecule of the metal complex. The SCF_3 group is disordered in two orientations (ratio 60:40). The measured crystal refined as a racemic twin (BASF: 0.48) The structure is of excellent quality (no A- and B-alerts) and publishable with a R1 value of 2.62 %.

Cyclic voltammetry analysis

A 5 mL volumetric flask was charged with complex X (0.015 mmol, 3 mM) and [NBu4][PF6] (390 mg, 1.0 mmol, 0.2 M). The solids were dissolved in DCM, mixed thoroughly and then the solvent was filled up to the line. Approximately 4 mL of the solution was transferred via a syringe to an argon filled special Schlenk containing a stir bar and the electrodes. Glassy carbon was used as the working electrode and the counter electrode, and SCE (standard calomel electrode) was used as the reference

---

[26] Data collection with APEX II version v2013.4-1. Bruker (2007). Bruker AXS Inc., Madison, Wisconsin, USA.

[27] Data reduction with Bruker SAINT version V8.30c. Bruker (2007). Bruker AXS Inc., Madison, Wisconsin, USA.

[28] SADABS: V2012/1 Bruker (2001). Bruker AXS Inc., Madison, Wisconsin, USA. Blessing, Acta Cryst. **1995**, A51, 33-38.

[29] SHELXT; V2014/4 (Sheldrick 2014). Sheldrick, G.M. *Acta Cryst*. **2015**, A71, 3-8.

[30] SHELXle; C.B. Huebschle, G.M. Sheldrick & B. Dittrich; J. Appl. Cryst. **2011**, 44, 1281-1284.

[31] SHELXL; SHELXL-2014/7 (Sheldrick 2014). Sheldrick, G.M. *Acta Cryst*. **2015**, C71, 3-8.

electrode. CV-s were recorded with scan rates ranging from 25 mV/s to 10000 mV/s. The uncompensated resistance of the solution was determined before each scan by CI (Current Interrupt) method. During the measurement the applied potential was dynamically corrected by the uncompensated resistance. The solution was stirred for a few seconds between subsequent data acquisitions. After data was recorded with multiple scan rates the Schlenk was opened under a gentle flow of Ar and ferrocene (2-3 mg) was added. CV-s were recorded in the presence of Fc to adjust the potential scale to the Fc/Fc$^+$ couple.

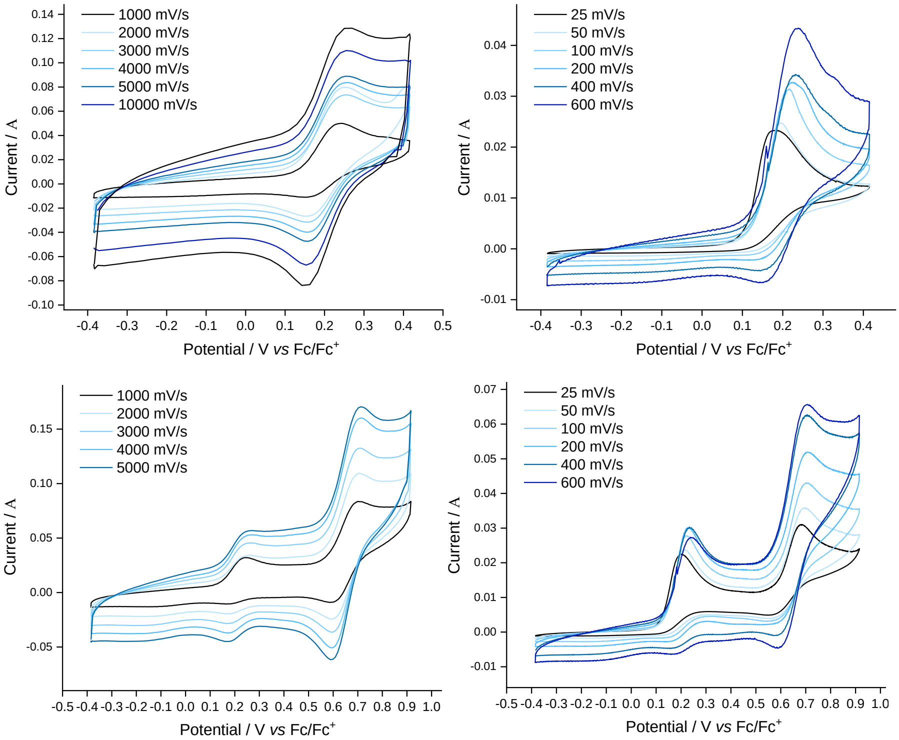

Figure 4.24 Cyclic voltammogram of complex **1$_{amd}$-I** vs Fc/Fc$^+$ in DCM/*n*NBu$_4$PF$_6$ at different scan rates.

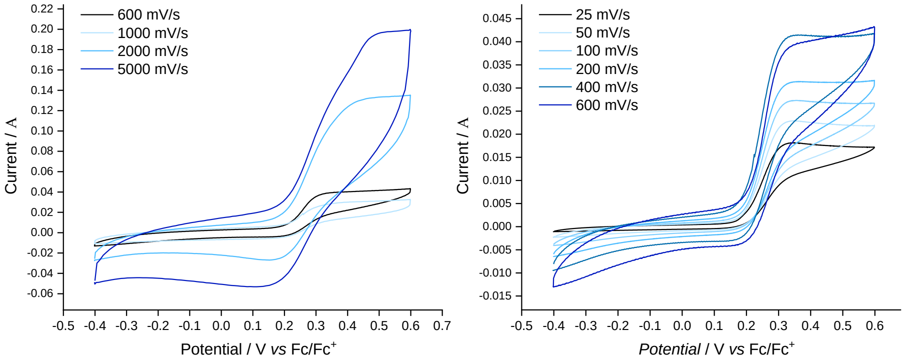

Figure 4.25 Cyclic voltammogram of complex **1$_{imi}$-I** vs Fc/Fc$^+$ in DCM/nNBu$_4$PF$_6$ at different scan rates.

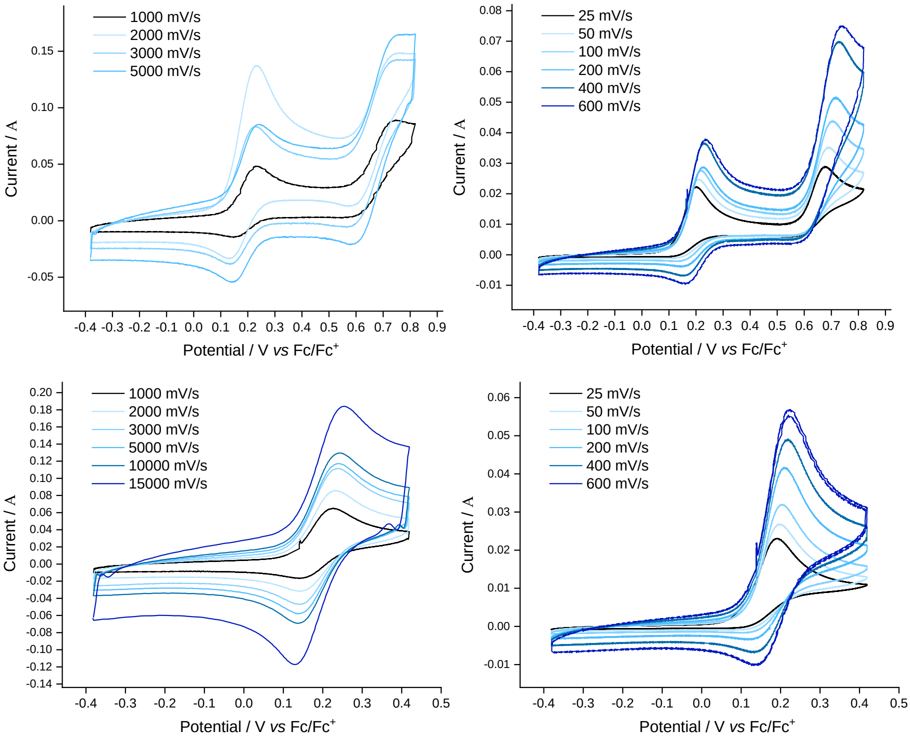

Figure 4.26 Cyclic voltammogram of complex **1$_{tBu\text{-}amd}$-I** vs Fc/Fc$^+$ in DCM/nNBu$_4$PF$_6$ at different scan rates.

UNIVERSITAT ROVIRA I VIRGILI
UNCOVERING THE MECHANISTIC SCENARIOS OF NUCLEOPHILIC COUPLINGS IN CP*CO SYSTEMS
Sara López Pesano

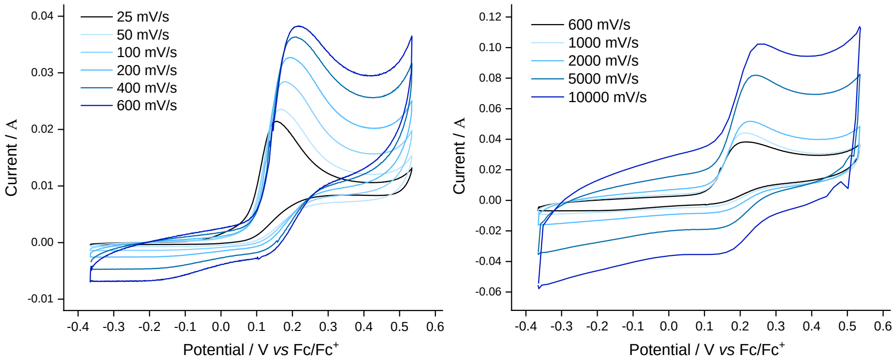

Figure 4.27 Cyclic voltammogram of complex **1_{amd}-I** vs Fc/Fc$^+$ in DCM/nNBu$_4$PF$_6$ at different scan rates.

Using electrochemical analysis to calculate the rate constant of the reductive elimination reaction (EC mechanism)

Using the method developed by Minteer and Sigman with this data we are able to calculate the rate of the chemical reaction that occurs after the redox process.[32] The Randles-Sevcik equation at room temperature is the following:

$$i_p = (2.69 \text{ x } 10^5) n^{3/2} A D^{1/2} C v^{1/2} \qquad (1)$$

where i_p is the peak current, n corresponds to the number of electrons transferred in the redox event, A is the electrode surface area, C is the concentration of the species undergoing electron transfer and v is the scan rate. According to it, the peak current is directly proportional to the concentration. The ratio between peaks can be calculated as follows:

$$\frac{i_{pc}}{i_{pa}} = \frac{[A^{n+1}]_t D_{A^{n+1}}^{1/2}}{[A^{n+1}]_0 D_{A^n}^{1/2}} \qquad (2)$$

For a reversible oxidative electron transfer, the concentration of the oxidized species, [A^{n+1}] at the electrode is equal to the initial concentration of the species being oxidized, [A^n] before the CV. Assuming that the diffusion coefficient (D) for both species is the same, the ratio between the current peaks (i_{pc}/i_{pa}) should be 1,[33] and independent of the scan rate, then,

---

[32] a) D. P. Hickey, C. Sandford, Z. Rhodes, T. Gensch, L. R. Fries, M. S. Sigman, S. D. Minteer, *J. Am. Chem. Soc.* **2019**, *141*, 1382–1392. b) C. Sandford, M. A. Edwards, K. J. Klunder, D. P. Hickey, M. Li, K. Barman, M. S. Sigman, H. S. White, S. D. Minteer, *Chem. Sci.* **2019**, *10*, 6404–6422.

[33] In some cases, it is not exactly one because of the decaying baseline.

$$\frac{i_{pc}}{i_{pa}} = \frac{[A^{n+1}]_t}{[A^{n+1}]_0} \qquad (3)$$

However, when there is an electrochemical electron transferred, followed by a chemical reaction (EC mechanism), the concentration of the oxidized species decreases, resulting in a decrease in the i_{pc} and the i_{pc}/i_{pa} ratio. Changing the scan rate of the CV alters the time for the chemical reaction, causing irreversibility and a decrease in the i_{pc}/i_{pa} ratio. Depending on the kinetic order of the reaction, the rate constant can be determined by plotting the concentration of oxidized species over time.

In our case, since we observed a difference in the cathodic current peak, we can calculate the time elapsed between the peaks and the concentration of [Co(IV)] remaining after that time. By doing so, we can determine the reaction rate of the reductive elimination from the electrogenerated Co(IV). The reaction time (t) can be calculated for a CV potential window from E_R to E_i using the following equation:

$$t = \frac{(E_i - E_{ipa}) + (E_i - E_{ipc})}{v} \qquad (4)$$

Where E_{ipa} is the peak anodic potential and E_{ipc} is the peak cathodic potential. The concentration of Co(IV) species remaining at t was determined by the ratio of i_{pa} and i_{pc} and can be calculated by equation (3).

Table 4.4 Kinetic data derived from the CVs of **1_{ald}-I** at different scan rates. The units of the data are: scan rate (Vs-1), E_{pa} and E_{pc} (V) i_{pc} and i_{pa} (A) t (s) and [Co(IV)] in M.

Scan rate	E_{pa}	i_{pa}	E_{pc}	i_{pc}	t	$[Co(IV)]_t$	$ln[Co(IV)]_t$	$1/[Co(IV)]_t$
0.025	0.39	4.83E-02	0.3	3.89E-04	20.4	2.42E-05	4.14E+04	-10.6308
0.05	0.4	6.20E-02	0.3	0.00138	10	6.68E-05	14975.85	-9.61419
0.1	0.41	6.26E-02	0.3	2.13E-03	4.9	1.02E-04	9796.557	-9.18979
0.2	0.42	6.87E-02	0.31	5.59E-03	2.35	2.44E-04	4096.601	-8.31791
0.4	0.42	8.85E-02	0.31	1.04E-02	1.175	3.53E-04	2836.538	-7.95034
0.6	0.41	8.33E-02	0.31	1.49E-02	0.8	5.37E-04	1863.535	-7.53023
1	0.41	1.05E-01	0.32	2.58E-02	0.47	7.37E-04	1356.589	-7.21273
2	0.42	1.79E-01	0.32	5.53E-02	0.23	9.27E-04	1078.963	-6.98376
3	0.43	1.96E-01	0.32	7.84E-02	0.15	1.20E-03	833.3333	-6.72543
4	0.44	2.33E-01	0.32	1.03E-01	0.11	1.33E-03	754.0453	-6.62545
6	0.44	2.56E-01	0.31	1.34E-01	0.075	1.57E-03	636.8159	-6.45648
8	0.45	3.24E-01	0.3	1.75E-01	0.05625	1.62E-03	617.1429	-6.4251

The reaction after oxidation of Co(III) exhibits second-order kinetics by the linear relationship between time (*t*) and the inverse of the concentration of Co(IV), Figure 4.28.[34]

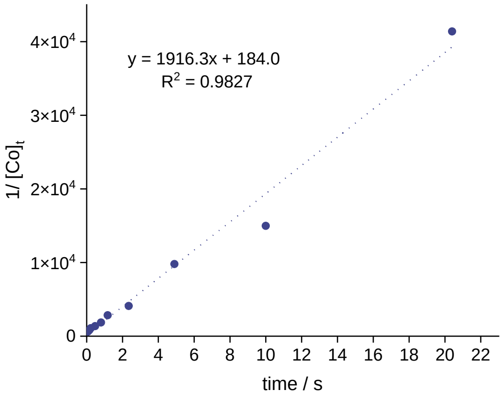

Figure 4.28 A second order kinetic plot describing the amount of electrochemically generated Co(IV) species remaining in solution after a time, t.

The slope of the plot ($2\cdot10^3$ M s^{-1}) corresponds to the reaction rate, k_{ORE} of the reductive elimination from the Co(IV) complex. As we can see the reaction is fast and the half-life of the Co(IV) species is in the scale of µs.

We also perform the same with complexes **1_{ald}-I** (Figure 4.29) and **1_{ald}-Br** (Figure 4.30). From the data obtained with the CVs we calculated the kinetic order of the disappearance of the Co(IV) species, in both cases they exhibit first-order kinetics by the linear correlation between time (*t*) and the natural logarithm of the concentration of Co(IV), Figure 4.29.

We observed different orders on Co depending on the nucleophile employed, while the brominated cobaltacycle **8** showed 1st order kinetics, the chlorinated species 9, shows a better fitting with 2nd order kintetics. The slope of the plot corresponds to the rate contance of the disappearance of the Co(IV) complex. In case of the brominated species is 0.1446 s^{-1} for the chlorinated compound is 288.5 M^{-1} s^{-1}.

---

[34] First-order kinetic plot does not fit into a straight line, the plot is included in the experimental appendix.

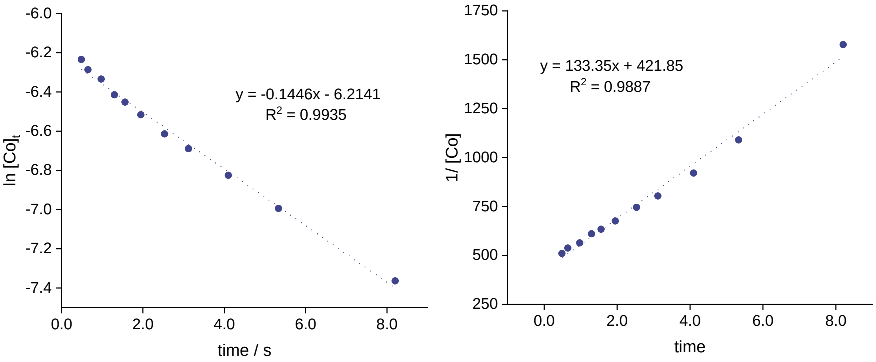

Figure 4.29 A first (left) and second (right) kinetic plot of **1**$_{\mathbf{ald}}$**-Br** describing the amount of electrochemically generated Co(IV) species remaining in solution after a time, t.

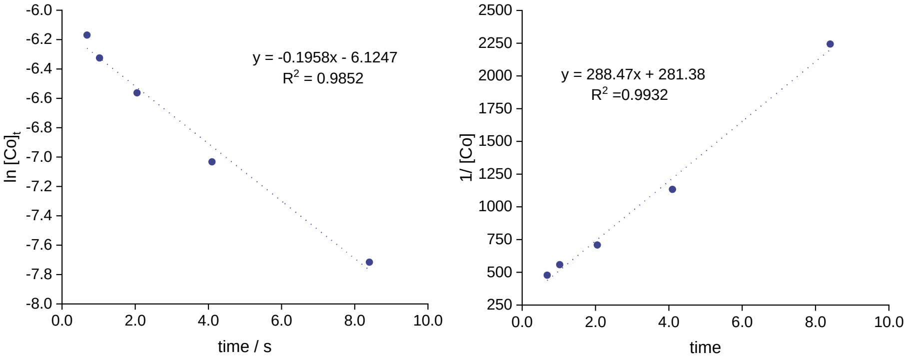

Figure 4.30 A first (left) and second (right) kinetic plot of **1**$_{\mathbf{ald}}$**-Cl** describing the amount of electrochemically generated Co(IV) species remaining in solution after a time, t.

Chronoamperometry experiments for the ORE

We used a SCE (Saturated Calomel electrode) reference electrode and carbon felt as high-surface area counter (12 x 12 x 30 mm) and working (4 x 3 x 40 mm) electrodes in a two-compartment cell to separate cathode and anode.

The cell was charged with first win 28 mL of DCM under Ar. After the height of the solvent was the same in both compartments the cell was transferred to the potentiostat, where **1**$_{\mathbf{DG}}$**-X** (0.01 mmol) and [NBu$_4$][PF$_6$] (30 mg, 0.08 mmol) dissolved in DCM (1 mL) was added to the WE compartment and [NBu$_4$][PF$_6$] (30 mg, 0.08 mmol) dissolved in DCM (1 mL) was added to the CE compartment. The two solutions were added at the same time via a syringe.

The required potential was applied until the necessary charge was transferred in order to fully oxidize cobaltacycle to cobalt(IV) species, (for 0.01 mmol 0.96 Coulombs) or until the current decrease to 0. Subsequently, the solution was filtered using a 0.2 mm PTFE filter and transferred to a Schlenk flask to evaporate the solvent. A known amount of internal standard was added and the final product was analyzed by ^{1}H and/or ^{19}F NMR spectroscopy.

1_{DG}-I

We explored the use of electrochemistry as a selective means to oxidize the Co(III) species to Co(IV) and facilitate C–I bond formation. We obtained preliminary results using two amide-containing complexes, **$1_{tBu\text{-}amd}$-I** and **1_{amd}-I**. However, the desired product was only obtained in low yield.

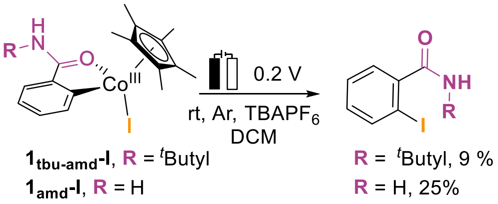

Scheme 4.7 Electrochemical oxidation of the Co(III) complexes. Applied potential values are referenced to Fc/Fc^{+}.

*Additional reactivity studies with **1_{ald}-C_6F_5***

We conducted a detailed investigation into the reactivity of the pentafluorophenyl cobaltacycle complex **1_{ald}-C_6F_5**. Through cyclic voltammetry analysis, we observed an irreversible oxidation peak at 0.51 V vs Fc/Fc^{+}. Remarkably, this oxidation peak remained consistent even at high scan rates. This behavior suggests that once the Co(IV) species is generated, it undergoes a rapid chemical reaction, leading to the consumption of the Co(IV) species.

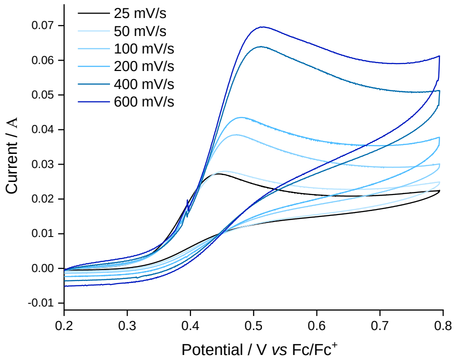

Figure 4.31 Cyclic Voltammograms of **21** recorded at different scan rates.

We explored the reactivity of complex **1_{ald}-C_6F_5** towards oxidatively induce reductive elimination under various conditions. Initially, we examined its reactivity with F^+ oxidants, and interestingly, only NFSI proved to be effective. Surprisingly, the reaction proceeded quite slowly, we monitored its progress using 1H NMR at different times (1h, 2h, 5h, 24h, 48h, and 96h). After an extended reaction time of 96 hours, we achieved a yield of 97%.

Given that the thermal decomposition of the complex was completed faster within 18 hours, we decided to explore the combination of thermal and oxidative conditions to expedite the reaction. Gratifyingly, by subjecting the reaction to both conditions simultaneously, we were able to obtain an excellent yield of 95% within just 5 hours. We also investigated the possibility of promoting the reaction electrochemically. Applying a potential of 0.48 V vs Fc/Fc$^+$ for 4 hours, obtained a 31 % yield.

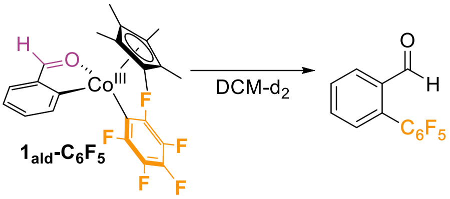

Conditions	Time	NMR yield
Thermolysis 100 ºC	18 h	92 %
[a] NFTPB	96 h	traces
[a] NFSI	96 h	97 %
[a] NFSI at 100 ºC	5 h	95 %
[b]CA at 0.48 V	4	31 %

Table 4.5 C-C_6F_5 bond formation reaction at different conditions. [a]2 equivalents of the oxidant were used. [b]The potential is referenced vs Fc/Fc$^+$ couple.

4.5.2. Computational appendix

DFT calculations were performed using the Gaussian09[35] package with the M06-D3 (where D3 stands for GD3[36] empirical dispersion) functional.[37] All geometry

---

[35] Gaussian 09, Revision D.01, M. J. Frisch, G. W. Trucks, H. B. Schlegel, G. E. Scuseria, M. A. Robb, J. R. Cheeseman, G. Scalmani, V. Barone, B. Mennucci, G. A. Petersson, H. Nakatsuji, M. Caricato, X. Li, H. P. Hratchian, A. F. Izmaylov, J. Bloino, G. Zheng, J. L. Sonnenberg, M. Hada, M. Ehara, K. Toyota, R. Fukuda, J. Hasegawa, M. Ishida, T. Nakajima, Y. Honda, O. Kitao, H. Nakai, T. Vreven, J. A. Montgomery, Jr., J. E. Peralta, F. Ogliaro, M. Bearpark, J. J. Heyd, E. Brothers, K. N. Kudin, V. N. Staroverov, T. Keith, R. Kobayashi, J. Normand, K. Raghavachari, A. Rendell, J. C. Burant, S. S. Iyengar, J. Tomasi, M. Cossi, N. Rega, J. M. Millam, M. Klene, J. E. Knox, J. B. Cross, V. Bakken, C. Adamo, J. Jaramillo, R. Gomperts, R. E. Stratmann, O. Yazyev, A. J. Austin, R. Cammi, C. Pomelli, J. W. Ochterski, R. L. Martin, K. Morokuma, V. G. Zakrzewski, G. A. Voth, P. Salvador, J. J. Dannenberg, S. Dapprich, A. D. Daniels, O. Farkas, J. B. Foresman, J. V. Ortiz, J. Cioslowski, D. J. Fox, Gaussian, Inc., Wallingford CT, 2013.

[36] S. Grimme, Semiempirical GGA-type density functional constructed with a long-range dispersion correction, *J. Comput. Chem.* **2006**, *27*, 1787.

[37] Y. Zhao, D. G. Truhlar, *Theor. Chem. Account.* **2008**, *120*, 215.

UNIVERSITAT ROVIRA I VIRGILI
UNCOVERING THE MECHANISTIC SCENARIOS OF NUCLEOPHILIC COUPLINGS IN CP*CO SYSTEMS
Sara López Resano

optimizations were carried out in solution without symmetry restrictions with LANL2DZ as the basis set for cobalt and silver,[38]and 6-31G(d)[39] for the remaining atoms. Implicit solvent was modeled through the SMD method.[40] Calculations were carried out in DCM (ε = 8.93). For all calculations, vibrational frequency calculations were computed to establish the nature of all stationary points (zero imaginary frequencies for minima and one for transition states). All the calculations have been carried out at 298.15K and 1 atm.

---

[38] LANL2DZ T. H. Dunning Jr. and P. J. Hay, in *Modern Theoretical Chemistry*, Ed. H. F. Schaefer III, Vol. 3 (Plenum, New York, **1977**) 1.

[39] (a) W. J. Hehre, R. Ditchfield, J. A. Pople, *J. Chem. Phys.* **1972**, *56*, 2257; (b) J. D. Dill, J. A. Pople, *J. Chem. Phys.* **1975**, *62*, 2921; (c) M. M. Francl, W. J. Petro, W. J. Hehre, J. S. Binkley, M. S. Gordon, D. J. DeFrees, A. J. Pople, *J. Chem. Phys.* **1982**, *77*, 3654.

[40] S. A. V. Marenich, C. J. Cramer, D. G. Truhlar, *J. Phys. Chem. B* **2009**, *113*, 6378.

UNIVERSITAT ROVIRA I VIRGILI
UNCOVERING THE MECHANISTIC SCENARIOS OF NUCLEOPHILIC COUPLINGS IN CP*CO SYSTEMS
Sara López Resano

Chapter 5. General Conclusions

UNIVERSITAT ROVIRA I VIRGILI
UNCOVERING THE MECHANISTIC SCENARIOS OF NUCLEOPHILIC COUPLINGS IN CP*CO SYSTEMS
Sara López Resano

This Doctoral Thesis delves into the mechanistic intricacies of nucleophilic couplings with Cp*Co-based systems involving C–X and C–C bond forming reactions. The most relevant remarks for each research chapter a are the following:

In *Chapter 2* we presented a comprehensive investigation of the mechanism underlying the formation of C–SCF_3 bonds in Cp*Co-catalyzed C–H functionalizations. By combining experimental and computational studies, our research challenges the previously proposed mechanism that involved direct reductive elimination from a Co^{III} species. By synthesizing a reactive intermediate implicated in catalysis, we have provided compelling evidence of the intermediacy of oxidatively induced reductive elimination steps via Co^{IV} species. Moreover, these reactions can be promoted not only through the application of chemical oxidants ($AgSCF_3$ and $Mn(OAc)_3·2H_2O$) but also by utilizing electrochemical methods.

In *Chapter 3* we combined fundamental studies to demonstrate that F^+ oxidants (NFTPT and NFSI) can be used to trigger high-yielding nucleophilic C–I couplings via high-valent cobalt species under mild conditions. Through various experimental techniques and computational calculations, we discovered that these oxidative reactions proceed via Co^V species, yet following slightly different reaction pathways considering the resulting cobalt species after the reductive elimination. We anticipate that the ability of Co^V complexes to engage in nucleophilic couplings can ultimately be exploited in catalysis.

In *Chapter 4* we compared the reactivity a family of metalacyclic Cp^*Co^{III} complexes that contain different heteroatom- and carbon-based nucleophilic moieties towards reductive elimination events using F^+ oxidants. Throughout these studies, we revealed a remarkable influence of the employed nucleophile. While oxidatively induced reductive elimination to form C–X (X= I, Br) and C–S bonds were successfully achieved, the formation of C–Cl, C–O posed greater challenges. Additionally, the nature of the directing group has a profound impact on the feasibility of OREs. Weakly directing groups containing amides, and the strong directing group imine exhibited good reactivity to form C–I bonds, whereas the widely used 2-phenylpyridine moiety showed the poorest performance. Surprisingly, by using well-defined and isolable metalacyclic Co^{III} compounds, we showed the promotion of C–C reductive elimination events without modifying the oxidation state of the cobalt center. The experimental and

UNIVERSITAT ROVIRA I VIRGILI
UNCOVERING THE MECHANISTIC SCENARIOS OF NUCLEOPHILIC COUPLINGS IN CP*CO SYSTEMS
Sara López Resano

computational studies described demonstrate the complementary reactivity of the distinct oxidation states.

In summary, this thesis uncovers unprecedented mechanistic understanding on nucleophilic coupling from Cp*Co-based systems. We envision that the detailed studies described herein will ultimately prove valuable in the development and optimization of new C–H functionalization reactions, opening the door to new reactivity patterns in catalysis.